PROPERTY-MICROSTRUCTURAL RELATIONSHIPS IN GFRP

BY

FELICITY JEAN GUILD

This thesis was submitted in accordance with the Regulations of the Council for National Academic Awards for the Degree of Doctor of Philosophy.

School of Engineering Science,
Plymouth Polytechnic.

March, 1978.

Contents

List of Tables

Page No.

List of Figures

Acknowledgements

This work was carried out under the financial support of the School of Engineering Science, Plymouth Polytechnic. I am indebted to Mr. David Short for many useful discussions, and for his continuing help and enthusiastic support since I left Plymouth. I would like to thank Mr. Barrie Undy, of the School of Mathematical Sciences, for his help with and interest in the statistical work. My thanks are due to many members of the technical staff, particularly Mr. David Burridge and Mr. Brian Lord. My grateful thanks are also due to Miss Margaret Moreland and other staff of the Computer Centre for their assistance with the extensive computing.

I gratefully acknowledge the use of Specific Damping Capacity measurement equipment at the Department of Mechanical Engineering, University of Bristol. I would like to express my appreciation to Dr. Robert D. Adams for many useful discussions and his supervision of that work. My thanks are also due to Dr. David Walton for his help with rig design, and to Mr. Brian Smith for making the rigs.

I gratefully acknowledge the use of the Quantimet and Stereoscan at the Department of Metallurgy and Materials Science, University of Cambridge. My thanks are due to Mr. John Ward for his help with taking Quantimet measurements. Finally, I am indebted to Dr. Brian Ralph for many useful discussions regarding the microstructural work, and for his kind help and encouragement throughout the course of the work.

DECLARATION

I hereby certify that this work has not been accepted for any degree, and is not being concurrently submitted in candidature for any degree other than the degree of Doctor of Philosophy of the Council for National Academic Awards.

Candidate: ....Felicity Guild.....

Felicity Jean Guild

ABSTRACT

This work consists of an investigation into the microstructure and mechanical behaviour of glass fibre reinforced polyester resin beams. The volume fraction occupied by glass fibres was 20-30%, which is that typically used in boat building. The beams tested were all unidirectional, with fibres oriented parallel or perpendicular to the long axis of the beam. Various techniques have been developed which may be applicable to other composite materials.

The microstructure of the beams was investigated by observation of cross-sections using a Quantimet 720 Image Analysing Computer. Volume fractions and the distribution of fibre cross-sectional areas were measured. Methods have been developed for the quantitative definition of the microstructure in terms of the fibre arrangement.

Cracks were grown in four-point flexural loading while monitoring acoustic emission. The acoustic emission circuit was built in the laboratory, and designed to monitor fibre failures only, one count being associated with one fibre failure. The processes of crack growth were further investigated by observation of fracture surfaces using a scanning electron microscope and measurement of crack profiles. The factors controlling the processes of crack growth have been elucidated.

The material condition was monitored by specific damping capacity measurements. A free-free rig with excitation at the ends of the beam was developed. In addition measurements were made using a cantilever rig. Simple analyses involving

the solution of the classical wave equation were carried out; a receptance analysis was also developed which allows the undamaged and cracked portions of the beam to be separated in the analysis. Invisible cracks, which had been indicated by acoustic emission, were successfully detected in both rigs.

The correlation between recorded acoustic emissions and specific damping capacity measurements supports the validity of both techniques. Some correlation between properties and measured microstructures has been obtained here. These quantitative methods for the measurement of the microstructure of composite materials should prove very useful in a wide range of applications.

Nomenclature

A	=	Coil calibration factor
	=	Cross-sectional area of beam
	=	Area of cell
A_t	=	Area of test cell
A,B,C,D	=	Constants used in solution of classical wave equation
a_o, a_1, a_2, a_3, a_4	=	Stress dependence coefficients of specific damping capacity
a, b	=	Substitution constants used in receptance analysis
B	=	Flux density
b	=	Beam width
C	=	Capacitance
C_1, C_2	=	Capacitance values in diode pump
C_1, C_2	=	Constants used in variance analysis
C_3, C_4	=	Constants used in sparse analysis
E	=	Young's modulus
F	=	Force
$F_1, F_2, F_3, F_4, F_5, F_6$	=	Substitution constants used in receptance analysis
G	=	Shear modulus
h	=	Beam height
I	=	Second moment of area
	=	Direction perpendicular to glass layers
I_c	=	Rotary inertia of exciting coil
i	=	Current
J	=	Direction parallel to glass layers
K	=	Thermal conductivity
k	=	Wavelength number
l	=	Beam length
	=	Conductor length
l_c	=	Length of exciting coil

M	=	Total end mass
m	=	Mass
m_1, m_2, m_4	=	First, second and fourth moments about zero of area distribution of fibres
n	=	Mode number
	=	Number of samples
n_t	=	Number of test cells in cell
P	=	Mass of exciting coil
q	=	Heat transfer
R	=	Resistance
R_f	=	Forward resistance of diode
R_0,R_1,R_2,R_3,R_4	=	Constants for a given beam used in calculation of stress dependent specific damping capacity
r	=	Radius of sphere
r, s	=	Substitution constants used in receptance analysis
s^2	=	Observed variance of fractional area covered
T	=	Period
T_N	=	Time constant for negative fall
T_P	=	Time constant for positive rise
ΔT	=	Temperature difference
t	=	Time
U	=	Total strain energy stored during a cycle
U_B	=	Bending strain energy stored during a cycle
U_S	=	Shear strain energy stored during a cycle
ΔU	=	Energy input per cycle
	=	Energy absorbed by beam per cycle
ΔU_B	=	Energy dissipated in beam by bending per cycle
ΔU_S	=	Energy dissipated in beam by shear per cycle
u	=	Deflection
u_B	=	Bending deflection

u_S = Shear deflection

u_1, u_2 = Amplitudes of consecutive cycles

V = Voltage

v = Velocity

X = Constant for a given free-free beam in solution of classical wave equation

x = Distance along beam length

Y = Constant for a given cantilever beam in solution of classical wave equation

Z = Energy loss per cycle

z = Distance from neutral axis

= Depth of sphere

α, β, γ, δ, ε = Receptances

Δ = Constant used in receptance analysis

δ = logarithmic decrement

θ = Angular displacement

λ = Frequency number

= Mean number of particles per cell

λ_S = Shear Constant

ρ = Density of beam material

σ = Longitudinal bending stress

σ^2 = Theoretical variance of fractional area covered

τ = Shear stress

ψ = Specific damping capacity

ψ_m = Measured specific damping capacity

ψ_T = True specific damping capacity

w = Angular frequency

Chapter 1 Introduction

Glass fibre reinforced polyester resin composites are established materials for many applications including the production of yachts and small boats. The most usual process is still that of hand lay-up, which produces a fibre volume fraction of 20-30%. The resin is left to cure at ambient temperature. Typically very little control can be exercised over this process and the fibre content and arrangement are variable.

Original designs of GFRP hulls were identical to proven designs in wood. The inherent anisotropy of the material was ignored and minimised by the use of random mats. Modern designs increasingly seek to make use of the anisotropy of the material; considerable weight savings can thus be achieved. Such design requires known and consistent mechanical behaviour of the material.

1.1 Principles of Fibre Reinforcement

Fibre reinforced materials allow the use of strong stiff materials which would be unrealistic engineering materials by themselves, usually because of their brittle nature and susceptibility to surface damage. When glass fibres are embedded in polyester resin the length of a continuous crack in the glass is restricted and the interface stops or diverts the crack, thus increasing the energy required to propagate the crack, or the fracture toughness. The role of the resin is therefore to protect the fibres and to prevent the

propagation of unstable brittle cracks which occur in bulk glass. The glass fibres provide stiffness and strength, so the resin must transfer stress to the fibres at the fibre/resin interface. Tensile stress is transferred at the interface by shear stress arising from the difference in moduli. The interface must obviously be continuous to allow the shear stress to exist. The importance of the interface can thus be clearly seen; the condition of the interface is the most usual fault in commercial mouldings, as described in Chapter 4.

1.2 Mechanical Behaviour

1.2.1 Elastic Constants

The elastic behaviour of composite materials is stated in terms of elastic constants. The assumption that consistent elastic constants for a composite material can both be measured experimentally and predicted from theoretical considerations is based on the definition of average stress and strain in the composite. This means that the material must be macroscopically homogeneous, that is, the fibre cross-sectional dimensions must be negligibly small compared with both the structural dimensions of the specimen under test, and the dimension over which significant variation in applied load or displacement occurs. Experimental experience confirms that meaningful material moduli may be defined, and the assumption of macroscopic homogeneity is thus justified.

The theoretical prediction of the elastic constants of a fibre reinforced composite material from the properties of the fibre and matrix is the subject of micromechanics. The material may be considered in its real physical form, that is,

as a true heterogeneous material, and details such as the interactions between individual filaments and the properties of the interfacial zone may be taken into account.

Macromechanics is the study of the behaviour of a laminated composite in terms of the properties of the single plys, by, for example, classical laminated plate or shell theory. The present work does not extend into this area since all material tested was unidirectional.

Various theories for the prediction of the mechanical behaviour of fibre composite materials have been proposed; a review has been made, for example, by Chamis and Sendeckyj (1968). The most commonly applied prediction for the longitudinal modulus of unidirectional fibre composites is the rule of mixtures, and these predictions are, in general, well fulfilled. The theory is essentially a parallel spring model in which all interactions between constituents are ignored. The theory, however, yields very low values for transverse Youngs modulus and shear modulus.

There are various approaches for more rigorous consideration of the material. Variational methods use the energy theorems of classical elasticity to obtain bounds. Identical bounds were obtained independently by Hill (1964) and Hashin and Rosen (1964); Hill showed by formal and physical arguments that these bounds are the best obtainable without taking into account the detailed geometry.

Estimates of elastic constants can be gained from strength of materials approaches, of which there are numerous examples.

The averaged stress-strain state of the composite is expressed in terms of the state of the constituents, with appropriate boundary conditions. However the assumptions made regarding the stress and strain distributions are hard to justify.

There are several possible approaches if assumptions are made regarding the arrangement of the fibres. If an exact filament arrangement is assumed, an exact solution may be obtained. Finite element techniques may be used if the fibre arrangement is defined. It is postulated that the techniques of measuring fibre arrangement developed here may be applicable to the prediction of elastic constants using finite element techniques.

1.2.2 Failure of Fibre Composites

The failure processes in composite materials may be described mechanistically in terms of the extension of a crack. Such processes in carbon/epoxy composites have been described by Mullin and Mazzio (1972). Crack growth in glass/polyester composites has been described by Harris et al (1975); crack growth in model composites was observed and analysed. This work is further described and compared with results obtained in the present work in Chapter 6.

The extension of a crack is quantitatively described for isotropic materials using the techniques of linear elastic fracture mechanics. There have been numerous attempts to extend these methods to composite materials. The mathematical modelling has been extended to include anisotropic materials (Sih et al 1965). It is generally accepted that the technique

is applicable when the failure is essentially brittle, for example when fibres are parallel to the direction of crack growth (Owen and Bishop 1973), or when failure occurs by transverse splitting (Wright and Iannuzzi 1973). Difficulty arises when energy is used by several different, irreversible, processes such as those discussed by Harris et al (1975). As may be anticipated, the techniques of linear elastic fracture mechanics underestimate the measured parameters (e.g. Beaumont and Phillips 1972). It therefore seems likely that the failure of composite materials may be best described by the work of fracture approach. However discrepancies may be encountered from different sizes and test methods (Ellis and Harris 1973). The author believes that some explanation of these discrepancies may be found from the work of Harris et al (1975). Different sizes and test methods may lead to different pull-out lengths which would lead to different values of work fracture.

Some attempts have been made to describe the overall failure of composite materials. Zweben and Rosen (1970) proposed a statistical model of cumulative failure arising from progressive failure of the weaker fibres. Wu (1974) has shown the extension of fracture models for isotropic materials to anistropic materials, but concludes that the failure of composite materials may best be described by a critical volume approach.

1.3 Experimental Programme

1.3.1 Material and its Microstructural Definition

The glass fibres and polyester resin used are described in

Chapter 4. The material under investigation is intended to be typical of that used in boat building. However, as described in Chapter 4, material made commercially is unsuitable for this investigation; beams were therefore prepared in the laboratory. The beams were all unidirectional, with fibres oriented parallel to the long axis of the beam, 0^{o} beams, or with fibres oriented perpendicular to that axis, 90^{o} beams. The microstructure of the beams was quantitatively determined by observations of sections cut perpendicular to the fibre direction using a Quantimet 720 Image Analysing Computer.

The operation of the Quantimet will be very simply described. A scanner produces an image on a television screen, from either a microscope or an epidiascope. The picture on the screen is divided into small areas known as picture points; the entire screen area, or frame, contains 500,000 picture points. Measurement from the Quantimet is in terms of picture points. Measurement can take place in the whole screen, or standard frame, or in a smaller frame of variable size and position. The contrast on the screen is divided into 64 different grey levels; the threshold for detection is set in terms of grey levels. Detected features can be modified in various ways; for example, an annulus can be changed to a disc using 'fill'. Detected features, as detected or after modification, can be analysed in terms of shape and size. The operation of the Quantimet used in this work is controlled both by its hard wiring and by a Hewlett-Packard 9835 programmable calculator.

The Quantimet allowed the microstructure of the beams to be quantitatively determined. As described in Chapter 4, volume fractions occupied by fibres were simply found from area fraction measurements. The distribution of the fibre cross-sectional areas was determined, as described in Chapter 4, and thus the number of fibres in a given area could be estimated after volume fraction measurement. This procedure was used to estimate the numbers of broken fibres from measurement of crack profiles, as described in Chapter 6.

In addition to these measurements, the Quantimet was used to develop quantitative methods for the definition of the microstructure in terms of the fibre arrangement. The development of these statistical methods is described in Chapter 5. Correlation between these measurements and properties is sought in Chapter 8.

1.3.2 Crack growth and its Monitoring by Acoustic Emission

Cracks were grown in four-point flexural loading, using an Instron screw driven testing machine, while monitoring acoustic emission. A literature survey of the acoustic emission technique is presented in Chapter 2. An acoustic emission circuit, designed to record counts from fibre failures only, one count being associated with one fibre failure, was built in the laboratory. The design and development of this circuit is described in Appendix 2. The four-point bend tests and the fracture and acoustic emission results are described in Chapter 6. The processes of crack growth were further elucidated by observation of fracture surfaces using a scanning electron microscope, and measurement of crack profiles.

1.3.3 Specific Damping Capacity Measurements

Specific damping capacity measurements provide an insight into material condition of a beam without destruction of the beam. The development of the rigs, and the analyses, is described in Chapter 3. Free-free vibration is the form of flexural vibration least likely to introduce extraneous energy losses. The free-free rig available requires the clamping of a coil in the centre of the beam, the region where cracks would be present after the flexural loading. A new rig with excitation at the ends of the beam was therefore developed. A cantilever rig was also available; this was found to be very much quicker and simpler to use than the free-free rig, and measurements were also made using this rig. Two different types of analyses were undertaken. The classical wave equation was solved for the appropriate boundary conditions for both rigs. This analysis is simple to use and requires little computer time: it was used for all undamaged beams. A receptance analysis was also undertaken for the analysis of cracked beams; this analysis allows the separation of the undamaged and cracked portions of the beam. The various analyses are given in the appendices of Chapter 3.

Specific damping capacity measurements from undamaged and cracked beams are described in Chapter 7. Both the free-free and cantilever rigs successfully detected cracks which had been indicated by acoustic emission, even before such cracks were visible.

1.4 Objectives

The author intends the work described in this thesis to

elucidate the mechanical behaviour of the material under investigation, and to establish various techniques applicable to this and other composite materials.

Composite materials are increasingly being used in applications where economic factors or strength/weight ratios require the use of minimum material; the mechanical behaviour of the material must therefore be known and consistent. The author believes that the wide scatter of properties and behaviour reported for supposedly similar composite materials may in many cases be explained by different microstructures. The methods of microstructural definition developed in this work should be applicable to a wide range of composite materials. Some application of the techniques to the material used in this work is described in Chapter 8, but much further work is required to fully investigate the application of these techniques of quantitative microscopy to the material used here, and to other materials.

The processes of crack growth in this material are studied. The crack growth is monitored by acoustic emission, and the material condition is further assessed by specific damping capacity measurements. Considerable effort was applied to the development of these techniques; the techniques are shown to be useful for the material investigated here, and should be applicable to other composite materials.

Chapter 2* Acoustic Emission

2.0 Introduction

Acoustic Emission, or stress wave emission, is the name given to the low level, sometimes audible, energy emissions from a material when it is deformed. Well known examples of such emission include the creaking of timber and the cry of tin. It is known that emissions from both these materials give warning of impending failure. Emissions from other materials which may not be audible to the human ear could therefore contain useful information.

The modern research into the field of acoustic emission was initiated in Germany in the early 1950's by Joseph Kaiser and his co-workers (Kaiser 1950). The discovery of the general rule of the irreversibility of acoustic emissions is attributed to him, being known as the Kaiser effect. Much work has since been carried out into such areas as instrumentation improvement, nature and sources of acoustic emission in various materials, data presentation and the comparison of such data with other parameters such as fracture mechanics constants. Field applications of acoustic emission for testing various structures, for example pressure vessles, are now well advanced. An assessment of the state of the art as revealed by a literature survey is presented below.

2.1 Source and Propagation of Acoustic Emission

An acoustic emission is the result of a release of strain energy inside the material. The processes of strain energy

---

* The literature survey in this chapter is partially covered in a published paper: Guild et al 1976

release which may be detected by acoustic emission are described below. The source of the strain energy release may be assumed to be at a point and to produce an expanding spherical wave with its energy distributed over a very broad frequency band (Pollock 1970, Bell 1972).

Three possible waveforms may be postulated, namely step, pulse and oscillatory. Egle and Tatro (1967) deduced from observations of the response of an acoustic emission detection system to artificial excitation, that the waveform is oscillatory. Stephens and Pollock (1971) concluded from consideration of the theoretical constraints that a pulse waveform is most likely; such a waveform represents a finite constant change in mean stress within the material leaving an increase in static stress after reverberations have finished. Assuming the pulse to be a Gaussian pulse, it may be shown that the frequency spectrum is broadband from zero up to a frequency inversely proportional to the pulse duration.

As the wave expands it loses energy at a rate proportional to the inverse square of the radius until it reaches a free surface. At the surface it is converted into Rayleigh waves in a thick structure or Lamb waves in a thin structure, which move along the surface of the material with an energy that decreases inversely with distance (Bell 1972). Additional attenuation may occur from material inhomogeneities: such attenuation is at a maximum when the wavelength is comparable to the separation of the inhomogeneities. Thus high frequency components tend to be attenuated, particularly in composite materials.

The original wave may excite different waveforms or resonances in the material or structure. The different waveforms or resonances may then excite different resonances in the detection system. Thus if a given fracture mechanism may be correlated with a given material or structure response, which may in turn be correlated with a given response of the detection system, analysis of the detected signal may provide information regarding the fracture mechanism. Such correlation has been successfully applied to the definition of fracture processes during failure of a single adhesive bond of conventional overlap design (Stephens and Pollock 1971). Different fracture mechanisms, such as internal cracking of the adhesive, or peeling from the metal strips, generated different waveforms which excited different resonances of the detection system.

Material fracture mechanisms are not so readily correlated with acoustic emission. The large low frequency response which is commonly observed is probably attributable to the excitation of flexural waves (Egle and Tatro 1967, Stephens and Pollock 1971). Fundamental frequencies arising from resonances in grains have been deduced (Liptai et al 1970) but the predicted frequencies are higher than those normally observed experimentally. Trends during tests on steels have been examined (Hutton 1968, Ono et al 1972), and changes may be associated with changes in fracture mechanisms during tests or with different fracture mechanisms expected for different types of steels. Such association is possible

when test conditions remain constant so that the material and structure responses remain unchanged. This condition was not fulfilled during the work of Speake and Curtis (1974). Very sophisticated instrumentation, with no resonances of the detection system, was used to analyse acoustic emission from the failure of unidirectional carbon fibre reinforced epoxy resin. Frequencies observed were successfully correlated with material and structure resonances. However, in order to initiate different fracture mechanisms, test conditions were changed; different resonances were observed for different fracture mechanisms but such change may therefore be associated with either change in fracture mechanism or change in test conditions.

Thus the signal arriving at the transducer contains information regarding the material and structure; information regarding the original event may be present. The position of the transducer should be as close as possible to the source of the events both to minimise attenuation and to maximise the proportion of information regarding the original event.

2.2 Instrumentation

The instrumentation required for acoustic emission testing can be divided into four parts. These are the transducer, signal amplification, signal processing and data recording.

2.2.1 Transducer

The transducer must convert the mechanical energy signal into an electrical signal which is suitable for amplification and further signal processing. The two most commonly used devices

are accelerometers and piezoelectric transducers. Accelerometers are less sensitive by a factor of approximately thirty (Tatro 1972), but they are very robust and have been used for field applications outside the laboratory.

Piezoelectric transducers are more normally used. These essentially consist of a piezoelectric ceramic disc mounted in acoustic contact with the specimen under test. The most popular ceramic is lead zirconate titanate, PZT-5. There are several variations of this ceramic, the most mechanically sensitive being PZT-5H. The design of the transducer may be simple. The crystal must be electrostatically shielded by a metal case. It must be acoustically connected to the specimen but acoustically isolated from the case. For maximum sensitivity the crystal may be unrestrained; it will therefore respond to an energy impulse by resonating at its most easily excited resonance, with a sharp rise and slow fall-off envelope. A transducer behaving in this way is said to be in the resonant mode, and no information regarding the frequency of the energy pulse arriving at the transducer can be obtained.

Frequency information may be obtained using commercial piezoelectric transducers with a wide frequency response. The response of such transducers must be determined; such calibration has been described and evaluated by Bell (1972). Alternatively frequency information may be obtained at a lower sensitivity using an accelerometer. A capacitance transducer (Speake and Curtis 1974) has been developed to allow high sensitivity frequency analysis.

2.2.2 Signal Amplification

The signals from the transducer are typically of the order of a few microvolts. Thus high-gain low-noise amplification is required before further signal processing. Charge amplifiers are very suitable if the transducer is operating in the resonant mode at a single resonance since their time constant may be tuned to that resonance, and very high amplification can be achieved at that frequency. This tuning cannot be used for signals containing frequency information from other types of transducer, and voltage amplifiers must then be used.

2.2.3 Signal Processing

Elimination of noise from the loading machine and random acoustic noises is often obtained by using a fast cut-off high pass active filter. Cut-off of approximately 24dB/octave is normally required. The suitable cut-off point is found for the system under test, and is commonly found to be in the range 10-100 kHz. Noise from a hydraulic loading machine is sometimes hard to eliminate as noise from bubbles bursting in the hydraulic fluid may be at frequencies comparable to those of acoustic emissions. Screw driven machines are thus preferable for acoustic emission testing. Other mechanical noise sources which have been found hard to eliminate include noise from gripping the specimen during tensile tests, and noise from the interface between the transducer and specimen. Such noise sources probably contributed to a controversy regarding the applicability of the Kaiser effect in cyclic testing of carbon fibre/epoxy composites (Kim et al 1972, Stone and Dingwall 1973, Kim et al 1973).

Further signal processing may be undertaken, or the signal may be recorded direct. A single acoustic emission is now represented as a ring-down envelope, the frequency in the envelope being either a function of the frequency of the energy pulse arriving at the transducer, or a function of a resonance of the transducer. For simple counting of integrated count or count rate there are two alternatives; counting can take place at every rise above a set threshold or the ring-down envelope can be taken as a single count.

Both methods have been extensively used. The advantage of the simple threshold method is that emissions of initial high amplitude are weighted in number of counts with respect to smaller emissions; thus a measure of energy has been obtained. Information regarding actual number of events is however lost using this method.

Other methods of signal processing include amplitude sorting and frequency analysis. Amplitude sorting solves the dilemma of count method described above since a measure of energy may subsequently be made from the amplitude distribution. Techniques of frequency analysis are continually being pursued; the difficulties regarding the interpretation of the results has been described above.

2.2.4 Data Recording

The various methods of data recording have been described (Pollock 1969). The simplest method is to take the output of a digital counter, as either integrated count or count rate, carry out digital/analogue conversion and record this on one

Y-axis of an X-Y-Y recorder. Load and strain may be recorded on the X-axis and other Y-axis. It has been shown for metallic specimens that the count rate curve is more symmetrical when plotted against stress rather than strain (Dunegan et al 1968). Similar definitive results are not available for composite materials, but the same convention of plotting acoustic emission against stress is most normally used.

Results from amplitude sorting or frequency analysis require separate recording for each channel. The most useful device for such recording is a multi-track tape recorder. Other methods in use include on-line computer facilities (Speake and Curtis 1974). Further recording facilities are required for flaw detection from triangulation methods when arrival times at different transducers are used to locate the source of emissions.

2.3 Acoustic Emission from Metallic Materials

Acoustic emission from metals is generally associated with dislocation movements which take place during plastic deformation. Gillis (1971) has considered the generation of acoustic emission from sources of stored strain energy, and concludes from qualitative discussion that the common feature required for an acoustic emission source is the rapid separation of closely packed dislocations with a consequent release of their elastic interaction energy. He defines dislocation motions into two categories (Gillis 1972); homogeneous motions which are dislocation motions which tend to produce homogeneous deformation of the specimen, that is, they do not accentuate existing flaws or create new ones, and non-homogeneous motions.

Acoustic emissions observed from metals can be divided into two types which are associated with the two types of dislocation motion.

2.3.1 Continuous Emissions

Continuous emissions are associated with homogeneous disclocation motions and are therefore observed during tests before significant crack growth develops. They consist of a train of low energy releases which exhibit no repeated pattern and could be confused with background electrical noise. The emissions exhibit the Kaiser effect, that is no emission is detectable in repeated loading until the previous level of stress has been exceeded.

The amount of continuous emission may be qualitatively correlated with dislocation activity. During a test on an unflawed specimen, in the absence of micro-cracking, the graph of integrated count against strain rises rapidly until just after general yield, flattens during work hardening, and finally rises rapidly again just prior to failure (Dunegan et al 1968). It is found that even before the formation or growth of flaws more acoustic emission is detectable from high strength brittle materials than from ductile materials; this is consistent with the higher energy levels associated with dislocation pile up and breakaway in these materials. An increase in acoustic emission activity is found after irradiation of steels (Pickett et al 1971); this is consistent with the increased dislocation density arising from irradiation.

Acoustic emission has been considered from the kinetics of

dislocation motions (Gillis 1972), and predictions from this analysis have been obtained experimentally (Fisher and Lally 1967). Frederick and Felbeck (1972) attempted to find a quantitative relationship between acoustic emission and dislocation activity by experimentally determining the minimum slip region diameter to develop detectable acoustic emission; they successfully applied the model to aluminium in various forms. The detection of plastic strain by acoustic emission has been discussed quantitatively (Gillis and Hamstad 1974); they concluded that acoustic emission events may be associated with only a small fraction of the total plastic strain.

2.3.2 Burst Type Emissions

Burst type emissions are associated with more massive non-homogeneous dislocation movements such as those occurring in the growth of micro-cracks. They are discrete emissions in a ring-down envelope; these emissions are generally of the order of 10^{10} larger than continuous emissions. Micro-cracking for which no emission was observed has been found, but it was shown that the process in this case was not that of dislocation movements but of void coalescence (Palmer 1973).

In addition to laboratory applications, the monitoring of burst type emissions is used as a detection system for unstable micro-crack growth in components in service.

2.3.2.1 Laboratory Tests

The growth of micro-cracks is a process that generally takes place around flaws. The quantification of this process is the subject of fracture mechanics. The simplest use of

acoustic emission in fracture mechanics testing is as a detection system for unstable micro-crack growth. If all other conditions are defined, the stress intensity factor can be found from this point, known as pop-in. Values obtained from acoustic emission measurements and compliance measurements show, in general, excellent agreement (Hartbower et al 1968). Acoustic emission has indicated crack growth significantly before such growth has been observed visually (Hutton 1968).

The development of the technique beyond that of a simple detection system involves the derivation of direct relationships between acoustic emission and the parameters of fracture mechanics. Such relationships may be theoretically justified if acoustic emission may be quantitatively related to the amount of plastic deformation; the stress intensity factor at the flaw tip is controlled by the same factors as the amount of plastic deformation, namely the size of the flaw, its location with respect to the principal stresses, and the stress in the material.

A qualitative correlation between acoustic emission and fracture toughness has been demonstrated by amplitude sorting. Larger amplitude signals are more dominant from materials with higher fracture toughness (Nakamura et al 1972, Pollock 1973).

The simplest quantitative relationships between acoustic emission and fracture mechanics parameters are derived from energy considerations (Gerberich and Hartbower 1967, Hartbower et al 1968; Radon and Pollock 1972, Tetelman and Chow 1972). Such relationships have been successfully applied to specific

materials. More sophisticated relationships are derived from the assumption that the total acoustic count is proportional to the plastic volume ahead of the crack. With the usual assumptions of linear elastic fracture mechanics, the theoretical analysis predicts that acoustic emission due to plastic deformation processes taking place at the crack tip should vary as the fourth power of the stress intensity factor (Dunegan et al 1968). Experimental tests of such a relationship lead to a wide range of indices (Dunegan et al 1968, Dunegan and Harris 1969, Pickett et al 1971, Hartbower et al 1972). Palmer and Heald (1973) have proposed that the assumptions of linear elastic fracture mechanics are not applicable and have used a more fundamental stress field relationship. The analysis shows that the exponent in the power law relating acoustic count to stress intensity factor would be a function of the ratio of applied stress to yield stress. The trends predicted by this analysis are identified in previously published results. The same approach has been successfully used to describe the relationship between acoustic emission and crack opening displacement (Palmer et al 1974).

2.3.2.2 Applications outside the laboratory

The detection of burst type emission is sufficiently easy for the technique to be used as a non-destructive testing tool outside the laboratory. The requirements for such testing have been well described (Hutton and Parry 1971, Hutton 1972). The system must be sufficiently robust and able to differentiate between acoustic emission from the structure under test and background electrical and mechanical noise.

A considerable effort has recently been applied to the assessment of the structural integrity of pressure vessels, which has become more critical as the vessels concerned are now often in nuclear applications and are being built increasingly often near centres of population. The advantages of acoustic emission monitoring have been described (Schofield 1972). A system for the continuous monitoring of U.S. nuclear pressure vessels has been developed (Vetrano et al 1972). A similar system for use in the U.K. has been developed (Bentley et al 1972), but difficulties with background noise, particularly that arising from coolants, were experienced. This difficulty is solved in the U.S. system by using a coincident detection technique; only signals which can be accurately located as arriving from a repeating source are recorded.

A complete acoustic emission analysis system in a self-contained mobile test laboratory has been developed (Parry 1971). The system has been successfully used for an integrity analysis of a nuclear pressure vessel and for integrity analyses of transmission and drill pipes. Acoustic emission has been successfully used to assess the structural integrity of pressure vessels in applications other than nuclear (Cross et al 1972). The technique has been used for the proof testing of a military bridge (Pollock and Smith 1972). Changes in acoustic emission spectra have been used to identify worn bullet forming dies during fabrication (Hutton 1971).

2.4 Acoustic Emission from Fibre Reinforced Composite Materials

The complex nature of the failure of fibre reinforced composite

materials is reflected by the complex nature of acoustic emission from such materials. Plastic deformation of the matrix or fibres produces low level emissions: such emissions are not usually detected. Higher level emissions are generated by macroscopic events such as fibre fracture, interface failure and pull-out, and matrix cracking. Although acoustic emission results may be dominated by emissions from a particular process, contributions from other processes may inevitably be present.

2.4.1 Fibre Fracture

Acoustic emission events from fibre fracture are those of highest energy. This may be deduced intuitively since such events involve the release of the greatest strain energy, and it has also been confirmed experimentally by simultaneous acoustic emission recording and observation during tests on model composites (Mehan and Mullin 1971). It has been shown by theoretical argument that the fracture of a glass filament in an epoxy matrix should always be detectable assuming that the glass always fractures at its fracture stress and ultimate strain (Rathbun et al 1971); this condition may be assumed for tests on model composites when a single event can be associated with a single fibre fracture (Rathbun et al 1971, Mehan and Mullin 1971). However if fibres fracture below their ultimate stress, which may occur in real composites, the energy release may be insufficiently large for detectable acoustic emission. This has been considered for Al_3 Ni fibre reinforced aluminium (Harris et al 1972). The material was produced from unidirectionally solidified Al-Al_3Ni eutectic alloy for which fibre misalignment is minimal. Agreement is found between

theoretical results, calculated assuming that the energy released is proportional to the square of the stress in the fibre at fracture, and experimental results from optical examination; for that material as many as 50% of fibre failures occurred below the threshold for counting.

Since fibre fractures are the events of highest energy, if the gate is correctly set recorded events may be almost entirely attributable to fibre fracture. Such a gate setting was used for compression tests of cylinderical glass/epoxy specimens (Liptai 1972); the graph of integrated count against load rises progressively to failure when the fibres were oriented transversely to the compression axis and failure occurred with fibre fracture; when the fibres were oriented parallel to the compression axis and failure occurred without fibre fracture very few emissions were recorded.

The correlation of a single event with a single fibre fracture in model composites and in a composite with nearly perfect alignment has been described above. The relationship in a real composite may however be complicated by the occurrence of fractures which cannot be detected, as described above, and by fibre misalignment, simultaneous failure and multiple failures; thus a one to one relationship between fibre failure and emission event may not exist. This was confirmed for spherically filament wound composite structures (Rathbun et al 1971); although they were able to locate the failure region using triangulation techniques, they failed to find a significant relationship between acoustic emission and number of broken fibres.

An indication of a significant relationship between fibre failure and acoustic emission during failure of NOL rings has been obtained (Liptai 1972). Striking agreement was found between emission from a ring at 21°C and the cumulative fracture model proposed by Zweben and Rosen (1970). This correlation did not occur at 70°C indicating either a failure of this relationship or another failure mode occurring at the higher temperature. Fitz-Randolph et al (1971) tested edge notched and triangular section boron/epoxy specimens in three-point flexural loading with acoustic emission monitoring. Large acoustic emission bursts were observed at load drops, that is during crack growth, while smaller bursts were associated with reloadings. The number of broken fibres was monitored by electrical resistance measurements and by a compliance calibration technique. Relationships between total acoustic emission count and the other monitoring techniques were obtained, both of which approached linearity. Thus a relationship between acoustic emission counts and the number of fibre failures is indicated.

Significant acoustic emission from fibre fracture for glass, graphite and boron reinforced epoxy resins has been found to commence at around 50% of the failure load (Liptai 1972, Mehan and Mullin 1971, Fitz-Randolph et al 1972, Balderston 1972), and boron reinforced aluminium (Hancock and Swanson 1972). The behaviour can be associated with the premature failure of fibres due to misalignment, and the debonding of the fibre/matrix interface. Acoustic emission from misaligned fibres has been further examined by Swanson and Hancock (1972)

who tested boron/aluminium composites with the fibres oriented at 0^{o}, 30^{o} and 90^{o} to the loading axis. The material properties showed good agreement with the rule of mixtures so these results may be applicable to fibre/resin composites. The gate was set so that no counts were recorded from matrix deformation. A single count was registered for each filament break in the 0^{o} specimens. Multiple breaks occurred in each filament in the 30^{o} specimen, leading to a higher count than the 0^{o} specimens. The 90^{o} specimens underwent filament splitting; several counts were recorded for each split.

Acoustic emission from fibre fracture is the dominant source when the technique is used to investigate material or component failure. One of the earliest examples of a field application of acoustic emissions was in 1963 when it was used to verify the structural integrity of solid filament wound glass fibre motor cases (Green et al 1964). More recently acoustic emission has been used to study failure processes in filament wound composite pressure vessels (Hamstad and Chiao 1973). The technique has been used to study the behaviour of unidirectional carbon fibre reinforced epoxy resin in tension (Fuwa et al 1975a) and under cyclic loading (Fuwa et al 1975b), when a marked Kaiser effect was observed. There has been some discussion regarding the applicability of the Kaiser effect during cyclic loading of unidirectional carbon fibre reinforced epoxy resin (Kim et al 1972, Stone and Dingwall 1973, Kim et al 1973), but its reported absence probably arose from noise during reloading from spurious mechanical and electrical sources.

2.4.2 Fibre / Resin Debonding

Mehan and Mullin (1971) concluded from their identification of acoustic emission signals with visually observed failure events, that the signal arising from debonding is a more gradual event than the sudden energy release arising from fibre failure. Correlation between debonding and acoustic emission is shown by results from glass fibre reinforced polyester resin and glass fibre reinforced flexibilised polyester resin (Dukes 1972), when recorded counts were postulated to result from debonds or resin cracks. Counts from the ordinary resin show a steady count rate, while those from the flexibilised resin show an initial low count rate with a very rapid increase just before failure. Count rate changes just prior to failure were also noted by Balderson (1972), whose results include counts from fibre and matrix failure, and fibre debonding. The count rate rises until just before failure when there is a decrease in rate followed by a rapid rise to failure. An increase in count rate just prior to failure was also noted by Speake and Curtis (1974) during tests on notched unidirectional carbon fibre reinforced epoxy resin specimens, when failure occurred by debonding.

Similar changes in count rate were observed by Fitz-Randolph et al for boron reinforced epoxy resin (Fitz-Randolph et al 1971, Fitz-Randolph et al 1972). Their results and the analysis in terms of fibre failure (Fitz-Randolph et al 1971) have been described above. An alternative analysis in terms of fibre debonding has been carried out (Fitz-Randolph et al 1972). The fracture surface energy was measured by work of fracture,

linear elastic fracture mechanics and compliance variation; reasonable agreement was found between values obtained from these different measurements. The compliance data was analysed to find the change in fracture surface energy during crack propagation, and these values were compared with change in fibre pull-out length and acoustic emission. A strong correlation was found. The total acoustic count per unit of crack surface area was found to have an almost linear relation with fracture surface energy. The relation between fibre pull-out length and crack area is of the same form as both the total acoustic emission count per unit crack area and the fracture surface energy plotted against the crack area. Thus a relationship between the fibre pull-out length and acoustic count has been established.

2.4.3. Resin Cracking

Balderston (1972) concluded from tests on notched boron reinforced epoxy resin specimens that resin failure is characterised by much lower bursts of energy than those arising from fibre failure. Many published results may include emission from resin cracking, but the larger contributions of other mechanisms make the resin cracking contribution hard to distinguish.

Liptai (1972) claims that emission recorded during fatigue of NOL rings arises from resin micro-cracking since the fatigue degradation arises from the initiation and propagation of small cracks in the resin. Acoustic emission results indicate that micro-cracking increases with number of fatigue cycles. However no correlation could be found between accustic emission

results and the observation that a disproportionate amount of damage occurs during the first cycle.

2.4.4 Correlation of Acoustic Emission with Parameters of Fracture Mechanics

Considerable research effort has been directed towards the correlation of acoustic emission from metallic materials with the parameters of fracture mechanics, as described above.

General applicability of the concepts of linear elastic fracture mechanics to the failure of composite materials is not established, but there is some published work which attempts to correlate acoustic emission from composite materials with parameters of fracture mechanics.

The correlation of acoustic emission with fibre debonding for a boron/epoxy composite has been described above (Fitz-Randolph et al 1972). Correlation was also found between acoustic emission and fracture surface energy measured by compliance calibration. It is noted that such correlation was attempted only after the applicability of the compliance calibration to the fracture process under investigation had been established. Such applicability was not similarly investigated during a study of acoustic emission from a notched glass fibre reinforced epoxy resin composite (Barnby and Parry 1976), when a stress intensity factor calibration technique was used. An attempt was made to quantify the relationship between acoustic emission and stress intensity factor as a power law, as proposed for metallic materials, described in 2.3.2.1. The values of the exponent varied with the angle of the fibres to the notch. However, since the sources of the emission were not investigated, it is

postulated that the numerical values are not significant: a qualitative variation of acoustic emission with the angle of the fibres to the notch may be deduced.

2.5 Acoustic Emission Circuit

The acoustic emission circuit was designed in the context of the experience of other workers which had been revealed by the literature survey. The circuit was developed and built in the laboratory based on equipment which was already available. It was essential that any items to be purchased were low cost.

The failure of the material under the loading conditions used takes place by the growth of a tensile crack. The growth of the crack involves the fracture of fibres aligned perpendicular to the crack direction, parallel to the long axis of the beam. The failure could thus be well monitored by monitoring the fracture of fibres, and it was therefore decided that the acoustic emission circuit should be required to detect only fibre fracture, the events of highest energy. If the gate was correctly set it could be possible to correlate the number of events with the number of fractures. Thus a resonance envelope was to be recorded as a single count.

The design and development of the acoustic emission circuit is described in Appendix 2.

Chapter 3. The Measurement of Specific Damping Capacity in Flexure.

3.0 Introduction

The specific damping capacity of a material is a measure of the ability of that material to absorb energy. Such ability may be measured from the study of resonant vibration of a specimen of the material.

The specific damping capacity is defined from the behaviour during a single cycle:

$$\text{Specific Damping Capacity, } \Psi, = \frac{\text{Energy absorbed during cycle, } \Delta U}{\text{Total strain Energy stored during that cycle, U.}}$$

Alternatively material behaviour may be defined from the free decay of resonant vibrations:

$$\text{Logarithmic Decrement, } \delta, = \log_e\left(\frac{u_1}{u_2}\right)$$

where u_1, u_2 are the amplitudes of consecutive cycles.

The two measures of material behaviour are simply related:

$$\psi = 2\delta$$

The measurement of specific damping capacity thus requires the excitation of resonant vibration of a specimen of a material. The simplest vibration, the fundamental frequency, is used. The energy loss is considered to occur from energy loss within the material; it is thus essential to eliminate all significant losses from the excitation arrangement and the specimen support. Electrical excitation by passing an alternating current through a coil clamped to the specimen and moving between the poles of a magnet has been found to be satisfactory. For flexural measurements, losses from specimen

support may be minimised if free-free vibration is used and the specimen is supported at the nodes of the vibration. The satisfactory performance of a rig may be monitored by measurement of the specific damping capacity of an aluminium alloy containing 3-5% copper, Duralumin, which has a very low specific damping capacity, believed to be of the order of 0.01%.

3.1 Previous Flexural Measurements

The measurement of the specific damping capacity of composite materials in free-free flexure has been extensively examined (Bacon 1973). A free-free flexural rig was developed which enabled the measurement of Duralumin specific damping capacity of less than 0.1%; these measurements have been successfully repeated by the author. Measurements were made using beams with typical dimensions 250 x 12 x 3mm. However this rig was unsuitable for the present work since it requires a coil to be clamped at the mid-point of the beam, which is the region where cracks may be present after mechanical loading. Thus a new rig was developed with coils clamped at the ends of the beam. However much experimental technique and the approach to the classical wave equation analysis of vibration deduced in this previous work have been applied to the present work.

3.2 Principles of Flexural Measurements

The measurement of specific damping capacity in flexure requires the excitation of the fundamental frequency of the beam, and the measurement and analysis of this vibration. The vibration amplitude is measured at a known point along the beam, and from the vibration analysis amplitudes at all points can be calculated. The energy input is calculated from the previously

measured coil calibration factor, the input current to the coil and the amplitude at the coil, as shown in appendix 3.1. The total strain energy stored in bending is given by:

$$U_B = \frac{EI}{2} \int_0^l \left(\frac{\delta^2 u}{\delta x^2} \right)^2 \delta x$$

The total strain energy stored may therefore by calculated from the beam parameters and the mode shape, known from the vibration analysis and the measured amplitude. Thus the specific damping capacity, the ratio of the energy input to the energy stored, may be calculated.

3.2.1 Excitation of Steady State Resonant Vibrations

The excitation of steady state resonant vibrations is achieved by passing an alternating current through a coil clamped to the beam; the coil moves between the poles of a permanent magnet or electromagnet. The current flowing in the coil is controlled and measured using the circuit shown in figure 3.1. The frequency is adjusted to the resonant frequency of the beam. The detection of resonance is most easily carried out by observing an oscilloscope display from the detecting device suspended above the beam around the point of maximum deflection; the device may be a capacitance transducer if the beam is a conducting material, or a condenser microphone. At resonance the amplitude is a maximum and is the identical frequency to that of the input current to the exciting coil. The exact frequency of resonance is finely tuned by adjusting the frequency for minimum current flowing through the exciting coil; it was confirmed experimentally that such frequency is identical to that of maximum amplitude.

3.2.2 Measurement of Amplitude

The amplitude is measured at a known point along the beam. For maximum accuracy measurement should be made at the point of maximum deflection. Such measurement may be made directly, using an image shearing eye-piece, or electrically using a pick-up coil attached to the specimen.

Electrical measurement involves the use of an additional pick-up coil clamped to the specimen and moving between the poles of a magnet. The output voltage from this coil is measured, and from previous calibration the corresponding amplitude may be calculated. This method was extensively used during the previous work (Bacon 1973), using an additional coil clamped above the mid-point of the beam, when direct observation was impossible.

Almost all tests in the present work were carried out in laboratory conditions and direct measurement of amplitude using an image shearing eye-piece was thus possible. A few tests were carried out in the vacuum chamber using the free-free rig, when amplitude measurement was made at the end of the beam using an eye-piece extension tube through the wall of the vacuum chamber. However, as described below, electrical measurement from the free-free rig described in 3.4 is possible, using one coil for energy input and the other, at the opposite end, for amplitude measurement.

3.2.3 Presentation of Results

The calculation of specific damping capacity described above assumes the damping in all regions of the beam to be identical; thus the assumption is made that the damping is independent of

the stress in the material. This assumption has been broadly justified for undamaged materials (Bacon 1973); the stress dependence for cracked material will be investigated in the present work. Comparison of results from different beams should always, however, be made at comparable stress levels. Thus damping results are normally presented graphically as a function of the maximum surface stress in the beam, calculated from the measured amplitude and the analysis of the vibration.

3.3 Rig with Electromagnets

3.3.1 Rig and Coil Design

The initial rig and coil design is shown in figure 3.2. The design of this rig and coils is a direct development of the previous flexural rig with central excitation.

The lower portions of the coils, which are clamped at the ends of the beam, move between the poles of electromagnets. The dc currents in the electromagnets can be controlled separately by rheostats. The coils are oriented with their long axes parallel to the long axis of the beam so that during vibration there is no lateral movement of the coils with respect to the gap between the poles of the electromagnets; this gap could therefore be very small, maximising the flux density. The beam is supported at its nodes by lengths of cotton..

The coil design is that deduced for the previous rig except that the long axis is oriented parallel instead of perpendicular to the long axis of the specimen, for the reasons described above. The coils are clamped to the beam through silver steel rollers glued in V-grooves in the clamping pieces. Lateral movement of the coils along the beam is prevented by the use

of two rollers on the lower clamping piece.

The addition of weight at the ends of a beam vibrating at its fundamental frequency tends to move the nodes of the vibration towards the ends, reducing the vertical movement at the ends. The energy input is dependent on the vertical movement; thus the coils were designed to be as light as possible. The clamping pieces, which were fabricated from aluminium alloy in the previous rig, were therefore fabricated from magnesium alloy. It is essential that exciting coils are clamped securely to the beam so that energy losses at the interface are minimised. It was found that the magnesium alloy clamping pieces could not withstand the necessary clamping pressure, and bent. They were therefore replaced by aluminium alloy clamping pieces; sufficient clamping pressure could then be applied.

3.3.2 Calibration

The calibration factor, A, defined by equation 4 in appendix 3.1, is calculated from voltage and corresponding amplitude measurements when the coil is excited externally to vibrate in the magnetic field. The external excitation was achieved by clamping the coils to the ends of a Duralumin beam, and vibrating the beam at its fundamental frequency using a vibrator, in contact through sponge rubber with the mid-point of the beam. The dc currents in the electromagnets were adjusted to give identical calibration factors for both ends of the rig; currents of about 4 amps were required. The calibration was carried out using two Duralumin specimens with resonant frequencies at either end of the range used during tests;

identical calibration factors were obtained.

3.3.3 Initial Analysis

The analysis was carried out by solving the classical wave equation for the appropriate boundary conditions. The boundary conditions used in the initial analysis assume point masses at the ends, that is, the rotary inertia of the exciting coils is ignored. Shear deflections and rotary inertia of the beam are also ignored.

The analysis is shown in appendix 3.2. The frequency number is found as a function of the total end to beam mass; the relationship is shown graphically in figure 3.3. For a given value of mass ratio, the equation may be solved for the value of frequency number, λ, on a computer using Newton's Iteration.*

Thus the value of the beam dynamic modulus, E, may be calculated using:

$$E = \frac{m}{I l} \times \left(\frac{2\Pi}{T}\right)^2 \times \left(\frac{l}{\lambda}\right)^4$$

where m,I,l are the beam mass, second moment of area, and length, and T is the period of the vibration.

3.3.4 Consistency of Analysis and Experimental Results

The consistency of the analysis and experimental results may be tested from comparison of the measured and predicted mode shapes, and from values of dynamic moduli calculated using the observed frequency.

Comparison of experimental and theoretical mode shapes for a Duralumin specimen show good agreement, as shown in figure 3.4.

---

* The author would like to thank Mr. E.C. Tapper of the School of Mathematical Sciences, Plymouth Polytechnic, for his help with the iteration routine.

The analysis was therefore used with confidence to calculate frequency numbers and dynamic moduli values.

Dynamic moduli values thus calculated were considerably lower than expected values; experimental frequencies and apparent frequency numbers were lower than those predicted by the analysis using expected values of dynamic moduli. Results from two Duralumin. . beams and two GFRP beams are shown in Table 3.1. It may be concluded from these results that the coils are having a greater effect on the vibration than their measured mass.

3.3.5 Effect of Rotary Inertia of the Coils

The rotary inertia of the coils was neglected in the initial analysis. The effect of addition of rotary inertia on the frequency number would be the same as the addition of mass; the neglect of this factor could therefore explain the discrepancy described above.

The significance of the rotary inertia of the coils was demonstrated experimentally using a Duralumin. . beam. The beam was excited using a vibrator as used during calibration, described in 3.3.2. The fundamental frequencies were found for the free-free beam with no mass at the ends, for the beam with small steel cylinders glued to the ends of the beam, and for the beam with the coils clamped to the ends of the beam.

The results are shown in table 3.2. It may be seen that the analysis can be successfully applied to the result from the beam with small weights, with small rotary inertia, glued to the ends of the beam. However with the coils attached, the

same frequency as that found using the coils for excitation, analysed in table 3.1, was found. Thus it was concluded that the discrepancy with the coils attached arises from their rotary inertia.

3.3.6 Improved Analysis

Classical wave equation analysis was therefore carried out including the effect of rotary inertia of the end masses. Shear deflections and rotary inertia of the beam are ignored.

The analysis is shown in appendix 3.3. The frequency number is a function of the masses of the beam and end masses, the length of the beam and the rotary inertia of the end masses. The variation of frequency number with rotary inertia for a given beam length and mass, and end masses, is shown in figure 3.5. Comparison of this graph with that of figure 3.3 confirms the experimental results that the addition of rotary inertia of end masses changes the frequency number in the same direction as the addition of mass to the end masses. The frequency number for given conditions may be calculated on a computer using Newton's Iteration; thus values of dynamic moduli may be calculated as shown above. The rotary inertia of the coils was calculated from the periods of a Duralumin beam acting as a simple pendulum, with and without a coil attached at the free end.

3.3.7 Consistency of Improved Analysis and Experimental Results

The mode shape predicted by the improved analysis and that predicted by the initial analysis, for a Duralumin beam, are compared in figure 3.6. It may be seen that the addition of rotary inertia has negligible effect on the theoretical

mode shape.

The frequency numbers and dynamic moduli were calculated for two Duralumin beams and two GFRP beams. The results are shown in table 3.3. It may be seen that there is reasonable agreement between measured and predicted moduli for the thinner Duralumin and 90^{o} GFRP beams, which have lower resonant frequencies than the other two beams. The experimentally measured dynamic moduli of the thicker Duralumin and 0^{o} GFRP beams are lower than the expected values; thus at high frequencies the coils are having a greater effect than their measured mass and rotary inertia. The apparent coil inertias calculated assuming the expected moduli and experimental frequencies, beam parameters and end mass, are shown in table 3.3; the apparent inertia for the 0^{o} GFRP beam is greater than twice the measured value. The coil was examined using a stroboscope during vibration of the thicker Duralumin beam, for which a frequency discrepancy had been observed. It was seen that the coil has an axial resonance in the plane of the coil, of approximate frequency 180 Hz, which was excited by the vibration of the Duralumin beam. For the analysis of the beam vibration, axial vibration of the coil would act as an additional rotary inertia. This coil resonance would not be excited if the beam frequency was very much smaller than the coil resonant frequency. Thus an explanation for the results of table 3.3 has been found.

3.4 Rig with Permanent Magnets

3.4.1 Rig and Coil Design

It has been found that if the axial resonance of the exciting

coil is near the resonant frequency of the beam under test, the resulting coil vibration causes discrepancies between experimental frequencies and those predicted by the analysis. Such coil vibration may also be a source of energy loss. Thus a coil must be designed which has a very high axial resonant frequency which will not be excited by the beam vibrations. The coil must therefore by very stiff in its own plane; the design from the previous flexural work would not be satisfactory.

The new coil, designed for maximum stiffness, is shown in figure 3.7. Rotary inertia of this coil is minimised by clamping the beam at the centre of the coil. The aluminium alloy clamping frame in the centre of the coil maximises its stiffness. The coils are clamped to a beam through silver steel rollers glued in V-grooves in the clamping pieces, as described for the initial coils described in 3.3.1.

It was anticipated that for sufficient power input both upper and lower portions of the coils should move between the poles of permanent magnets. The rig is shown in figure 3.8. However it was found later that sufficient power input could be attained using the lower magnets only. Since this arrangement makes the rig far easier to set up, it was mostly used.

Because the coils are now oriented perpendicular to the long axis of the beam there is lateral movement of the coils during vibration. This movement was allowed for by using shaped pole pieces, as shown in figure 3.8, such that the whole coil

was never between the pole pieces. The beam was set up so that the coils were symmetrically oriented around the pole pieces. During calibration it was checked that this arrangement did not introduce any change of the coil calibration factor with amplitude; it was found that the behaviour was linear over the amplitude range used during tests.

The node supports could be most securely bolted to the outside of the channel section; the width of the channel section had been determined from that required to support the permanent magnets. The optimum length and tension of the cotton node supports had been deduced for the previous flexural rig, and it was considered preferable that similar length and tension should be used. The node supports therefore consist of a 25mm aluminium block bolted to the vertical aluminium bar.

3.4.2 Calibration

An initial calibration was carried out as described in 3.3.2 using a vibrator contacting the mid point of a Duralumin beam. Slightly different calibration factors were found for the two ends of the rig. The calibration factors could not be simply equalised as they had been in the electromagnet rig by altering the dc currents.

The effect of the unequal energy inputs at the two ends of the rig was investigated by removing the vibrator and exciting the beam from one coil while calibrating the other end. Identical calibration factors to those from the vibrator calibration were obtained, and it was therefore concluded that unequal energy inputs at the two ends has no effect on the vibration.

The calibration factors were checked at either end of the frequency range used during tests by using two Duralumin specimens; no change was found over this frequency range. Amplitudes up to the maximum used during tests were checked to ensure linearity, as described in 3.4.1. The two methods of amplitude measurement have been discussed in 3.2.2. An image shearing eye piece was always used in the present work. However the result above shows that electrical amplitude measurement using one coil could be made; the other coil would be used for excitation. The rotary inertia of the coils was calculated from the period of vibration about their mid-point. The arrangement used is shown in figure 3.9.

3.4.3 Consistency of Analysis and Experimental Results

The consistency of experimental and theoretical mode shapes had already been established. The analysis, including the effect of the measured rotary inertia, was used to calculate the frequency numbers and thus dynamic moduli for both Duralumin beams and for 0^{o} and 90^{o} GFRP beams; all moduli values were close to the expected values. Thus the analysis of the vibration could be confidently used to calculate values of specific damping capacity. The use of the measurement of the specific damping capacity of Duralumin as a monitor of the performance of a damping rig has been described above. Results are shown in figure 3.10; the measured values are rather high. Thus energy loss must be occurring.

3.4.4 Investigation of Source of Energy Loss

The possible sources of energy loss may be divided into three types, namely air damping, mechanical losses and electrical losses.

3.4.4.1 Air Damping

The importance of energy loss from air damping in the measurement of specific damping capacity of low damping materials in flexure has been demonstrated (Bacon 1973). A vacuum chamber was developed, and it was found that 0.5 Torr is sufficient vacuum to eliminate energy loss from this source. This vacuum chamber was used to repeat measurement of specific damping capacity of Duralumin at normal air pressure and at pressure less than 0.5 Torr. Amplitude was measured at one end of the beam using an image shearing eye-piece with an extension tube through the wall of the vacuum chamber. This amplitude measurement was rather inaccurate because of the small amplitude at the end of the beam, and because the movement at this point is diagonal, not vertical, making the vertical movement hard to measure. Thus the results, shown in figure 3.11, show considerable scatter. . However these results demonstrate that the high measured specific damping capacity of Duralumin cannot be accounted for by air damping.

3.4.4.2 Mechanical Losses

The deduction of optimum rig design to reduce mechanical losses, for example through the node supports, had been carried out during the design of the previous flexural rig (Bacon 1973). The present rig design had been based on the successful design of that previous rig, and it had therefore been anticipated that mechanical losses would be avoided. The rig was carefully examined using a stroboscope during excitation of the Duralumin beam; no extraneous vibrations were observed.

3.4.4.3 Electrical Losses

Electrical losses arise from energy loss from the excitation of eddy currents when a conductor moves in a magnetic field. Free decay damping measurements are used for the investigation of electrical losses since such measurements do not require the presence of exciting coils or magnets; the effect of their presence may thus be evaluated. The output of a capacitance transducer was used for amplitude measurement; the logarithmic decrement and thus the specific damping capacity was calculated from the time taken for the amplitude to reduce to half its original value. The tests were not fully instrumented and relied on measurements using a stop clock; Thus the free decay damping values are approximate only. They may, however, be used to investigate the effect of various conditions.

Since the effect of the presence of the coils and magnets is to be investigated mechanical excitation must be achieved without them. Mechanical excitation cannot be satisfactorily achieved in a free-free rig. A cantilever rig has been developed in the laboratory (Hazlerigg and Huckerby 1975), and this rig was used for the investigation since mechanical excitation is easily achieved. The cantilever rig was used later for comparative measurements and is described more fully below.

The Duralumin beam was clamped in the cantilever and one of the coils from the free-free rig was attached to its free end. A magnet was removed from the free-free rig and placed so that the lower horizontal portion of the coil moved between its shaped pole pieces. A capacitance transducer was suspended above the free end. The beam was excited by a tap at the free

end, and the resonant frequency was measured from an oscilloscope display of the output of the capacitance transducer. The half decay time was measured, and thus the specific damping capacity was calculated. Results are shown in table 3.4; it is postulated that the discrepancy between results with nothing at the free end and with the coil attached arises from the inaccuracy of the results. The half decay time is reduced by an order of magnitude and the measured specific damping capacity is increased by an order of magnitude when the magnet is introduced. Thus a source of energy loss arising from the coil moving in the magnetic field has been established.

The measurements described above were repeated using the coil developed for the previous flexural rig (Bacon 1973), shown in figure 3.12. A permanent magnet with flat pole pieces was arranged so that the lower portion of the coil moved between the pole pieces. No change in half decay time was observed when the magnet was removed.

Energy loss may arise from the coil windings or the yoke or frame and clamping pieces. Since the coil windings of the coils are very similar, it was deduced that the loss must arise from the frame and clamping pieces, which, during these tests, were moving far closer to the magnet pole pieces in the new coil design.

3.4.4.4 Comparison of the effect of Energy loss for the Present and Previous Free-Free rigs.

It is noted that in the previous flexural rig (Bacon 1973) both lower and upper horizontal portions of the coil move between the poles of an electromagnet. Thus the distance

between the aluminium alloy yoke and clamping piece is of the same order of magnitude as that distance using the stiff coils in the tests described above, when energy loss was detected. This source of energy loss in the previous flexural rig may be reduced or eliminated if the magnetic field from the electromagnet is more orented than that from the permanent magnet.

It may also be shown that the effect of a given energy loss is far greater for the present than for the previous flexural rig. For a given central deflection of a given beam, the energy stored for the previous flexural rig is an order of magnitude greater than that for the present flexural rig. This difference arises from the change in mode shape when the coils are at the ends of the beam instead of the middle. A simple relationship between true and measured specific damping capacities is derived in appendix 3.4; it is found that for a given energy loss, the difference between measured and true specific damping capacities is inversely proportional to the energy stored. Thus some energy loss may occur in the previous flexural rig, although the specific damping capacity of Duralumin may be measured as less than 0.1%. It may be shown that for the same Duralumin beam at the same central deflection, assuming the true specific damping capacity of 0.01%, the energy loss implied by a measured specific damping capacity of 0.1% using the previous flexural rig would result in a measured value of about 0.7% using the present flexural rig. Thus energy loss, regarded as insignificant in the previous rig, may be considered significant in the present rig using the criterion of the measured specific damping capacity of Duralumin.

3.4.5 Refabrication of Coils

The coils were refabricated using Tufnol, a non-conducting material, for the frames and clamping pieces. The design of the new coils is otherwise identical to the previous stiff coils, shown in figure 3.7.

3.4.6 Calibration

The coils were calibrated as described in 3.4.2 using one coil for excitation while calibrating the other end. The values of the calibration factors were checked at either end of the frequency range used during tests using two Duralumin beams, and found to be in agreement. The rotary inertia of the coils was measured as described in 3.4.2 and shown in figure 3.9.

3.4.7 Measured Specific Damping Capacity of Duralumin.

The specific damping capacity of Duralumin. was again measured, using the refabricated coils. The results are shown in figure 3.13. The values measured are lower than those measured using the coils with aluminium alloy frames and clamping pieces, but they are still rather high. It was therefore deduced that a source of extraneous energy loss was still present. The most probable source of such loss was considered to be again electrical.

3.4.8 Investigation of Electrical Energy Loss

3.4.8.1 Free Decay Measurement using the Cantilever Rig

Free decay damping measurement of the specific damping capacity of Duralumin on the cantilever rig, as described in 3.4.4.3, was again used to investigate any energy loss introduced by the

presence of an exciting coil or magnet. The results are shown in table 3.5; it is seen that the presence of the magnet decreases the half decay time and increases the measured specific damping capacity whether or not a coil is attached. However this change is far smaller than that observed in table 3.4 when the magnet was introduced when the coil with aluminium alloy yoke and clamping piece was attached. It is postulated that the difference between measured values with and without the coil attached, with no magnet present, arises from the inherent inaccuracy of the measurements.

The increase in measured specific damping capacity when the magnet is introduced indicates that conducting material is still moving inside a significant magnetic field. The increase when no coil is attached indicates that the Duralumin beam itself is in a significant magnetic field and is thus the source of energy losses. The increase when the coil is present may arise from the Duralumin beam only, or additional losses may also arise from conducting material associated with the coil. The conducting material used in the Tufnol coils consists only of the brass screw threads and nuts and washers, and the silver steel rollers. Losses from the coil windings should be negligible since they are very similar to the previous coil for which no electrical losses were observed, as described in 3.4.4.3. It is postulated that the very small volumes of conducting material on the coils would not cause significant losses and that the reduction of measured specific damping capacity with the coil attached when a magnet is introduced arises solely from losses in the beam.

An attempt was made to confirm this hypothesis using a glass fibre beam, a non-conducting material. However the half decay time of both types of beam is so short that any change could not be detected without instrumentation.

3.4.8.2 Free Decay Measurement using the Free-Free Rig .

Free decay damping measurements on a free-free rig can only be carried out with the coils and magnets in place and used for excitation; the ac coil current can be disconnected and the subsequent decay used for free decay damping measurement as described for the cantilever rig. The specific damping capacity of the Duralumin beam was measured by this method with all four, upper and lower, magnets in place, and with the lower magnets only. The results are shown in table 3.6; it is seen that the half decay time increases and the measured specific damping capacity decreases when the upper magnets are removed, decreasing the strength of the magnetic field. This result is consistent with electrical source of energy loss, but does not confirm whether the energy loss arises solely from the Duralumin beam. An attempt was made to confirm the energy loss source by repeating the measurements using a glass fibre beam, a non-conducting material. However the half decay time of both types of beam is so short that instrumentation would be required.

3.4.8.3 Measured Specific Damping Capacity of Stainless Steel

The specific damping capacity of stainless steel was measured using the normal steady state technique. Since stainless steel has a higher resistivity than Duralumin. energy loss from eddy currents in the beam should be much less significant

than for Duralumin. The results are shown in figure 3.14. These measured values are similar to values obtained on another rig (Adams 1977). Thus the high measured specific damping capacity of Duralumin does appear to arise from energy loss within the beam itself, and the rig should be satisfactory for the measurement of the specific damping capacity of non-conducting materials.

3.5 Cantilever Rig

An alternative to a free-free rig for the measurement of specific damping capacity in flexure is a cantilever rig with excitation from a coil attached at the free end. The advantage of such a rig is that it is very quick and easy to set up; the beam is clamped at the encastré end only and there are no node supports to be arranged. The disadvantage of such a rig is the experimental difficulty of obtaining a true encastré condition with no energy loss, particularly with soft materials. However a cantilever rig could be suitable for the present work since it does not require clamping or any constraint in the central portion of the beam where cracks may be present after mechanical loading.

3.5.1 Rig and Coil Design

A cantilever rig had already been developed in the laboratory (Hazlerigg and Huckerby 1975). The rig is shown in figure 3.15. The coil used was that developed for the previous flexural rig shown in figure 3.12. It was arranged that the lower portion of the coil should move between the flat pole pieces of a permanent magnet; during vibration the whole depth of the lower portion is always between the pole pieces.

The clamping arrangement is shown in figure 3.15. GFRP is too soft for the clamps to be applied directly; in previous measurements with this rig aluminium end tags, approximately 35 mm. long, had been bonded with Araldite to the upper and lower faces of the encastré ends of beams. The same arrangement was used in the present work. Initially Araldite was used, but this was found to be inconvenient both because of the time taken for the adhesive to cure, and because considerable adhesive was left on beams after tags had been removed. Beams with tags bonded with cyanoacrylate adhesive yielded results in agreement with those using Araldite; cyanoacrylate adhesive cures almost instantly and tags can be easily sheared off leaving little adhesive on beams. This adhesive was therefore used.

Calibration was carried out as described in 3.3.2 using a vibrator in contact with about the mid-point of Duralumin beams through sponge rubber. The calibration factor was checked at either end of the frequency range used during tests, and found to be constant.

The rotary inertia of the coil was calculated from the period of vibration about its clamping point, measured using a similar arrangement as that used for the free-free coils, shown in figure 3.9.

3.5.2 Analysis

The analysis was carried out by solving the classical wave equation for the appropriate boundary conditions. After the experience with the free-free analysis the rotary inertia of

the coil was included. Shear deflections and rotary inertia of the beam are ignored.

The analysis is shown in appendix 3.5. If rotary inertia is ignored the frequency number is related to the mass ratio as shown graphically in figure 3.16. If rotary inertia is included the frequency number is a function of the masses of the beam and end mass, the length of the beam and the rotary inertia of the end mass. The variation of frequency number with rotary inertia for a given beam length and mass, and end mass, is shown in figure 3.17. Comparison of this graph with that of figure 3.5 shows that rotary inertia has a far greater effect on frequency number for the free-free rig than it does for the cantilever rig.

3.5.3 Consistency of Analysis and Experimental Results

The mode shape predicted by the analysis and the measured mode shape of a Duralumin. beam are compared in figure 3.18. Good agreement is found, and thus the analysis may be used to calculate frequency numbers and thus dynamic moduli values.

Dynamic moduli values for two Duralumin. beams and two GFRP beams are shown in table 3.7; it is seen that these values are all slightly lower than the expected values. Beams were carefully examined using a stroboscope during excitation; no extraneous vibrations were observed. It was therefore considered that the discrepancy arises from the experimental difficulty of obtaining a true encastré condition; if any deflection or slope was occurring at the encastré end, this would decrease the frequency compared with that corresponding

to the true encastré condition, which is the direction of the discrepancy observed in table 3.7. The specific damping capacity of Duralumin was measured using the cantilever rig. Results are shown in figure 3.19; the measured values are rather high.

As described above, there are three possible sources of energy loss. The effect of air damping was found to be insufficient to account for the losses in the free-free rig. The cantilever rig does not fit into the available vacuum chamber; however in the light of the free-free rig results, it is postulated that air damping is not the source of energy loss. Electrical energy loss using the present coil and magnet had already been investigated during the investigation of electrical energy loss in the free-free rig, as described in 3.4.4.3; it had been shown that no electrical energy loss occurs. Thus the source of energy loss was deduced to be mechanical, and to be arising from the encastré end. This result is in agreement with the discrepancies in dynamic moduli, as described in the previous paragraph.

3.5.4 Application of the Cantilever Rig

The discrepancies in the results of the two previous sections may be attributed to the known experimental difficulty of obtaining a true encastré condition. The design of the clamping arrangement had been carefully considered (Hazlerigg and Huckerby 1975), but improvements may be possible. However it was decided that further rig design should not be carried out in the present work. Changes in specific damping capacity after mechanical loading may be detectable despite the back-

ground energy loss, and the cantilever rig could then be proved useful, especially since it is far quicker and easier to set up than the free-free rig.

3.6 Receptance Analysis*

The wave equation vibration analyses are applicable to uniform beams. However, after mechanical loading, cracks may be present in beams, and thus beams may not be uniform; the presence of a crack may be represented as a change in stiffness parameters. The assumption in the wave equation analyses, that the specific damping capacity is constant along the beam, and independent of stress, may not be applicable when a crack is present. The portion of beam containing the crack must be separable in the analysis.

A receptance analysis was therefore carried out, and is shown in appendix 3.6. The analysis may be easily applied to the free-free rig or cantilever rig by changing the receptances of one end mass. The receptances used include the effect of shear, and the analysis allows the separation of the shear and bending deflections, and the calculation of the strain energy stored in shear. The shear components were checked by applying the analysis to a short steel cantilever at low frequency, far below its resonance. The shear deflections found agree with those calculated from simple mechanics.

---

* The author would like to thank Dr. B.J. Stone, of the Department of Mechanical Engineering, University of Bristol, for his help with the receptance analysis.

Values of shear modulus, G, are needed for this analysis; they were obtained from torsion tests of beams which had been machined to a circular cross-section.*

The iteration programme to find dynamic modulus, the flowchart of which is shown in figure A.3.6.2, is unsuccessful when applied to 90^{o} beams; the analysis of 0^{o} beams and steel and Duralumin beams is however successful. The failure of the iteration for the 90^{o} beams therefore appears to arise from their low modulus.

Both the shear deflections and strain energy stored are found to be negligible for beams tested in this work. Theoretical mode shapes calculated using the receptance analysis agree with those calculated using the wave equation analysis for both the free-free and cantilever rigs. Values of dynamic modulus and specific damping capacity of undamaged free-free beams calculated using the two analyses are almost identical. However, values of dynamic modulus and specific damping capacity of undamaged cantilever beams calculated using the two analyses are slightly different. This may arise from the inclusion of shear in the receptance analysis; shear effects may have a small effect on frequency although its effect on deflection may be negligible (Stone, 1975).

---

*The author would like to thank Dr. N.D. Vaughan, of the Department of Mechanical Engineering, University of Bristol, for his help with these tests.

Chapter 4 Preparation and Preliminary Examination of the Material.

4.0 Introduction

It has been described in the introduction how the work consists of a quantitative investigation into material which, from its fundamental nature, is essentially variable. Results can only be meaningful if the conditions under which the material is prepared are constant, and the microstructure is defined.

Material was obtained both from boat builders and a commercial firm making hand lay-up plates for research purposes. The simplest fibre arrangement obtainable was from the use of uniaxial mat. Uniaxial mat consists of the majority of fibres in one direction, the warp direction, held in tows, bundles of around 10,000 fibres, by a few weft threads at around 10mm intervals. The weft threads tend to maintain the tow structure in the finished composite resulting in regions of high fibre concentration and regions of unreinforced resin. In addition the weft threads may themselves have an effect on the stress distribution within the material. Visual observation of the material indicated that the quality was rather poor and inconsistent. Bubble voids were present; the fibres were clearly visible indicating the presence of needle voids along them, arising from improper wetting. The upper surface from the lay-up process was very uneven making proper height measurement of beams impossible; such measurement is particularly important for flexural testing. In addition the uneven surface could introduce uneven stress distribution.

This material was therefore rejected for quantitative investigation, and beams were prepared in the laboratory. The inherent inhomogeneity of the material determines that, for maximum consistency, the dimensions of the beams should be as large as possible. The size used was deduced from both the testing methods used and the preparation method; typical beam dimensions were 300 x 12 x 10 mm.

4.1 Constituent Materials

The glass and resin used were those which had been granted approval to the Ministry of Defence (Ship Dept.) specification DG Ships 180A, and were used for the experimental G.F.R.P. minehunter.

E-glass fibre was obtained as uniaxial mat, Marglass type 280, finish A368. The mat has nominal thickness of 0.66 mm, and nominal weight of 612 gm m^{-2}. E-glass is a high lime borosilicate glass with a low alkali content, below 1%. Finish A368 is a pre-silane treated yarn, designed for compatibility with polyesters. The properties of the fibres were obtained from its manufacturers, who quoted:

Fibre Diameter = 14.9 ± 0.5 μm

Ultimate Tensile Strength = 1.53 ± 0.10 GN m^{-2}

Tensile Modulus = 59.1 ± 1.2 GN m^{-2}

Strain to Failure = 2.6%

Glass fibres are most easily handled in this form since the tows in the warp direction are maintained in good alignment by the weft threads. However the weft threads must be removed both for their possible effect on the stress distribution in

the composite, and to allow better dispersion of the fibres.

The resin used was BP 2785/CV. This is a chemical resistant, thixotropic, isophthalic polyester resin. The problem with this resin is that it is very difficult to wet: this difficulty was found by the author and had also been encountered in R.N. dockyard workshops. As discussed in 4.0, the material produced commercially was not properly wetted. However the author found that with care translucent material could be obtained. The catalyst and accelerator used were those recommended by the resin manufacturer, namely 60% MEK low activity peroxide and 0.6% cobalt solution. A gelation time of two hours was required for the preparation method. Typically 1.5% by weight of both catalyst and accelerator were used. The amounts required to produce the required gelation time varied slightly for different resin batches, but equal proportions by weight were always used.

4.2 Beam Preparation Method

The principles of the beam preparation method derive from the remarks above. The mat must be clamped to maintain alignment, and the weft threads may then be removed. The wetting difficulty means that fibres should be impregnated with resin in single tow layers, and the impregnated layers then laid up in a mould. The wetted fibres were transferred from the clamps to the mould on silicone coated paper, Bakewell parchment. After laying the wetted fibres in the mould the paper could be carefully peeled off the back without disturbing the fibres.

Two types of beam were produced: 0^{o} beams, with fibres parallel to the long axis of the beam, and 90^{o} beams, with fibres

perpendicular to the long axis of the beam. The lengths of fibres required for the two types of beam determined different clamping arrangements and moulds.

4.2.1 0^{o} Beams

The uniaxial mat was clamped onto sheets of glass, covered with Bakewell parchment, as shown in figure 4.1. The width of the beams was equivalent to two tows of glass. Separation of the layers was obtained by removing alternate pairs of tows. The weft threads were then removed; this introduced some slack in the remaining tows, which were therefore tightened by moving the upper clamp along the glass sheet without releasing the glass fibres from the upper clamping bar.

Wetting was best carried out by pouring the resin in the spaces between the pairs of tows. The resin ran along the paper wetting the fibres. Wetting was completed by stroking the fibres with a polythene bar until they were no longer visible in the resin. Sharp scissors were then used to cut the wetted layers from the unwanted material in the clamps, as indicated by the arrows in figure 4.1. The paper was slit with a Stanley knife along the spaces between the layers.

The mould used is shown in figure 4.2. Rocol MRS advanced mould release agent was sprayed liberally over the mould, lid and spacers. The single layers of impregnated glass were lifted on the paper and placed face downwards in the mould; the paper was carefully peeled off the back. Air bubbles were removed by pushing them to one end using a polythene bar. Ten layers produced the required fibre volume fraction of 20-30%.

The lid was carefully positioned and the spacers placed around the middle of the long edge of the mould. The mould was pressed in a hydraulic testing machine. Load of around 100 kg was applied slowly and steadily until the excess resin had been expelled and the mould was entirely closed. The slow application of the load should remove any remaining air bubbles with the excess resin. The load was maintained overnight; reasonably consistent conditions were maintained overnight by covering the machine containing the mould with a polythene sheet and placing a 60 Watt electric light bulb controlled by a central heating thermostat, set at 15°C, inside. The material was removed from the mould after 15-20 hours, and allowed to rest for at least 20 days.

4.2.2 90° Beams

The length of the fibres required for the 90° beams was too small for the fibres to be handled even with the aid of paper; thus the material had to be prepared as small plates for subsequent slitting into beams. The uniaxial mat was clamped on aluminium plates covered with the silicone coated paper, as shown in figure 4.3. No means of tightening was required since the much shorter lengths of mat used mean that the tows do not slack significantly after the weft threads are removed. The mat and paper were cut around the aluminium plates to match their edges. The weft threads were then removed, and the resin poured over the fibres. Wetting was considerably more difficult to obtain than with the 0° beams since the resin could not flow from gaps. The fibres were stroked with a polythene bar until they were no longer visible.

The mould used is shown in figure 4.4; the layers of glass cut around the edges of the aluminium plates fit exactly into the mould. The excess resin is designed to run along the fibres, removing any air bubbles, as for the 0^{o} beams. The long edges are not however open since it was anticipated that this could lead to too much resin being expelled; instead the mould lid is shaped such that only the centre region of the plate is pressed. The outer edges, containing the region which had been clamped and the excess resin, were discarded.

The layers of glass were laid up in the mould which was pressed in the hydraulic testing machine, as described for the 0^{o} beams. Ten layers produced the required fibre volume fraction of 20-30%. After the rest period of at least 20 days three beams were cut from the central portion of the plate using a diamond saw.

4.3 Overall Beam Appearance

The beams produced were generally translucent. Such appearance is often deduced to indicate that the fibres are properly wetted by the resin with no voids at the interface. Visual detection of such voids is however obviously limited by the wavelength of light. Thus the translucence of the material can only indicate the absence of voids larger than about 1 μm. Interfaces between fibres and resin were examined using the Stereoscan; figure 4.5 shows the base of a fibre which has been pulled out, but on which some resin remains attached. All interfaces between the fibre and resin appear continuous. It is postulated that if a void length greater than 0.5 μm was present at an interface, particularly at that between the fibre

and resin still attached, it would be visible on this print. From the magnification of the print it may be calculated that no void greater than 800 $\overset{o}{A}$ diameter is present.

A few of the 0^o beams had surface defects, and some of the beams contained oval shaped air bubbles towards the ends of the beams. The 90^o plates more frequently showed surface defects arising from the collection of air bubbles or excess resin being expelled; such areas could often be avoided by cutting only two beams from a plate.

The height of the 90^o beams was constant along the beam length, and constant width was obtained from cutting. However the beams did tend to bend after cutting, dependent apparently on the direction in which the cutting had been carried out. This effect could not be eliminated, but flexural tests could be carried out. The height of the 0^o beams was not very constant along the beam length, arising apparently from a tendency of the mould to tip. The width, determined from the mould, was constant. The 0^o beams showed no tendency to bend.

Exact beam measurements applicable along the whole length of the beam are vital for meaningful measurements of specific damping capacity. Surface grinding of the 0^o beams was therefore considered essential. This procedure also allowed the use of several beams which had been previously discarded owing to surface defects. The surface grinding did however itself produce surface defects visible under the Stereoscan (figure 4.6). Such surface defects must affect the crack initiation process; this was therefore observed using beams which had not been surface ground, as described in Chapter 6. However after

initiation, the process of further crack growth should be unaffected by surface condition.

4.4 Preparation of Beam Cross-Sections

The nature of the material was investigated by microscopical examination of cross-sections of beams cut perpendicular to the fibre direction. The cross-sections were mounted in cold setting mounting resin. The specimens were preground, using water as a lubricant, on silicone carbide papers grades 320, 400 and 600. Three stage diamond polishing was required: 14 μm on PAD-K plain disc for about one hour; 6 μm on PAD-K plain disc for about 30 minutes; finally 1 μm on Lam-Plan 410 disc for about 15 minutes.* Load of about 200 grams per specimen was applied throughout.

On completion of polishing the glass fibres were barely distinguishable from the resin. Contrast was however introduced by the use of Nomarski interference, indicating that resin had been preferentially removed (figure 4.7). Careful observation of groups of fibres using Nomarski interference indicates that the fibres do not actually touch each other. Numerous etchants were tried to establish contrast under normal illumination. Eventually it was found that immersion in 40% hydrofluoric acid for 5-10 seconds attacks the glass such that it appears black under low magnification (figure 4.8). Over-etching polishes the glass and the fibres become indistinguishable again. If a specimen is held in the vapour only, for 5-10 seconds, the acid attacks only the interface between the glass and resin and the fibres are outlined with black rings (figure 4.9).

---

* The author would like to thank Mr. Bray of Engis Ltd. for his help with establishing the polishing routine.

4.5 Preliminary Material Definition

The common definition of a composite material is the volume fraction occupied by the fibres. The present material consists of unidirectional continuous fibres. The volume fraction occupied by the fibres is therefore identical to the area fraction occupied by fibres on planes perpendicular to the fibre direction, if it can be assumed that the fibres are absolutely straight and of constant cross-section. Some justification of these assumptions may be found; the fibres appear round in optical sections at high magnification; Stereoscan observation of failure along the interface shows the fibres to have constant cross-section. Thus the volume fraction may be obtained by examination of polished and etched cross-sections as shown in figure 4.8: the volume fraction occupied by fibres is identical to the area fraction which is black, which may be easily obtained using the Quantimet.

Values of volume fraction obtained from such measurements should be very accurate. It is noted that values of area fraction may be distorted by the detection of dirt or scratches, but this error should be avoidable both by careful preparation of cross-sections and use of Quantimet'controls. In addition an unsatisfactory field can easily be discarded. Further distortion of results may arise from the picture point size being significant with respect to the fibre size on the screen; such error should be easily avoided by using sufficient magnification. Conventional measurements of volume fraction include resin burn-off and density measurement. Possible sources of considerable errors from both measurements may be

postulated. After burn-off it cannot be known whether all the resin has indeed been removed or whether some glass has also been vapourised. Density measurements may easily be distorted both by inaccurate or variable values for the resin and glass, and by the presence of voids. The accuracy of such conventional methods could be evaluated by comparison of results with results from Quantimet measurements.

Examination of micrographs such as figure 4.8 indicates that even an accurate measurement of volume fraction does not provide a complete definition of the microstructure of the material. Although volume fractions may be identical, both fibre sizes and their arrangement in the matrix may be different. A meaningful definition of the microstructure must include measurement of these factors.

The simplest measurement of this material using the Quantimet is that of fibre area fraction on etched cross-sections such as figure 4.8. The low magnification used means that many fibres appear to touch. Separation of the fibres is not required for the area fraction measurement, but a meaningful count of number of features cannot be made. Thus if the fibre arrangement is to be found from area fraction measurements, the distribution of fibre cross-sectional areas must first be measured.

4.6 Measurement of Fibre Cross-Sectional Areas

Fibre cross-sectional areas may be simply measured since the fibres are aligned and the measurement is completed in two dimensions; no stereology is required to interpret results into

three dimensions. The data was collected as equivalent diameters, calculated from measured areas assuming circular fibres.

4.6.1 Experimental Method

Measurements were made on cross-sections which had been etched in the vapour of hydrofluoric acid so that the fibres are outlined with black rings, as shown in figure 4.9. Unlike the fully etched cross-sections, these rings are still distinct at high magnifications. Fairly high magnification was required to minimise the appearance of fibres touching; the magnifications used were x63 microscope objective, x8 scanner objective, resulting in a magnification of x1750 on the screen, with one picture point equivalent to $0.177\,\mu m$.

Despite the magnification used, and the fact that Nomarski interference shows that fibres do not truly touch, a significant number of groups of two or more fibres were detected as single features. Such data could naturally cause gross distortion of the results, and was therefore discarded using shape classification of feature specific data. The shape of a feature may be classified by its form factor:

$$\text{Form Factor} = \frac{\text{Area}}{(\text{Perimeter})^2}$$

The area of the feature may be found after modification of the image using 'fill'. The perimeter of the feature may be found from the length of the black ring in the unmodified image. It is noted that the form factor is non-dimensional. The form factor of a circle is $1/4\pi$; the form factor of a group of fibres detected as a single feature would be smaller than that

of a circle. Data from all features with form factors of less than 60×10^{-3} was therefore discarded.

Another form of distortion could arise from the detection of dirt or scratches. Scratches are discarded from their shape, as described above, but small specks of dirt could be included. The smallest fibres observed had diameters of around 45 picture points, equivalent to about 8μm, that is areas of about 160 picture points. Data from features with areas of less than 100 picture points, equivalent to diameter of 4.7μm, was therefore discarded.

Area data from features which had not been discarded in the Quantimet by either of the two criteria described above was passed to the calculator, and equivalent diameters, assuming circular fibres, were calculated. The results were sorted into 1μm bins. The size of the smallest bin was derived from observation of the smallest fibres, as described above; the smallest bin was 5-6μm. The largest bin size was derived from similar observation of the largest fibres; the largest bin was 24-25μm. Twenty size bins were therefore used.

4.6.2 Measured Distribution of Fibre Diameters

The histogram of results is shown in figure 4.10. The histogram has no discontinuities indicating that a sufficient number of fibres has been measured. The total number of fibres measured was 2448. The mean fibre diameter is 14.48μm with a standard deviation of 1.90μm; these measurements may be compared with the manufacturers estimates given in 4.1. The mean diameter measured is within the error bound given.

The sections used for the derivation of this histogram were from a 90° beam which had been rejected for mechanical testing owing to a surface defect. The consistency of the distribution of fibre cross-sectional areas was checked using sections from three 0° beams which had been tested and whose microstructures had been measured. The sections had been fully etched and thus lower magnification was necessary for the fibres to remain distinct. The magnifications used were x12.5 microscope objective, x8 scanner objective, resulting in a magnification x350 on the screen, with one picture point equivalent to 0.885μm.

Results from the sections of tested beams and their comparison with the results shown in the histogram are shown in table 4.1. It may be seen that for all three sections the difference between the mean fibre diameter measured on the section and that shown by the histogram is less than three times its standard error. The samples measured on the tested sections are therefore assumed to be drawn from the same population as that shown by the histogram. The distribution of fibre cross-sectional areas shown by the histogram is therefore applied to sections of tested beams.

4.7 Further Material Definition

Further material definition in terms of fibre arrangement can now be obtained from area fraction measurements using fully etched cross-sections. Such definition will be described in the next chapter.

Chapter 5* Description of Fibre Arrangement

5.0 Introduction

Two possible approaches to the definition of the fibre arrangement may be deduced from visual observation of the microstructure. Two micrographs at low and high magnification are shown in figure 5.1

Observations of sections at low magnification reveals that there are some regions of empty space containing no fibres. Such empty space must arise from failure of the tows to disperse properly. Distinct regions of empty space are more pronounced in the 90^{o} beams than in the 0^{o} beams; this observation may be correlated with the greater difficulty of tows to disperse in the 90^{o} beams since smaller lengths of mat are used. Observations of sections at the higher magnification reveals another form of inhomogeneity in that the fibres tend to cluster in small groups.

Thus qualitative examination suggests two possible approaches to the definition of the microstructure. The first method arises from the fibres aggregating in clusters; the second method arises from the regions of empty space. The quantification of these observations presents difficulties which are illustrated by considering the measurement of an idealised pattern (figure 5.2). If the number of dots is measured in units, or cells, marked with the solid lines the results would indicate a very clustered density; the variance of the number of dots would be a maximum and half the cells are empty. If however the number of dots is measured in the cells marked with the dotted lines the results would indicate a uniform

---

* The results described in this chapter are partially covered in a paper submitted for publication: Guild & Silverman 1977.

density; the variance would be zero and empty cells are never found. Thus quantification requires both careful choice of cell size, and the derivation of theoretical results with which experimental results may be compared.

5.1 The Null Hypothesis

Theoretical results may be calculated assuming a null hypothesis. The null hypothesis used here is that the fibres are a random distribution of point particles; that is, no particle is precluded from occupying any position by the presence of another particle. The fibres are given their measured area distribution, and theoretical variances and probabilities that cells are empty can then be calculated. It may be shown that (Silverman 1976):

Theoretical variance (fractional area covered) $= \frac{\lambda m_2}{A^2}$

where: λ = mean number of particles per cell

m_2 = second moment about zero of area distribution of fibres.

A = area of cell

Standard deviation (variance of fractional area covered)

$$= \left(\frac{\lambda m_4 + 2\lambda^2 m_2^2}{A^2} \right)^{\frac{1}{2}}$$

where: m_4 = fourth moment about zero of area distribution of fibres.

The probability that a cell is empty follows immediately from standard properties of the Poisson distribution:

Theoretical probability (cell is empty) $= e^{-\lambda}$

The assumption that the fibres are point particles is obviously an approximation. The effect of this approximation has been discussed (Guild and Silverman 1977); differences

between experimental and theoretical results, calculated using this assumption, would be increased if the finite particle sizes were taken into account.

5.2 Experimental Method

The problem of the choice of cell size was solved by the experimental method. Measurements of area covered by fibres were taken using a small test cell, moved around the cross-section in a contiguous grid. Since the measurement grid is contiguous, data additions may subsequently be made to determine values of area covered in larger square and rectangular cells which are multiples of the test cell.

The magnifications used were x12.5 microscope objective, x8 scanner objective, resulting in magnification x350 on the screen, with one picture point equivalent to 0.885μm. The size of the test cell was chosen to be smaller than half the size of any observed pattern, for the reasons discussed in 5.3.1.2; the size used was 45 picture points square, equivalent to 39.8μm square. A contiguous grid could not be achieved using the automatic microscope stage. The test cell was therefore moved around the Quantimet frame using the variable frame controls, controlled by hand or automatically; when a Quantimet frame had been completely scanned the microscope stage was carefully moved by hand. The total number of samples was 52 test cells in the I direction, perpendicular to the glass layers, and 80 test cells in the J direction, parallel to the glass layers. Thus 4160 test cells were examined, a total area of about 6.6 square mm, containing about one and a quarter tows, about 12,000 fibres. The numbers of black picture points per test

cell, that is area covered by fibres, were taken as paper tape output.

Both the shape and arrangement of cells larger than the test cell may be varied. Figure 5.3 shows the different cell shapes. If experimental measurements are to be related to the area of pattern, square and rectangular cells are used. If however experimental measurements are to be related to the dimensions of pattern, long thin cells, or transects, are used in two perpendicular directions. The different cell arrangements are shown in figure 5.4. The arrangement may be such that all cells are adjacent; alternatively all possible cells, including overlapping ones, may be considered. It can be seen that the use of overlapping cells increases the number of samples for a given cell size. In addition the decrease in number of samples as the cell size increases is gradual and even.

5.3 Variance Analysis

The first method of analysis arises from the visual observation that fibres tend to cluster. The problem of defining such a distribution is similar to spatial distribution problems encountered in ecology and geography. There has been considerable discussion of the characterisation of such distributions in the literature; this is briefly surveyed below.

5.3.1 Literature Survey

A method of examining spatial distribution was first proposed in 1952 (Greig-Smith 1952). The method is described more fully in ecological texts (Greig-Smith 1964, Kershaw 1964).

A variable defining the distribution is measured in a contiguous grid of cells, the size of the test cell being smaller than the anticipated cluster size or scale of pattern. Larger cells, square and rectangular, are often formed from two cells of the preceding size, with cells being adjacent and not overlapping. The variances of the variable values for the different cell sizes are calculated, and a graph is drawn. As shown by consideration of figure 5.2, if the cell size is such as to exactly contain a pattern, either fibre clusters or empty space, the variance at that cell size would be a maximum. Any peaks in the graph are therefore deduced to indicate scales of pattern at those cell sizes.

5.3.1.1. Significance of Peaks

The simplest qualitative assessment of the significance of peaks arises from their consistency. This approach was proposed by Kershaw (1957), who demonstrated the reliability of this approach by tests on artificial communities. This subjective approach is also considered valid by Greig-Smith (1961)

Further assessment of the significance of the peaks or the meaning of the graphs may be derived from the work of Thompson (1955, 1958). For a random distribution of points he derived tables showing the limits of the ratio of the observed/expected variances for the 95% and 80% significance levels. This table was later extended by Greig-Smith (1961). The tables show that, owing to the behaviour of the significance bands, the variance is likely to increase with increasing cell size, and that, at higher cell sizes, apparently significant peaks may occur purely from chance.

Such effects can only be minimised by increasing the number of samples. Comparison of experimental results with theoretical results, calculated assuming a null hypothesis, is used in the present work. The null hypothesis is a random distribution, as in the work of Thompson, but the variable measured is area fraction covered and so the area distribution of the particles must be included in the calculation of the theoretical results.

Ecological and geographical data has been fitted to theoretical distributions, with parameters which may be calculated. Some examples of theoretical distributions and their use to describe various data are given by Dacey (1966), Rogers (1969), Carter (1972). If the data has been fitted to a theoretical distribution, the significance of peaks can be tested using classical statistical tests. It should however be noted that such comparison is only truly valid if the observed values are derived from random sampling. The normal experimental method, as described above, is to use a contiguous grid. Rogers (1974) concluded however that results from the two sampling methods tend to coincide as the number of samples is increased.

5.3.1.2. Relationship of Peak Position to Distribution

Thompson (1958) considered expected results from a particular case of underdispersion chosen on ecological grounds. The results are generally applicable to underdispersion. He showed that any peaks in the graph may be related to the mean area of clumps, the peak in the graph usually occurring at a cell size slightly greater than the mean area of the clump. Such tendency for the peak to drift to the right has been further considered by Greig-Smith (1961) who concluded that this

effect may arise from an inadequate sample size. Kershaw (1957) showed that it may occur if the basic sampling unit is too large, and concluded that the basic unit must be less than half the size of any pattern. Usher (1969) demonstrated the possibility of a drift to the left if the sample grid starts towards the centre of a clump; he concluded that the possibility must be eliminated by making various analyses of grids started at different points, and that the peak obtained furthest to the right represents the best estimate of the mean area of the clump. Such procedure would not however be necessary if sufficient samples are taken.

Most examples described in the literature use square and rectangular cells, resulting in a measure of area being represented by peaks in the graph. Transects, resulting in a measure of dimension being represented by peaks in the graph, have however been used for both artificial and real distributions (Kershaw 1957, Hill 1973).

5.3.2 Comparison of Experimental and Theoretical Results Using Statistical Tests

Classical statistical tests are only applicable if samples are independent. Thus for the application of classical statistical tests, analysis was carried out for square and rectangular cells using adjacent cells only. The observed and theoretical variances of the fractional area covered were compared using the Chi-Square test:

$$\chi^2 = \frac{(n-1)s^2}{\sigma^2}$$

where: n = number of samples

s^2 = observed variance of fractional area covered

σ^2 = theoretical variance of fractional area covered

It is noted that the use of this test assumes that values are drawn from a normal distribution or that the sample sizes are sufficiently large for the central limit theorem to apply.

All the values lead to values of χ^2 which are significant at the 99.99% level. Most values are very much higher than the 99.999% level. The highly significant deviation of experimental results from the null hypothesis is further illustrated by table 5.1 which expresses the difference between experimental and theoretical variances in terms of the theoretical standard deviation of the variance, calculated as described in 5.1.

Thus the application of classical statistical tests has established to a very high confidence level that the fibres are not randomly distributed. The nature of their distribution may be further explored by comparison of experimental results with those predicted by the null hypothesis.

5.3.3 Comparison of Sampling Methods

Results from transects were calculated using adjacent cells only, and using all possible cells, including overlapping ones. The graph of the results using adjacent cells only has peaks, but these peaks correspond to discontinuities in the graph of number of samples against cell size (figure 5.5). However the graph from the analysis of the same results using all possible cells, including overlapping ones, is monotonic (figure 5.6). Thus the uneven changes in number of samples when adjacent

cells only are analysed can cause distortion in results; peaks in the graph may be related to the sampling, not to scales of pattern.

5.3.4 Variance Matrices for Overlapping Cells

Analysis was carried out using all possible cells, including overlapping ones. All cell sizes, square and rectangular, were analysed. The resulting matrices are most easily examined as contour maps (figure 5.7). It may be seen that the surface defined by the matrix is smooth, indicating that there is no distinct scale of pattern. There is a small difference between the two directions parallel and perpendicular to the glass layers, but the surface shape is represented along one transect only.

Results are compared with theoretical variances calculated assuming the null hypothesis (figure 5.8). It is noted that the graph of experimental variances becomes linear at large cell sizes. This effect has been discussed (Guild and Silverman 1977); it is postulated that the curvature at small cell sizes arises from the fibre size being significant with respect to the cell size at small cell sizes. It can be concluded empirically that the equation of this line for reasonably large cell sizes obeys a power law.

The form of the power law for experimental results may be compared with that for theoretical results calculated assuming the null hypothesis. From the results of 5.1, the variance of the fractional area covered in terms of the cell size for the null hypothesis is given by:

Theoretical variance (fractional area covered) =

$$\frac{m_2}{m_1} \times \frac{\text{Mean fract. area cov.}}{A}$$

where: m_1, m_2 = first and second moments about zero of area distribution of fibres

A = Area of cell

For a given cross-section, this may be expressed as:

$$\text{Theoretical variance (fractional area covered)} = \frac{C_1}{n_t} C_2$$

where: C_1, C_2 = constants

n_t = number of test cells in cell

For the null hypothesis:

$C_2 = 1$

The value of C_1 for theoretical results for this cross-section is:

$C_1 = 0.0204$

The values of C_1 and C_2 for the experimental results may be found from the graph:

$C_1 = 0.0442$

$C_2 = 0.868$

Thus an assessment of the results from the variance analysis may be obtained by comparison of theoretical and experimental values of the constants C_1 and C_2.

Results from the ten cross-sections, from five 0^o beams and five 90^o beams, were analysed for transects in the I and J directions, perpendicular and parallel to the layers of glass. The results are shown in table 5.2. No apparent relationship exists between the experimental values of C_1 and C_2; however when the experimental values are divided by the theoretical

values, in an attempt to cancel out the effect of the varying mean fractional area covered, the constants do appear to show a relationship. This is shown graphically in figure 5.9. It is noted that this relationship shows considerable scatter, but does appear to be of the same form as the relationship between the theoretical constants. The range of ratios of the constant C_1 is very much greater than that of the constant C_2.

5.4 Sparse Analysis

The second method of analysis arises from the visual observation that the microstructure includes distinct regions of empty space. The method leads to the definition of the microstructure in terms of its relationship to regions of empty space. A similar approach to the definition of a structure in terms of its relationship to a smaller unit, designated the structuring unit, has been used (Delfiner 1972, Serra 1972); the mathematical expression of such relationships using sets theory has been derived (Matheron 1972). Relationships deduced in the present work are expressed graphically.

The analysis was carried out by initially designating each test cell sparse or dense. Sparse occupation is defined as occupation by less than the equivalent of half a fibre; thus empty cells, or cells with dirt or scratches, or a small corner of fibre are defined as sparse. The proportion of sparse cells is found, and thus an estimate of the probability of finding a sparse test cell has been obtained. Square and rectangular larger cells were analysed, all possible cells, including overlapping ones, being considered. Larger cells are only designated sparse if all the test cells they contain are sparse.

For a given cell size, the proportion of sparse cells is found, and thus an estimate of the probability for that cell size has been obtained. The meaning of these proportions has been discussed in more detail (Guild and Silverman 1977).

5.4.1 Sparse Analysis Results

The resulting probability matrices are most easily examined as contour maps (figure 5.10). It may be seen that the surface defined by the probability matrix is smooth. There is a small difference between the two directions parallel and perpendicular to the layers of glass, which represent the extremes of the surface shape; the shape is thus represented by these two transects.

Results are compared with theoretical probability results calculated assuming the null hypothesis (figure 5.11). The experimental probabilities are larger than the theoretical probabilities. This result is in agreement with results from the variance analysis which indicate that fibres tend to cluster; if clusters are present empty space is more likely to be present. The probabilities are greater for transects along the J direction, parallel to the layers of glass. This result may be related to the preparation method of the beams using glass fibres in tows; empty space arises when the tows are not properly dispersed in the resin, which is more likely to occur in the direction parallel to the layers of glass.

Examination of figure 5.11 shows that at intermediate cell size the experimental points lie on a straight line. It is postulated that this is a meaningful observation since it was found for all cross-sections. It can be concluded empirically that the

equation of this line for intermediate cell sizes obeys a power law.

The form of the power law for experimental results may be compared with that for theoretical results calculated assuming the null hypothesis. From the results of section 5.1, the probability that a cell is empty in terms of the cell size for the null hypothesis is given by:

$$\text{Theoretical probability (cell is empty)} = \exp\left(\frac{-A}{m_1} \times \text{Mean fract. area cov.}\right)$$

where: A = area of cell

m_1 = first moment about zero of area distribution of fibres

For a given cross-section, this may be expressed as:

$$\text{Theoretical probability (cell is empty)} = C_3 e^{-n_t C_4}$$

where: C_3, C_4 = constants

n_t = number of test cells in cell

For the null hypothesis:

$$C_3 = 1$$

The value of C_4 for theoretical results for this cross-section is:

$$C_4 = 1.80$$

The values of C_3 and C_4 for the experimental results may be found from the graph:

$$C_3 = 0.375$$

$$C_4 = 0.810$$

Thus an assessment of the results from the sparse analysis may be obtained by comparison of theoretical and experimental values of the constants C_3 and C_4.

Results were analysed for the same ten cross-sections described in 5.3.4. The results are shown in table 5.3. No apparent

relationship exists between the experimental values of C_3 and C_4. The experimental values were divided by the theoretical values in an attempt to cancel out the effect of the varying mean fractional area covered. The results are shown graphically in figure 5.12. No relationship between the ratios is apparent; the ranges of the ratios are similar. The scatter is not reduced if the results from cross-sections showing greatest scatter in the variance results are removed.

There are two possible deductions from the results above. It could be concluded that the values of the constants are meaningless because the straight line used in their deduction passes through results from only a few intermediate cell sizes. Alternatively it could be concluded that the constants represent separate and unrelated measures of the distribution of the fibres.

5.5 Comparison of Results from Variance and Sparse Analyses

The analyses are compared by seeking correlation between the results in tables 5.2 and 5.3. Figure 5.13 compares the ratios of the experimental/theoretical values of the constants C_1 and C_2 from the variance analysis with the values of the ratios of the constant C_3 from the sparse analysis. A relationship between the constants C_1 and C_3 is indicated, which is of the same form as the theoretical relationship; the range of the C_1 ratios is very much greater than that of the C_3 ratios. No relationship is found between the constants C_2 and C_3.

Figure 5.14 compares the ratios of the experimental/theoretical values of the constant C_1 and C_2 from the variance analysis with the values of the ratios of the constant C_4 from the sparse

analysis. No relationship or similarities with theoretical relationships are indicated.

The theoretical values of the constants C_1 and C_4 are both directly proportional to the mean fractional area covered. The experimental values of these constants are therefore directly compared (figure 5.15). A relationship, with very considerable scatter, may be indicated between these constants; this relationship is of the same form as the theoretical relationship.

Some correlation between the various measures of the fibre distribution has therefore been obtained. The significance of the different measurements may be further assessed when material parameters for different beams are compared.

5.6 Derivation of Representative Area

All results discussed above were obtained from the sample sizes described in 5.2, namely 52 test cells in the I direction, perpendicular to the layers of glass, and 80 test cells in the J direction, parallel to the layers of glass. This is equivalent to an area of approximately 2.07 x 3.19 mm, covering about 2 tows in the I direction and 0.5 tows in the J direction.

It was anticipated that the inherent inhomogeneity of the material may be so great that the area described above would not represent the entire cross-section. A larger area of one cross-section was therefore scanned. The area examined was 112 test cells in the I direction, perpendicular to the layers of glass, and 216 test cells in the J direction, parallel to the

layers of glass. This is equivalent to an area of approximately 4.46 x 8.60 mm. The mean and variance of the area covered by fibres inside all the test cells were calculated. Means and variances calculated from smaller areas were calculated, and the percentage deviations of values calculated from smaller areas from the values calculated from the whole area were calculated. The matrices of results are shown in table 5.4.

The shape of the surface defined by the matrix of means is investigated in figure 5.16, and that defined by the matrix of variances in figure 5.17. Examination of figure 5.16 reveals that the surface defined by the means is distinctly flattened along the J direction at the value J = 180 test cells; no such point is observed along the I direction. Examination of figure 5.17 reveals that the surface defined by the variances is distinctly flattened along the I direction at the value I = 100 test cells; some indication of flattening occurs along the J direction at the value J = 180 test cells.

These results indicate that the entire area measured could be reasonably represented by an area of 100 test cells in the I direction and 180 test cells in the J direction. This area is equivalent to about 4 tows in the I direction and 1.2 tows in the J direction. The total number of tows within the cross-section is 10 tows in the I direction and 2 tows in the J direction; representation by this area derived thus appears reasonable. Examination of the matrices in table 5.4 indicates that errors of 2.5% and 1.5% should be applied to the mean and variance results respectively.

Chapter 6* Fracture and Acoustic Emission Results

6.0 Introduction

Cracks were grown in 0° and 90° beams using four-point flexural loading; acoustic emission was monitored using the circuit described in appendix 2. This loading method was chosen for several reasons. As described in Appendix 2, noise problems which can distort acoustic emission results are eliminated both from grips and the transducer/beam interface. The region in which crack growth takes place, between the central rollers is defined, and is always close to the acoustic emission transducer. Tensile and compressive stresses only, constant along the beam length, are present in this region. Pure tensile failure, without shear, is very hard to attain in simple tensile tensile testing of composite materials. The processes of crack initiation and growth were illuminated by observation of fracture surfaces using a scanning electron microscope, and measurement of crack profiles.

6.1 Experimental

The four-point bend test arrangement is shown in figure 6.1. The acoustic emission transducer is on the upper surface of the beam, between the central rollers, held in place by an elastic band. A displacement transducer, type BPA F71/05, attached to the moving central rollers, is centred on the lower face. The displacement transducer is fed via a transducer meter, type BPA C52 and plotted on one Y-axis of the X-Y-Y recorder. Total acoustic count is plotted on the other Y-axis, as described in appendix 2. The load signal is taken from the Instron, just prior to the chart amplifier

---

* The acoustic emission results in this chapter are partially covered in a conference paper: Guild and Short, 1977

to bypass its damping circuits, and plotted on the X-axis. The load axis is calibrated using Instron calibration weights. The displacement axis is calibrated from known displacements achieved by moving the cross-head at known speed, with the displacement transducer attached and being displaced by a fixed bar; displacement is plotted against time. Flexural moduli, the average of the Youngs moduli in tension and compression, and tensile and compressive stresses in the beam, may be calculated from the load/displacement curves (e.g. Cottrell 1964). The flexural strength is defined as the stress on the beam outer surface at failure, assuming the neutral axis to be in the centre of the beam.

Examination of Figure 6.1 reveals that the distance between and outer and inner roller is approximately equal to the distance between the inner rollers; this arrangement was used for all tests. The more usual arrangement is for the distance between an inner and outer roller to be half the distance between the inner rollers, thus reducing the required length of beams. It was found that with the usual arrangement shear failure in 0^{o} beams occurred between the inner and outer rollers, before the tensile failure process was complete. With the arrangement shown in Figure 6.1 no evidence of subsidiary failures could be found, and no damage occurred from any rollers. Cracks in a few beams, both 0^{o} and 90^{o}, grew under the inner rollers. Since the stress distribution at these points is not known, results from such beams were discarded.

The cross-head speed used was very slow such that dynamic effects should be avoided; the cross-head speed generally

used was 3.33 μm sec^{-1}. Load to failure of a 0^{o} beam typically took around 90 minutes; crack growth could be halted at any time by reversal of the cross-head and rapid removal of the load. It may be noted that this procedure could not introduce any unintentional compressive loads as can occur during rapid load removal in simple tensile testing.

6.2 Failure of Resin

Crack growth in resin was observed using the four-point bend arrangement in the Instron. Failure could not however be achieved since the displacement went beyond the range of the displacement transducer. Failure was concluded by three-point loading in a hydraulic testing machine, at a much higher strain rate.

Figure 6.2 shows the four-point bend record. It is noted that at around two thirds of the maximum load of this test load drops occur; it is postulated that these load drops are associated with crack growth in the resin. No acoustic emission is recorded during the test confirming that the threshold for counting is set such that events arising from resin failure are not recorded.

The flexural modulus calculated from the four-point bend test of the pure resin beam is 2.8 GN m^{-2}; while that from the three-point bend test is 3.4 GN m^{-2}. It is postulated that the difference arises from the much faster strain rate in the three-point bend test. The occurrence of dynamic effects is confirmed since the stress on the outer surface at failure in the three-point bend test, 74 MN m^{-2}, is smaller than that maximum stress reached in the four-point bend test,

85 MN m^{-2}. Both values of flexural modulus are considerably below the manufacturers estimate of Youngs modulus in tension for post-cured resin of 4 GN m^{-2}; it is postulated that this difference arises from the post-curing.

The stress on the beam outer surface at the first significant load drop in the four-point bend test is 59 MN m^{-2}. This compares with the manufacturers figure for the tensile strength of the resin of 48.2 MN m^{-2}. The value given for the flexural strength is 107 MN m^{-2}; this difference presumably arises from the stable crack growth under increasing load as observed here.

Using the values obtained from the four-point bend test for the modulus and stress at the outer surface at the first load drop, an approximate value of the strain in the resin at the onset of crack growth may be obtained, namely 2.1%

6.3 Failure Records of 0^{o} Beams

6.3.1 Load to Failure

An example of a complete acoustic emission record and load/deflection curve for a 0^{o} beam is shown in Figure 6.3. Significant acoustic count commences at around 50% of the failure load. This is a similar result to that obtained by other workers using various composite materials (Mehan and Mullin 1971, Balderston 1972, Fitz-Randolph et al 1972, Hancock and Swanson 1972, Liptai 1972). The load/deflection curve is linear until after significant acoustic count has occurred; this is the result anticipated if the occurrence of counts is equivalent to crack growth. Failure occurs by the growth of a tensile crack initiated at a corner on the

lower, tensile, face of the beam. The crack grows towards the neutral axis spreading across about one third of the face. Stable crack growth under increasing load continues until the crack depth is around 1.5 mm, when failure occurs via splitting parallel to the neutral axis, along the fibre/matrix interface.

6.3.2 Repeated loading

Tests were halted with rapid removal of the load and, after a recovery period of at least twenty days, tests were repeated. For comparison acoustic emission and displacement curves must be scaled in terms of the tensile stress on the outer tensile face since equipment and instrumentation settings cannot be repeated exactly. Unfortunately the experimental error in the load/displacement curves, increased by the changed settings, obscures any trend in measured modulus values which could have been related to fibre breakages which had occurred in a previous test.

Acoustic emission results obtained from two tests when only a few counts have been recorded during the first test are shown in Figure 6.4. This is a good demonstration of the 'Kaiser' effect, that is, no counts are recorded during the second test until the previous level of stress has been exceeded. This indicates that no further crack growth occurs until after the previous level of stress has been exceeded, which is the result anticipated from the stable nature of the crack growth. When the previous test has included more counts however, the result is shown in Figure 6.5. It may be seen that some counts are recorded before the previous level of stress has been exceeded, although the count rate

appears lower until the previous level of stress has been exceeded. This effect is clearly seen when the integrated count is plotted on a logarithmic scale, as shown in Figure 6.6. A straight line may be drawn through the experimental lines denoting the occurrence of counts. The slope of this straight line for the later test increases to that of the previous test when the previous stress level has been exceeded. Thus it may be deduced that the early counts arise from a source other than fibre breakage, and it is postulated that this source may be frictional movement of the crack faces. This hypothesis is supported by results obtained when a previously failed 90^{o} beam is reloaded, as described in 6.4.2. The threshold for the different behaviour shown in figure 6.4 and 6.5 is not distinct, but seems to occur at around 100 counts recorded for the first test.

6.3.3 Flexural Moduli and Flexural Strengths

Some measured values of flexural moduli and flexural strengths are shown in Table 6.1, and compared with volume fractions measured using the quantimet as described in chapter 4. No relationship can be seen between any of the measured parameters. The rule of mixtures moduli were calculated using the manufacturers value for the tensile modulus of the glass, and the measured modulus for the resin. All values are below experimental values. Even using the manufacturers value for the tensile modulus of the resin, the predicted values are below the experimental values. The same discrepancy is found between predicted and experimental dynamic moduli, as described in Chapter 7. This discrepancy could arise from inaccuracy in the moduli values of the

constituents, or from difference in the tensile and flexural moduli of this material.

It is postulated that the variations in volume fraction are too small for any trend in moduli values to be noticeable above the experimental error; it is believed that the major source of this error arises from the displacement transducer. Flexural strengths are therefore expected to be more accurate, but no trend with volume fraction, and considerable scatter, is found. Explanation of these differences may be sought from consideration of the fracture processes. The flexural strength is the stress at the outer surface at failure, at the maximum applied load; maximum load occurs when stable crack growth ceases and splitting occurs parallel to the neutral axis. Possible parameters controlling the onset of splitting are discussed in 6.6.3.

6.4 Failure Records of 90° Beams

6.4.1 Load to Failure

An example of a complete acoustic emission record and load/deflection curve for a 90° beam is shown in Figure 6.7. It may be seen that the number of acoustic counts recorded prior and during failure is insignificant. The load/displacement curve is linear until failure. The crack growth is instantaneous and unstable, taking place at the maximum load. The crack initiates on the tensile face, spreading across the whole face, and grows towards the neutral axis. The crack overshoots the neutral axis, but the beam remains continuous along the compression face, to a small depth.

6.4.2 Repeated Loading

No change in behaviour is observed when tests are repeated on beams which have been stressed to just prior to anticipated failure. Acoustic emission is however recorded when a previously failed 90^{o} beam is tested; an acoustic emission record and load/displacement curve from such a test is shown in Figure 6.8. It is believed that the deviations in the load/displacement curve may be due to uneven displacements arising from the presence of the crack, and not from further crack growth, which would not be anticipated at the low loads at which the greatest deviations occur. It is postulated that the emissions may arise from frictional movement of crack faces as postulated for the re-loading of 0^{o} beams, described in 6.3.2.

6.4.3 Flexural Moduli and Flexural Strengths

Some measured values of flexural moduli and flexural strengths are shown in Table 6.2, and compared with volume fractions measured using the Quantimet, as described in Chapter 4. No relationships can be seen between any of the measured parameters.

It is postulated that the lack of a relationship between volume fractions and moduli may arise from the experimental error, as described in 6.3.3. The values of flexural strength represent the average tensile stress required to initiate the crack. The point at which the crack initiates must however be the point of some stress concentration. This stress concentration may arise from surface defects, although the 90^{o} beams were not surface ground and did not

therefore contain the gross surface defects introduced in the surfaces of 0^{o} beams, shown in Figure 4.6. Stress concentration may also arise from the arrangement of the fibres. The magnitude of the stress concentration at the point of crack initiation is therefore an unknown variable, and the average stress required for crack initiation would not be expected to be constant. The results in Table 6.2 may however be used as an approximate measure of the stress required to initiate a crack along the fibre/matrix interface.

6.5 Study of Failure Processes using a Scanning Electron Microscope*

Failure surfaces of 0^{o} and 90^{o} beams were examined using a scanning electron microscope in secondary electron mode; the microscope used was a Cambridge Stereoscan 2A. Surfaces were coated first with carbon and then with gold.

6.5.1 Crack Initiation in 0^{o} Beams

The process of crack initiation was studied using a beam which had not been surface ground, and which therefore did not contain the gross surface defects as shown in Figure 4.6. A corner at which a crack initiated is shown in Figure 6.9. The regions of the corner at which the crack initiated has striations which tend to a maximum at the point at which the crack initiated. These striations may arise from stress concentrations, or from stress relaxation when the crack starts to grow. Examination of the detail of a striation reveals that within the region resin has been removed, leaving the tips of the fibres showing.

---

* The author would like to thank Mr. D. Grey for operating the Stereoscan

6.5.2 Fracture Surfaces of 0^{o} Beams

An overall view of a fracture surface of a 0^{o} beam is shown in Figure 6.10. Fibres have pulled-out, and their pull-out lengths can be measured. The fracture plane contains steps; a detail of one is shown in Figure 6.11. These steps do not appear to be particularly associated with either resin rich or fibre filled regions. The resin failure surface contains many 'river lines', which can be seen in Figures 6.11 and 6.12; such markings are generally associated with slow crack growth which was the observed failure process. The fibre fracture surface has a typically brittle appearance, as shown in Figure 6.13. Such a brittle process may be anticipated to be associated with a single release of acoustic energy which would be recorded as a single count; correlation between numbers of counts and numbers of fibres broken is therefore sought, as described in 6.6. The pulled-out fibres have small pieces of resin still attached along their pulled-out lengths.

As described above, failure occurs when splitting occurs parallel to the neutral axis along the fibre/matrix interface. The appearance of this debonding plane is shown in Figure 6.14.

6.5.3 Fracture Surfaces of 90^{o} Beams

An overall view of the fracture surface of a 90^{o} beam is shown in Figure 6.15. It may be seen that crack growth takes place around the fibres without their failure. Views of the fracture surface at higher magnifications are shown in Figure 6.16. It may be seen that failure takes place at the

fibre/resin interface; fibres which have been pulled-out of the matrix have small pieces of resin still attached to them, as observed for pulled-out fibres in 0^{o} beams. Cylindrical holes are left where fibres have been pulled-out.

Comparison of the 90^{o} fracture surfaces shown in Figure 6.16 with the debonding plane of a 0^{o} beam, shown in Figure 6.14, reveals no differences in appearance. Failure takes place at the interface, with a few small pieces of resin remaining stuck to the fibres. Cylindrical holes are left where fibres have pulled-out. 'River lines' in the resin occur in resin rich areas.

6.6 Discussion

6.6.1 Failure of 90^{o} Beams

Crack growth in 90^{o} beams is instantaneous and catastrophic; the onset and process of crack growth may be suitable for characterisation by fracture mechanics (Babb 1976). Crack initiation in the present work took place in the absence of gross stress concentration, although, as described in 6.4.3, unknown stress concentrations were probably present in all beams. Measured flexural strength may be regarded as an approximate measure of the stress required to initiate a crack along the fibre/matrix interface.

6.6.2 Stable Crack Growth in 0^{o} Beams

Initial crack growth in 0^{o} beams takes place under rising load. The acoustic emission results indicate that no further crack growth takes place until the previous level of stress has been exceeded. The behaviour of the material is therefore unaffected by the presence of a crack; the material is

not notch sensitive. The process of the stable crack growth cannot therefore be described by linear elastic fracture mechanics.

Fibre pull-out occurs during the stable crack growth, and the pull-out lengths can be measured from Stereoscan photographs. Results from measurements near crack initiation and just prior to splitting are shown in Table 6.3. It may be seen that the difference between mean pull-out lengths is less than one standard error of the difference; the fibre pull-out length does not therefore change significantly between crack initiation and final failure. The histogram of all fibre pull-out lengths measured is shown in Figure 6.17.

The significance of the fibre pull-out length in the study of fracture processes in fibre reinforced composites has been studied for model materials and extensively discussed (Harris et al 1975). The mean pull-out length for all fibres measured here is 29.0 μm. From the usual assumption that the critical length is four times the mean pull-out length, the critical length is found to be 116 μm. This value is about two orders of magnitude smaller than the value generally reported, 13 mm (Harris et al 1975). The relationship between fibre pull-out length and critical length arises from the transfer of stress to the fibre which occurs when the crack has crossed the fibre leaving the fibre as a 'bridge'; this process is expected to occur when the failure strain of the resin is smaller than that of the fibre. However even when the crack in the resin had crossed the fibre and extensive debonding had occurred, fibres in model

composites often fractured at the crack plane (Harris et al 1975). In the present case the failure strain of the resin is 2.1% and that of the fibres is 2.6%. The discrepancy between the measured pull-out length and generally reported critical length may therefore arise from the process of crack growth being continuous without the occurrence of fibre 'bridges', or from failures occurring in the crack plane despite the occurrence of 'bridges'. It is noted from the histogram of fibre pull-out lengths (Figure 6.17) that although the peak occurs at small pull-out lengths, near the mean value, there is a long tail stretching to much higher lengths approaching that appropriate to the generally accepted critical length.

No attempt has been made to evaluate the energy required for the crack growth. The contributions of the various processes to the overall fracture energies has been studied for model composites (Harris et al 1975). The main contribution to the fracture energy had been previously considered to be the process of debonding. It was however concluded that this contribution may be small with respect to the contribution arising from the work done against friction between fibres and matrix after the debonding, including the work done in fibre pull-out. The work of fibre pull-out is dependent on the pull-out length, which, as discussed above, is not necessarily that calculated from the critical length. The factors affecting the pull-out length have not been established, but it is postulated that these may include the geometry of the test piece, the size and arrangement of

the fibres, and the crack speed. Different test methods and materials lead to different values of such parameters; it is therefore postulated that the considerable discussion in the literature regarding values of fracture energy and the applicability of linear elastic fracture mechanics could be enlightened by study of the fracture processes and pull-out lengths. The controlled method of crack growth used here may be applicable for such a study.

6.6.3 Failure of 0^{o} Beams

Maximum load is reached and failure occurs when splitting occurs on the plane parallel to the neutral axis along the fibre/matrix interface. Failure of notched 0^{o} beams loaded in four-point bend always occurs by this process without any fibre failure (Babb 1976).

Stereoscan observation of the fracture surfaces of 90^{o} beams and the plane of the splitting in the 0^{o} beams reveals no differences in the appearances of the fracture surfaces. It is therefore postulated that the failure processes are the same, namely a tensile process. The tensile stress which would cause such failure is at a maximum just ahead of the crack (e.g. Kelly 1966). This tensile stress has been observed to cause interface failure ahead of the crack tip in timber (Jeronimidis 1976), and in ausformed steels (McEvily and Bush 1962, Tetelman and McEvily 1967). Using the Inglis (1913) expressions for the stresses around an eliptical crack, Cook and Gordon (1964) have shown that the magnitude of this tensile stress tending to cause interface failure is one fifth of the tensile stress at the crack tip

tending to cause mode 1 failure. Stresses ahead of a notch in a carbon/epoxy composite have been shown to agree well with the Inglis calculations (Bishop 1974). The experimental results of Cooper and Kelly (1967) find the critical ratio for splitting to occur to be 13.2, considerably larger than the theoretical value derived by Cook and Gordon (1964).

The stress required for mode 1 failure may be approximated as the stress required to initiate crack growth in the 0^{o} beams. As previously discussed, acoustic emission results show that such crack growth starts at around half the maximum load, so the stress required is around half the flexural strength, shown in Table 6.1, around 168 MN m^{-2}. The tensile stress required for interface failure may, as previously discussed, be found from the flexural strength of 90^{o} beams, shown in Table 6.2, around 28 MN m^{-2}. Thus the two stresses are different by a factor of 6, lying between the calculated difference required for interface failure (Cook and Gordon 1964) and that experimentally observed (Cooper and Kelly 1967). The onset of splitting along the interface must occur when there is sufficient tensile strength in that direction. During stable crack growth the average stress imposed is that required for mode 1 crack growth, taking into account the stress concentration at the crack tip. For splitting to occur there must be an increase in the relative magnitude of the stress ahead of the crack to cause interface failure with respect to the stress to cause mode 1 failure. Such change occurs during change from plane stress to plane strain conditions (Knott 1973). It is postulated that the onset of splitting

is controlled by the change from plane stress to plane strain conditions as the crack grows into the beam; notches in tests reported in the literature on notched specimens, when failure occurred by interface splitting, may have been sufficiently deep for plane strain conditions to apply. It is noted that the onset of splitting after crack growth has taken place across the fibres is the opposite transition to that theoretically anticipated from fracture mechanics considerations (Antolovich et al 1973); failure by delamination was shown to be favoured for short cracks.

The change from plane stress to plane strain would be a function of the distance the crack has grown into the material and the width over which it has grown. A typical crack profile is shown in figure 6.18. The crack generally spread across about one third of the tensile face of the beam, but there was considerable variation in this distance. Crack profiles were traced and the tracings were examined using the epidiascope of the Quantimet. Results are shown in Table 6.4. It may be seen that there is considerable scatter between crack areas and between values of maximum distance across the beam and maximum distance the crack has grown into the beam. The shape of a crack profile may be defined by its form factor:

$$\text{Form Factor} = \frac{\text{Area}}{\text{Perimeter}^2}$$

It is noted that the values of form factors of the crack profiles show much smaller scatter. The onset of splitting may thus be characterised by the form factor of the crack profile. It has been observed that the crack initiates at

a corner. It is postulated that the crack spreads across the face before splitting occurs; this is confirmed by the appearance of cracks from beams when flexural tests were halted before final failure. The distance which the crack grows into the material is therefore controlled by the width over which the crack spreads, which must be controlled by many factors including the surface condition, geometric inhomogeneities and the fibre arrangement.

Some confirmation of this hypothesis was gained by testing two beams rotated 90^{o} thus increasing their height and reducing their width. The form factors of their crack profiles are 0.0490 and 0.0368; these values are within 1.5 standard deviations of the mean value of form factor obtained for other beams. The point at which splitting occurs appears therefore to be independent of beam dimensions. The onset of splitting could therefore be controlled by the change from plane stress to plane strain conditions.

The failure of these beams is controlled by the onset of splitting. It is hoped that the failure process has been illuminated by the present work. Considerable further work could however be applied to gain further insight into the parameters controlling the onset of splitting.

Chapter 7 Specific Damping Capacity Results

7.0 Introduction

Measurements of specific damping capacity were carried out on both undamaged and cracked beams. Results were analysed by classical wave equation analysis or receptance analysis; for undamaged beams results from the two methods of analysis were in agreement. The simpler wave equation analysis, which requires far shorter computing time, was therefore used for analysis of undamaged beams.

7.1 Crack Detection from Specific Damping Capacity Measurement

The detection of cracks from the measurement of specific damping capacity is based on the prediction that if a crack is present in a beam subjected to vibration the crack will be a significant source of energy loss, resulting in an increased value of measured specific damping capacity. Such energy loss may arise from frictional movement of the crack surfaces. If the magnitude of the energy loss is proportional to the square of the amplitude of the vibration, the increase in measured specific damping capacity arising from the crack would remain constant with increasing stress. If however, the magnitude of the energy loss is a higher function of the vibration amplitude, stress dependent specific damping capacity, increasing with increasing stress, would be measured. This is the result obtained for torsional testing when shear cracks are present (Flitcroft 1977). Values of specific damping capacity would reduce with increasing stress if the magnitude of the energy loss is a lower function than the square of the

vibration amplitude.

An alternative method of crack detection arises from the position of the crack. As previously described, crack growth takes place from the tensile face during four-point loading. The magnitude of the energy loss at the crack during vibration would be dependent on conditions at the crack surfaces. It may be anticipated that if the static stresses, neglecting those imposed by the vibration, tend to close the crack surfaces together, the energy loss would be less than if such stresses tend to hold the crack surfaces open. Static bending moments, arising from the mass of the beam material and the mass of the coils, were therefore compared with dynamic bending moments. Results for typical 0^{o} and 90^{o} beams in the free-free rig and in the cantilever rig are shown in Figures 7.1 and 7.2 respectively. It may be seen that, in the free-free rig, the static bending moment is very much smaller than the dynamic bending moment but, in the cantilever rig, they are of the same order of magnitude. For both rigs, the static bending moment tends to hold together crack surfaces on the lower face. A change in measured specific damping capacity may thus be found when beams containing cracks are turned over.

7.2 Specific Damping Capacity of Undamaged Beams

Specific damping capacity values of the same 0^{o} and 90^{o} beams measured in the free-free rig and cantilever rig are shown in Figures 7.3 and 7.4. It may be seen that the measured values are higher from the cantilever rig than from the free-free rig; this is the result anticipated from the measured values of the

specific damping capacity of Duralumin, described in Chapter 3.

Damping values of the 0^{o} beam from the cantilever rig show insignificant stress dependence, while those from the free-free rig are higher at low stress levels, falling to a constant value as the stress level increases. This is the result expected if there is a small source of energy loss; such loss becomes less significant with respect to the total energy input as the stress level increases. Damping values of the 90^{o} beam from the cantilever rig show some tendency to increase as the stress level increases; this effect was frequently, but not invariably, found. It is postulated that this effect may arise from increasing energy loss at the encastré end. The brittle nature of the 90^{o} beams made it impossible to apply as much clamping pressure as for the 0^{o} beams.

The mechanical behaviour of polyester resin is very temperature dependent, and a small change in ambient temperature can extensively alter measured values of specific damping capacity. This effect is illustrated by figure 7.5 which shows results from a 90^{o} beam measured in the cantilever rig at $22^{o}C$ and $25^{o}C$. Dynamic moduli are also temperature dependent; the measured values for this beam at $22^{o}C$ and $25^{o}C$ were $6.27GNm^{-2}$ and $6.12GNm^{-2}$ respectively. Thus care must be taken that all comparisons are made for the same test conditions. A useful test for the detection of cracks would not include the necessity for comparison with previous results.

Values of specific damping capacity and dynamic modulus for various 0^{o} and 90^{o} beams, measured in the free-free rig and cantilever rig, are shown in Tables 7.1 and 7.2 respectively. Measured values of specific damping capacity are higher, and measured values of dynamic modulus are lower, in the cantilever rig. Values of dynamic flexural modulus are generally greater than the rule of mixtures predictions; this is the same discrepancy as that found for flexural moduli calculated from the four-point bend tests, as described in Chapter 6. No relationship is evident between volume fractions and values of specific damping capacity or measured modulus.

7.3 Crack Detection using the Free-Free Rig

7.3.1 0^{o} Beams

Typical measurements from an undamaged beam have been shown in Figure 7.3. Typical values obtained from a beam after halting a flexural test at the onset of acoustic emission are shown in Figure 7.6. It may be seen that the behaviour shown in these results is no different from that obtained from an undamaged beam. The measured values of specific damping capacity confirm the acoustic emission result that no crack growth has taken place.

A typical result from a beam after acoustic emission had been recorded, but when no crack was visible, is shown in Figure 7.7. It is seen that the presence of a crack may be detected both from stress dependence of measured specific damping capacity and by the change in values when the beam is turned over. Both the stress dependence and the values at a given stress are greater when the crack surfaces are

being held open by the static bending moment. Results from the undamaged beam are also shown in Figure 7.7. It is seen that, after stressing, all values have increased. However, the temperatures during tests were 20°C, 23°C and 22°C respectively and so the difference cannot be quantified. Comparison of absolute values of specific damping capacity cannot be a reliable test under normally variable test conditions.

The measurements obtained when a visible crack is present are shown in Figure 7.8. The same trends noted in Figure 7.7 are found, and the magnitudes of the effects are greatly increased. The results of Figure 7.8 may be used to find the implied values of energy absorbed by the crack at the various stress levels, assuming a constant known value of specific damping capacity for the remaining beam material. Results from a previous test must be used in this calculation so the values calculated are only approximate since identical test conditions cannot be ensured. The values of energy absorbed are shown in Figure 7.9. The values of energy absorbed increase at a higher function than the square of the maximum surface stress, or vibration amplitude; this is known since measured values of specific damping capacity increase with increasing stress.

Flexural tests were halted at various stages after acoustic emission monitoring had indicated that further crack growth had taken place, and damping measurements were made. Although the assumptions made in the wave equation analysis are not strictly applicable since the beam properties are not constant along its length, specific damping capacities calculated

using this analysis do give a qualitative indication of the process of crack growth, as shown in Figure 7.10. Such results cannot be further quantified because of both the inadequacy of the analysis and the probable differences in test conditions between various measurements.

7.3.1.1 Quantification of Results using the Receptance Analysis

The stress dependence of specific damping capacity may be quantified as a polynomial in stress using the receptance analysis, as described in Appendix 3.6. In addition, the use of this analysis allows the calculation of the specific damping capacity of a cracked portion of the beam at a given value of energy stored, taking into account the position of the crack; the effect of a given crack on the overall measurement of specific damping capacity of a beam is dependent on its position along the beam since energy stored varies along the beam.

The calculation of the coefficients of the fourth order polynomial relating values of specific damping capacity and stress involves the solution of five simultaneous equations, as described in Appendix 3.6. Unfortunately, using the standard Fortran routine available, the deflection differences between readings were too small and, after rounding errors, the R matrix was singular, so the equations could not be solved. The equations could only be solved assuming a first order polynomial, using values from the highest and lowest deflections.*

---

* The author would like to thank Mr. G.F. Harley, of the School of Mathematical Sciences, Plymouth Polytechnic, for useful discussions regarding the solution of these equations.

Values of specific damping capacity for a cracked beam calculated using the wave equation analysis and the receptance analysis are compared in Figure 7.11. Values calculated using the wave equation analysis are for the whole beam, assuming that the beam is uniform. Values calculated using the receptance analysis are for the cracked portion only; the modulus in the cracked portion is different from that in the undamaged portions. It may be seen that analysis of only the cracked portion yields higher values of specific damping capacity and greater stress dependence; this result is anticipated since averaging the effect of the crack over the whole beam would be expected to reduce changes in values.

Five cracked beams were analysed using the receptance analysis. The results may be summarised by the values of the coefficients from the fitting of the polynomial. As described above, only a first order polynomial could be successfully fitted. The results are shown in Table 7.3. No correlation can be found between the values of the coefficients and the numbers of recorded acoustic emission counts.

7.3.2 90^{o} Beams

Typical measurements from an undamaged beam have been shown in Figure 7.3. The apparent catastrophic nature of the failure of 90^{o} beams has been described in Chapter 6. Results obtained from a beam stressed to just prior to anticipated failure are shown in Figure 7.12. It may be seen that no stress dependence is found, and that results obtained when the beam is turned over are unaltered. These observations are in agreement with the observations made during mechanical

tests; no change in material condition occurs until catastrophic failure.

After failure the beams remain intact to a small depth only from the face which had been the compression face during the flexural test. The failed beams are very fragile but, with care, their specific damping capacity can be measured. Resonant frequency decreases with increasing deflection, so retuning was necessary between measurements. The values of dynamic moduli implied for the beam, when the tensile face from which the crack has grown was at the top or bottom, are shown in Figure 7.13. No real difference in measurements when the beam is turned over can be seen; this may arise because the beam is intact along such a small depth that any change is obscured by inherent scatter.

The variation of specific damping capacity with cyclic stress of the whole beam, calculated taking into account the change in modulus, is shown in Figure 7.14. It should be noted that the values are higher at low stress levels, implying that the extra energy absorption arising from the crack increases at a lower function than proportional to the square of the amplitude of the vibration. Values of energy absorbed by the crack were calculated as for the 0^{o} beam, described in 7.3.1, and are shown in Figure 7.15. It may be seen that the relationship between the absorbed energy and maximum surface stress is approximately linear. Thus the energy absorbed by the 90^{o} crack is proportional to the amplitude of the vibration. As described in 7.3.1, the energy absorbed by a 0^{o} crack is proportional to a higher function than the square of the

vibration amplitude. This difference appears reasonable when the values of energy absorbed by the 0^{o} crack, shown in Figure 7.9, are compared with those absorbed by the 90^{o} crack, shown in Figure 7.15; the values of energy absorbed by the 90^{o} crack are an order of magnitude greater than those absorbed by the 0^{o} crack.

7.4 Crack Detection using the Cantilever Rig

7.4.1 0^{o} Beams

Typical measurements from an undamaged beam have been shown in Figure 7.4. Typical values obtained from a beam after a flexural test had been halted at the onset of acoustic emission are shown in Figure 7.16. It may be seen that these results are no different from those obtained from an undamaged beam. The measured values of specific damping capacity confirm the acoustic emission result that no crack growth has taken place.

A typical result from a beam after acoustic emission has been recorded, but when no crack was visible, is shown in Figure 7.17. The measured values of specific damping capacity are greater when the crack surfaces are held open by the static bending moment. However,no stress dependence was found; this may be associated with the lack of sensitivity in the cantilever rig arising from the inherent experimental difficulty of obtaining a true encastré condition. In addition, the mode shapes are such that the stress levels used in the cantilever rig are smaller than those used in the free-free rig.

Measurements obtained when a visible crack is present are shown in Figure 7.18. These results are similar to those of

Figure 7.17; the difference between results when the beam is turned over is not greater for the visible than for the invisible crack.

7.4.1.1 Crack Detection from Temperature Difference

Estimates of the energy absorbed by the crack in the results shown in Figure 7.18 cannot be calculated by comparison of these values with those obtained when the beam was undamaged since they are almost identical. It is postulated that the order of magnitude of energy absorbed by the crack can be calculated from the difference in measured values of specific damping capacity when the beam is turned over. Some justification of this assumption is found when failed 90^{o} beams are tested, as described in 7.4.2. The value of energy absorbed by the crack using this assumption, at the highest stress level used, is found to be 440 μJ per cycle, that is 1.29 μWatts.

This cracked beam was examined using an Aga Thermovision 680 camera, which can detect a temperature difference of $0.2^{o}C$ in a black body. At the stress levels used in this work, the crack was not detected by the camera, although it was clearly visible (Pye 1977). It is noted that the specific damping capacity measurements unambiguously detect the presence of such visible cracks as well as the presence of smaller, invisible cracks.

An estimate of the temperature difference expected between the crack tip and the remaining material was calculated assuming all the energy to be absorbed in a sphere at the crack tip. The temperature difference, ΔT, between the sphere and the

surface, in this case the beam surface, is given by (Ede,1967):

$$q = K\Delta T \frac{4r}{1 - r/2z}$$

where: q = heat transfer

K = thermal conductivity

r = radius of sphere

z = depth of sphere

The depth of the crack is about 0.5 mm. The radius of the sphere absorbing the energy for the temperature difference to be 0.2°C is calculated to be around 1.7 μm, and almost independent of the value of z. This sphere radius is an order of magnitude smaller than a fibre diameter, and therefore would never occur. A temperature difference of 0.2°C would therefore not arise at the stress levels used in this work.

7.4.1.2 Quantification of Results using the Receptance Analysis

Results from the cantilever rig were quantified using the receptance analysis as described for the free-free rig in 7.3.1.1. As discussed for the free-free rig, values were not measured at sufficiently different deflections, and only a first order polynomial, using values from the highest and lowest deflections, could be fitted.

Values of specific damping capacity for a cracked beam calculated using the wave equation analysis and the receptance analysis are compared in figure 7.19; values were measured with the tensile face up. Values calculated using the wave equation analysis are for the whole beam, assuming the beam is uniform. Values calculated using the receptance analysis are for the cracked portion only; the modulus in the cracked portion is

different from that in the undamaged portions. It may be seen that analysis of the cracked portion only yields higher values of specific damping capacity, and stress dependence; significant stress dependence is not observed in results analysed using the wave equation analysis. This difference illustrates the lack of sensitivity of the wave equation analysis arising from the effect of the crack being averaged over the whole beam.

The same five cracked beams as for the free-free rig were analysed using the receptance analysis. The results may be summarised by the values of the coefficients from the fitting of the polynomial. As described above, only a first order polynomial could be successfully fitted. The results are shown in Table 7.4. No correlation can be found between the values of the coefficients and the numbers of recorded acoustic emission counts.

7.4.2 90^{o} Beams

Typical measurements from an undamaged beam have been shown in Figure 7.4. Results obtained from beams stressed to just prior to anticipated failure again confirm the catastrophic nature of the failure of 90^{o} beams. Typical measurements are shown in Figure 7.20; no stress dependence is found, and values when the beam is turned over remain unchanged.

Failed beams, intact to a small depth only, can be tested. The resonant frequency decreases with increasing amplitude, so retuning was necessary between measurements. The apparent values of dynamic moduli for the whole beam when the tensile face from which the crack has grown is at the top or bottom,

are shown in Figure 7.21. It is noted that when the tensile face is down, so that the crack surfaces are held together by the static bending moment, the apparent modulus is not much lower than the modulus measured when the beam was undamaged, 6.23 GNm^{-2}, and is hardly stress dependent. When the crack surfaces are held open by the static bending moment the modulus is reduced and becomes very stress dependent. The same cracked beam measured in the free-free rig showed no significant change in implied moduli when the beam was turned over (Figure 7.13). This different behaviour may be correlated with the difference between the bending moments in the two rigs, shown in Figure 7.1 and 7.2; the static bending moment is far more significant with respect to the dynamic bending moment in the cantilever rig than in the free-free rig.

Values of apparent specific damping capacity of the whole beam measured with the crack surfaces held open by the static bending moment, calculated taking into account the changes in apparent modulus, are shown in Figure 7.22. It is found that, unlike results from the free-free rig, the apparent specific damping capacity increases with increasing stress. When the crack surfaces are held open by the static bending moment, the values are far higher and show more stress dependence; when the crack surfaces are held closed by the static bending moment the values are not much greater than that from the undamaged beam, 15.2%.

An explanation for the difference in stress dependence between the two rigs may be sought from consideration of energy

levels. The apparent energy absorbed by the crack at the highest stress level, calculated as previously described, is 9.9 μJ. This is an order of magnitude smaller than the apparent energy absorbed at maximum stress by the same crack in the free-free rig; it is the same order of magnitude as that energy for the 0^{o} cracked beam in the free-free rig when similar stress dependence was found.

7.5 Comparison of Results from the Two Rigs

Results from the two rigs show general qualitative agreement. Invisible cracks in 0^{o} beams which have been indicated by acoustic emission monitoring are successfully detected in both rigs, using either wave equation or receptance analysis. In the free-free rig, wave equation analysis gives values of specific damping capacity which are stress dependent, and which change when the beam is turned over; the stress dependence is increased when the receptance analysis is used and the cracked portion is analysed separately. In the cantilever rig, wave equation analysis gives values of specific damping capacity which are independent of stress, but which change when the beam is turned over; however values calculated using the receptance analysis are stress dependent. No correlation between the number of acoustic counts recorded and stress dependence is found for either rig.

Dynamic moduli of failed 90^{o} beams, intact to a small depth only, calculated using the wave equation analysis, decrease with increasing stress in both rigs. No change when the beam is turned over is detected in the free-free rig, but the change is marked in the cantilever rig; this may be

correlated with the difference in the ratios of static to dynamic bending moments in the two rigs. Values of specific damping capacity calculated using the wave equation analysis show different stress dependence in the two rigs; a possible explanation of this may be found from comparison of values of apparent energy absorbed by the crack.

Chapter 8 Microstructural Correlation and Conclusions

8.0 Introduction

Results presented in the last two chapters have been compared with volume fractions measured using the Quantimet as described in Chapter 4. No correlation has been found between values of volume fraction and any measured property. However, as described in Chapter 4, the volume fraction occupied by the fibres is a very incomplete description of the microstructure of these beams. A method for the quantitative definition of the microstructure has been derived, as described in Chapter 5. Correlation between such quantitative microstructural definition and measured properties is now sought.

The properties available for such quantitative correlation are the values of specific damping capacity and dynamic flexural modulus measured using the free-free rig and the cantilever rig, and the values of flexural modulus measured in the four-point bend tests. The flexural strength is not a property which might be dependent on the microstructure, as described in Chapter 6. Measured properties from the free-free rig and the cantilever rig show general agreement, as described in Chapter 7, but it is considered that values from the free-free rig are likely to be more accurate since the clamping at the encastré end in the cantilever rig may be variable. Values of flexural modulus measured in the four-point bend tests show considerable scatter, probably arising from inaccuracies in displacement measurement, as described in Chapter 6. Comparison is therefore made between measured microstructures and properties measured in the free-free rig.

It was ensured that the measurements in the free-free rig had all been taken at similar temperatures.

8.1 Experimental Method

The derivation of the representative area for these cross-sections is described in 5.6; it was found that with the magnification used there and the test cell size, a cross-section could be reasonably represented by an area of 100 test cells in the I direction, perpendicular to the layers of glass, and 180 test cells in the J direction, parallel to the layers of glass. This is equivalent to an area of about 28.6 square mm. containing about 5 tows, about 50,000 fibres.

The area measured was 98 test cells in the I direction and 180 test cells in the J direction; this area fits exactly into 70 Quantimet frames. The test cell was moved automatically around the Quantimet frame; after completion of a Quantimet frame the microscope stage was moved carefully by hand. The numbers of black picture points per test cell, that is area covered by fibres, were taken as paper tape output.

Unfortunately considerable difficulty was encountered in transferring the data from the paper tapes into computer files for analysis. Only four of the seven tapes obtained have been successfully filed and analysed.*

---

* This problem arises from incompatibility of computer peripherals at Plymouth and Cambridge rather than from some weakness in the method.

8.2 Results

8.2.1 Mechanical Properties

Table 8.1 shows values of specific damping capacity and dynamic flexural modulus, measured in the free-free rig, for the four beams whose microstructures have been measured and analysed. The measured values of specific damping capacity and dynamic flexural modulus all have the same ranking. The results are normalised to a volume fraction of 20%. The normalisation changes the ranking which is not then identical for the two properties. The range of values of specific damping capacity is however the greater, and it is anticipated that this property may be more sensitive to microstructure.

8.2.2 Results from the Variance Analysis

Variance analysis was carried out as described in Chapter 5. Results are shown in Figure 8.1; these graphs show the experimental values for transects in the J direction, parallel to the layers of glass. The graphs of the experimental values for transects in the I direction, perpendicular to the layers of glass, are of the same form and the comparison between different sections is the same. The ranking of these graphs is different from that of the measured properties shown in Table 8.1.

Theoretical values of the variances, assuming the null hypothesis, were calculated as described in Chapter 5. Flexural variances for the first ten cell sizes were expressed in terms of theoretical variances; the results are shown in Figure 8.2. The ranking of these graphs is the opposite to that which might have been anticipated; the beam with the lowest measured

value of specific damping capacity has the highest values of the ratio experimental/theoretical variance. This result is discussed in 8.3.

The variance curves were analysed in terms of the constants C_1 and C_2 defined in 5.3.4. The variance follows a power law which may be expressed as:

$$\text{Variance (fractional area covered)} = \frac{C_1}{n_t^{C_2}}$$

where: n_t = no. of test cells in cell

For the null hypothesis:

$$C_1 = m_2 \times \frac{\text{Mean fractional area covered}}{A_t}$$

where: m_1, m_2 = first and second moments about zero of area distribution of the fibres

A_t = area of test cell

$$C_2 = 1$$

Theoretical and experimental values of the constants are shown in Table 8.2.

It is noted that the ranking of the C_2 ratios is the same as that of the experimental variances, shown in Figure 8.1, and that the ranking of the C_1 ratios is the same as that of the ratios experimental/theoretical variance, shown in Figure 8.2. Thus the values of C_1 also show the reverse order of ranking to that anticipated.

The values of the constants C_1 and C_2 provide a description of the results from the variance analysis. As described in 5.3.4, a relationship between the constants may exist. However since

the ranking of the constants in the present results is not the same, it was considered that a combined assessment of the values of the two constants should be obtained. The deviations between the theoretical and experimental values were expressed as a percentage of the theoretical value, and results for the two constants were summed. The average for the two directions I and J, perpendicular and parallel to the layers of glass, was calculated. The results are shown in Table 8.3. The ranking of the percentage deviations is the same as that of the C_1 ratios, the opposite to that anticipated.

8.2.3 Results from the Sparse Analysis

Sparse analysis was carried out as described in Chapter 5. Results are shown in Figure 8.3; these graphs show the experimental values for transects in the J direction, parallel to the layers of glass. The graphs of the experimental values for transects in the I direction, perpendicular to the layers of glass, are of the same form and the comparison between different sections is the same. The ranking of these graphs is different from that of the measured properties shown in Table 8.1.

Theoretical values of the probabilities, assuming the null hypothesis, were calculated as described in Chapter 5. Experimental probabilities for the first five cell sizes were expressed in terms of the theoretical probability; the results, plotted logarithmically, are shown in Figure 8.4. The relationships for the different sections are not of the same form, and the curves cross. This may indicate that this sparse analysis is more sensitive than the variance analysis.

The probability curves were analysed in terms of the constants C_3 and C_4 defined in 5.4.1. The probability that a cell is empty follows a power law which may be expressed as:

$$\text{Probability (cell is empty)} = C_3 e^{-n_t C_4}$$

where: n_t = No. of test cells in cell

For the null hypothesis:

$C_3 = 1$

$C_4 = \frac{A_t}{m_1}$ x Mean fractional area covered

Where: A_t = area of test cell

m_1 = first moment about zero of area distribution of fibres

Theoretical and experimental values of the constants are shown in Table 8.4. It may be seen that the ranking of the two constants is not the same. The ranking of the constants C_3 is identical to that of the normalised values of specific damping capacity shown in Table 8.1.

The values of the constants C_3 and C_4 provide a description of the results from the sparse analysis. As described in 5.4.1, there is no apparent relationship between the constants, and it was therefore considered that a combined assessment of the values of the two constants should be obtained. The deviations between the theoretical and experimental values were expressed as a percentage of the theoretical value, and results for the two constants were summed. The average for the two directions, I and J, perpendicular and parallel to the layers of glass, was calculated. The results are shown in Table 8.5.

The ranking of the percentage deviations is identical to that of the C_3 ratios; the ranking is identical to that of the normalised values of specific damping capacity shown in Table 8.1.

8.3 Discussion

Correlation has been found between results from the sparse analysis and values of specific damping capacity. It is postulated that if better values for flexural modulus had been available, similar correlations may have been obtained. Values of dynamic flexural modulus are known to vary inversely with values of specific damping capacity. The value of specific damping capacity is reduced, that is the value of flexural modulus is anticipated to be increased, as the fibre arrangement approaches that predicted by the null hypothesis, a random distribution.

The effect of the fibre arrangement on properties appears to be better described by the sparse analysis than by the variance analysis. This result is not unexpected since the variance values describe only the second order structure, that is, the position of a particle with respect to another particle; all variance calculated here may be expressed in terms of covariances. The sparse analysis provides a more complete, but as yet undefined, description of the fibre arrangement (Silverman 1977).

8.4 Concluding Remarks

The author hopes that the work described in this thesis has elucidated the mechanical behaviour of the material investigated, and established various techniques applicable to this and other

composite materials.

The Quantimet was an invaluable tool for gaining a quantitative assessment of the material. Volume fractions of all beams were accurately measured; this accurate measure of volume fraction could be used to assess the accuracy of other common measures of volume fraction, such as density measurement and resin burn-off. The measurement of the distribution of fibre cross-sectional areas allowed numbers of fibres within a given area to be estimated after volume fraction measurement.

The author believes that quantitative measurement of the microstructure of composite materials is becoming increasingly important with the increasing use of these materials in critical applications. Methods of such quantitative measurements have been derived. Application of such measurements would allow composite materials to be realistically compared, and may provide explanation for discrepancies in measured properties and behaviour in materials which, according to the simple definition of volume fraction, should be identical. Some correlation between measured values of specific damping capacity and measured microstructures has been obtained in the present work. The use of these quantitative measures of microstructure is an area for much further work.

Cracks were grown in four-point flexural loading. 0^{o} beams showed a region of stable crack growth under increasing load. Maximum load was reached when the stable crack growth stopped and splitting occurred parallel to the neutral axis, along the fibre/matrix interface. The onset of this splitting denotes the occurrence of failure in these beams, and the factors

controlling the onset of splitting are therefore important. From the results available here it was deduced that failure occurs when the crack profile reaches a certain shape; this shape is apparently independent of the dimensions of the beam. It is therefore postulated that the onset of splitting is controlled by the change from plane stress to plane strain as the crack grows into the beam. Further experiments using beams of different dimensions could be carried out to confirm this conclusion. Such confirmation may allow the development of fail-safe design for composite beams; the remaining beam after splitting has occurred could be sufficient to prevent catastrophic failure.

There has been much recent development of the instrumentation required for acoustic emission monitoring, and its application to metallic materials. The technique is increasingly being applied to composite materials. Sophisticated equipment was not available for this work, and a simple and cheap circuit, designed to monitor fibre failures only, was built in the laboratory. The author believes that this circuit accurately monitored crack growth in 0^{o} beams by monitoring the failure of fibres. This result indicates that acoustic emission monitoring is a very useful technique to monitor the failure of composite materials, particularly when, as here, the ring-down envelope is recorded as a single count. The limitations of the circuit meant that events from fibre failures only could be reliably measured. More sophisticated equipment, with amplitude sorting, may allow further investigation into the process of crack growth in this and other composite materials.

Specific damping capacity measurement provides a sensitive measure of material condition. The development of rigs and analyses was rather protracted, but eventually predicted frequencies and sensible values of specific damping capacity were obtained. Invisible cracks, which had been indicated by acoustic emission, could be detected by specific damping capacity measurements in both rigs. The author believes that the free-free rig may give more accurate and numerically reproducible results, but successful detection also occurred in the cantilever rig. This rig is very much easier and quicker to set up, and may therefore be more useful as a routine tool for crack detection.

The receptance analysis is a sophisticated tool for the analysis of cracked beams. The analysis can easily be applied to the free-free rig or the cantilever rig. This analysis allows calculation of the dynamic flexural modulus and specific damping capacity of the cracked region, using known values for the undamaged parts of the beam. Quantitative correlation between changes in dynamic flexural modulus and specific damping capacity with size of crack may therefore be anticipated, particularly in the free-free rig when results are believed to be numerically accurate. Unfortunately such quantitative correlation was not obtained in the present work. The author believes that insufficient results may be available here to obtain such correlation; in addition the values of dynamic flexural modulus and specific damping capacity for undamaged material used in the analysis of the cracked beams in the free-free rig had been obtained during a previous test.

These properties are known to be very temperature dependent, and ambient conditions did vary between tests. Further work involving the measurement of specific damping capacity of known cracks, using the receptance analysis, under controlled conditions, may reveal quantitative correlation.

The work described in this thesis has suggested much further work regarding the material investigated here, and further development and application of the various techniques to this and other composite materials. It is hoped that the work described here and future work may lead to more confident and reliable use of composite materials in critical applications.

REFERENCES

ADAMS, R.D.	Private communication	1977
ANTOLOVICH, S.D., CHANANI, G.R., SAXENA, A. & WANG,I.C.	Fracture mechanism transitions in laminate composites. J. Phys.D: Appl. Phys. Vol. 6.	1973
BABB, P.	Private communication	1976
BACON, D.G.C.	The dynamic properties of carbon and glass fibre reinforced plastic. Ph.D. Thesis, University of Bristol.	1973
BALDERSTON, H.L.	The broad range detection of incipient failure using the acoustic emission phenomena. Acoustic emission ASTM STP 505	1972
BARNBY, J.T. & PARRY, T.	Acoustic emission from a notched glass-fibre-reinforced polymer in bending. J. Phys.D: Appl. Phys. Vol. 9.	1976
BEAUMONT, P.W.R. & PHILLIPS, D.C.	Tensile strengths of notched composites. J. Comp. Mat. Vol. 6.	1972
BELL, R.L.	Acoustic emission transducer calibration transient pulse method. 32nd Nat. Conf. Amer. Soc. Non-destructive Testing.	1972
BENTLEY, P.G., BURNUP, T.E., BURTON, E.J., COWAN, A. & KIRBY, N.	Acoustic emission as an aid to pressure vessel inspection. Periodic Inspection of Pressure Vessels. Inst. of Mech. Eng.	1972
BISHOP,R.E.D., & JOHNSON, D.C.	The mechanics of vibration. Cambridge University Press.	1960

BISHOP, S.M.	Deformation of notched fibre composites. J.Phys.D: Appl.Phys. Vol. 7	1974
CARTER, M.C.	A model for thunderstorm activity: use of the compound negative binomial-positive binomial distribution. J. Appl. Statistics Vol. 21.	1972
CHAMIS, C.C. & SENDECKYJ, G.P.	Critique on theories predicting thermoelastic properties of fibrous composites. J.Comp.Mat. Vol.2	1968
COOK, J. & GORDON, J.E.	A mechanism for the control of crack propagation in all-brittle systems. Proc.Roy.Soc. Series A Vol. 282	1964
COOPER, G.A. & KELLY, A.	Tensile properties of fibre-reinforced metals: fracture mechanics. J.Mech.Phys.Solids Vol. 15.	1967
COTTRELL, A.H.	The mechanical properties of matter. J. Wiley and Sons.	1964
CROSS, N.O., LOUSHUN, L.L. & THOMPSON, J.L.	Acoustic emission testing of pressure vessels for petroleum refineries and chemical plants. Acoustic Emission ASTM STP 505	1972
DACEY, M.F.	A compound probability law for a pattern more dispersed than random and with areal inhomogeneity. Econ.Geog. Vol. 42.	1966
DELFINER, P.	A generalisation of the concept of size. J. Microsc. Vol. 95 pt. 2.	1972
DUKES, R.	Materials requirement and validation for large marine structures in fibre reinforced plastics. PI-RPG symposium. Reinforced plastics - recent advances in the marine field.	1972

DUNEGAN, H.L. & HARRIS, D.O.	Acoustic emission - a new nondestructive testing tool. Ultrasonics. Vol. 7.	1969
DUNEGAN, H.L., HARRIS, D.O. & TATRO, C.A.	Fracture analysis by use of acoustic emission. Eng.Fract.Mech. Vol. 1.	1968
EDE, A.J.	An introduction to heat transfer principles and calculations. Pergamon Press.	1967
EGLE, D.M. & TATRO, C.A.	Analysis of acoustic emission strain waves. J. Acoustical Soc. of Amer. Vol.41.	1967
ELLIS, C.D. & HARRIS, B.	The effect of specimen and testing variables on the fracture of some fibre reinforced epoxy resins. J. Comp. Mat. Vol. 7.	1973
FISHER, R.M. & LALLY, J.S.	Microplasticity detected by an acoustic technique. Canadian J. of Phys. Vol. 45.	1967
FITZ-RANDOLPH, J. PHILLIPS, D.C., BEAUMONT, P.W.R. & TETELMAN, A.S.	Acoustic emission studies of a boron-epoxy composite. J. Comp. Mat. Vol. 5.	1971
FITZ-RANDOLPH, J. PHILLIPS, D.C., BEAUMONT, P.W.R. & TETELMAN, A.S.	Acoustic emission and the fracture energy of a boron-epoxy.composite. J. Mat. Sci. Vol. 7.	1972
FLITCROFT, J.E.	Non-destructive testing of glass and carbon reinforced plastics. Ph.D. Thesis, University of Bristol.	1977
FREDERICK, J.R. & FELBECK, C.K.	Dislocation motion as a source of acoustic emission. Acoustic Emission. ASTM. STP 505	1972
FUWA,M., BUNSELL, A.R. & HARRIS, B.	Tensile failure mechanisms in carbon fibre reinforced plastics. J. Mat. Sci. Vol. 10.	1975a

FUWA, M., HARRIS, B. & BUNSELL, A.R.	Acoustic emission during cyclic loading of carbon-fibre-reinforced plastics. J. Phys. D: Appl. Phys. Vol. 8.	1975b
GERBERICH, W.W. & HARTBOWER, C.E.	Some observations on stress wave emissions as a measure of crack growth. Int. J. Fract. Mech. Vol. 3.	1967
GILLIS, P.P.	Dislocation mechanisms as possible sources of acoustic emission. Mat. Res. and Stand. Vol. 11.	1971
GILLIS, P.P	Dislocation motions and acoustic emission. Acoustic Emission ASTM STP 505	1972
GILLIS, P.P. & HAMSTAD, M.A.	Some fundamental aspects of the theory of acoustic emission. Nat. Sci. and Eng. Vol. 14.	1974
GREEN, A.T., LOCKMAN, C.S. & STEELE, R.K.	Acoustic verification of structural integrity of Polaris chambers. Modern Plastics Vol. 41.	1964
GREIG-SMITH, P.	The use of random and contiguous quadrats in the study of the structure of plant communities. Annals of Botany. Vol. 16.	1952
GREIG-SMITH, P.	Data on pattern within plant communities. 1. The analysis of pattern. J. Ecology Vol. 49	1961
GREIG-SMITH, P.	Quantitative Plant Ecology. Butterworths.	1964
GUILD, F.J. & SHORT, D.	Acoustic emission during crack growth in unidirectional glass fibre reinforced polyester resin composites. Proc. Inst. of Acoustics.	1977

GUILD, F.J. & SILVERMAN, B.W.	The microstructure of glass fibre reinforced polyester resin composites. Paper submitted to J. of Microsc.	1977
GUILD, F.J., WALTON, D., ADAMS, R.D., & SHORT, D.	The application of acoustic emission to fibre-reinforced composite materials. Composites Vol. 7.	1976
HAMSTAD, M.A. & CHIAO, T.T.	Acoustic emission produced during burst tests of filament-wound bottles. J. Comp. Mat. Vol. 7.	1973
HANCOCK, J.R. & SWANSON, G.D.	Toughness of filamentary boron/ aluminium composites. Composite Materials: testing and design (2nd conf.) ASTM STD 497	1972
HARRIS, B., MORLEY, J. & PHILLIPS, D.C.	Fracture mechanisms in glass-reinforced plastics. J. Mat. Sci. Vol. 10	1975
HARRIS, D.O., TETELMAN, A.S. & DARWISH, F.A.I.	Detection of fibre cracking by acoustic emission. Acoustic Emission ASTM STP 505	1972
HARTBOWER, C.E., GERBERICH, W.W. & LIEBOWITZ, H.	Investigation of crack growth stress wave relationships. Eng. Fract. Mech. Vol. 1	1968
HARTBOWER, C.E., REUTER, W.G., MORAIS, C.F. & CRIMMINS, P.P.	Use of acoustic emission for the detection of weld and stress corrosion cracking. Acoustic Emission ASTM STP 505	1972
HASHIN, Z. & ROSEN, B.W.	The elastic moduli of fibre-reinforced materials. J. Appl. Mech. Vol. 31.	1964
HAZLERIGG, M.K. & HUCKERBY, R.J.	The effect of environment on glass fibre reinforced plastics. Undergraduate Report, Dept. of Mech.Eng., University of Bristol	1975

HILL, A.R.	THe distribution of drumlins in County Down, Ireland. Annals Assoc. Amer. Geog. Vol. 63	1973
HILL, R.	Theory of mechanical properties of fibre-strengthened materials: 1 Elastic behaviour. J. Mech. Phys. Solids Vol. 12	1964
HUTTON, P.H.	Acoustic emission in metals as an N.D.T. tool. Materials Evaluation Vol. 26.	1968
HUTTON, P.H.	Identification of worn bullet forming dies by acoustic signature in process. Proc. 8th Symp.on nondestructive evaluation in aerospace, weapons systems and nuclear applications.	1971
HUTTON, P.H.	Acoustic emission applied outside of the laboratory. Acoustic Emission ASTM STP 505	1972
HUTTON, P.H. & PARRY, D.L.	Assessment of structural integrity by acoustic emission. Mat. Res. and Stand. Vol. 11	1971
INGLIS, C.E.	Stresses in a plate due to the presence of cracks and sharp corners. Trans.Inst.of Naval Architects. Vol. 55.	1913
JERONIMIDIS, G.	The fracture of wood in relation to its structure. Leiden Botanical Series No. 3.	1976
KAISER, J.	Untersuchungen uber das Auftreten von Gerauschen beim Zugversuch. Ph.D. Thesis, Technische Hoch schule, Munich.	1950
KELLY, A.	Strong Solids. Oxford University Press.	1966

KERSHAW, K.A.	The use of cover and frequency in the detection of pattern in plant communities. J. Ecology Vol. 38	1957
KERSHAW, K.A.	Quantitative and Dynamic Ecology Edward Arnold.	1964
KIM, H.C., RIPPER, A.P. & STEPHENS, R.W.B.	Some observations on acoustic emission during continuous cyclic testing in C.F.R.P. Nature Physical Sci. Vol. 237.	1972
KIM, H.C., RIPPER, A.P. & STEPHENS, R.W.B.	Reply to comments in Stone and Dingwall (1973) Nature Physical Sci. Vol. 241.	1973
KNOTT, J.F.	Fundamentals of Fracture Mechanics Butterworth.	1973
LIPTAI, R.G.	Acoustic emission from composite materials. Composite Materials: testing and design (2nd conf) ASTM STP 497	1972
LIPTAI, R.G., HARRIS, D.O., ENGLE, R.B. & TATRO, C.A.	Acoustic emission techniques in materials research. Advanced experimental techniques in the mechanics of materials. Gordon and Beach science publishers	1970
McEVILY, A.J. & BUSH, R.H.	An investigation of the notch-impact strength of an ausformed steel. Trans. ASM Vol. 55	1962
MATHERON, G.	Random sets theory and its application to stereology. J. Microsc. Vol. 95 pt. 1.	1972
MEHAN, R.L. & MULLIN, J.V.	Analysis of composite failure mechanisms using acoustic emission. J. Comp. Mat. Vol. 5.	1971
MULLIN, J.V.& MAZZIO, V.F.	Basic failure mechanisms in advanced composites. NASA report CR - 121621.	1972

NAKAMURA, Y. VEACH, C.L. & McCAULEY, B.O.	Amplitude distribution of acoustic emission signals. Acoustic Emission ASTM STP 505	1972
ONO, K., STERN, R., & LONG, M.	Application of correlation analysis to acoustic emission. Acoustic Emission ASTM STP 505	1972
OWEN, M.J. & BISHOP, P.T.	Critical stress intensity factors applied to glass reinforced polyester resin. J. Comp. Mat. Vol. 7.	1973
PALMER, I.G.	Acoustic emission measurements on reactor pressure vessel steel. Mat. Sci. and Eng. Vol. 11.	1973
PALMER, I.G. & HEALD, P.T.	The application of acoustic emission measurements to fracture mechanics. Mat. Sci. and Eng. Vol. 11.	1973
PALMER, I.G., BRINDLEY, B.J. & HARRISON, R.P.	The relationship between acoustic emission and crack opening displacement measurements. Mat. Sci. and Eng. Vol. 14.	1974
PARRY, D.L.	Acoustic emission analysis of pressure vessels and piping. Proc. 8th Symp. on nondestructive evaluation in aerospace, weapons systems and nuclear applications.	1971
PICKETT, A.G., REINHART, E.R. & YING, S.P.	Acoustic emission from irradiated steels. Proc. 8th Symp. on nondestructive evaluation in aerospace, weapons systems and nuclear applications.	1971
POLLOCK, A.A.	Stress wave emission in ndt. Non-destructive testing Vol. 2.	1969
POLLOCK, A.A.	Acoustic Emission. Engineering Outline 232	1970

POLLOCK, A.A.	Acoustic emission - 2. Acoustic emission amplitudes. Non-destructive testing. Vol. 6.	1973
POLLOCK, A.A. & SMITH, B.	Stress wave emission monitoring of a military bridge. Non-destructive testing. Vol. 5.	1972
PYE, C.J.	Private communication.	1977
RADON, J.C. & POLLOCK, A.A.	Acoustic emissions and energy transfer during crack propagation. Eng. Fract. Mech. Vol. 4.	1972
RATHBUN, D.K, BEATTIE, A.G. & HILES, L.A.	Filament wound materials evaluation with acoustic emission. Proc. 8th Symp. on non-destructive evaluation in aerospace, weapons systems and nuclear application.	1971
ROGERS, A.	Quadrat analysis of urban dispersion: 2 Case studies of urban retail systems. Environment and planning. Vol. 1.	1969
ROGERS, A.	Statistical Analysis of Spatial Dispersion. Pion.	1974
SCHOFIELD, B.H.	Utilization of acoustic emission for in-service inspection. Periodic Inspection of Pressure Vessels. Inst. of Mech. Eng.	1972
SERRA, J.	Stereology and structuring element. J. Microsc. Vol. 95 pt. 1.	1972
SIH, G.C., PARIS, P.C. & IRWIN, G.R.	On cracks in rectilinearly anisotropic bodies. Int. J. of Fract. Mech. Vol. 1.	1965
SILVERMAN, B.W.	Private communication.	1976
SILVERMAN, B.W.	Private communication.	1977

SPEAKE, J.H. & CURTIS, G.J.	Characterisation of the fracture processes in CFRP using spectral analysis of the acoustic emissions arising from the amplification of stress. Int. Conf. on Carbon Fibres, their place in modern technology. Paper 29.	1974
STEPHENS, R.W.B. & POLLOCK, A.A.	Waveforms and frequency spectra of acoustic emissions. J. of Acoustical Society of America. Vol. 50.	1971
STONE, B.J.	Private communication	1975
STONE, D.E.W. & DINGWALL, P.R.	Comments concerning Kim et al (1972) Nature Physical Sci. Vol. 241	1973
SWANSON, G.D. & HANCOCK, J.R.	Off-axis and transverse tensile properties of boron reinforced aluminium alloys. Composite Materials: testing and design (2nd conf.) ASTM STP 497	1972
TATRO, C.A.	Design criteria for acoustic emission experimentation. Acoustic Emission ASTM STP 505	1972
TETELMAN, A.S. & CHOW, R.	Acoustic emission testing and microcracking processes. Acoustic Emission ASTM STP 505	1972
TETELMAN, A.S. & McEVILY, A.J.	Fracture of structural materials. J. Wiley and Sons.	1967
THOMPSON, H.R.	Spatial point processes with application to ecology. Biometrika Vol. 42.	1955
THOMPSON, H.R.	The statistical study of plant distribution pattern using a grid of quadrats. Aust. J. of Botany. Vol. 6.	1958

USHER, M.B.	The relation between mean square and block size in the analysis of pattern. J. of Ecology Vol. 57	1969
VETRANO, J.B., JOLLY, W.D. & HUTTON, P.H.	Continuous monitoring of nuclear reactor pressure vessels by acoustic emission techniques. Periodic Inspection of Pressure Vessels. Inst. of Mech. Eng.	1972
WRIGHT, M.A. & IANUZZI, F.A.	The application of the principles of linear elastic fracture mechanics to unidirectional fibre reinforced composite materials. J. Comp. Mat. Vol. 7.	1973
WU, E.M.	Strength and Fracture of Composites. Composite Materials Vol. 5. Fracture and Fatigue. Academic Press	1974
ZWEBEN, C. & ROSEN, B.W.	A statistical theory of material strength with application to composite materials. J. Mech. and Phys. of Solids Vol. 18.	1970

Table 3.0 Parameters of Beams in Results Below

Identification	Mass (gm)	Length (mm)	Height (mm)	Width (mm)	Total End Mass (gm)
Duralumin 1					
Free-free	66.455	305.5	6.09	12.89	59.717
Cantilever	53.715	246.5	6.09	12.89	35.448
Duralumin 2					
Free-free	32.390	278.5	3.37	12.97	59.717
Cantilever	25.936	223.0	3.37	12.97	35.448
0^{o} GFRP					
Free-free	42.335	295.5	8.90	11.40	59.717
Cantilever	35.906	260.0	8.51	11.34	35.448
90^{o} GFRP					
Free-free	51.764	296.0	9.00	12.78	59.717
Cantilever	47.230	270.0	9.10	12.66	35.448

Table 3.1 Frequencies from the Free-Free Rig compared with those predicted by the wave equation analysis neglecting rotary inertia

Identification	Frequency No. predicted	Expt. Freq. (Hz)	Expt.E ($GN\ m^{-2}$)	Predicted E ($GN\ m^{-2}$)	Apparent Freq. No.	Predicted Freq. (Hz)
Duralumin 1	3.59	156	47.8	70.0	3.28	189
Duralumin 2	3.41	93.2	42.7	70.0	3.01	119
0^{o} GFRP	3.48	137	8.26	16.0	2.95	191
90^{o} GFRP	3.53	102	4.55	6.0	3.29	117

Table 3.2 Frequencies from the Free-free Rig and Calculated Moduli using the Wave Equation Analysis neglecting rotary inertia, for Duralumin. 1, with different end conditions

End Condition	Total End Mass (gm.)	Frequency No. predicted	Experimental Frequency (Hz)	Experimental E ($GN\ m^{-2}$)
Nothing	0	4.73	347	74.0
Small Weights	67.80	3.57	204	74.7
Coils	59.717	3.59	156	47.8

Table 3.3 Frequencies from the Free-Free Rig compared with those predicted by the wave equation analysis including rotary inertia

Identification	Frequency No. predicted	Expt. Freq. (Hz)	Expt.E ($GN\ m^{-2}$)	Predicted E ($GN\ m^{-2}$)	Measured Rotary Inertia ($gm\ mm^2$)	Apparent Rotary Inertia ($gm\ mm^2$)
Duralumin 1	3.39	156	60.28	70.0	22040	38000
Duralumin. 2	3.08	93.2	64.70	70.0	22040	26000
0^{o} GFRP	3.21	137	11.33	16.0	22040	53500
90^{o} GFRP	3.30	102	6.01	6.0	22040	22030

Table 3.4 Duralumin. Damping measured by Free Decay, using the Cantilever Rig and Stiff Coil with Aluminium Alloy Frame

Condition	Frequency (Hz)	Half Decay Time (sec)	S.D.C. (%)
Nothing	74.1	8.36	0.22
Coil Attached	40.9	10.46	0.32
Coil Attached + magnet in place	40.9	1.22	2.8

Table 3.5 Duralumin. . Damping measured by Free Decay, using the Cantilever Rig and Stiff Coil with Tufnol Frame

Condition	Frequency (Hz)	Half Decay Time (Sec)	S.D.C. (%)
Nothing	71.4	5.97	0.32
Magnet in place	71.4	2.93	0.66
Coil attached	38.5	8.60	0.42
Coil attached + magnet in place	38.5	2.61	1.38

Table 3.6 Duralumin Damping measured by Free Decay, using the Free-Free Rig and Stiff Coils with Tufnol Frames

Condition	Frequency (Hz)	Half Decay Time (sec)	S.D.C. (%)
Upper + lower magnets	192	1.26	0.57
Lower magnets	192	1.48	0.48

Table 3.7 Frequencies from the Cantilever Rig, compared with those predicted by the wave equation analysis

Identification	Frequency No.	Expt. Freq. (Hz)	Expt.E (GN m^{-2})	Predicted E (GN m^{-2})	Apparent Freq. No.	Predicted Freq. (Hz)
Duralumin. 1	1.380	42.09	65.61	70.0	1.358	43.47
Duralumin. 2..	1.185	20.53	59.18	70.0	1.136	22.33
0° GFRP	1.274	30.61	15.24	16.0	1.259	31.37
90° GFRP	1.347	20.82	6.08	6.0	1.343	20.68

Table 4.1 Comparison of Distribution of Fibre Diameters shown in the Histogram and measured using Tested Beams

	No. of fibres	Mean diameter (μm)	Variance (μm^2)	Difference between means (μm)	Standard error of difference (μm)
Histogram	2448	14.48	3.61		
0^o Beam 1	442	14.65	6.87	0.17	0.13
0^o Beam 2	311	14:55	5.12	0.07	0.32
0^o Beam 3	365	14.07	3.90	0.41	0.15

Table 5.1 Differences between Experimental and Theoretical Variances in terms of Theoretical Standard Deviation of Theoretical Variance

I dir.								
8	26.08	37.68	43.04	47.67	53.12	54.68	53.38	59.51
7	26.55	41.28	47.73	54.89	60.31	62.88	60.95	68.41
6	25.97	40.89	48.39	55.05	59.99	64.00	62.60	69.13
5	28.33	44.85	52.42	59.25	64.49	68.71	67.65	74.83
4	24.82	41.31	47.27	54.37	58.95	62.07	59.59	67.59
3	22.68	49.38	45.01	53.04	57.44	59.89	57.81	64.86
2	17.78	34.72	40.33	47.31	50.47	41.10	52.83	59.56
1	3.696	20.39	25.00	31.53	34.09	36.72	36.00	41.75
	1	2	3	4	5	6	7	8

Cell Size ⟶ J direction
(test cells)

Table 5.2 Variance Analysis Constants

No.	Cross-section direction	Theoretical Values C_1	C_2	Experimental Values C_1	C_2	ratio: expt./th. C_1	C_2
90° Beams							
1	I	.02769	1	.04235	.730	1.529	.730
1	J	.02769	1	.03889	.567	1.404	.567
2	I	.02870	1	.06543	.924	2.280	.924
2	J	.02870	1	.06132	.784	2.136	.784
3	I	.03370	1	.06063	.838	1.799	.838
3	J	.03370	1	.04962	.581	1.472	.581
4	I	.02324	1	.03019	.513	1.299	.513
4	J	.02324	1	.02699	.390	1.161	.390
5	I	.02338	1	.03996	.588	1.709	.588
5	J	.02338	1	.04128	.597	1.766	.597
0° Beams							
1	I	.02038	1	.04418	.868	2.168	.868
1	J	.02038	1	.03293	.584	1.616	.584
2	I	.02340	1	.04318	.593	1.845	.593
2	J	.02340	1	.03879	.482	1.657	.482
3	I	.02171	1	.03710	.564	1.709	.564
3	J	.02171	1	.04007	.605	1.846	.605
4	I	.01982	1	.03163	.726	1.596	.726
4	J	.01982	1	.03803	.673	1.919	.673
5	I	.01532	1	.01336	.507	.872	.507
5	J	.01532	1	.01335	.458	.871	.458

Table 5.3 Sparse Analysis Constants

Cross-section		theoretical values		experimental values		ratio: expt/th.	
No.	direction	C_3	C_4	C_3	C_4	C_3	C_4
90^o Beams							
1	I	1	2.449	.1981	.6966	.1981	.2844
1	J	1	2.449	.1544	.5796	.1544	.2367
2	I	1	2.538	.2212	.6319	.2212	.2490
2	J	1	2.538	.2181	.5799	.2181	.2285
3	I	1	2.980	.2624	1.0736	.2624	.3603
3	J	1	2.980	.1278	.6314	.1278	.2119
4	I	1	2.055	.1859	.2286	.1859	.1112
4	J	1	2.055	.1374	.1039	.1374	.0506
5	I	1	2.067	.2510	.4178	.2510	.2021
5	J	1	2.067	.2387	.3721	.2387	.1800
0^o Beams							
1	I	1	1.802	.3749	.8100	.3749	.4495
1	J	1	1.802	.3138	.6850	.3138	.3801
2	I	1	2.069	.3062	.5633	.3062	.2723
2	J	1	2.069	.2163	.4184	.2163	.2022
3	I	1	1.919	.2813	.5608	.2813	.2922
3	J	1	1.919	.2801	.5608	.2801	.2922
4	I	1	1.752	.1866	.5441	.1866	.3106
4	J	1	1.752	.1822	.3526	.1822	.2013
5	I	1	1.355	.3944	.2620	.3944	.1934
5	J	1	1.355	.3845	.2163	.3845	.1596

Table 5.4 Percentage Deviations of Means and Variances of Area Covered by Fibres when the Area Analysed is Reduced

Means

Area in I direction (test cells)	120	140	160	180	200	216
112	3.32	4.46	4.70	-.84	.31	0
106	4.64	5.81	5.60	.23	1.39	1.03
100	5.41	6.48	6.19	1.07	2.35	1.99
90	6.48	7.64	7.43	2.06	3.46	3.23
80	7.91	8.69	8.35	2.83	4.18	3.80
70	12.5	12.9	12.0	6.84	7.47	6.61

Area in J direction (test cells)

Variances

Area in I direction (test cells)	120	140	160	180	200	216
112	-2.49	-1.42	-2.71	0	-.57	0
106	-2.57	-1.64	-2.85	-.14	-1.07	-.28
100	-1.92	-1.42	-2.64	-.14	-1.35	-.36
90	-.36	.21	-1.14	1.92	.71	1.78
80	.29	-.43	-1.71	1.64	.57	1.92
70	.93	.57	-.43	2.71	.71	1.92

Area in J direction (test cells)

Table 6.1 Flexural Test Results for 0^{o} Beams

Volume Fraction (%)	Rule of Mixtures Modulus (GN m^{-2})	Measured Modulus (GN m^{-2})	Flexural Strength (MN m^{-2})
21.5	14.9	16.3	387
20.0	14.1	16.4	296
17.6	12.7	15.4	355
18.4	13.2	18.9	327
21.6	15.0	16.0	351
20.5	14.3	17.9	214
18.4	13.2	14.4	281
17.7	12.8	17.3	346
25.4	17.1	16.6	385
26.1	17.5	16.1	356
23.2	15.9	17.4	385
20.0	14.1	15.4	321
19.9	14.0	18.0	351

Table 6.2 Flexural Test Results for 90^{o} Beams

Volume Fraction (%)	Measured Modulus (GN m^{-2})	Flexural Strength (MN m^{-2})
31.7	5.28	21.7
33.4	5.27	25.5
31.2	5.74	33.4
32.2	5.43	31.8
26.2	5.84	32.3
28.1	5.96	33.7
32.9	5.21	27.1
32.0	5.55	24.9
30.9	6.10	20.4

Table 6.3 Fibre Pull-Out Lengths

	No. of fibres measured	Mean pull-out length	Variance (μm^2)	Difference in means (μm)	Standard error of the diff. (μm)
near initiation	94	25.2	8182	10.5	16.8
just prior to splitting	53	35.7	10,340		

Table 6.4 Measurement of Crack Profiles

Volume Fraction (%)	Crack Area (mm^2)	Max. dist. along beam face (mm)	Max. dist. into beam (mm)	Perimeter (mm)	$\frac{\text{Area}}{\text{Perimeter}^2}$
23.1	3.52	2.57	2.23	8.43	.0495
22.6	5.02	4.07	1.73	10.74	.0435
21.4	3.70	3.02	2.02	9.19	.0438
20.4	7.19	4.70	1.89	12.9	.0434
21.5	5.91	5.92	1.56	13.4	.0330
20.0	5.75	3.85	2.05	10.9	.0486
17.7	6.88	4.16	2.76	12.4	.0446
25.4	1.08	2.00	0.761	4.92	.0444
26.1	2.81	3.00	1.66	8.61	.0379
23.2	2.41	2.82	1.13	7.36	.0445
19.9	4.55	4.08	1.64	10.8	.038
mean	4.438	3.654	1.766	9.968	.0429
standard deviation	1.929	1.110	.534	2.560	.00473

Table 7.1 Specific Damping Capacities of Undamaged Beams measured in the Free-Free rig

	Volume fraction (%)	Mass (gm)	Length (mm)	Width (mm)	Height (mm)	Predicted E (GN m^{-2})	S.D.C. (%)	Measured E (GN m^{-2})
0° Beams	17.7	42.15	298.5	12.39	7.99	12.8	3.9	16.0
	18.2	40.99	292.0	12.47	7.99	13.0	4.5	14.9
	25.4	40.55	283.5	12.35	7.99	17.1	3.9	16.1
	19.9	41.53	292.5	12.50	7.98	14.0	3.8	16.2
	21.9	43.32	296.5	12.41	7.97	15.1	3.4	17.5
	26.1	43.16	296.0	12.35	7.99	17.5	3.5	17.7
	23.2	43.93	298.0	12.34	7.99	15.9	3.6	18.7
	20.0	41.59	298.0	12.25	8.00	14.1	3.8	16.0
90° Beams	31.7	52.89	303.5	12.65	9.14		12.4	6.5
	32.1	47.03	276.5	12.63	9.09		15.1	6.5
	30.9	47.31	273.0	12.62	9.23		14.1	6.4
	31.2	42.32	242.0	12.78	8.99		12.7	6.8
	Resin	29.07	287.5	9.86	8.57		13.1	4.3

Table 7.2 Specific Damping Capacities of Undamaged Beams Measured in the Cantilever Rig

	Volume fraction(%)	Mass (gm)	Length (mm)	Width (mm)	Height (mm)	Predicted E (GN m^{-2})	S.D.C. (%)	Measured E (GN m^{-2})
0° Beams	17.7	36.99	262.0	12.39	7.99	12.8	4.6	15.6
	18.2	35.87	255.5	12.47	7.99	13.0	5.5	14.0
	25.4	36.12	252.5	12.35	7.99	17.1	5.4	13.5
	19.9	36.49	257.0	12.50	7.98	14.0	5.2	15.1
	21.9	38.14	261.0	12.41	7.97	15.1	5.4	16.1
	26.1	37.83	259.5	12.35	7.99	17.5	4.6	15.8
	20.0	36.77	263.5	12.25	8.00	14.1	4.8	15.0
90° Beams	31.7	47.57	273.0	12.65	9.14		15.0	6.2
	32.1	40.82	240.0	12.63	9.09		17.5	5.9
	30.9	41.42	239.0	12.62	9.23		17.2	6.0
	31.2	45.63	261.0	12.78	8.99		15.6	6.4
	Resin	25.53	252.5	9.86	8.57		15.8	4.23

Table 7.3 Stress Dependence Coefficients Measured in the Free-Free Rig

Beam Identification	Acoustic counts recorded	Bending Stress dependence a_o	Bending Stress dependence a_1	Shear Stress dependence a_o	Shear Stress dependence a_1
1	778	$-.1366\times10^{-1}$	$.2601\times10^{-6}$	$-.1012\times10^{-4}$	$.4268\times10^{-10}$
2	1544	$.3512\times10^{-1}$	$.6327\times10^{-7}$	$.2598\times10^{-4}$	$.1060\times10^{-10}$
3	1419	$.3723\times10^{-1}$	$.1289\times10^{-7}$	.1225	$.1005\times10^{-5}$
4	885	$.5168\times10^{-1}$	$.5771\times10^{-7}$	$.6650\times10^{-2}$	$.3016\times10^{-7}$
5	2557	-1.732	$.7436\times10^{-5}$	-1.277×10^{-2}	$.1949\times10^{-8}$

Table 7.4 Stress Dependence Coefficients Measured in the Cantilever Rig

Beam Identification	Acoustic counts recorded	Bending Stress dependence a_o	Bending Stress dependence a_1	Shear Stress dependence a_o	Shear Stress dependence a_1
1	778	.1088	$.9378\times10^{-6}$	$.2428\times10^{-5}$	$-.9974\times10^{-12}$
2	1544	-5409×10^{-1}	$.3626\times10^{-7}$	$.1186\times10^{-5}$	$.1402\times10^{-13}$
3	1419	$.6375\times10^{-1}$	$.9574\times10^{-7}$	$.5945\times10^{-2}$	$.3086\times10^{-7}$
4	885	.1849	$.9597\times10^{-6}$	$.6718\times10^{-3}$	$.2598\times10^{-8}$
5	2557	$.4700\times10^{-1}$	$.4639\times10^{-7}$	$.1056\times10^{-5}$	$.2444\times10^{-13}$

Table 8.1 Properties Measured in the Free-Free Rig

Beam identification	Volume fraction (%)	Measured Properties S.D.C. (%)	Measured Properties E ($GN m^{-2}$)	Normalised Properties S.D.C. (%)	Normalised Properties E ($GN m^{-2}$)
A	17.66	3.9	16.0	3.44	18.1
B	18.16	4.5	14.9	4.09	16.4
C	23.16	3.6	18.5	4.17	16.0
D	19.87	3.8	16.2	3.78	16.3

Table 8.2 Variance Analysis Constants

Beam Identification	Direction	Theoretical Values C_1	Theoretical Values C_2	Experimental Values C_1	Experimental Values C_2	Ratios C_1	Ratios $\left[\frac{expt}{th}\right]$ C_2
A	I	.0194	1	.0303	.444	2.02	.444
	J	.0194	1	.0395	.410	2.03	.410
B	I	.0200	1	.0343	.656	1.72	.656
	J	.0200	1	.0349	.603	1.75	.603
C	I	.0254	1	.0341	.622	1.34	.622
	J	.0254	1	.0335	.541	1.32	.541
D	I	.0218	1	.0390	.549	1.83	.540
	J	.0218	1	.0373	.432	1.71	.432

Table 8.3 Percentage Deviations of Variance Analysis Constants

Beam Identification	Direction	$\%C_1$ diff.	$\%C_2$ diff.	$\Sigma\%$ diff.	average(%)
A	I	102.4	55.6	158.0	160.2
	J	103·4	59·0	162·4	
B	I	72.1	34.4	106.5	110.5
	J	74.8	39.7	114.5	
C	I	34.1	37.8	71.9	74.8
	J	31.7	45.9	77.6	
D	I	82.6	46.0	128.6	128.2
	J	71.0	56.8	127.8	

Table 8.4 Sparse Analysis Constants

Beam identification	Direction	Theoretical Values		Experimental Values		Ratios [expt/th]	
		C_3	C_4	C_3	C_4	C_3	C_4
A	I	1	1.72	.301	.222	.301	.130
	J	1	1.72	.252	.160	.252	.0933
B	I	1	1.76	.152	.351	.152	.199
	J	1	1.76	.140	.254	.140	.144
C	I	1	2.25	.114	.571	.114	.254
	J	1	2.25	.0429	.295	.0429	.131
D	I	1	1.93	.210	.422	.210	.218
	J	1	1.93	.185	.288	.185	.149

Table 8.5 Percentage Deviations of Sparse Analysis Constants

Beam Identification	Direction	$\%C_3$ diff.	$\%C_4$ diff.	$\Sigma\%$ diff.	average (%)
A	I	69.95	87.04	157.0	161.2
	J	74.83	90.67	165.5	
B	I	84.78	80.09	164.9	168.2
	J	86.01	85.60	171.6	
C	I	88.64	74.63	163.3	173.0
	J	95.71	86.90	182.6	
D	I	78.99	78.16	157.2	161.9
	J	81.49	85.07	166.6	

Figure 3.1 Block Diagram of Circuit used to Control and Measure Current in Exciting Coils

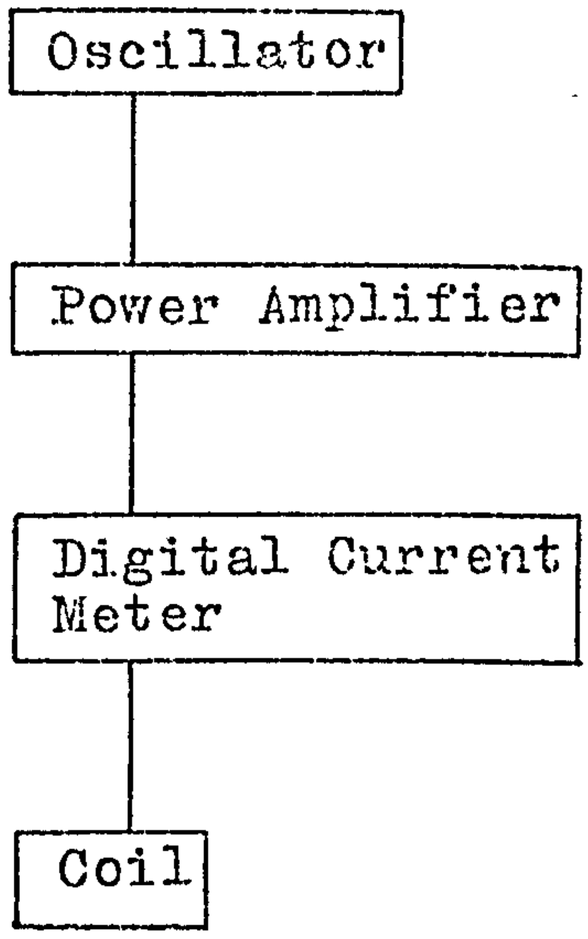

Figure 3.2 Rig with Electromagnets

(all dimensions in mm.)

Plan

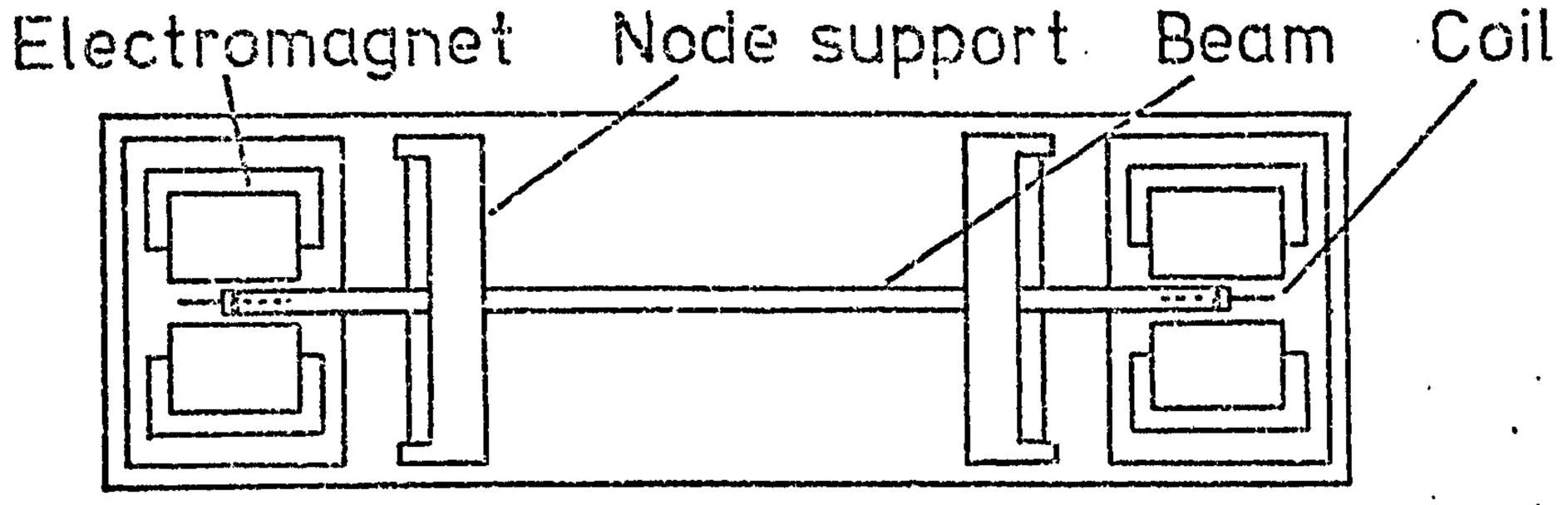

Cross-Section at Electromagnet

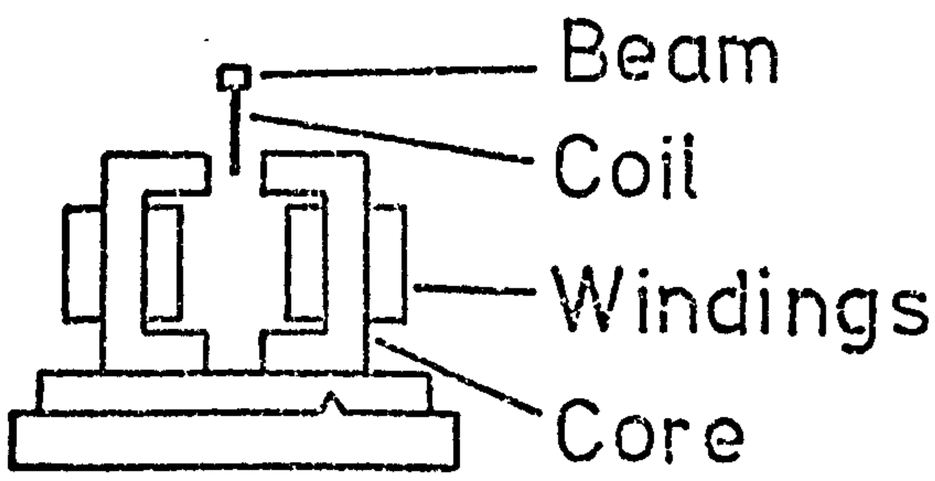

Cross-Section at Node Support

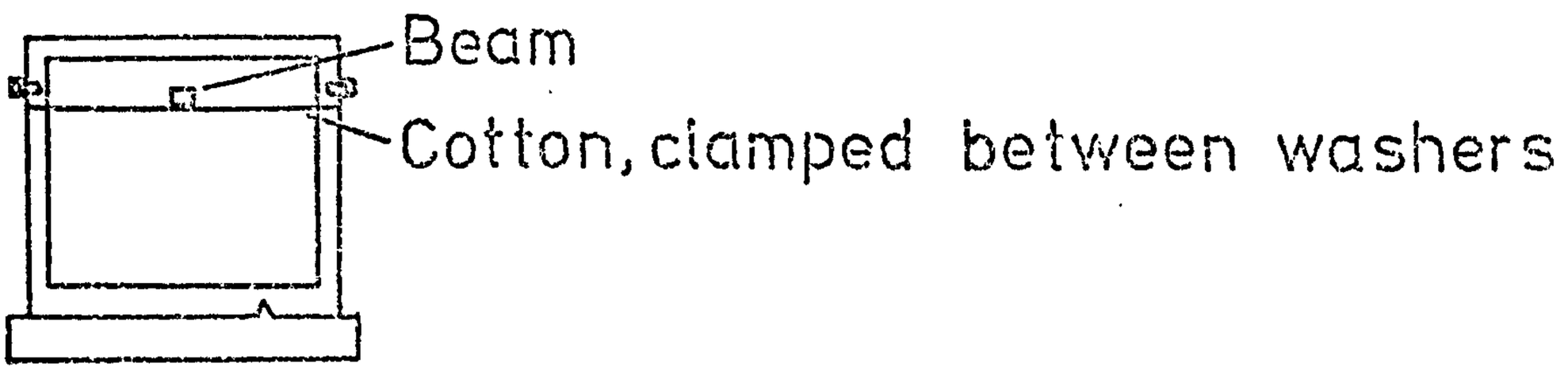

Coil

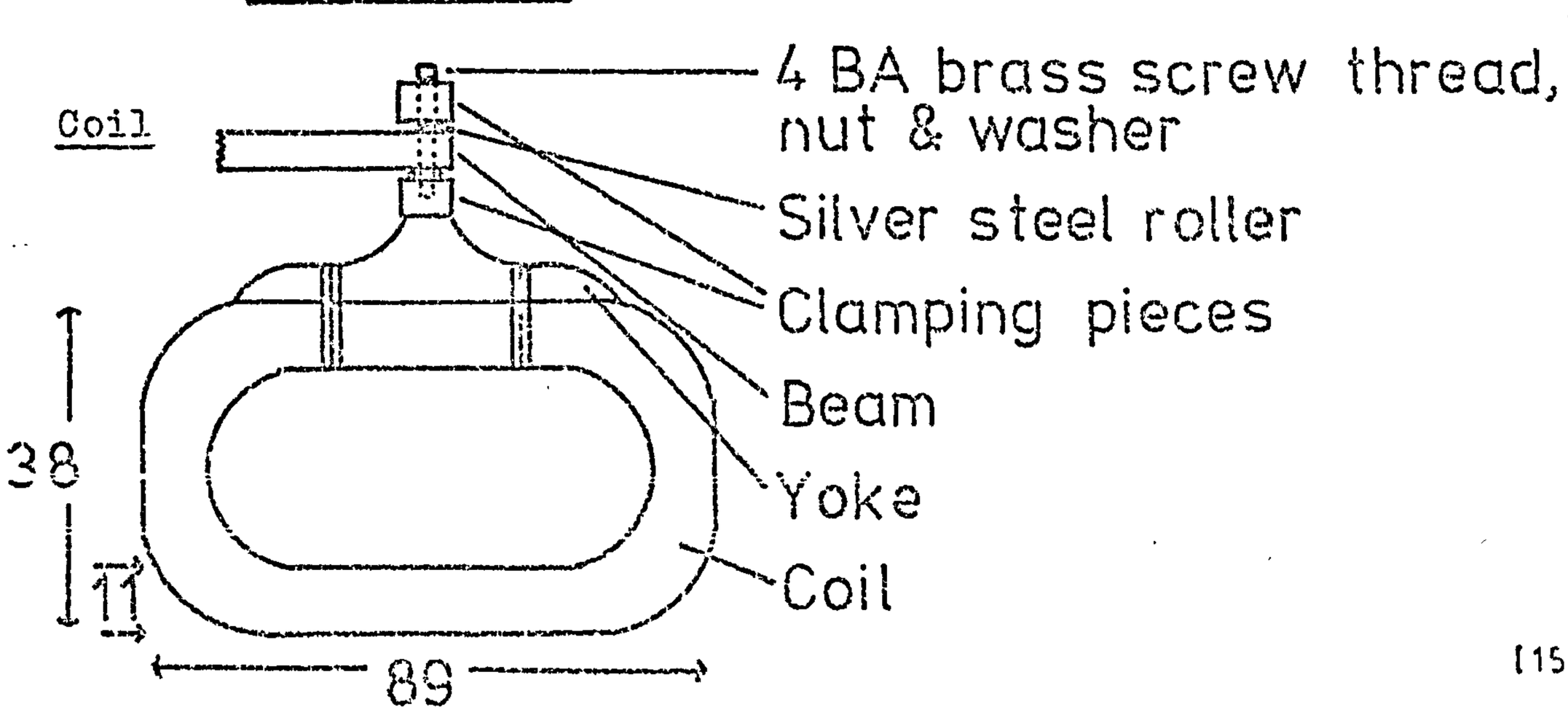

Figure 3.3 Theoretical Variation of Frequency Number with Mass Ratio (total end mass/beam mass) for the Free-Free Rig

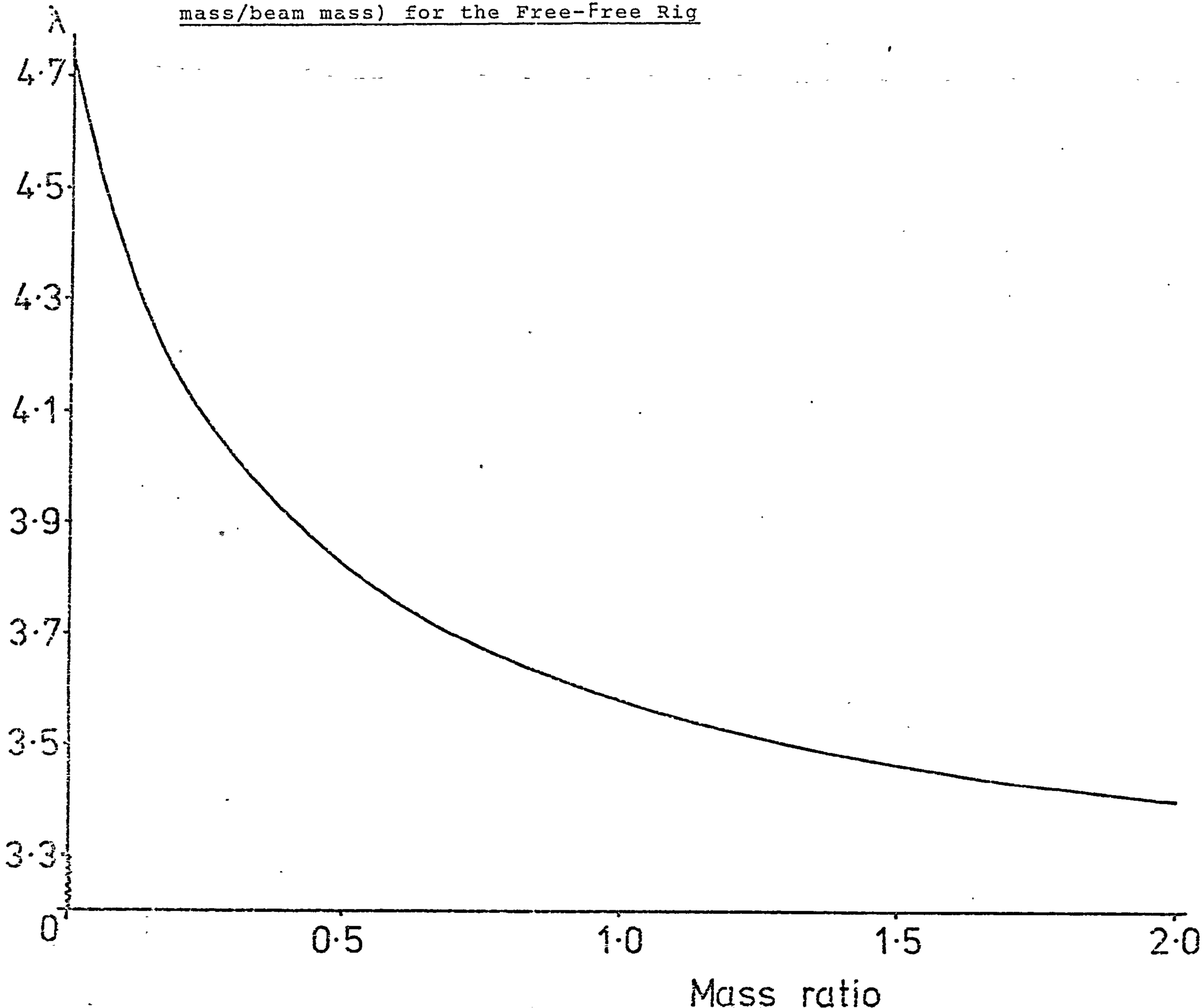

Figure 3.4 Comparison of Theoretical and Measured Mode Shapes for a Duralumin Free-Free Beam

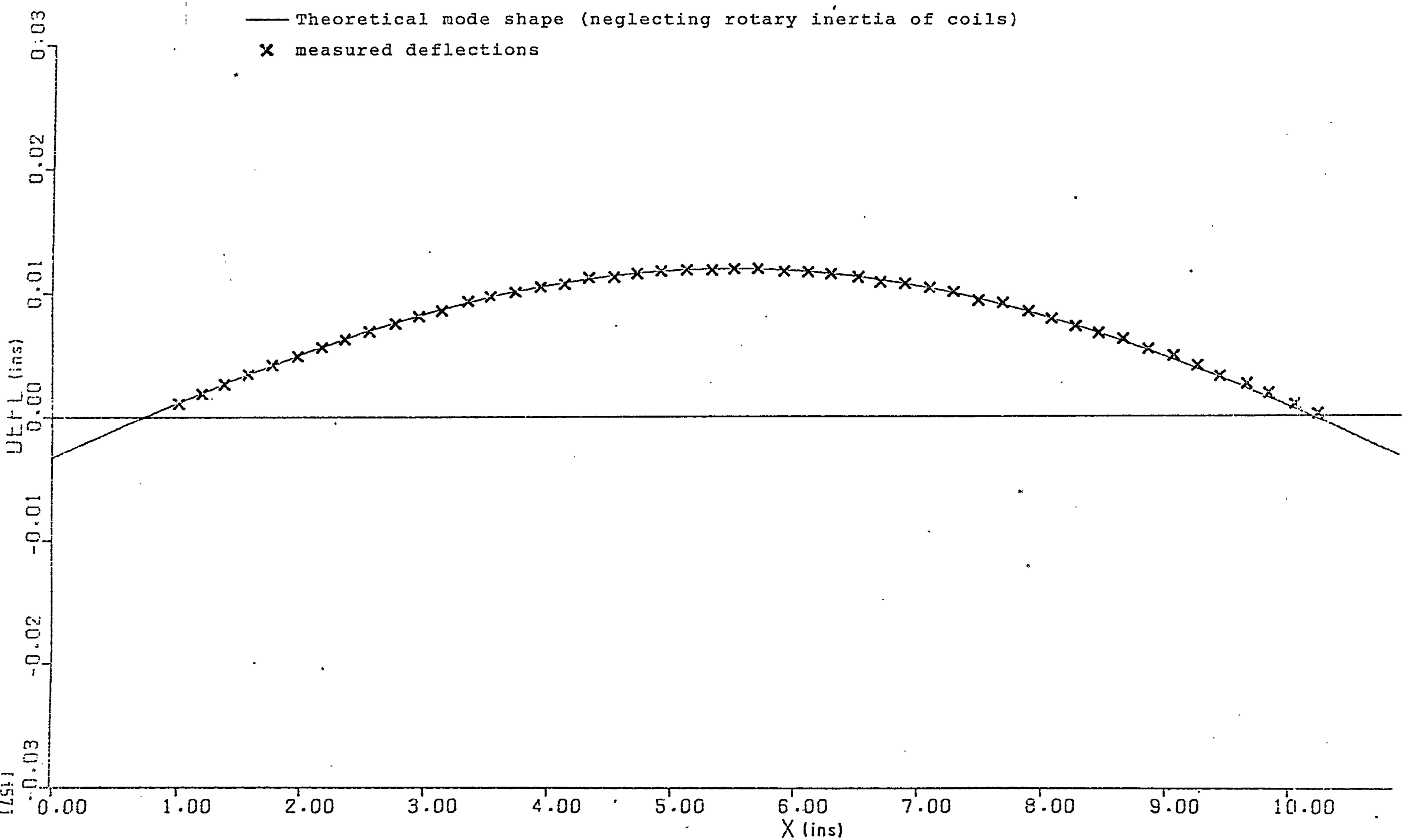

Figure 3.5 Theoretical Variation of Frequency Number with Rotary Inertia of End Masses for the Free-Free Rig

(Beam mass ≐ 66 gm, beam length ≐ 300 mm, total end mass ≐ 60 gm)

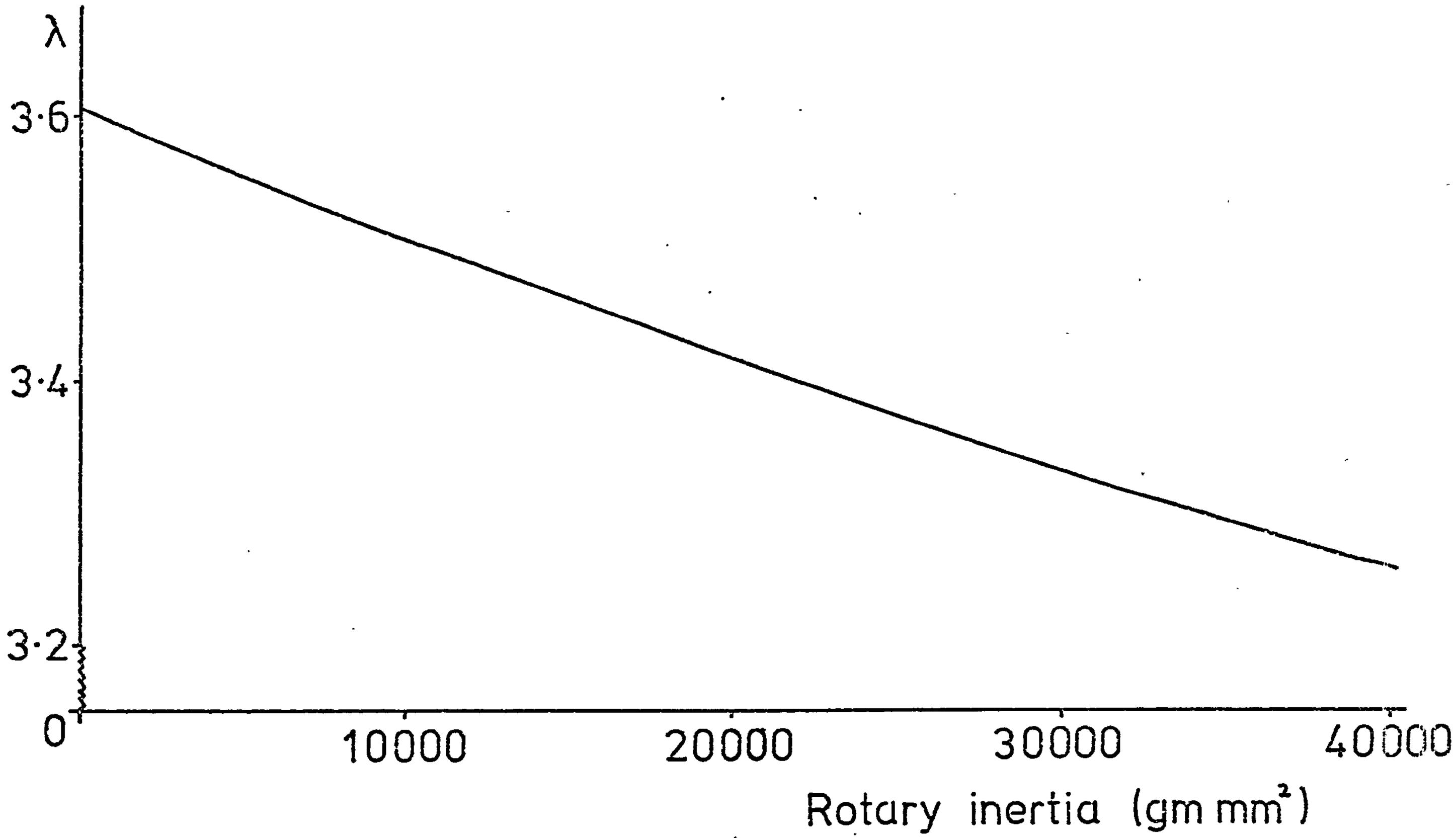

Figure 3.6 Comparison of Predicted Mode Shapes for a Duralumin Free-Free Beam, neglecting and including the Rotary Inertia of the Coils

——Neglecting rotary inertia

X Including rotary inertia

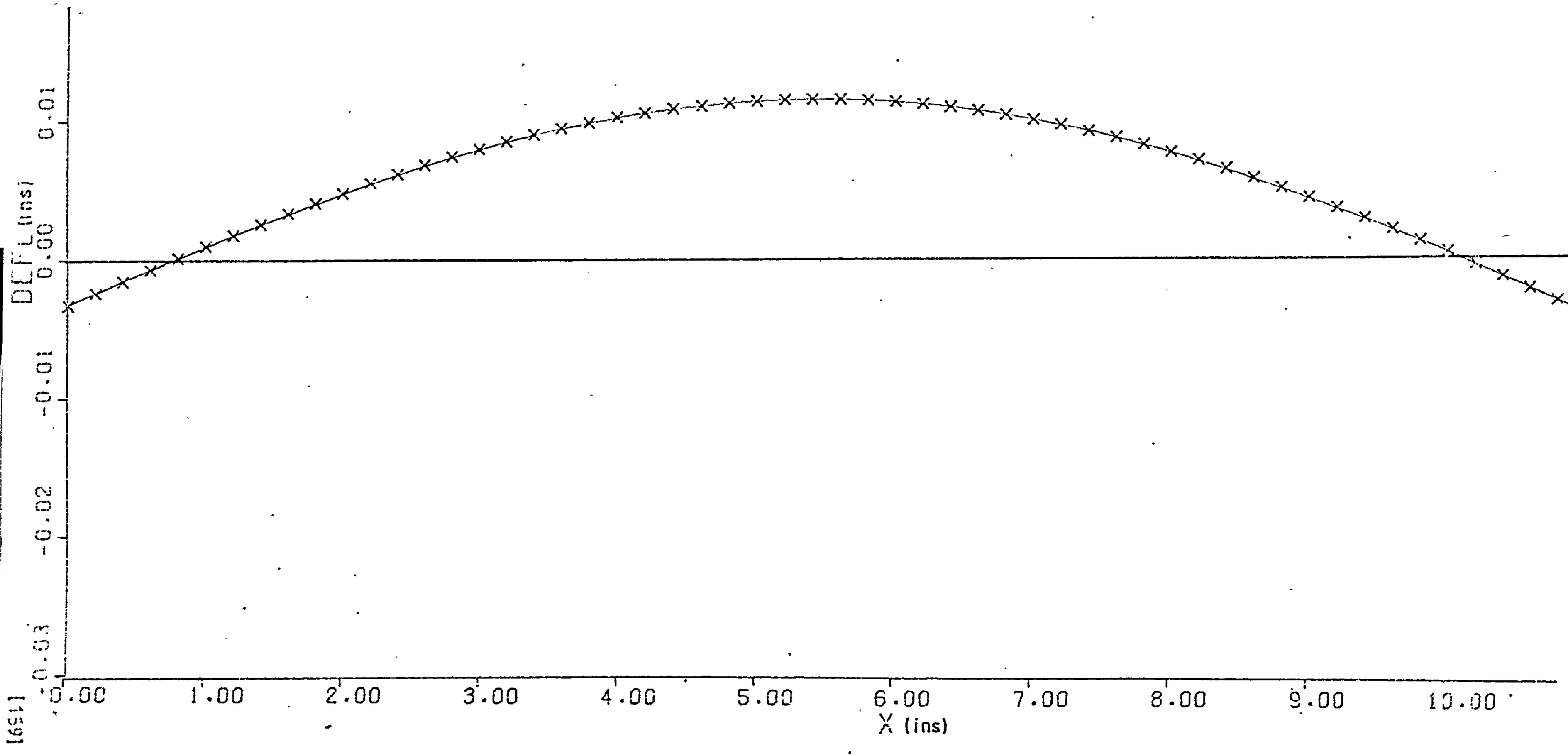

Figure 3.7 Coil Designed for Maximum Stiffness

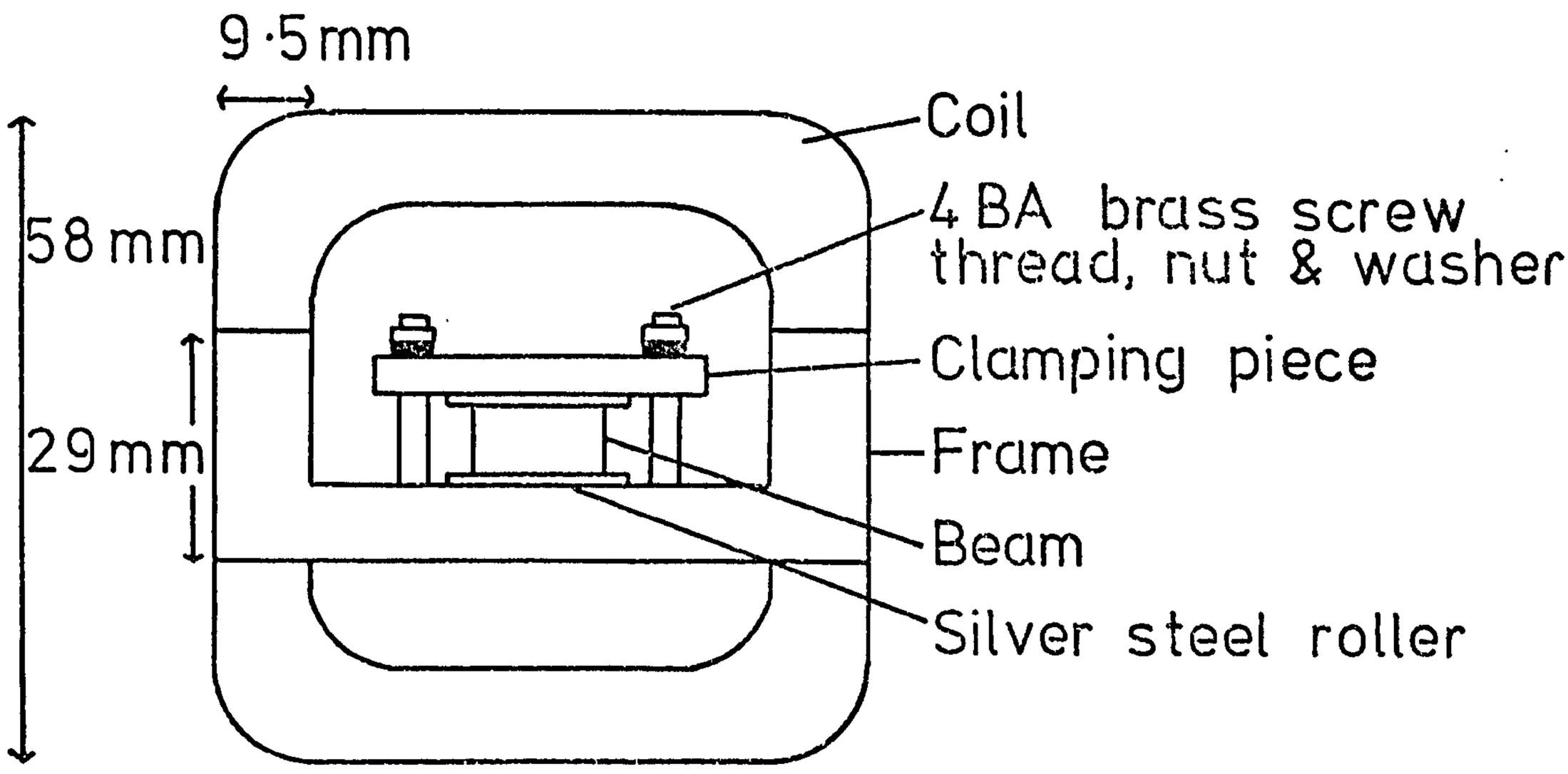

Figure 3.8 Rig with Permanent Magnets

(all dimensions in mm.)

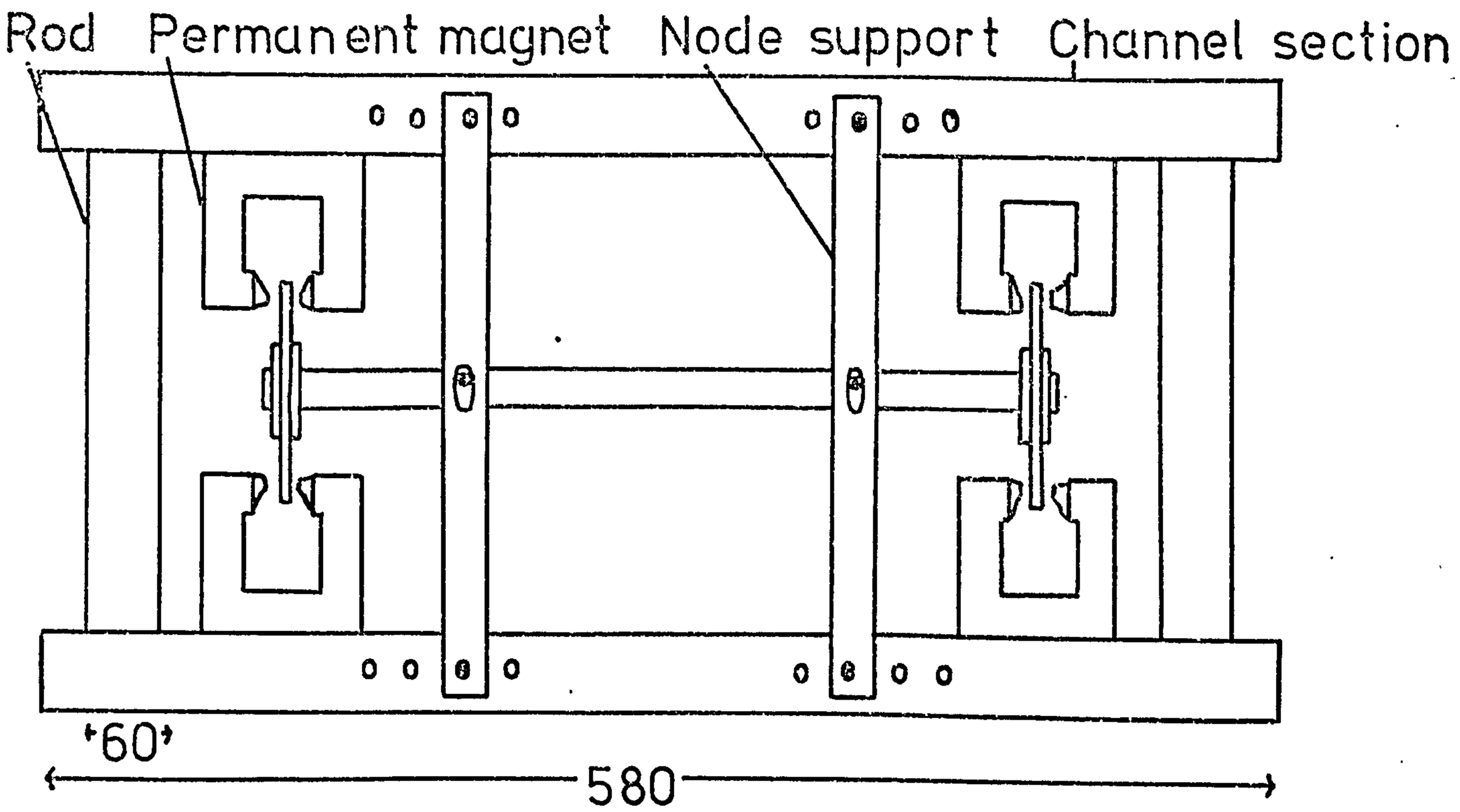

Cross-Section at Node Support

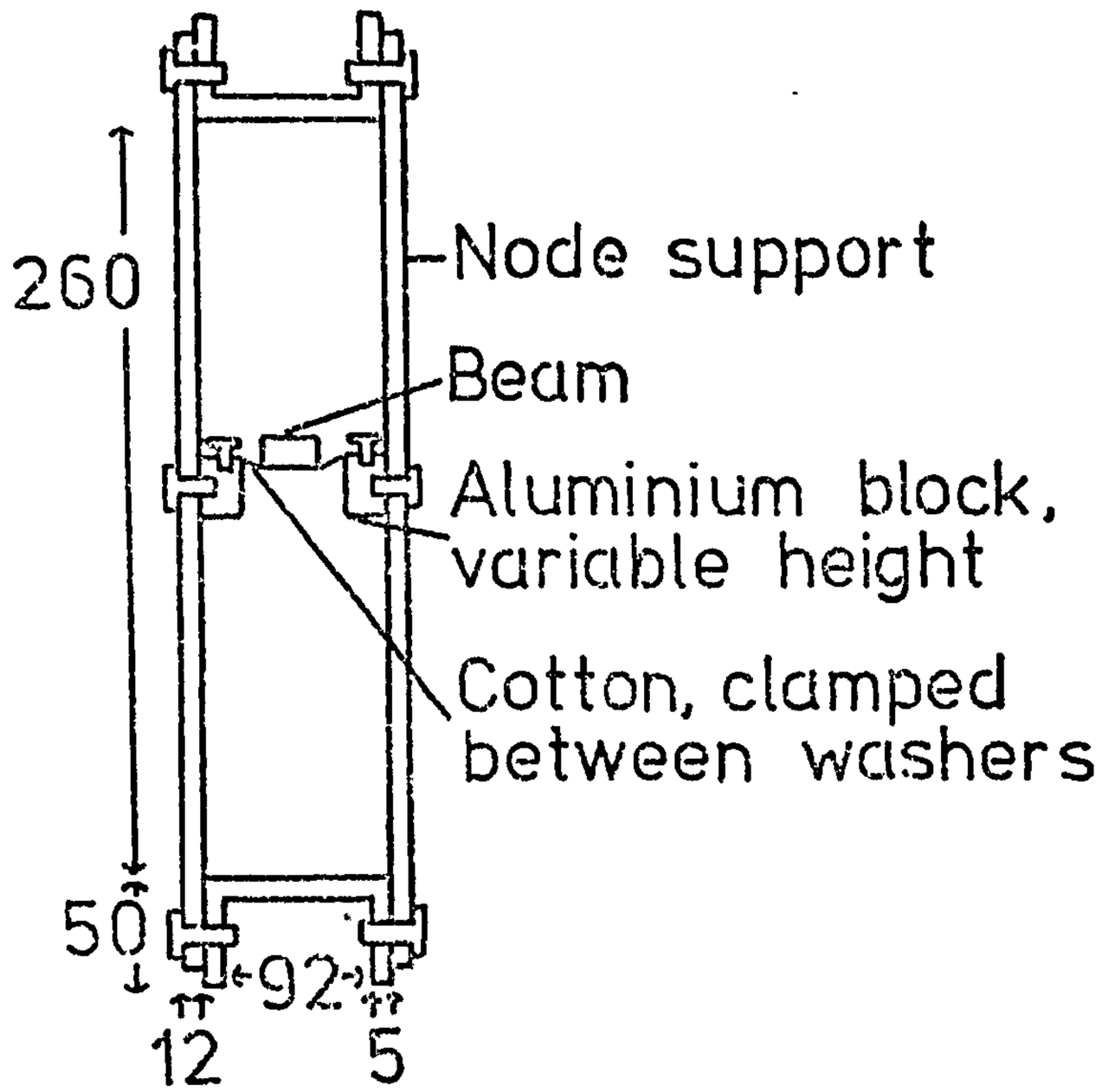

Figure 3.9 Rotary Inertia Measurement of Stiff Coils

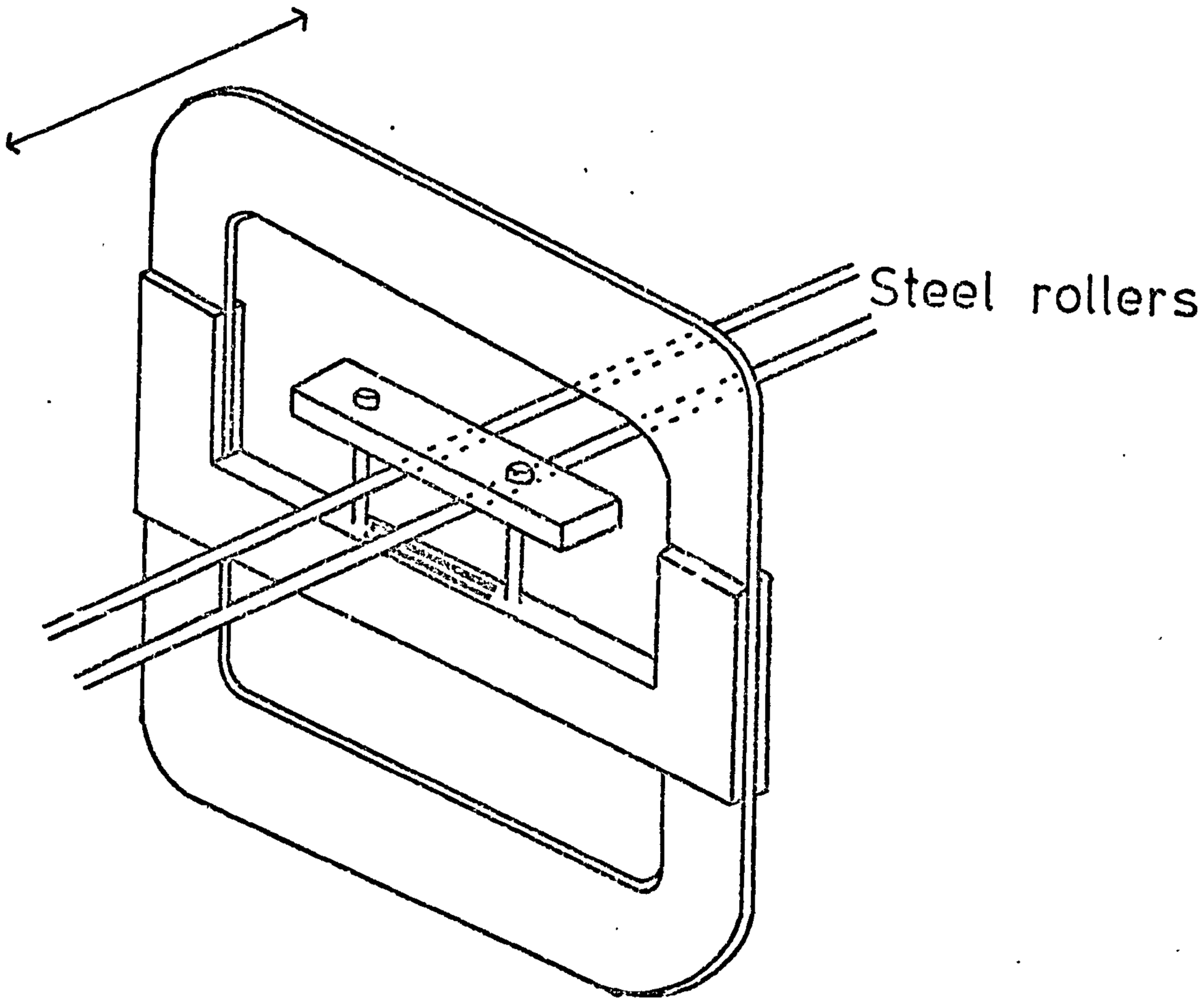

Figure 3.10 Specific Damping Capacity of Duralumin, measured using the Free-Free Rig and Stiff Coils with Aluminium Alloy Frames

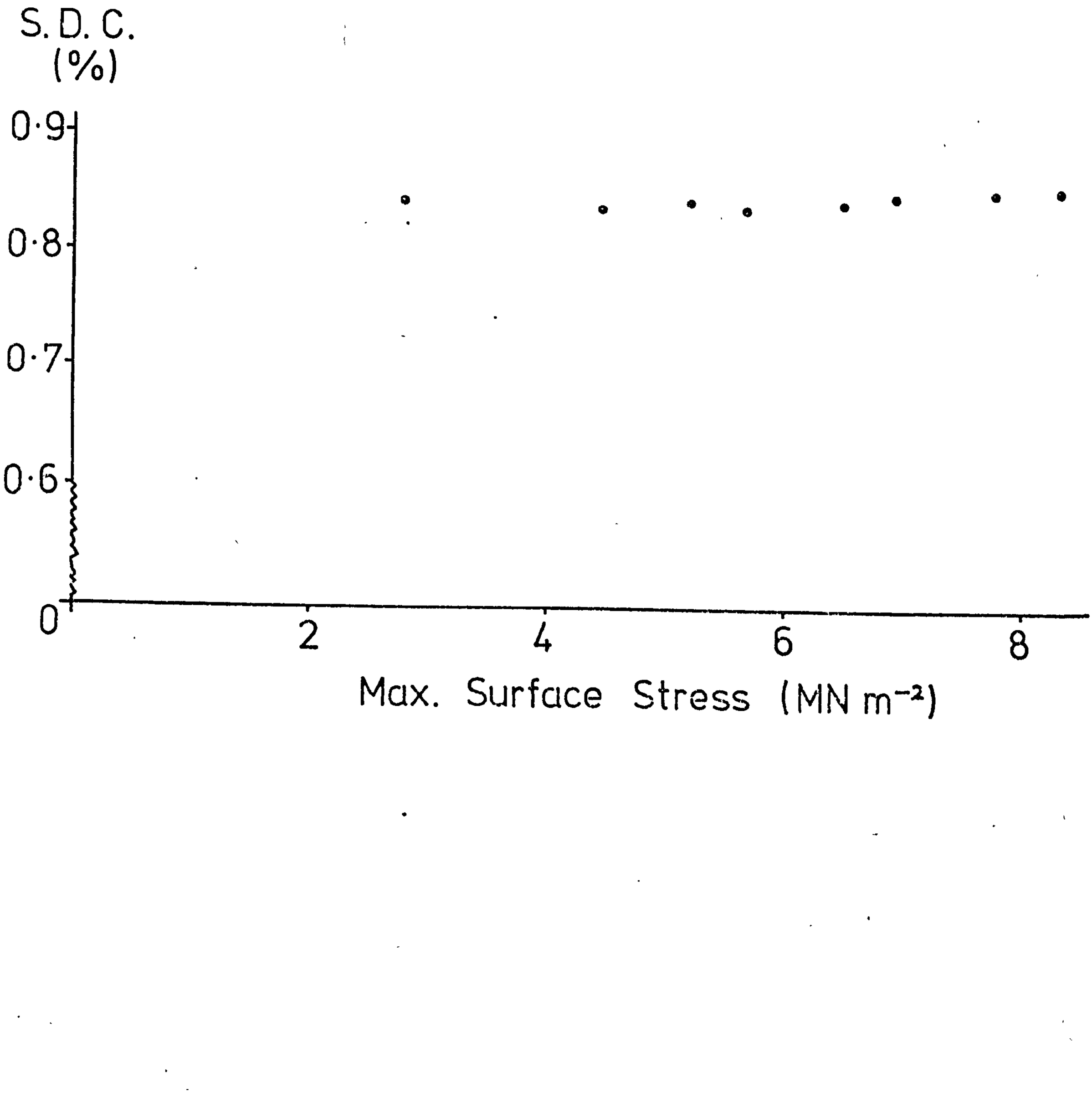

Figure 3.11 Specific Damping Capacity of Duralumin, measured using the Free-Free Rig and Stiff Coils with Aluminium Alloy Frames, in the Vacuum Chamber

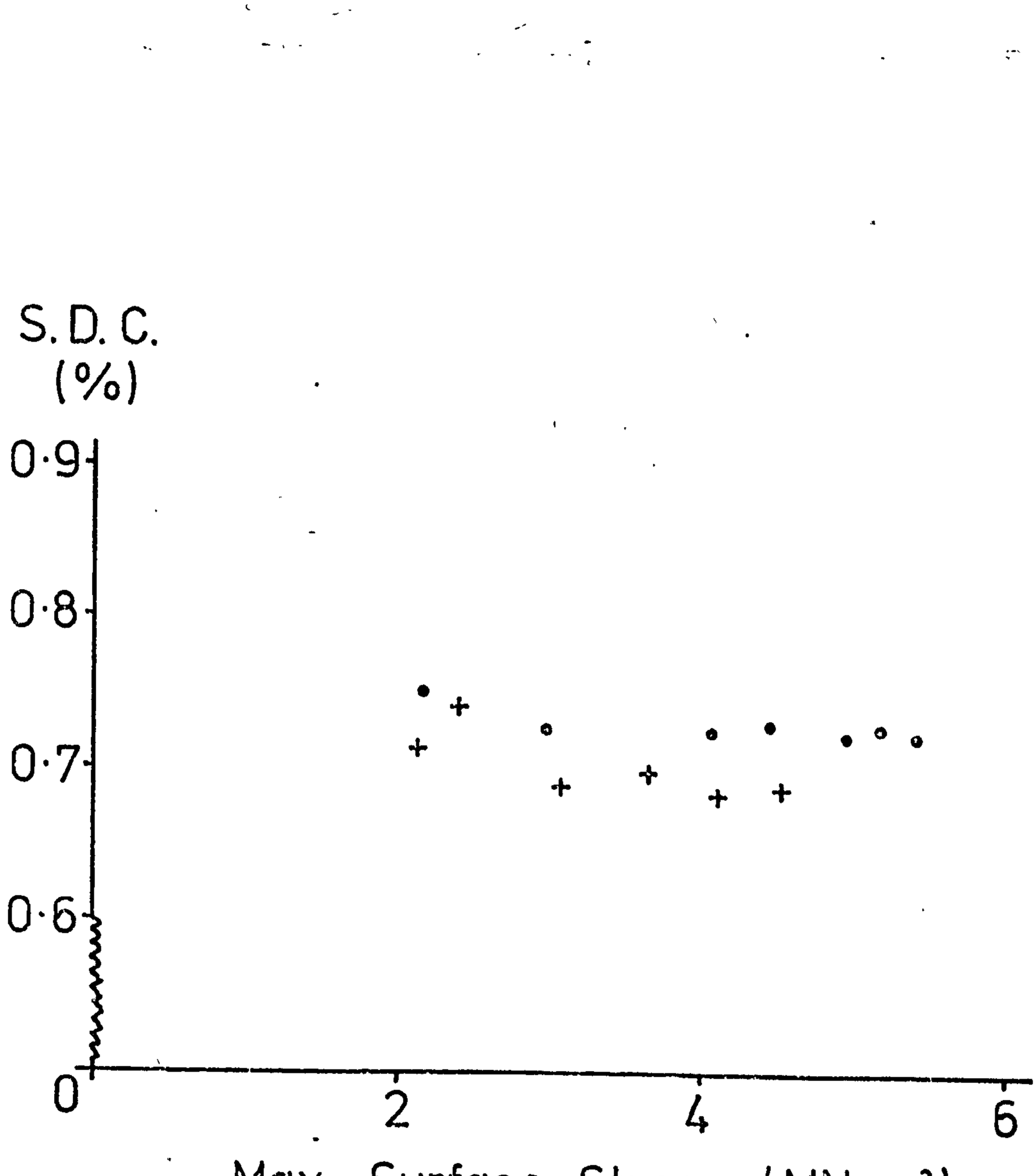

Figure 3.12 Coil developed for Previous Flexural Rig

(all dimensions in mm.)

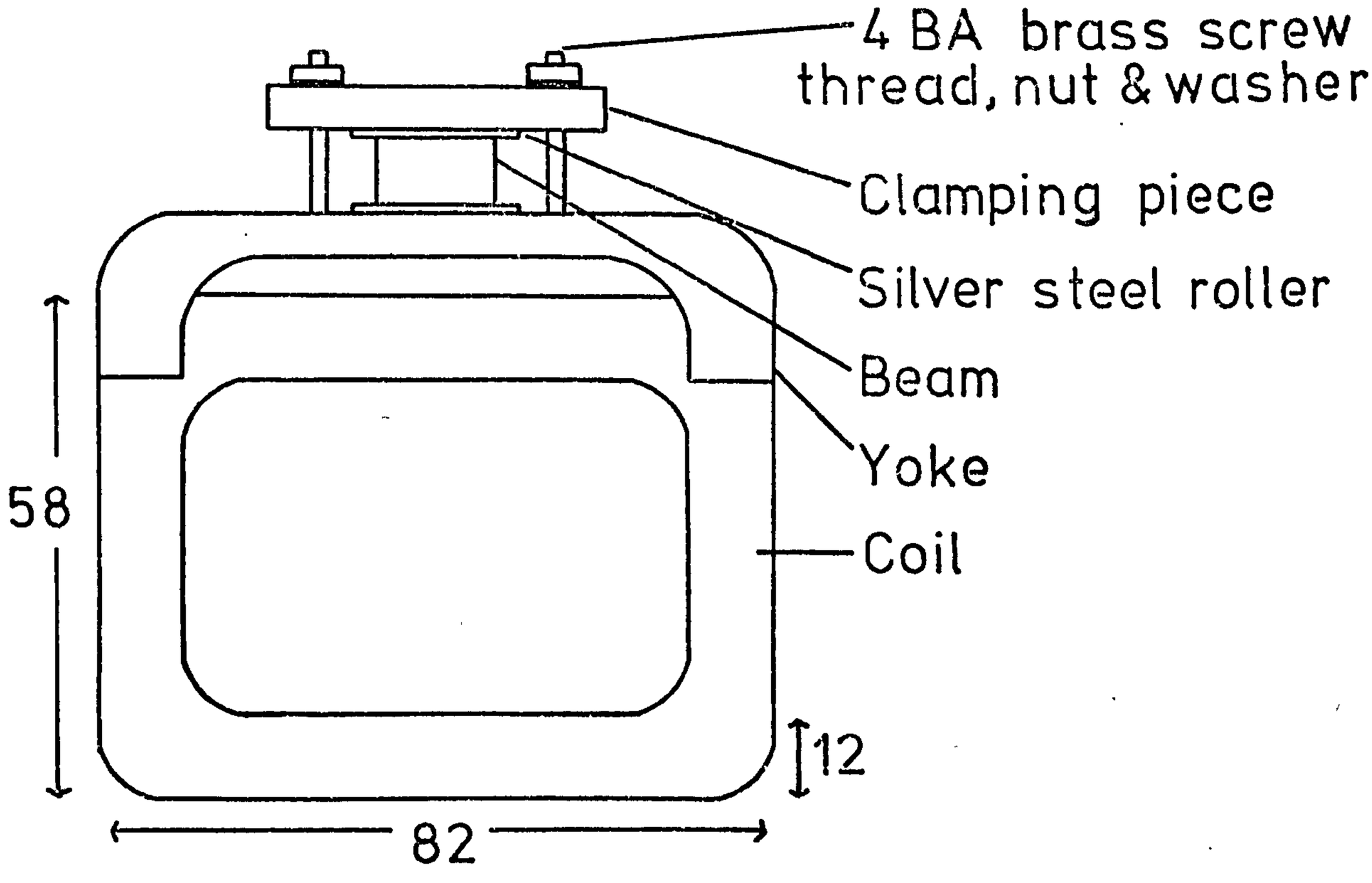

Figure 3.13 Specific Damping Capacity of Duralumin, measured using the Free-Free Rig and Stiff Coils with Tufnol Frames

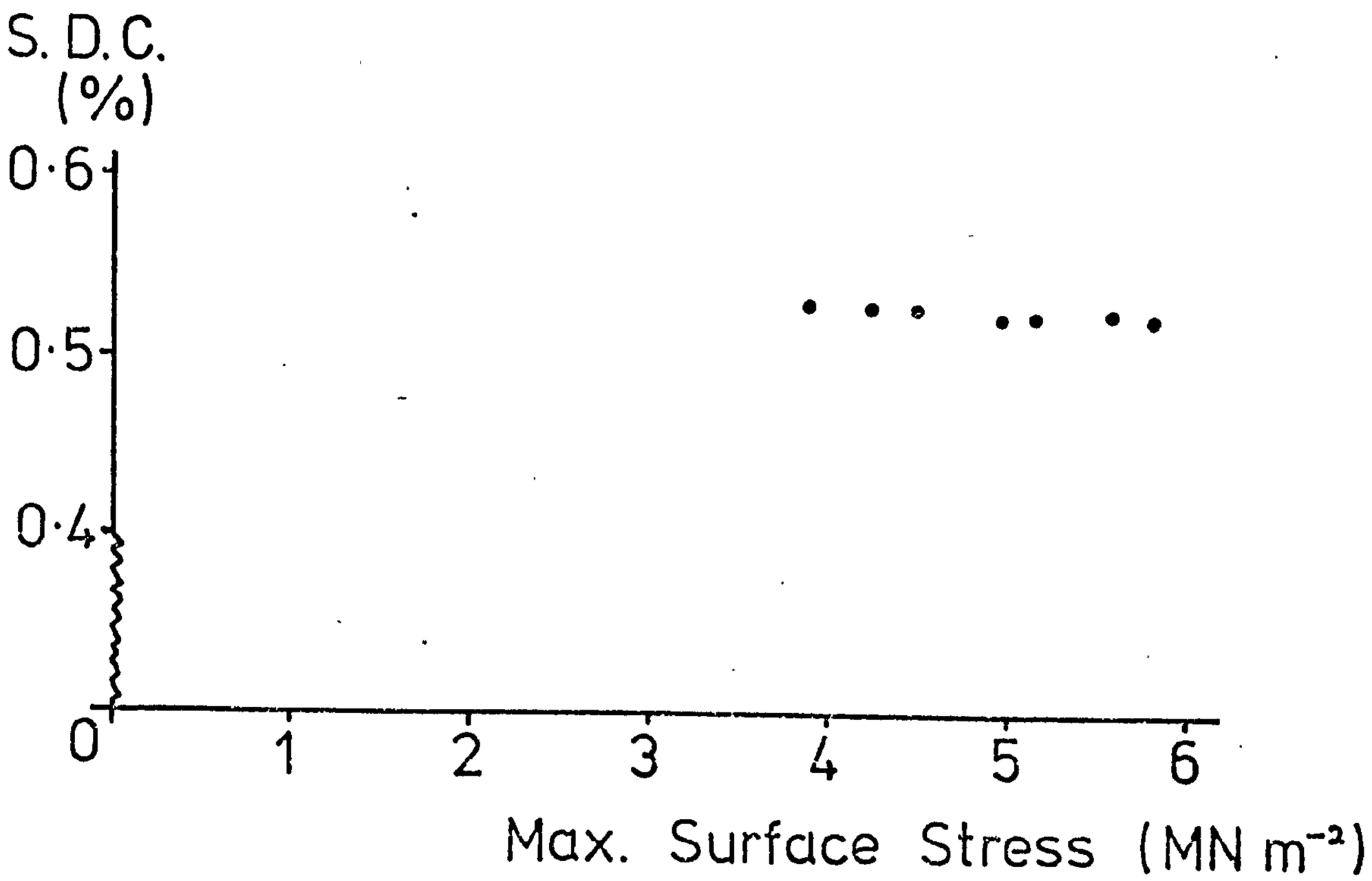

Figure 3.14 Specific Damping Capacity of Stainless Steel, measured using the Free-Free Rig and Stiff Coils with Tufnol Frames

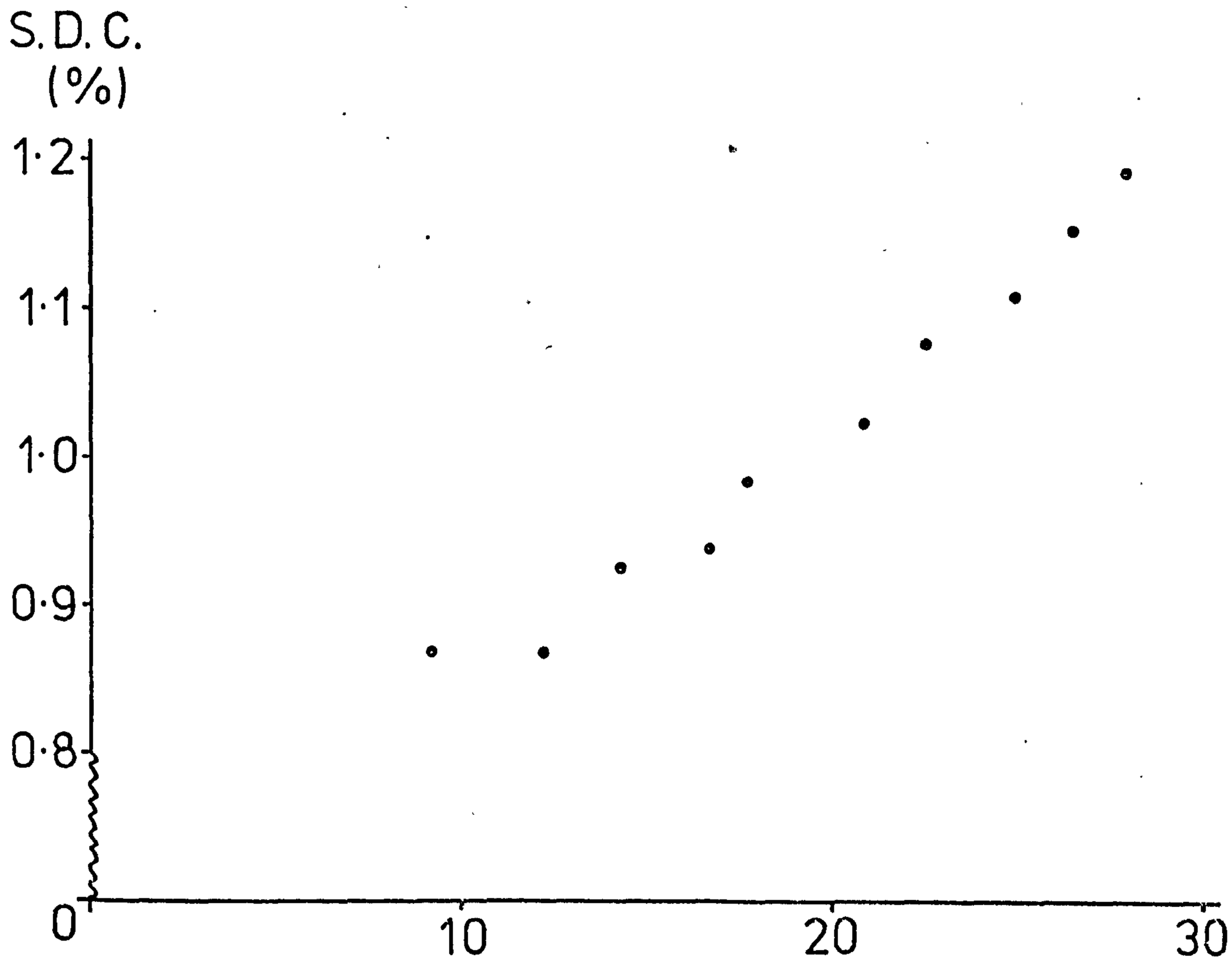

Figure 3.15 Cantilever Rig.

(all dimensions in mm.)

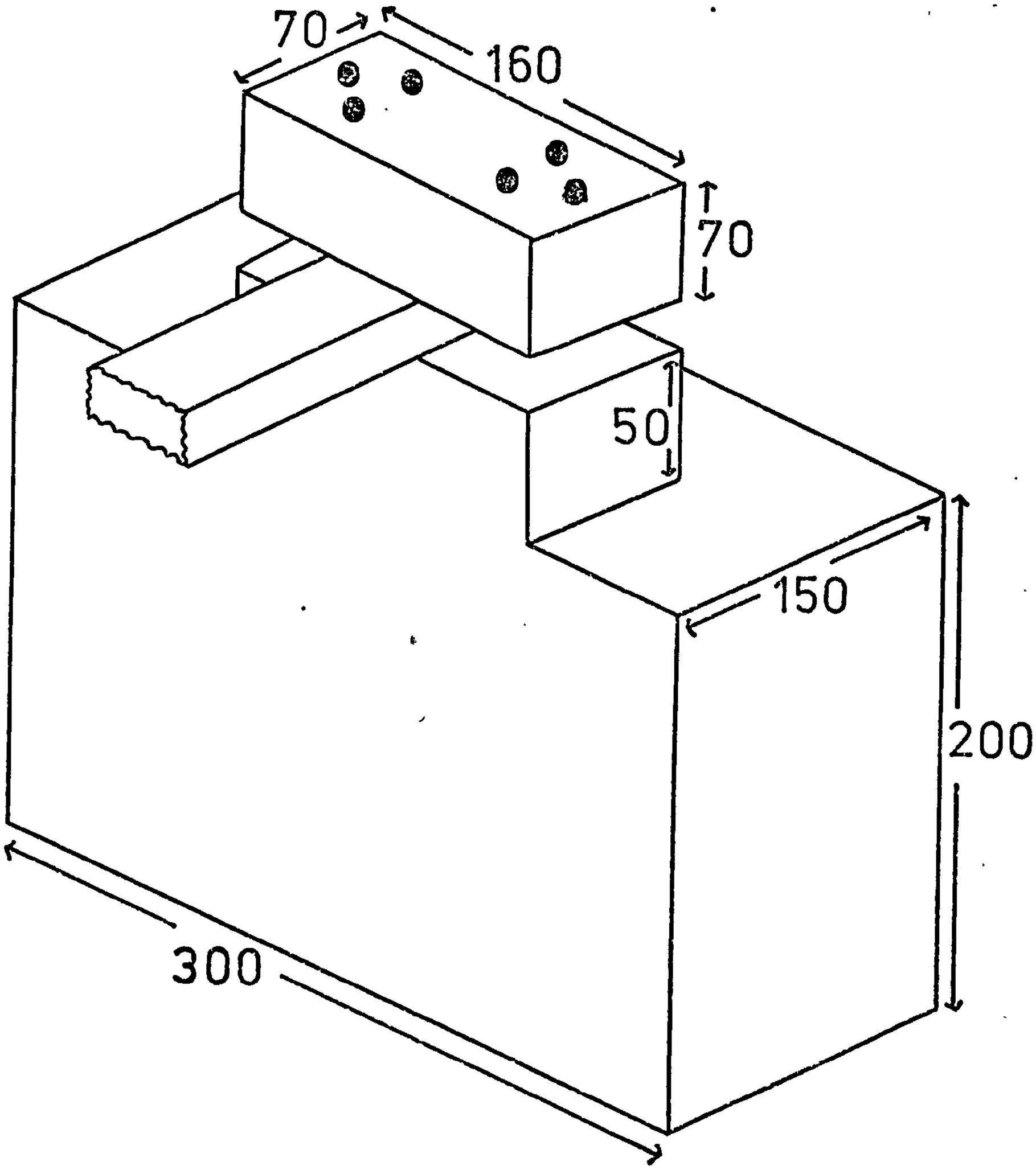

Cross-Section at Encastré End

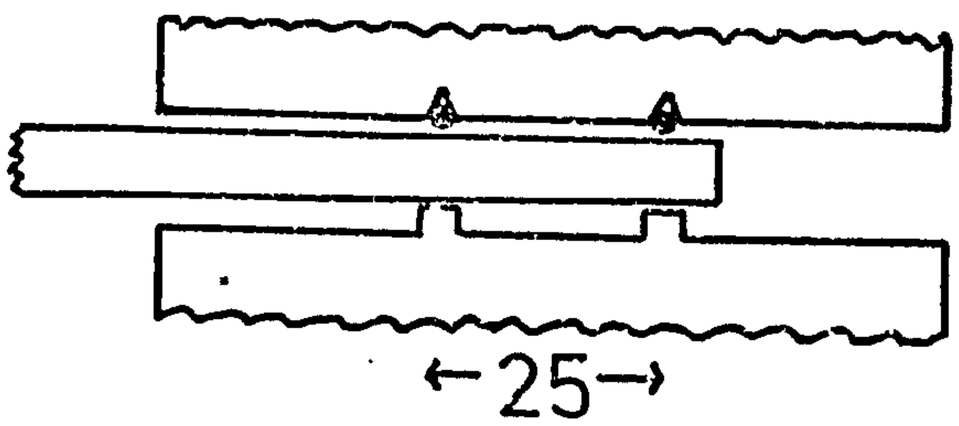

Figure 3.16 Theoretical Variation of Frequency Number with Mass Ratio (end mass/ beam mass) for the Cantilever Rig

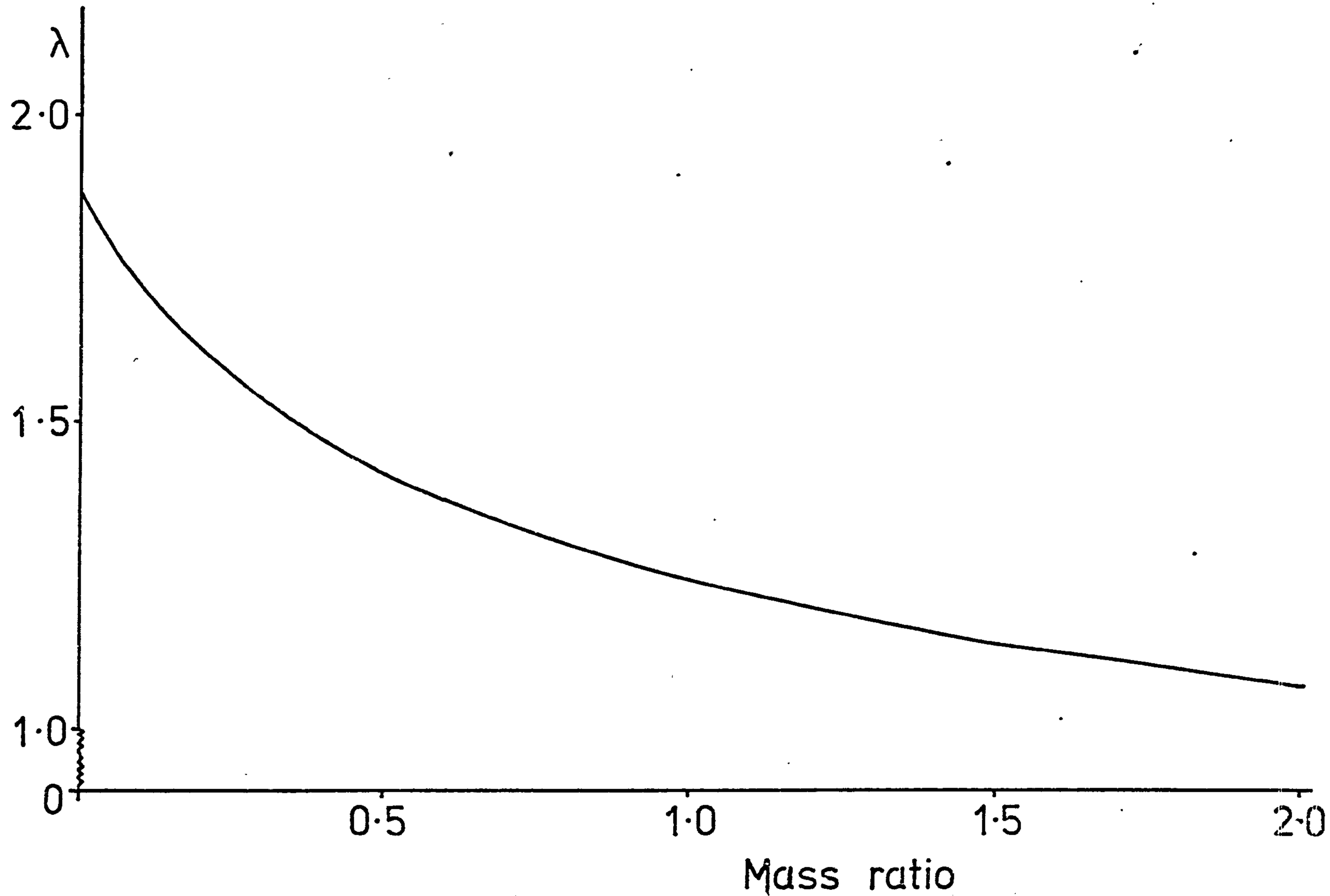

Figure 3.17 Theoretical Variation of Frequency Number with Rotary Inertia of End Mass for the Cantilever Rig

(beam mass = 66 gm, beam length = 300 mm, end mass = 30 gm)

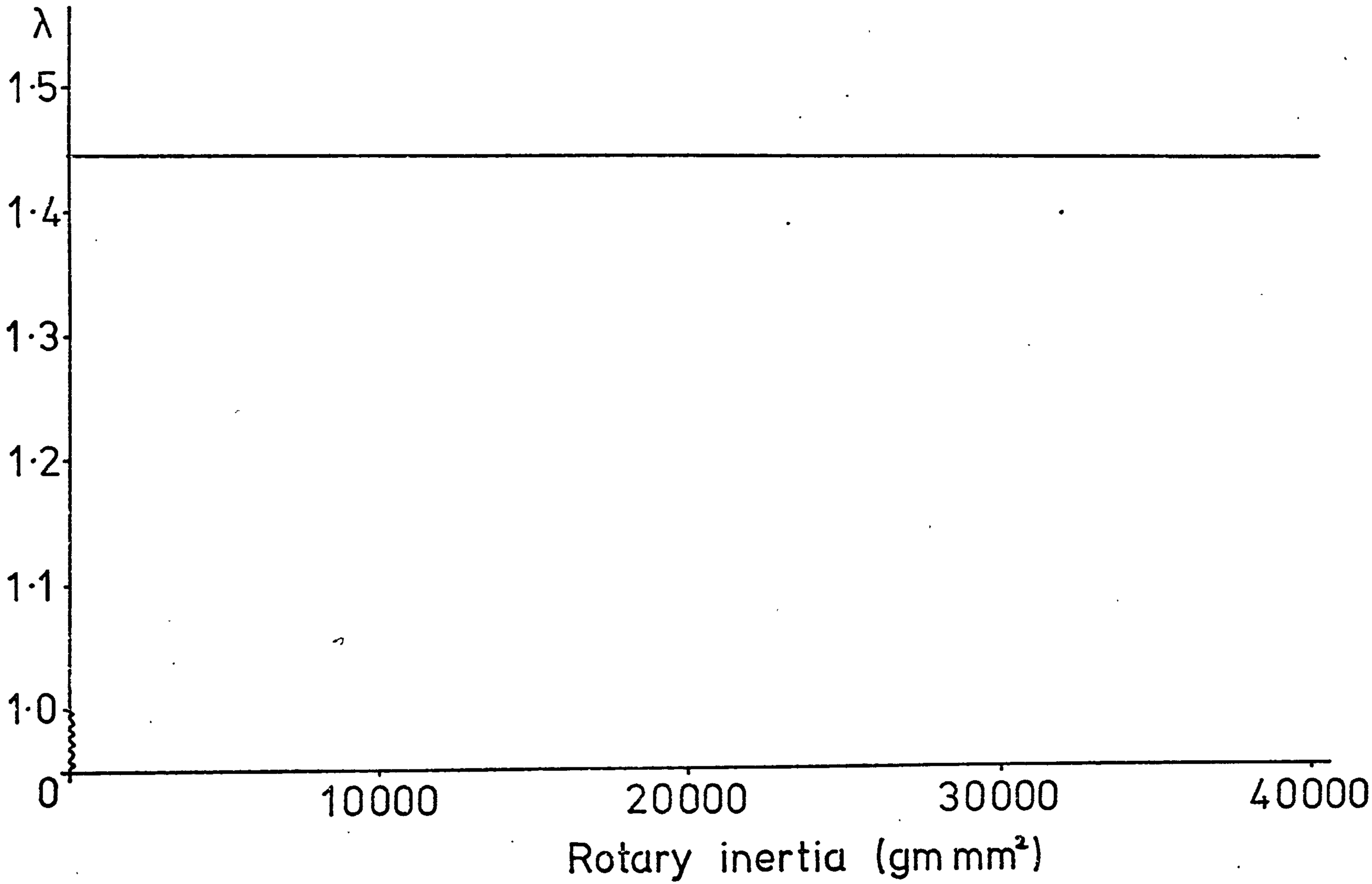

Figure 3.18 Comparison of Theoretical and Measured Mode Shapes for a Duralumin Cantilever

—— theoretical mode shape (including rotary inertia of coil)
× measured deflections

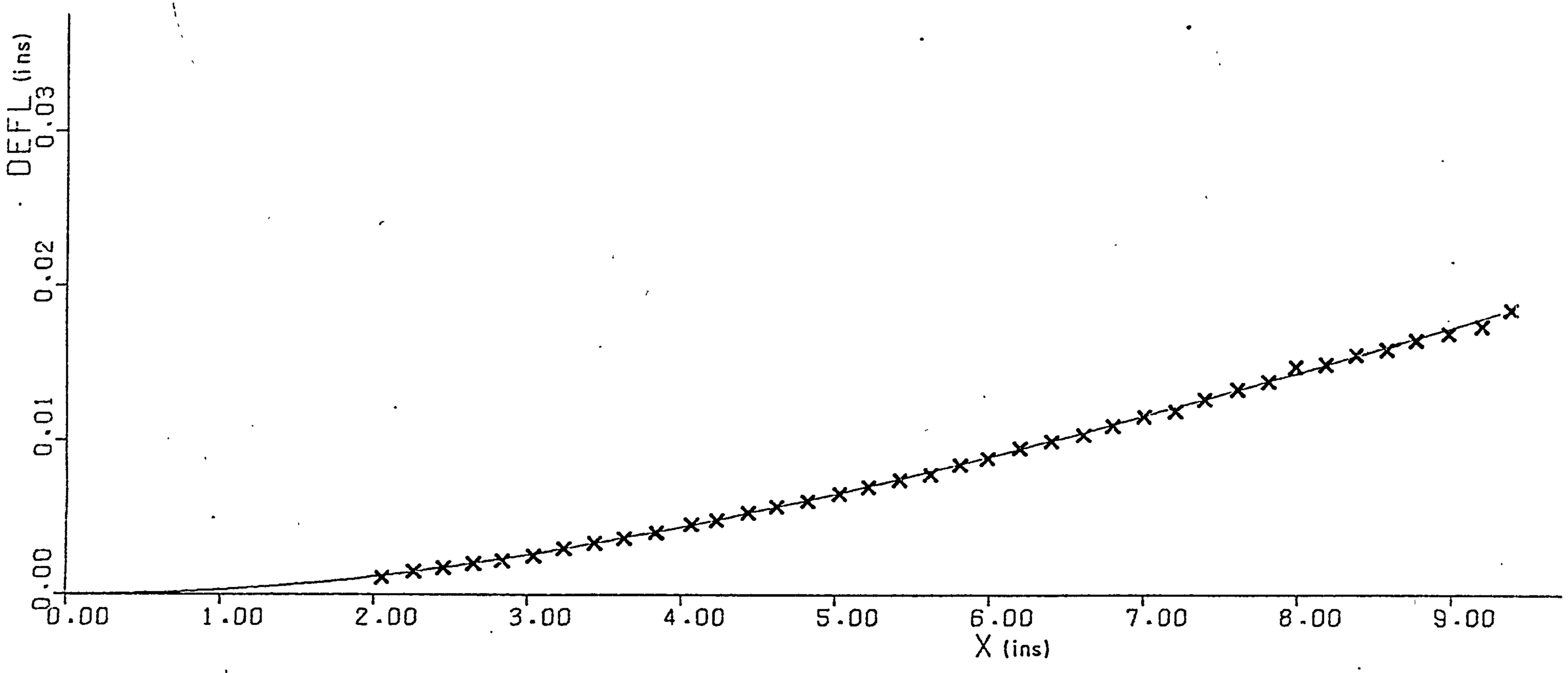

Figure 3.19 Specific Damping Capacity of Duralumin, measured using the Cantilever Rig.

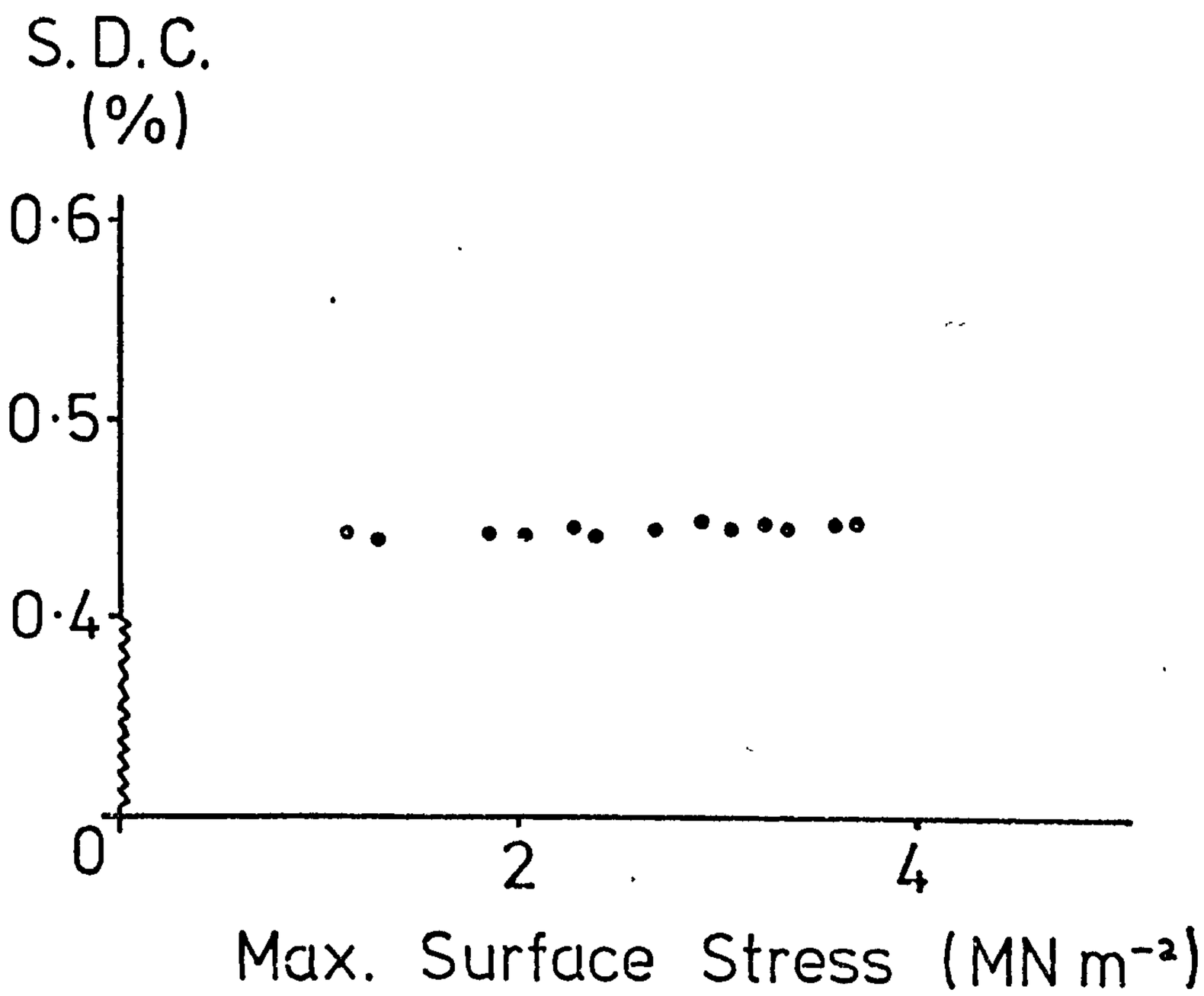

Figure 4.1 Clamping Arrangement for Glass Mat during the Preparation of 0^{o} Beams

(All dimensions in mm.)

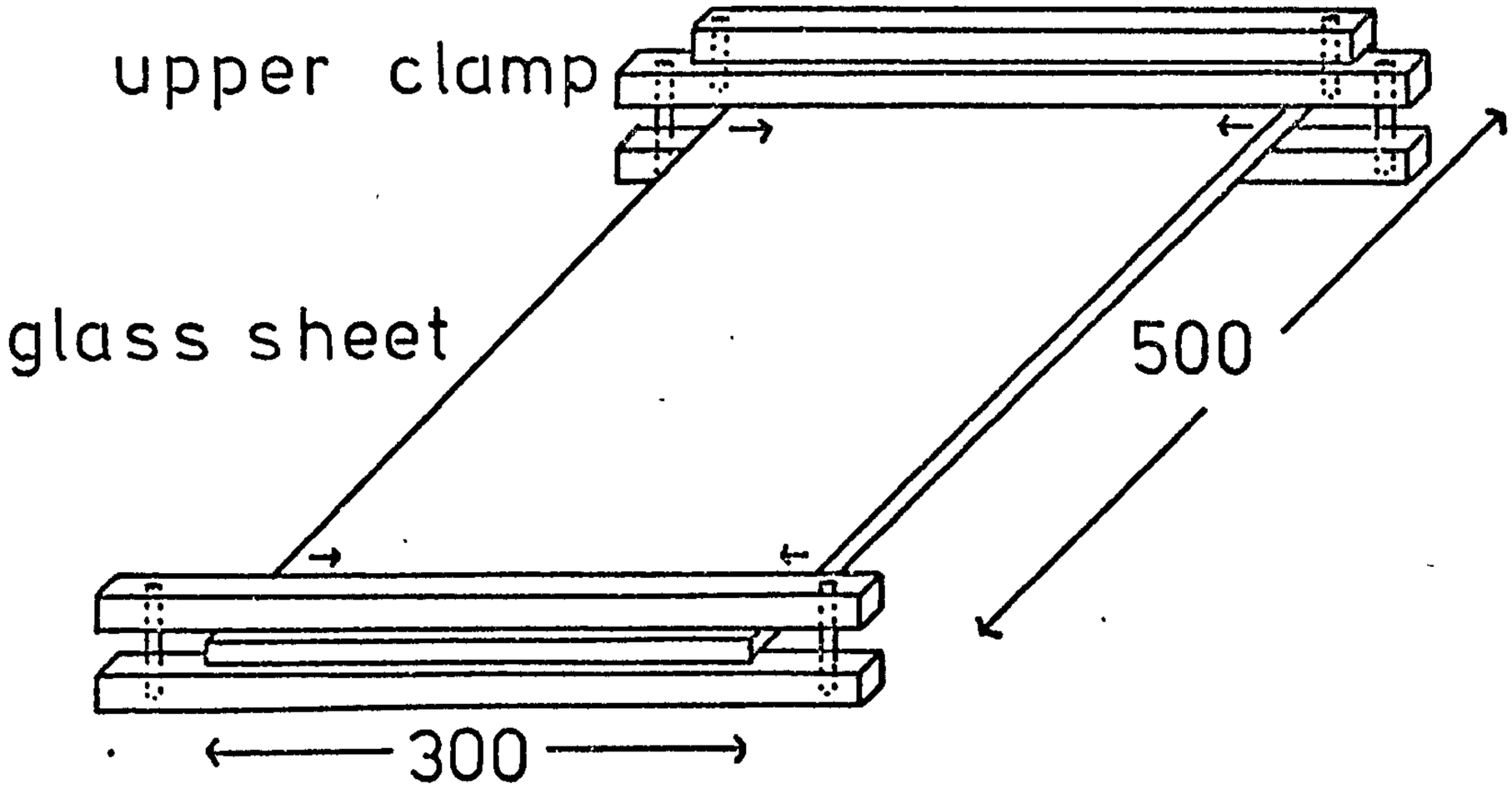

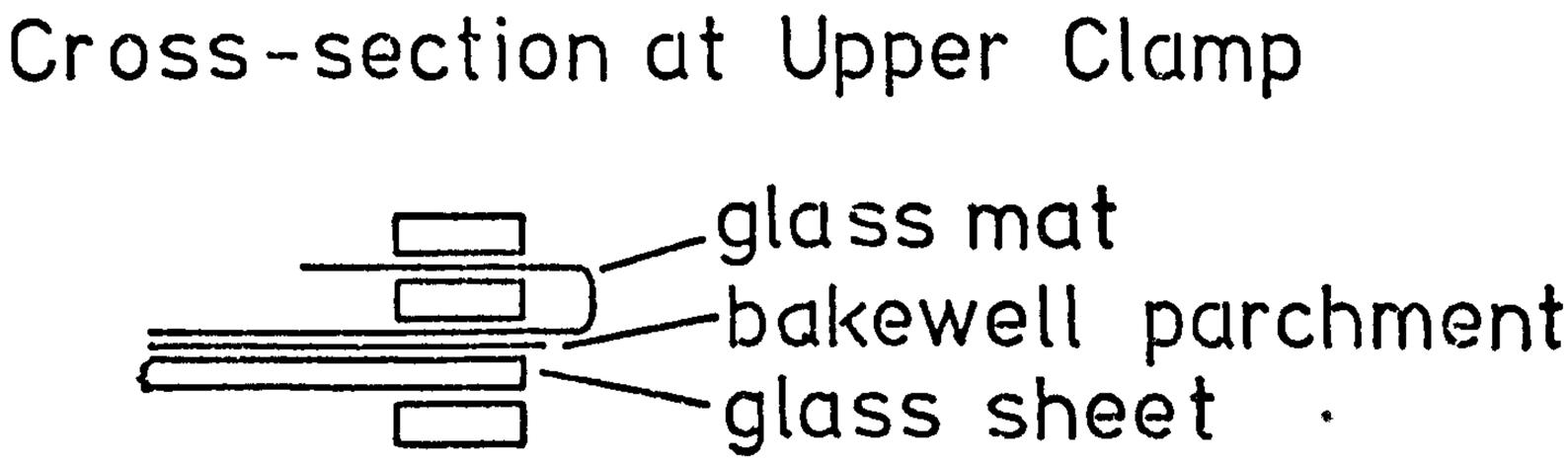

Figure 4.2 Mould for the Preparation of 0° Beams

(All dimensions in mm.)

Lid

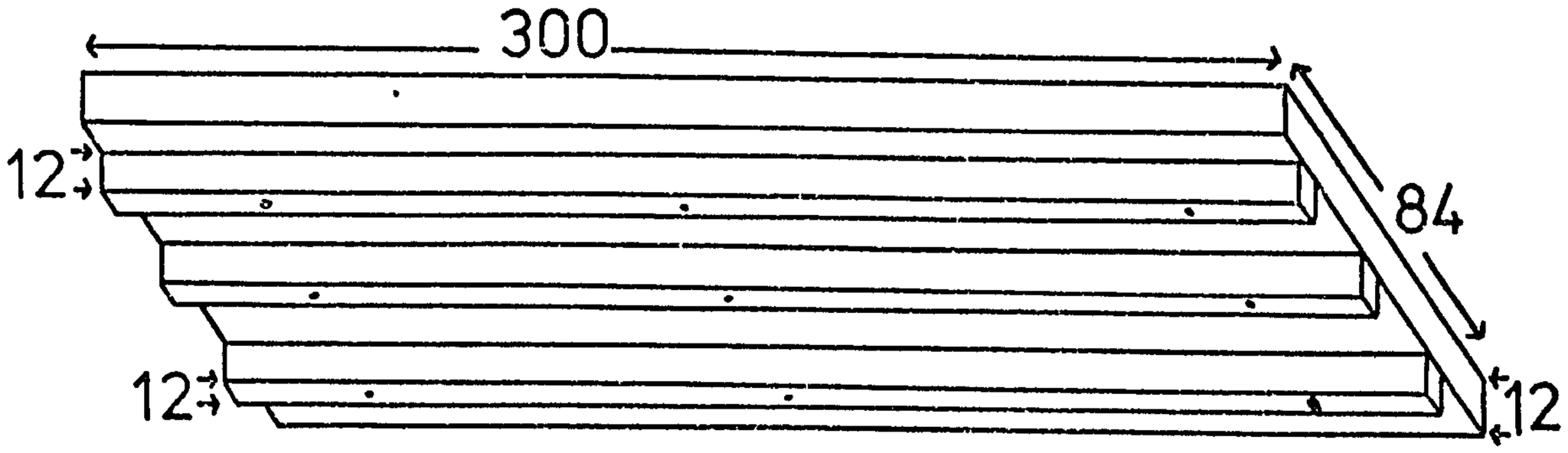

Base

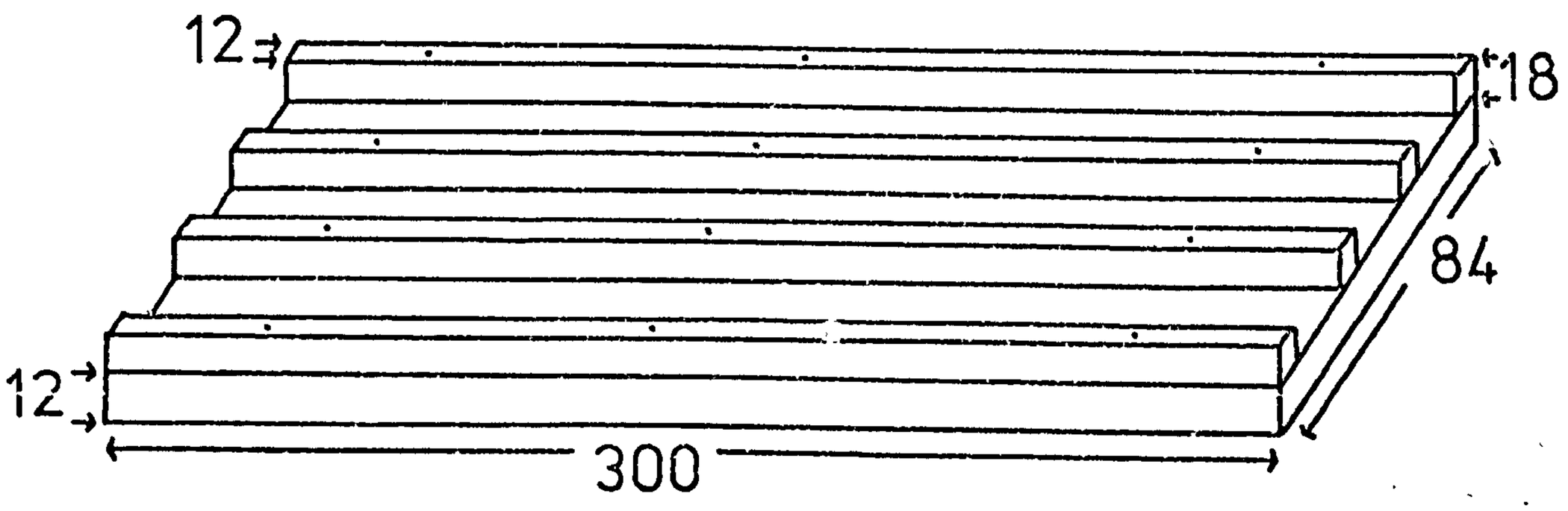

Spacers

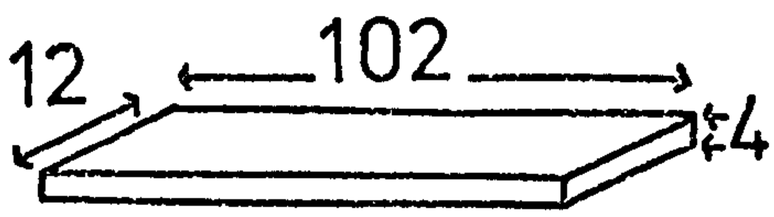

Figure 4.3 Clamping Arrangement for Glass Mat during the Preparation of 90° Beams

(All dimensions in mm)

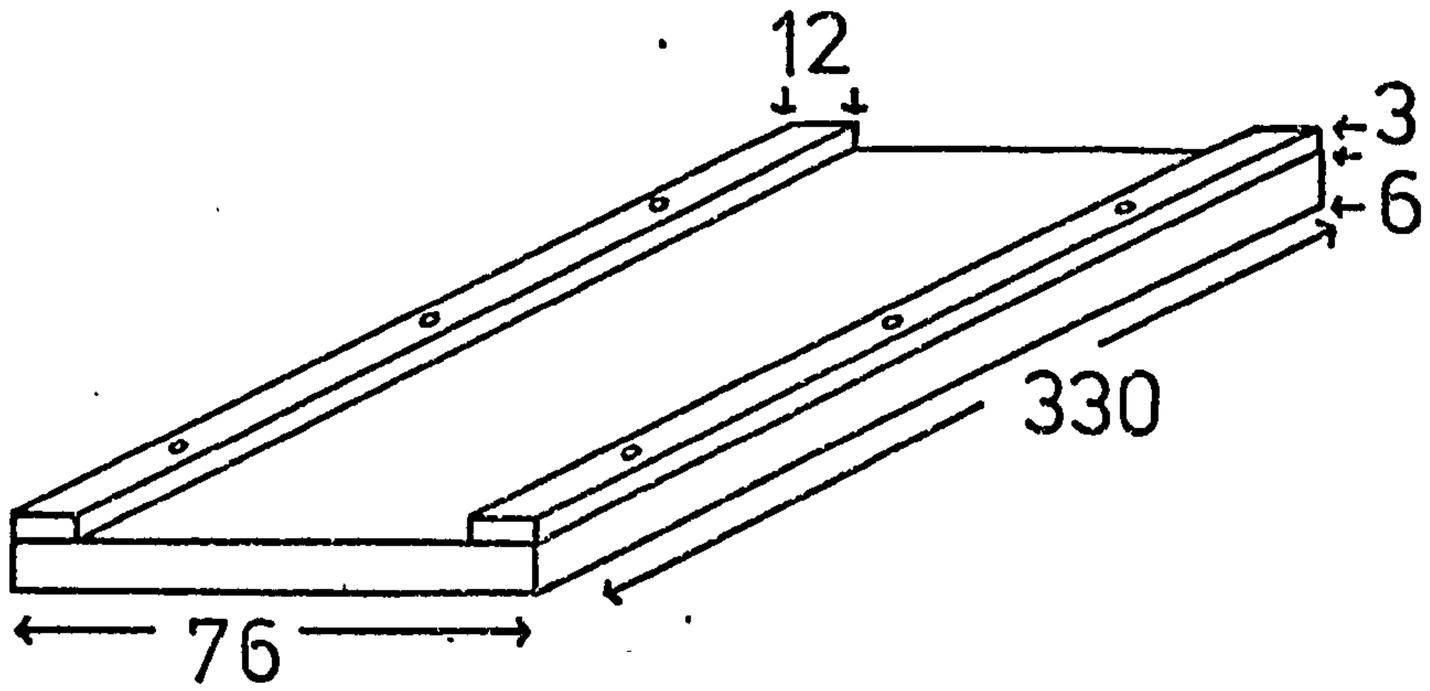

Figure 4.4 Mould for the Preparation of 90° Beams

(All dimensions in mm)

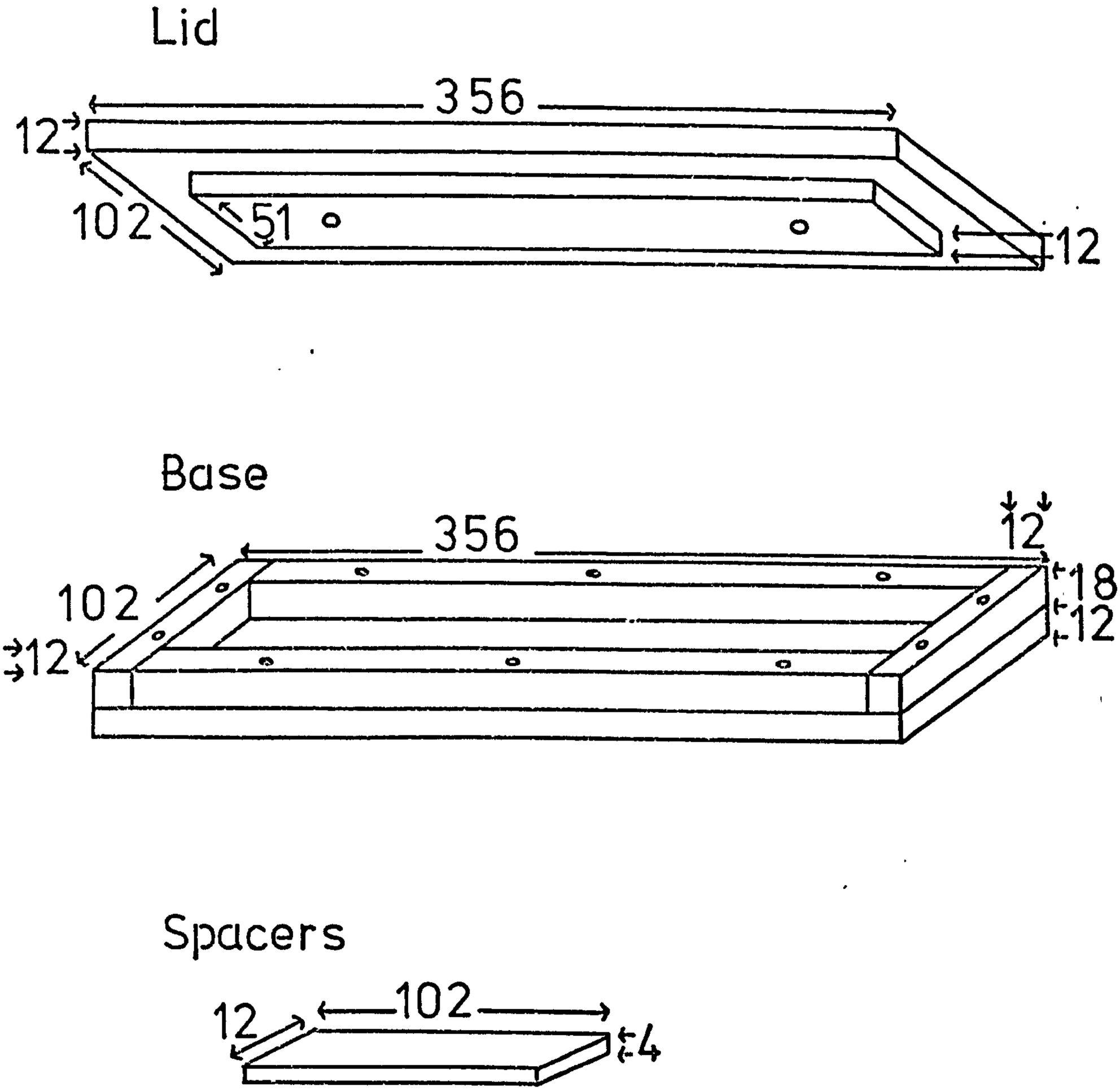

Figure 4.5 Base of Fibre Examined in Stereoscan

Figure 4.6 0° Beam Surface Examined in Stereoscan after Surface Grinding

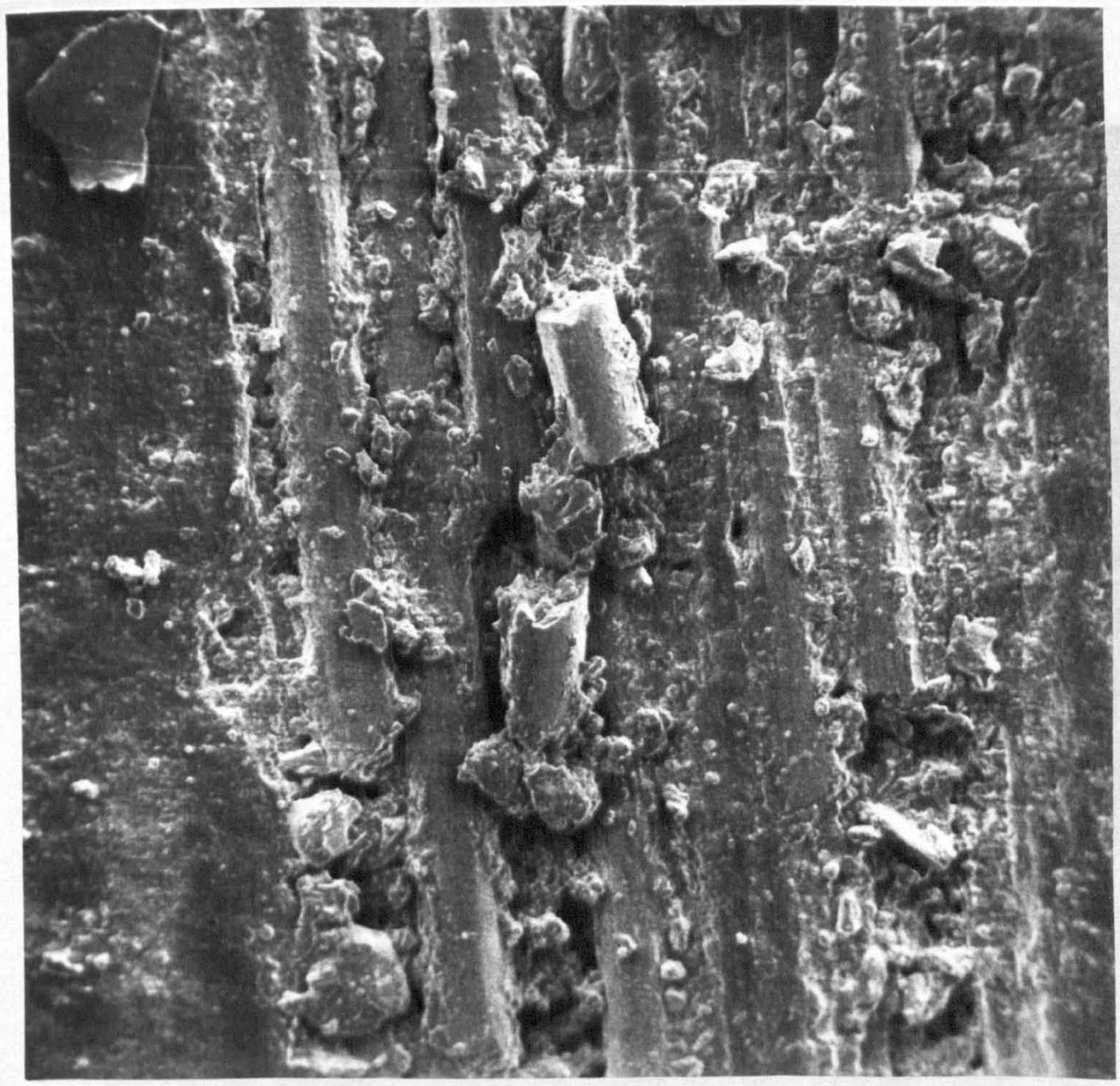

Figure 4.7 Polished Cross-Section

Magnification x 1500

Bright Field

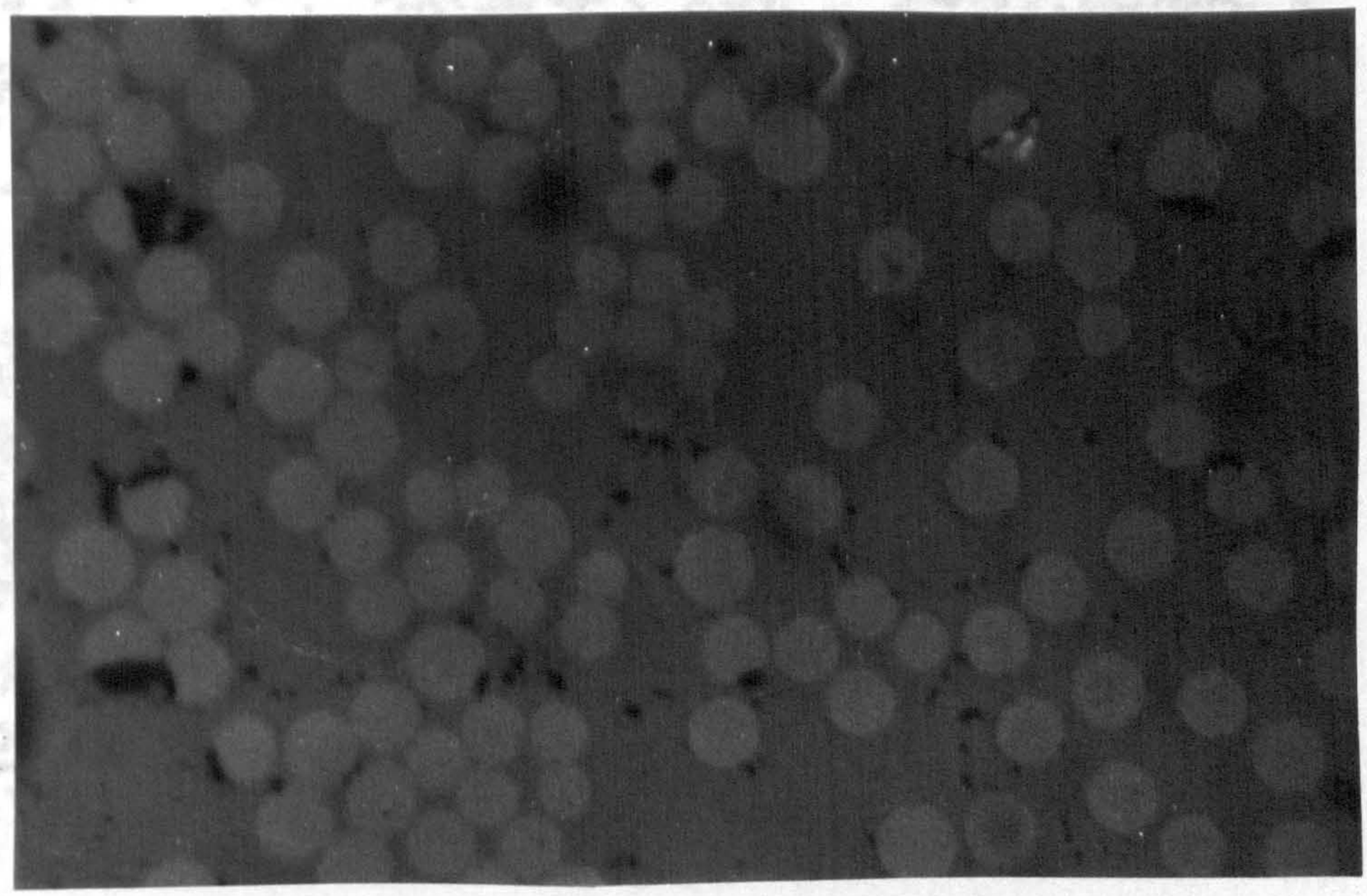

Nomarski Interference

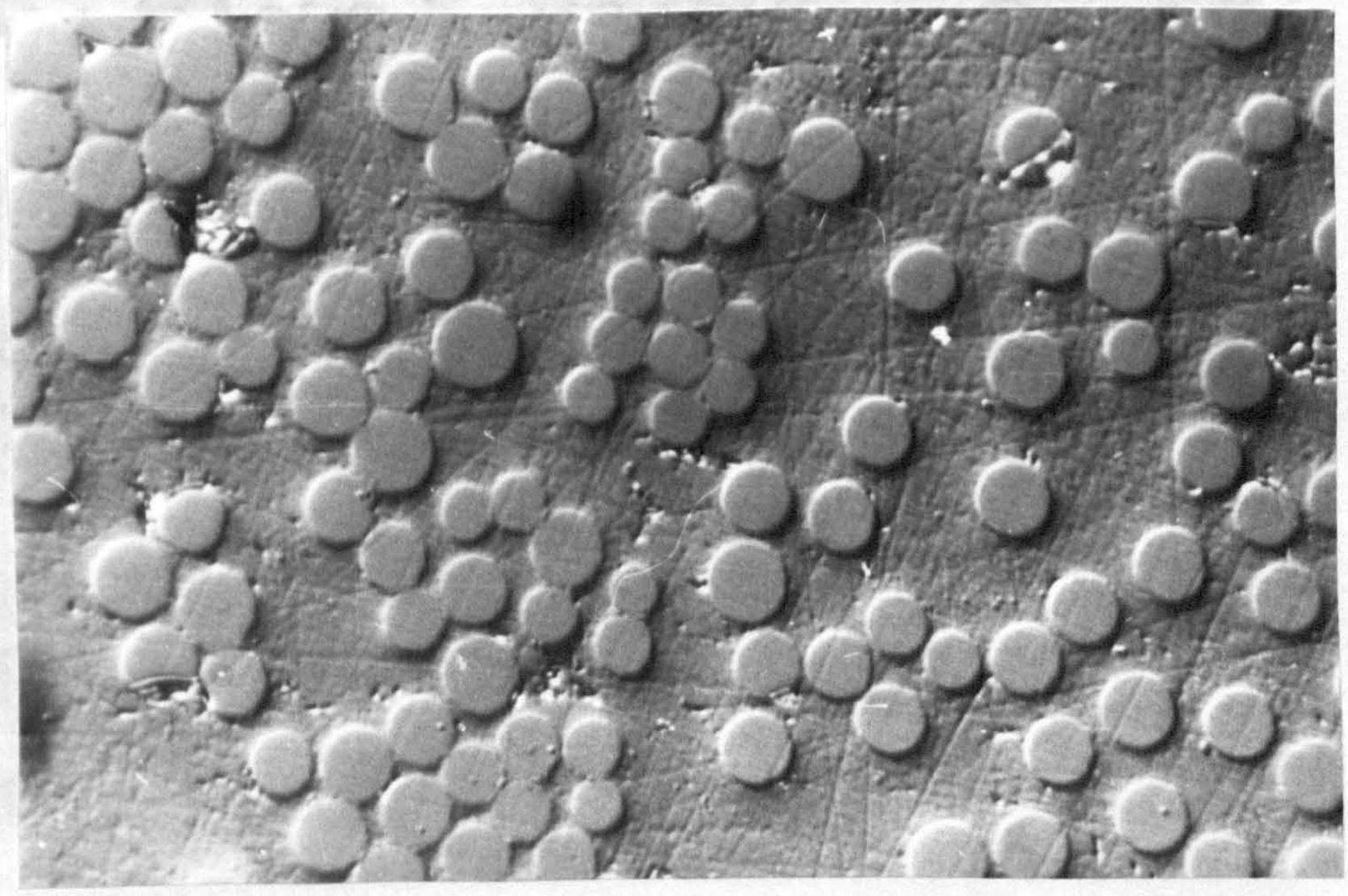

Figure 4.8 Polished Cross-Section Etched in Acid

Magnification x 280

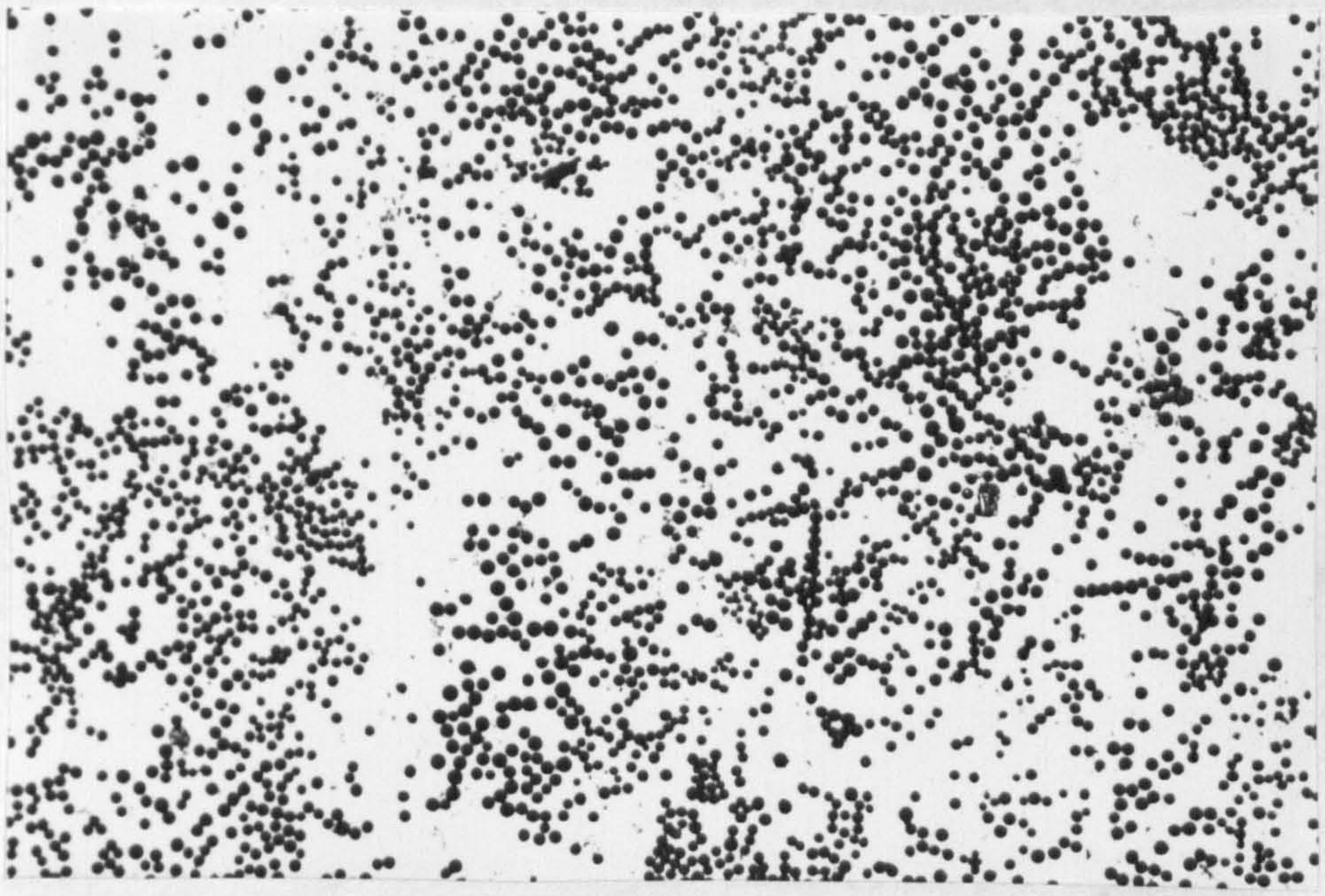

Figure 4.9 Polished Cross-Section Etched in Vapour

Magnification x 1100

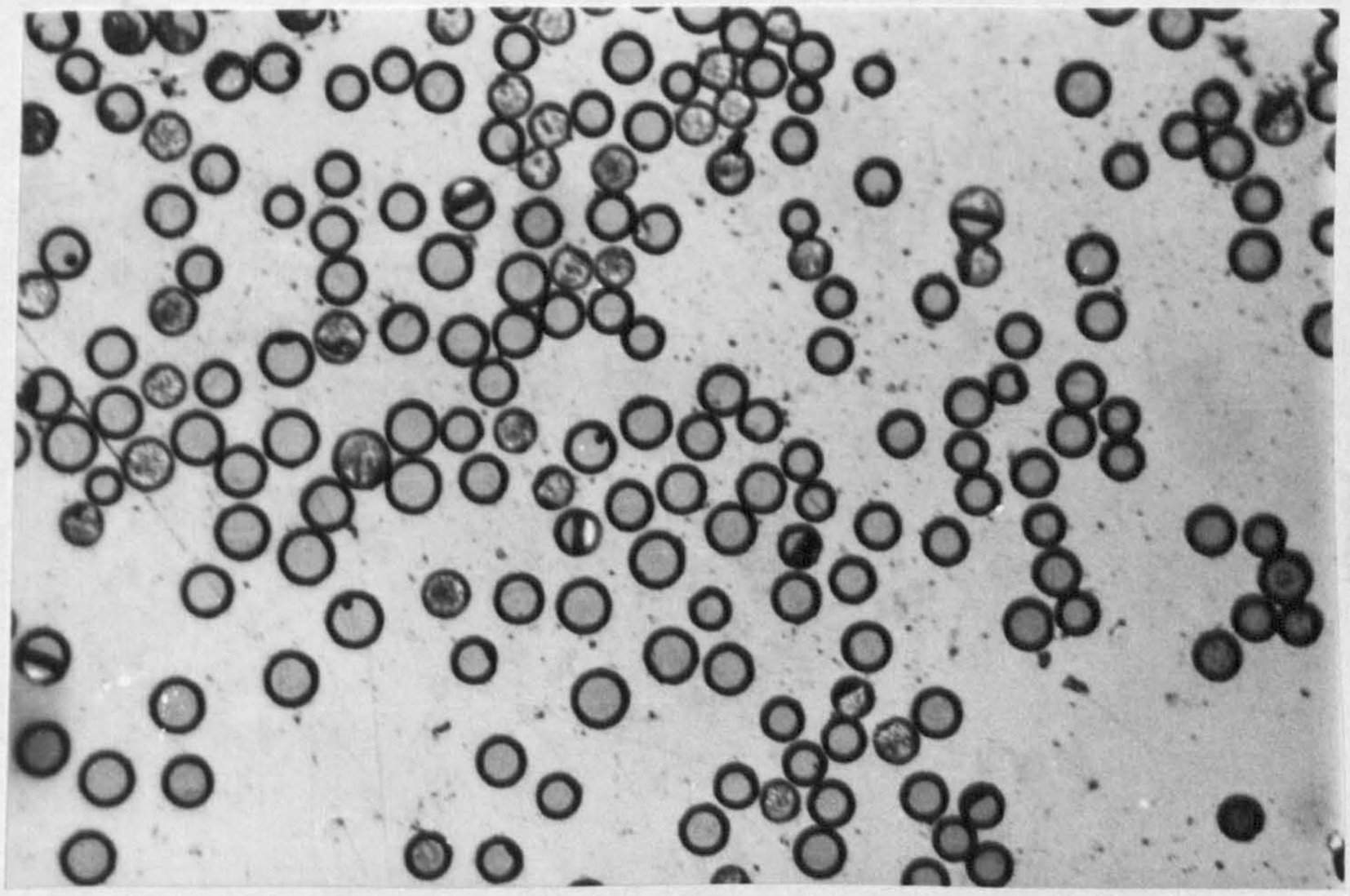

Figure 4.10 Histogram of Fibre Diameters

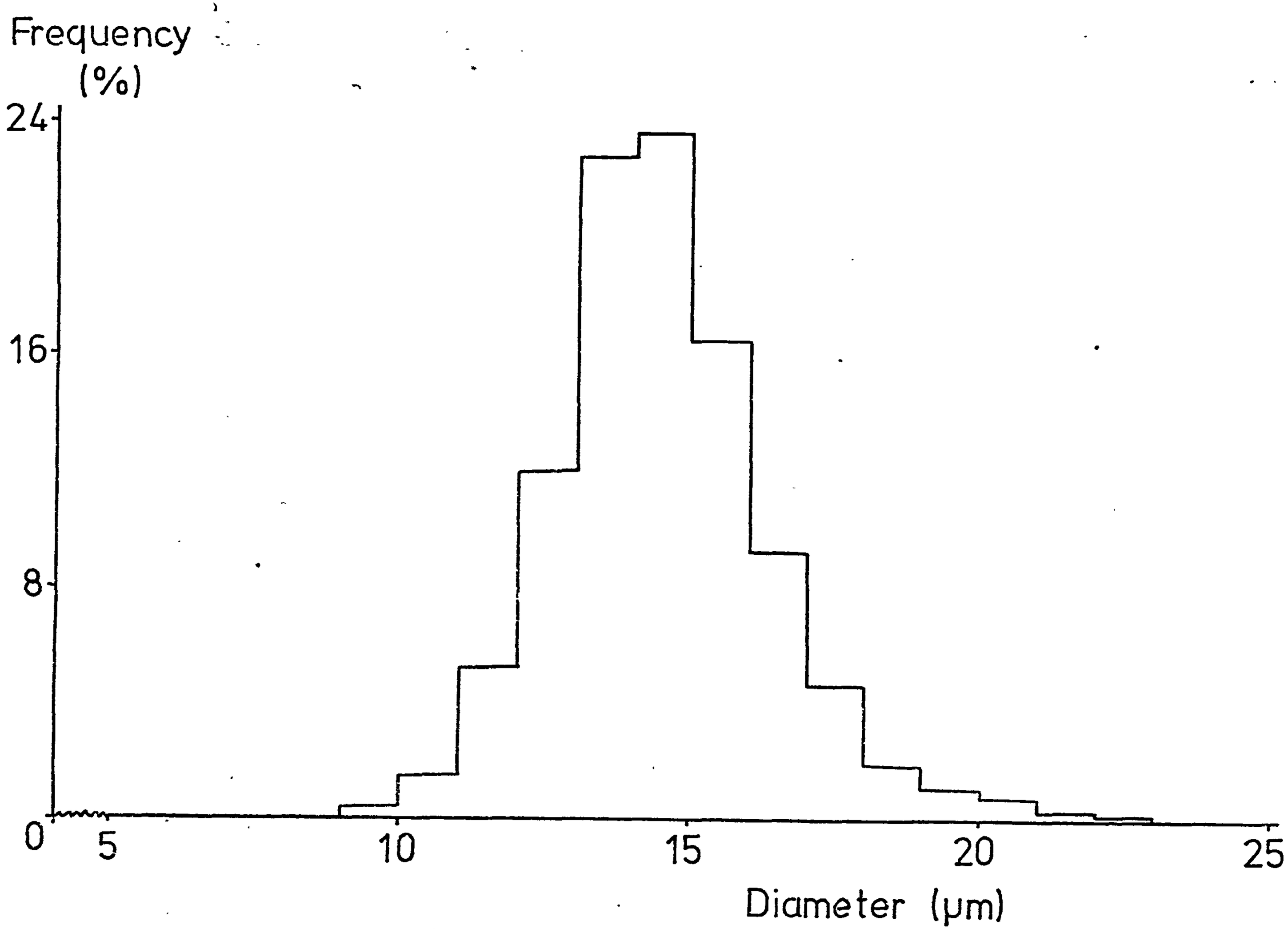

Figure 5.1 Polished Cross-Sections

Etched

Magnification x 250

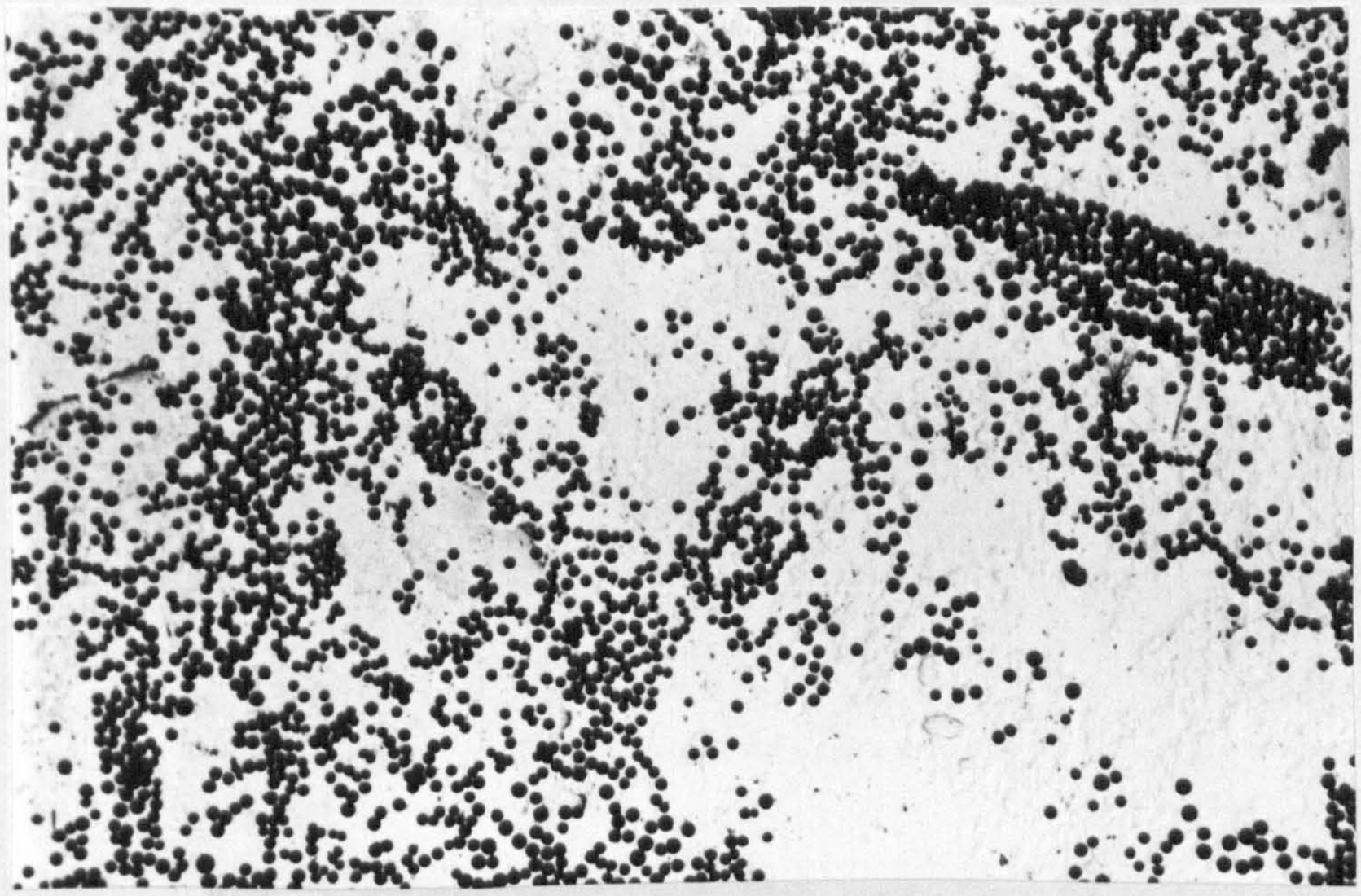

Nomarski Interference

Magnification x 1700

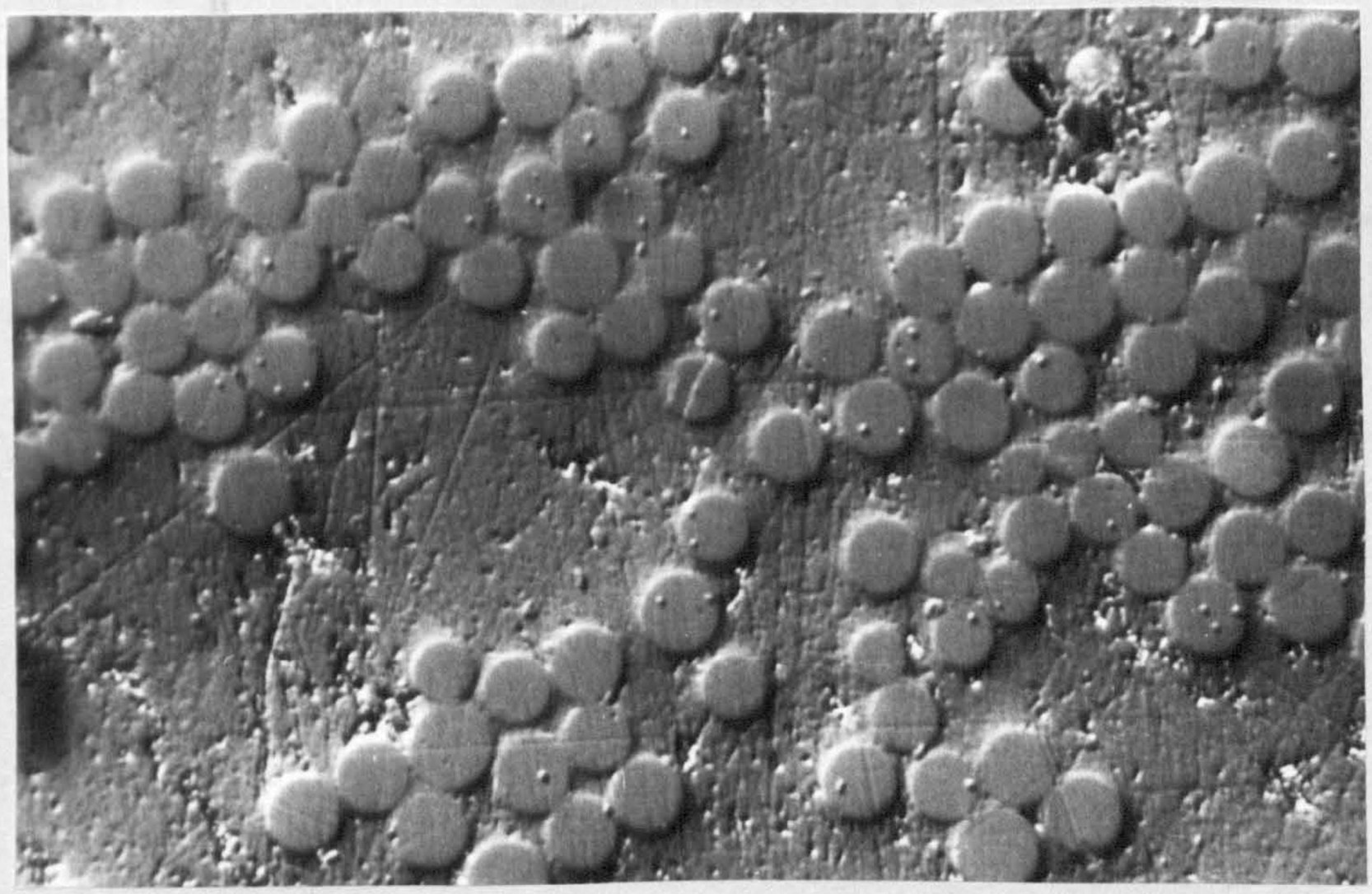

Figure 5.2 Measurement of an Idealised Pattern

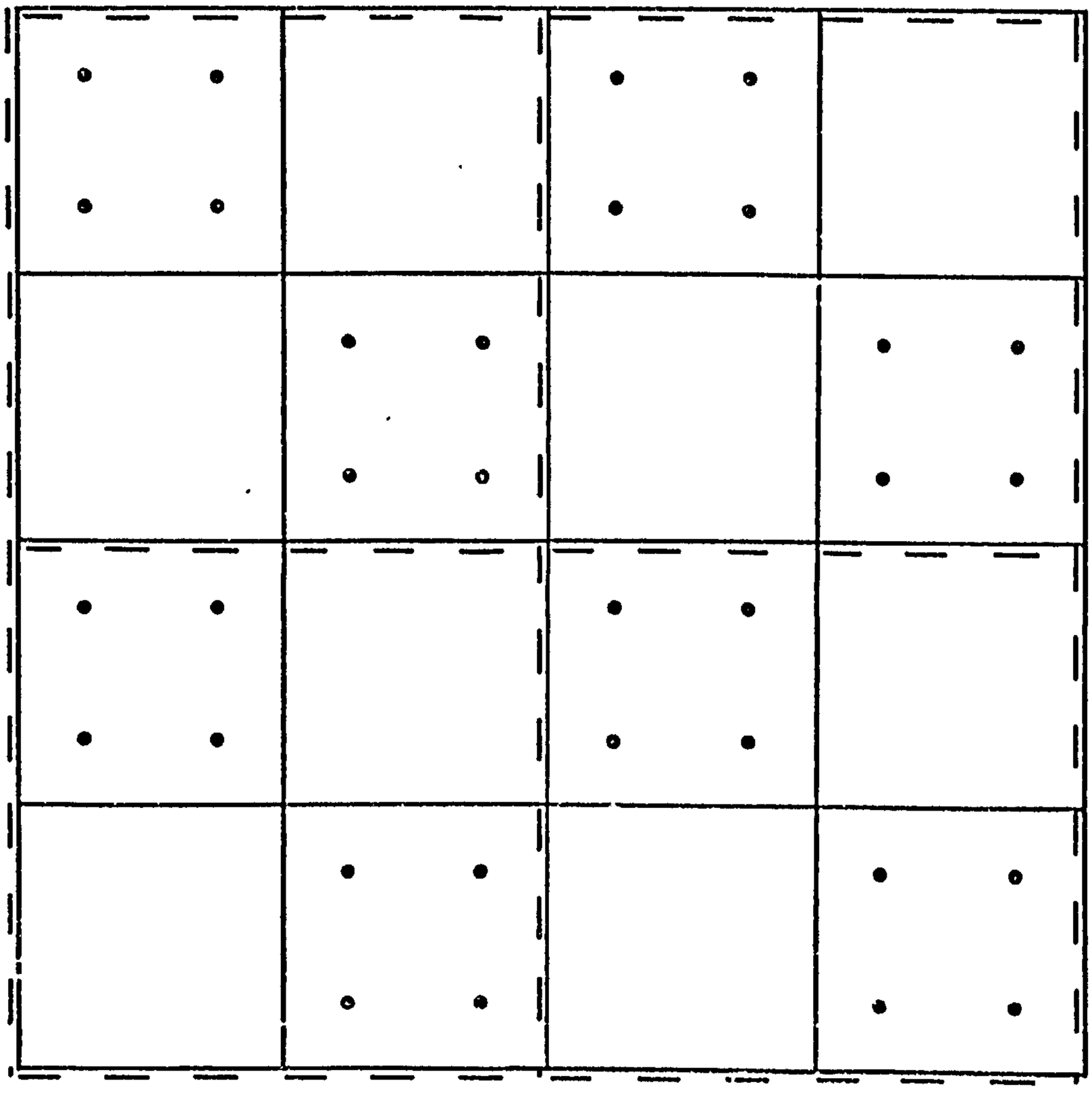

Figure 5.3 Alternative Cell Shapes

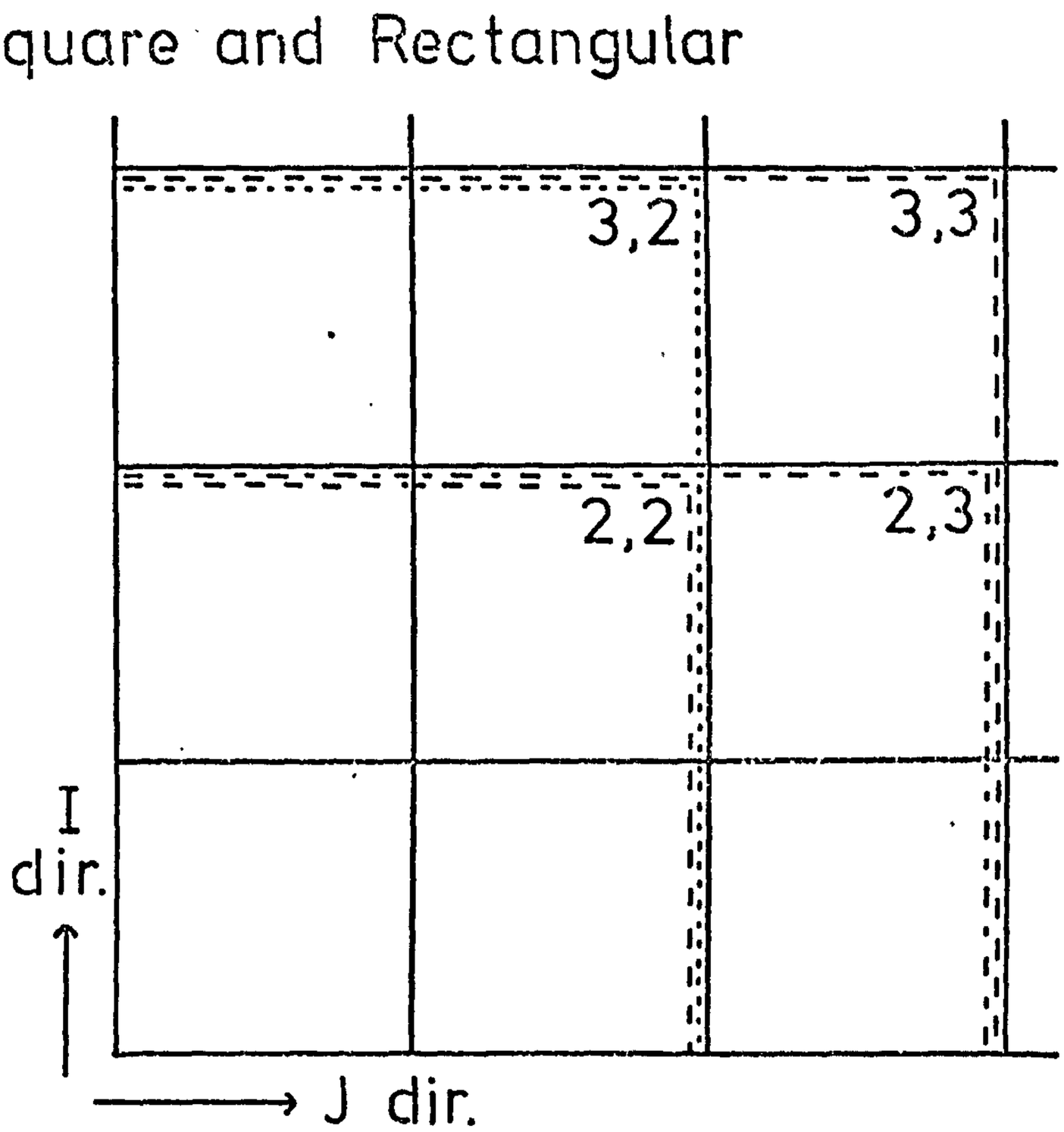

Figure 5.4 Alternative Cell Arrangements

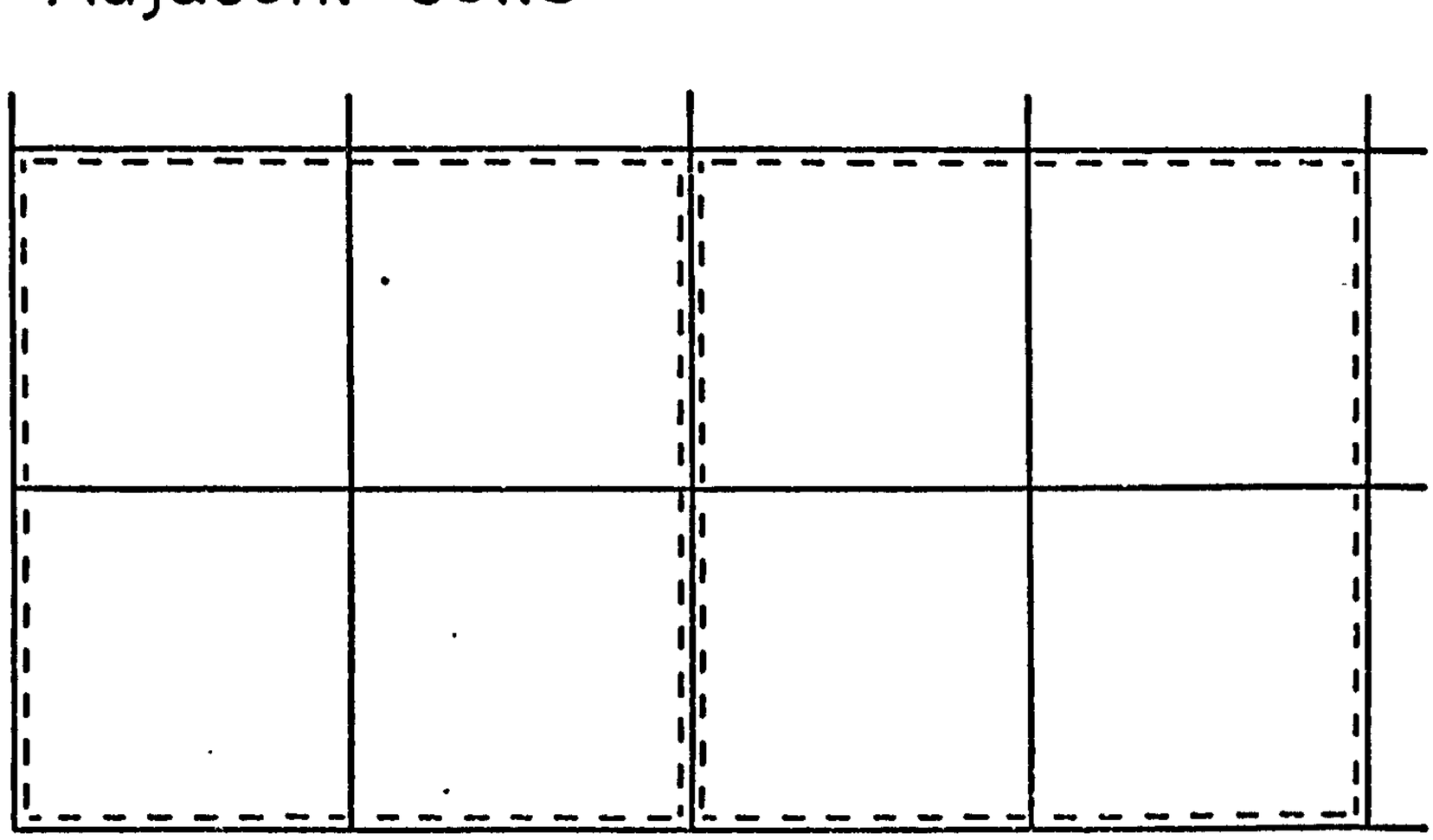

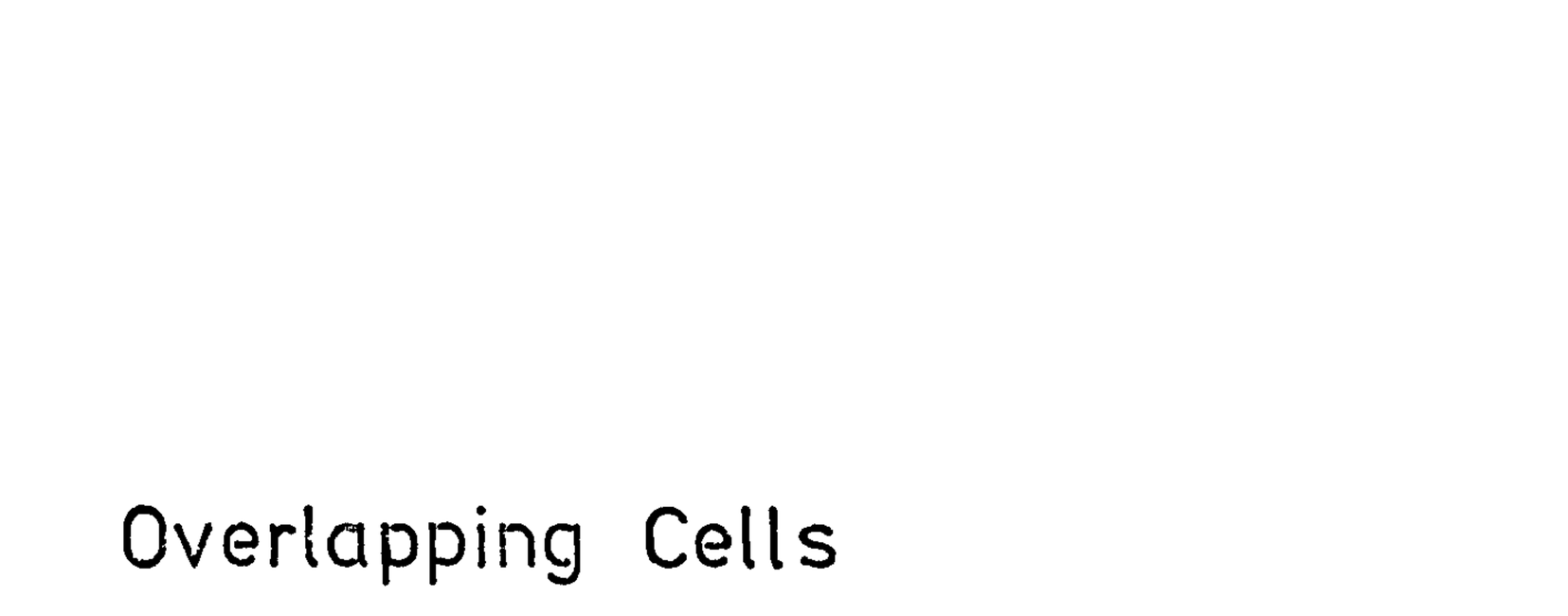

Figure 5.5 Variance (fractional area covered) for Adjacent Cells

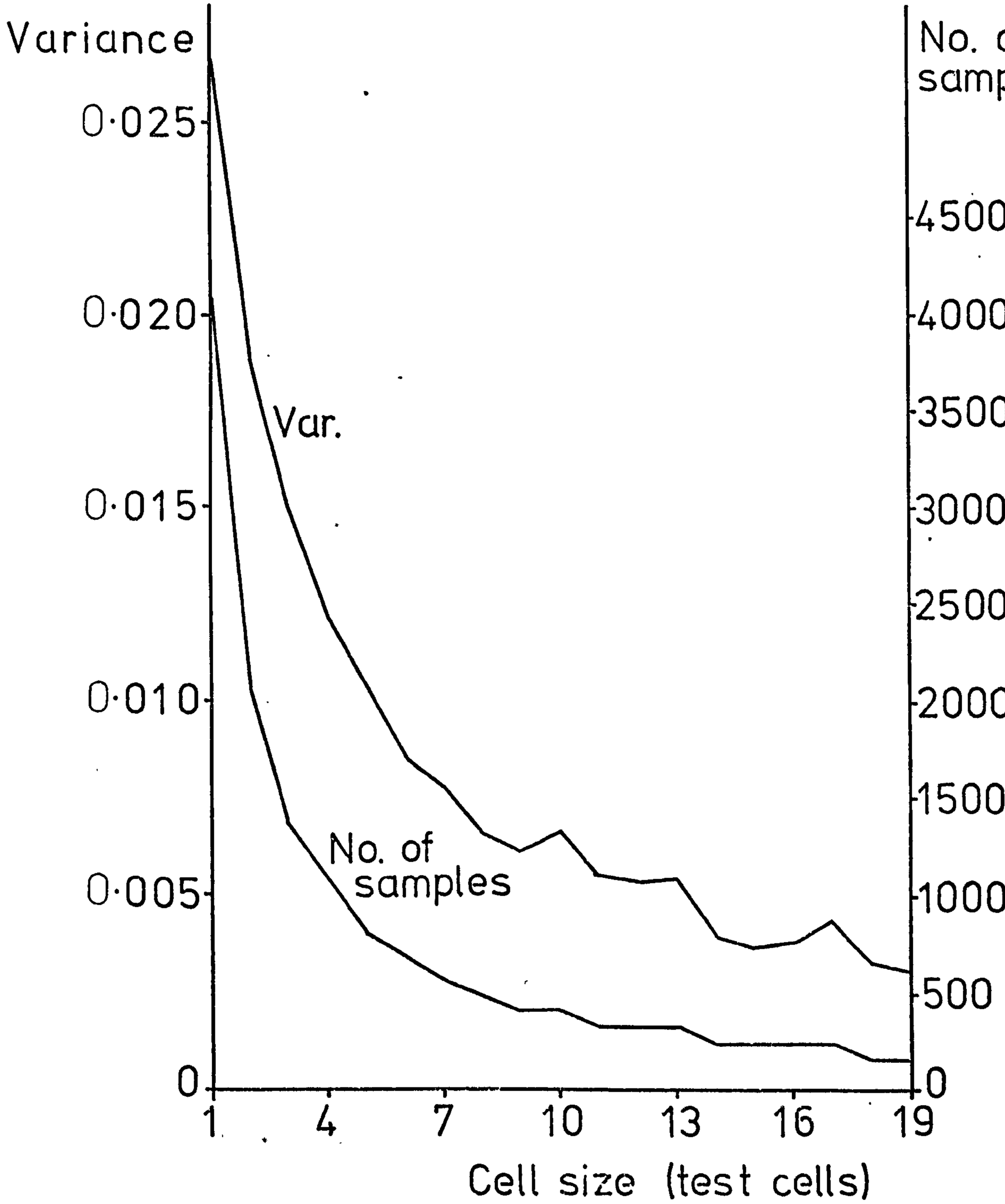

Figure 5.6 Variance (fractional area covered) for Overlapping Cells

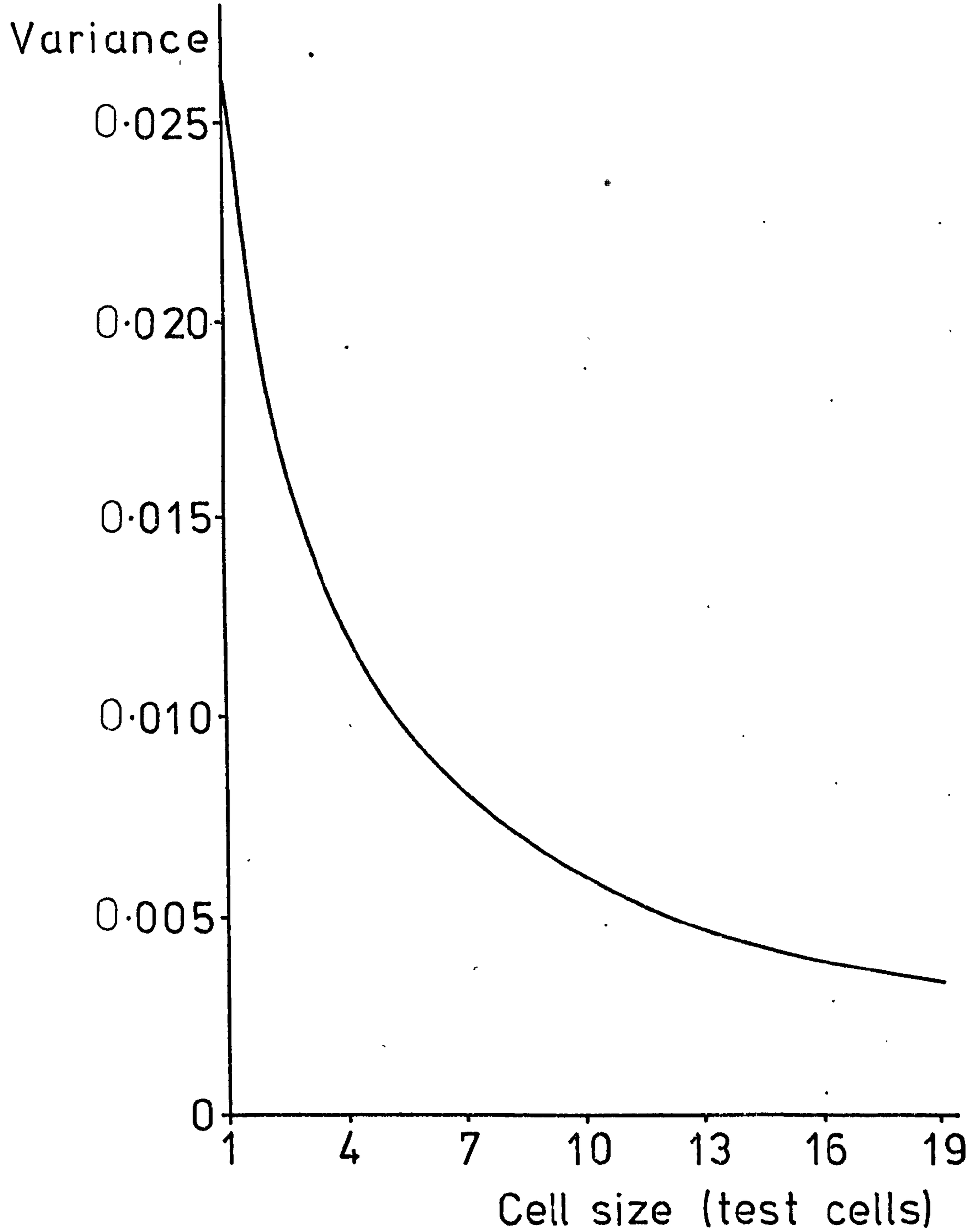

Figure 5.7 Contour Map of Variance (fractional area covered)

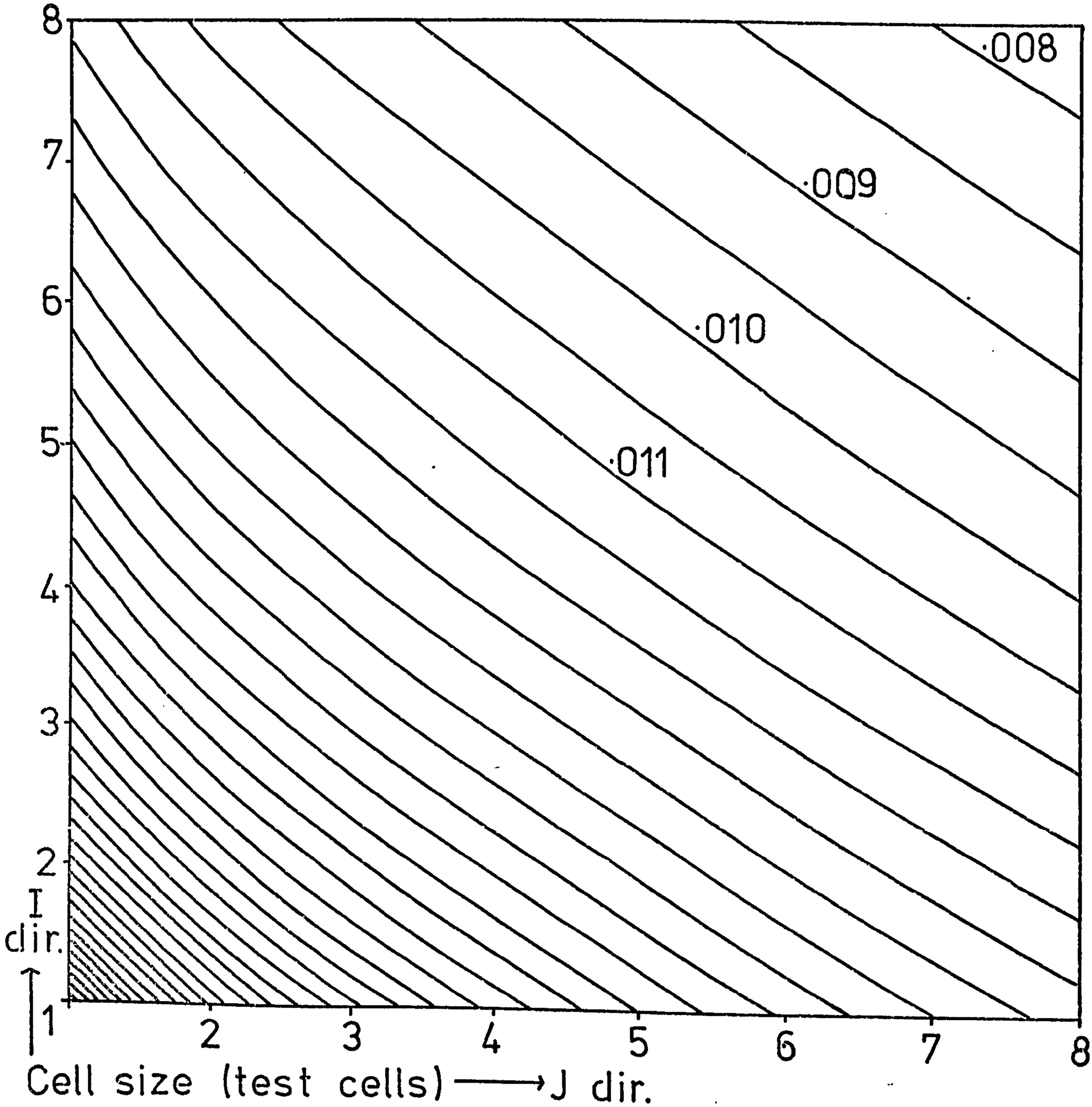

Figure 5.8 Comparison of Theoretical and Experimental Variances (fractional area covered)

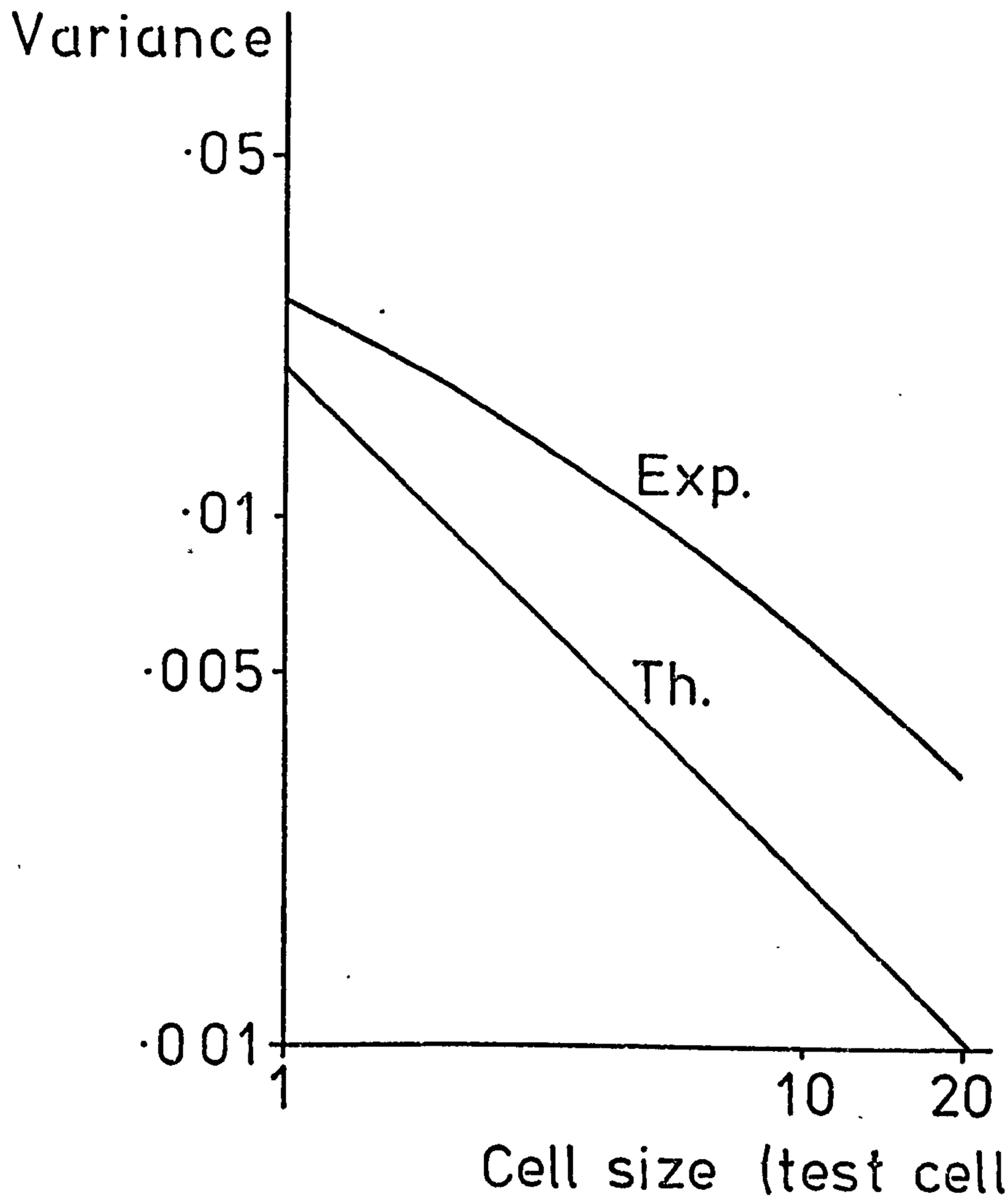

Figure 5.9 Comparison of C_1 and C_2 Ratios

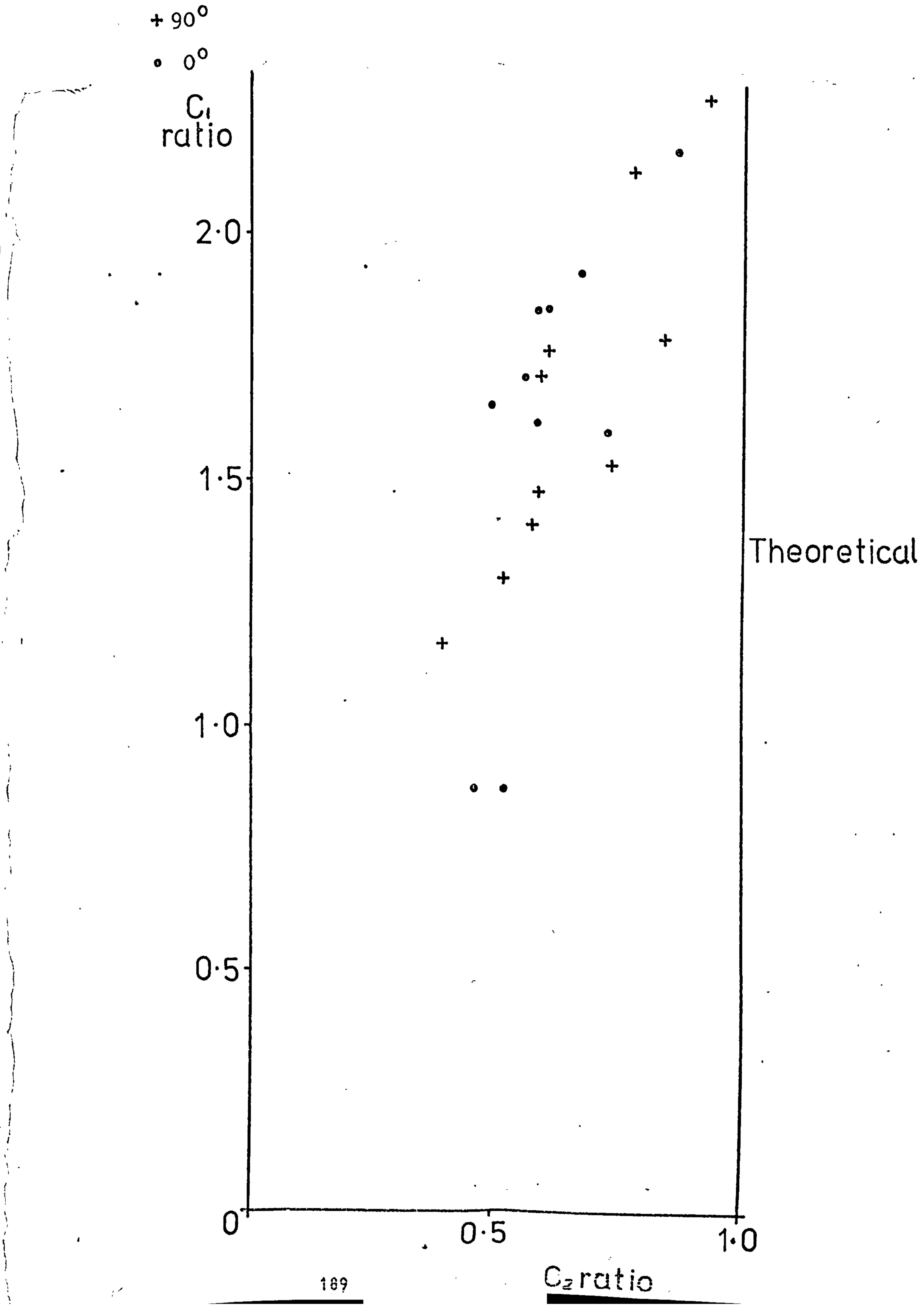

Figure 5.10 Contour Map of Probability (cell is empty)

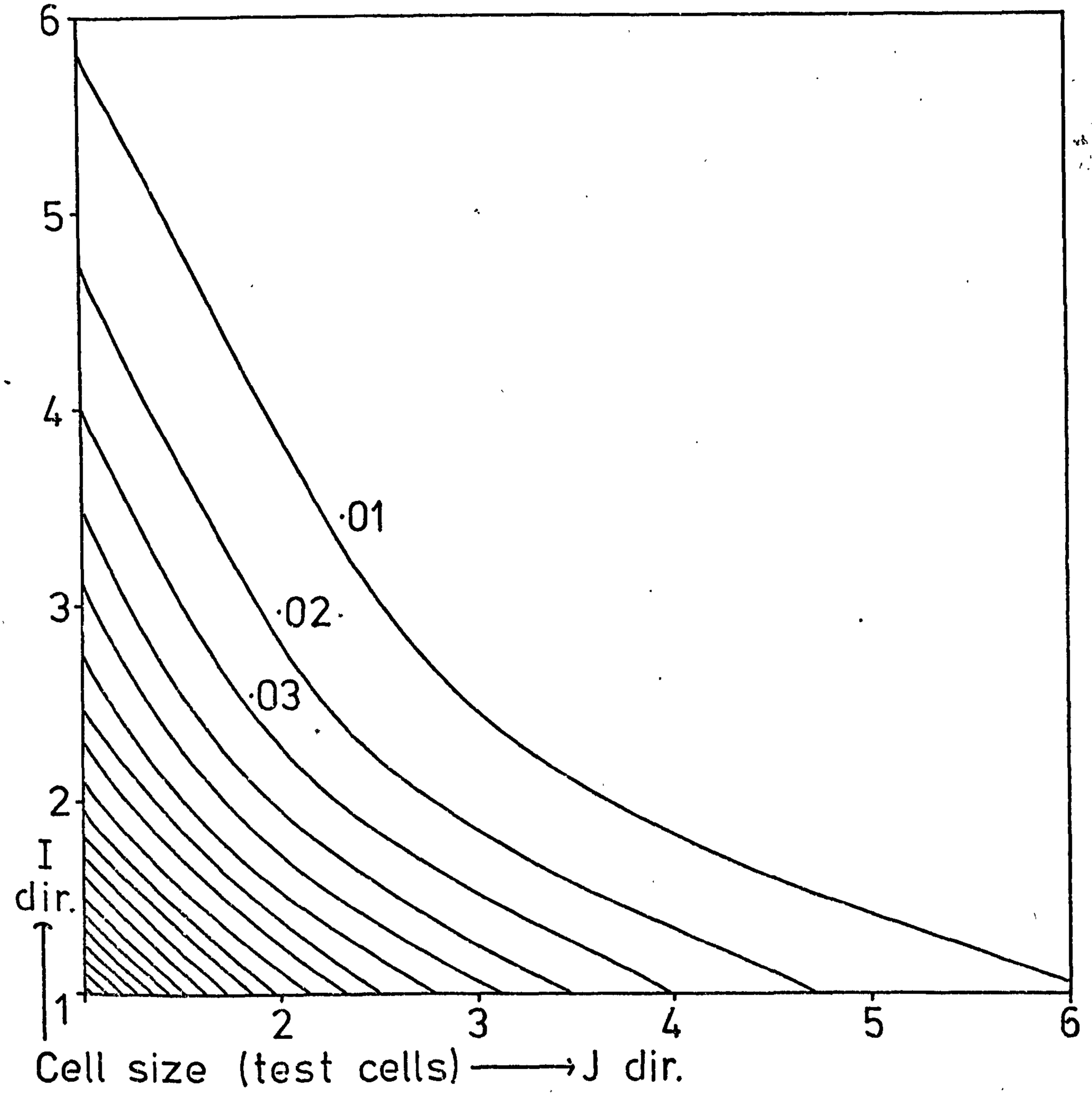

Figure 5.11 Comparison of Theoretical and Experimental Probabilities (cell is empty)

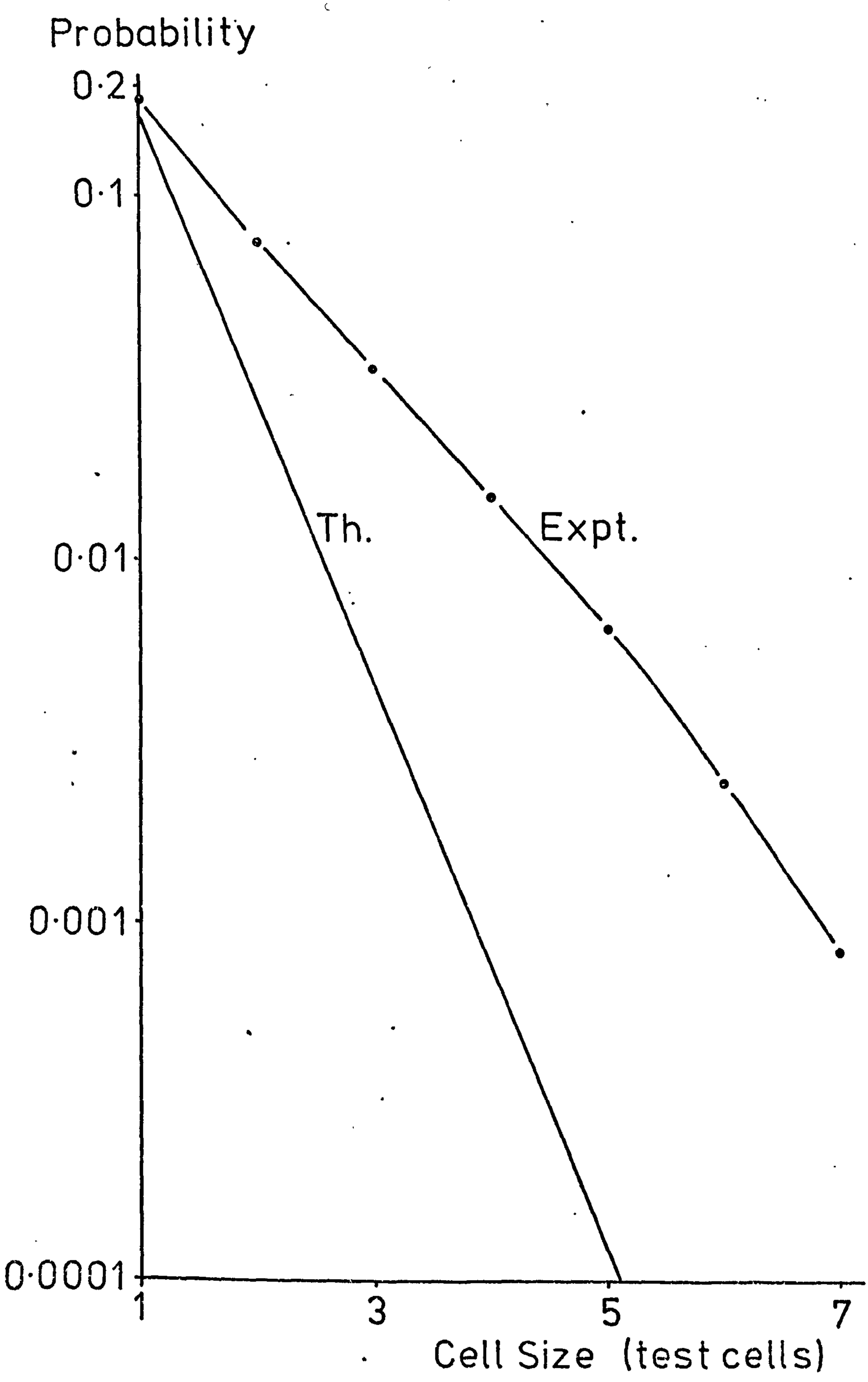

Figure 5.12 Comparison of C_3 and C_4 Ratios

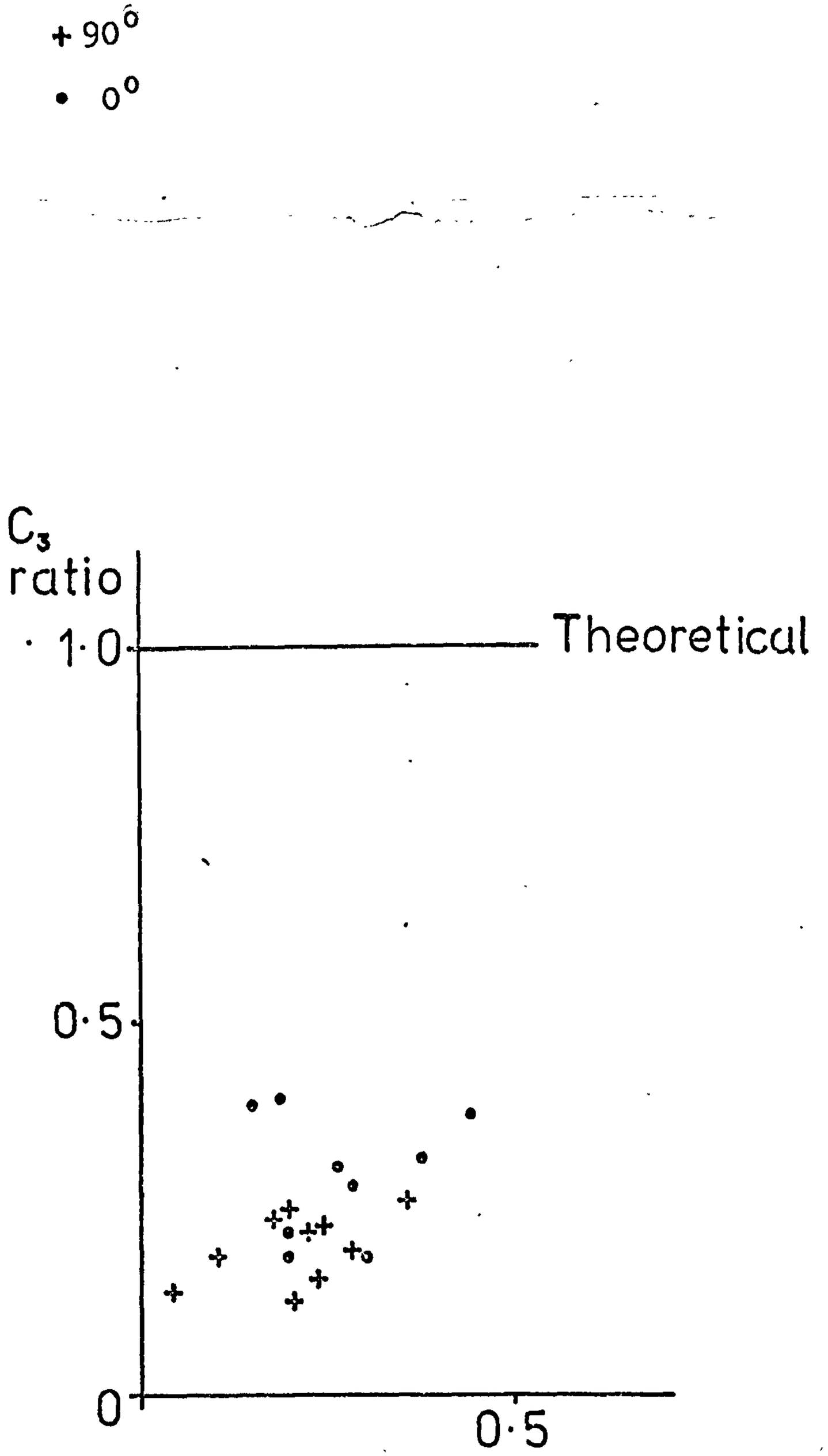

Figure 5.13 Comparison of C_1, C_2 and C_3 Ratios

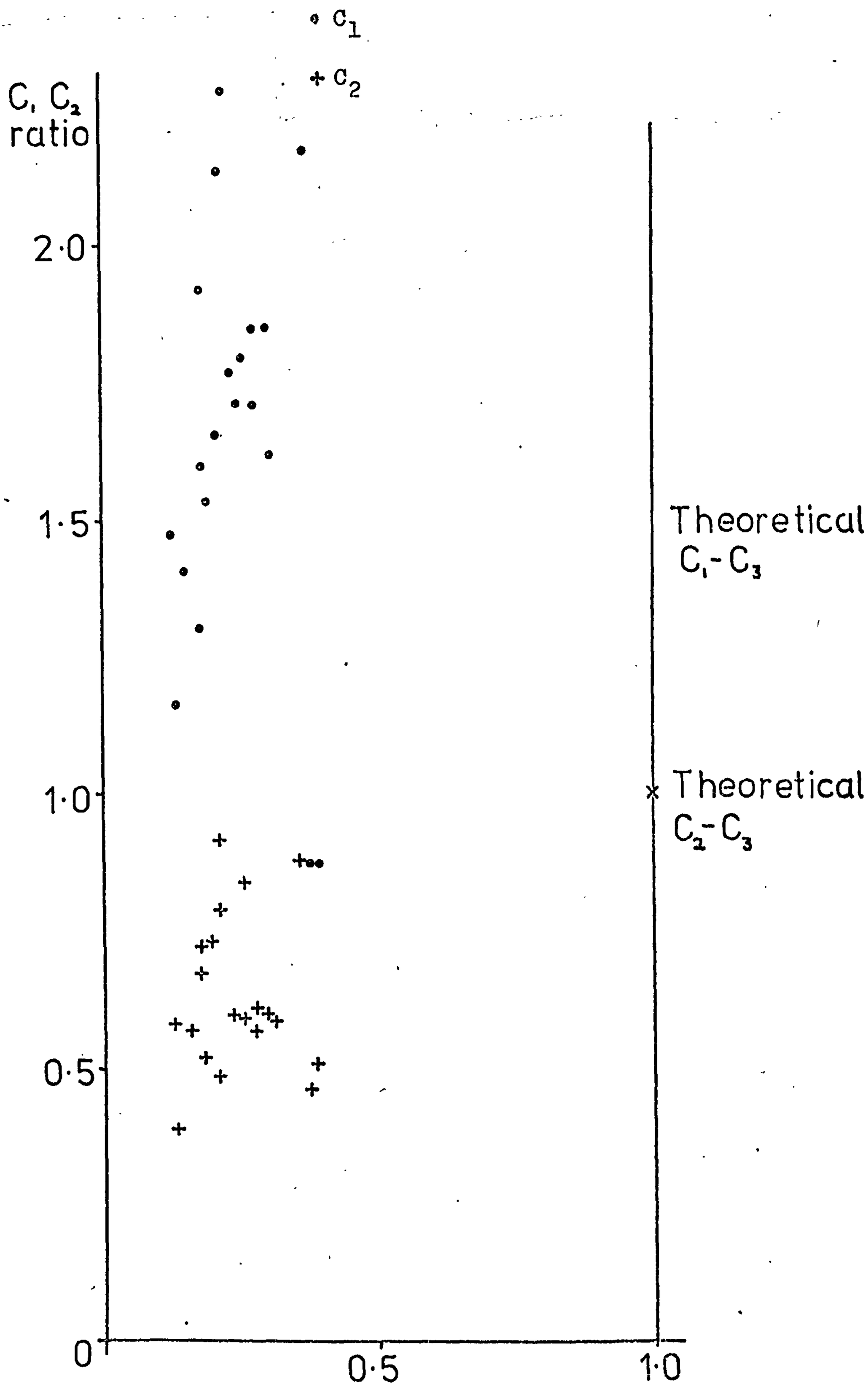

Figure 5.14 Comparison of C_1, C_2 and C_4 Ratios

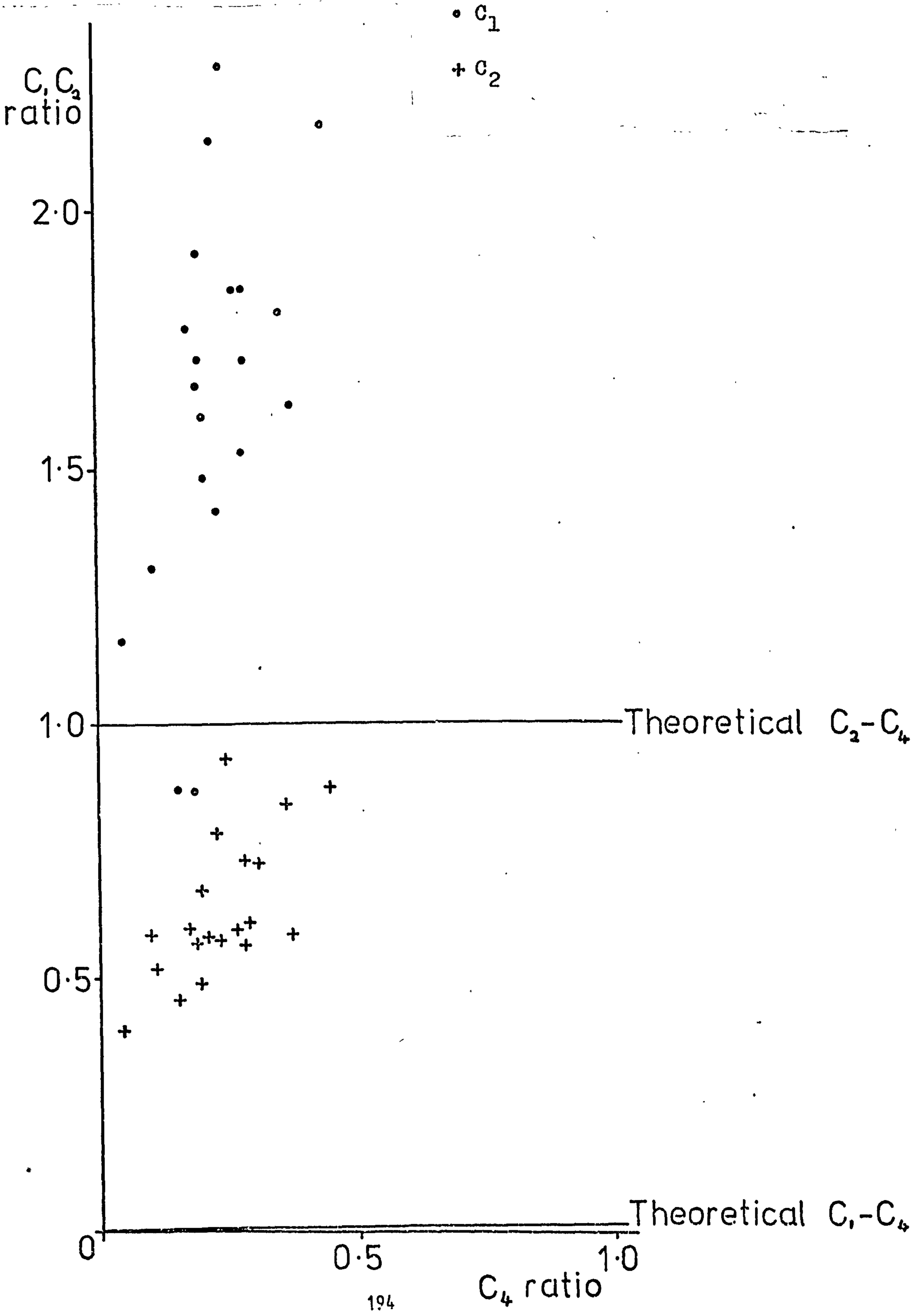

Figure 5.15 Comparison of C_1 and C_4 Values

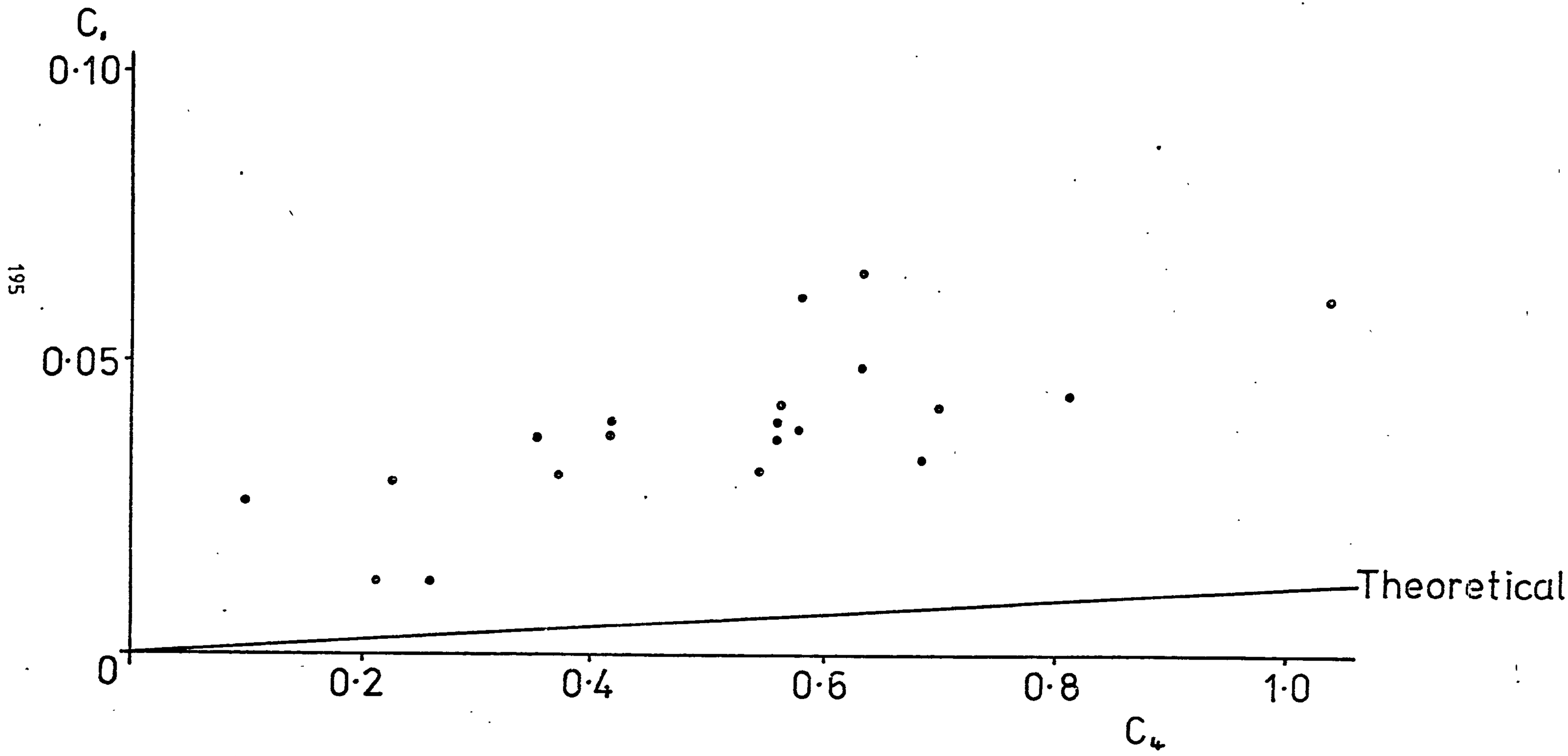

Figure 5.16 Percentage Deviations of Means from Table 5.4

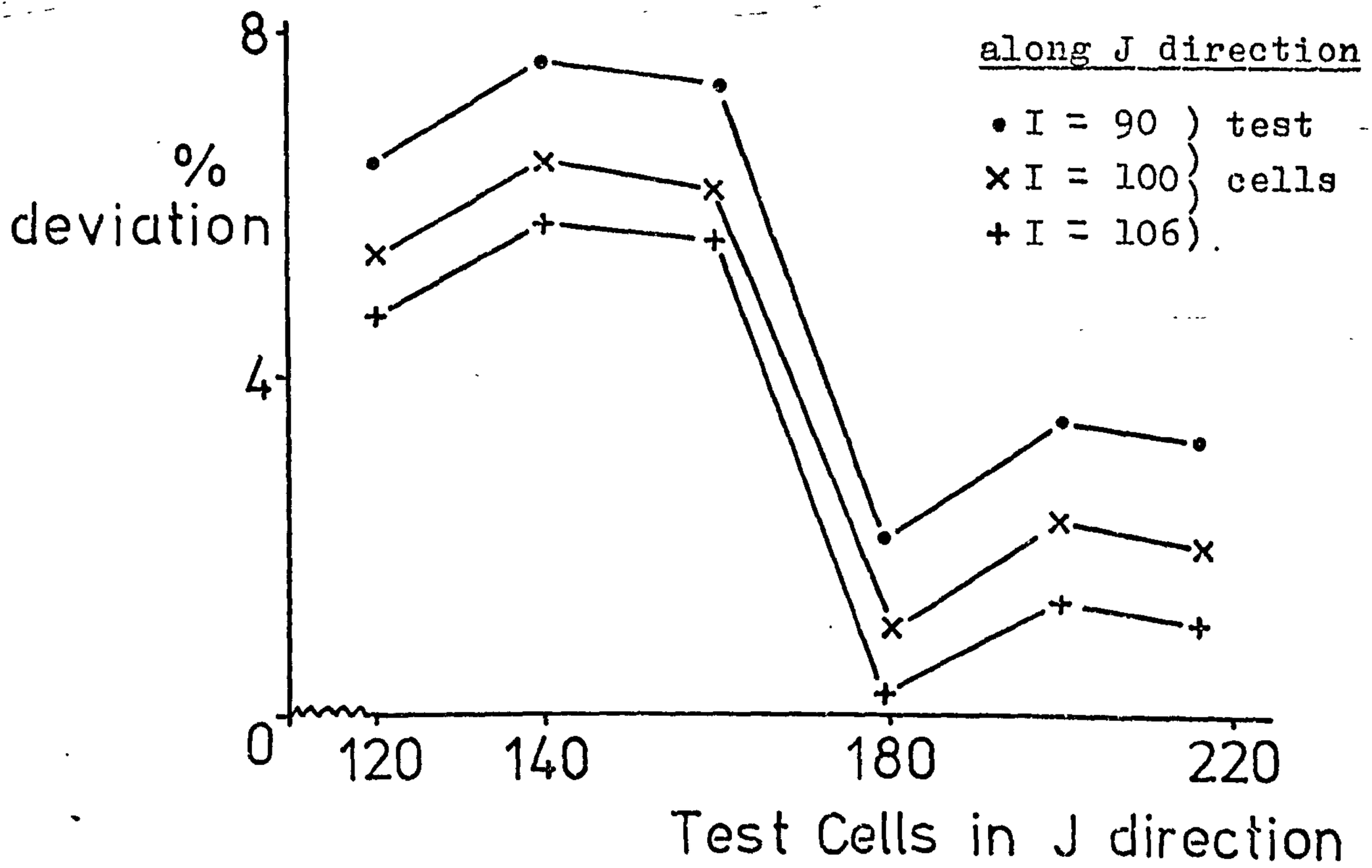

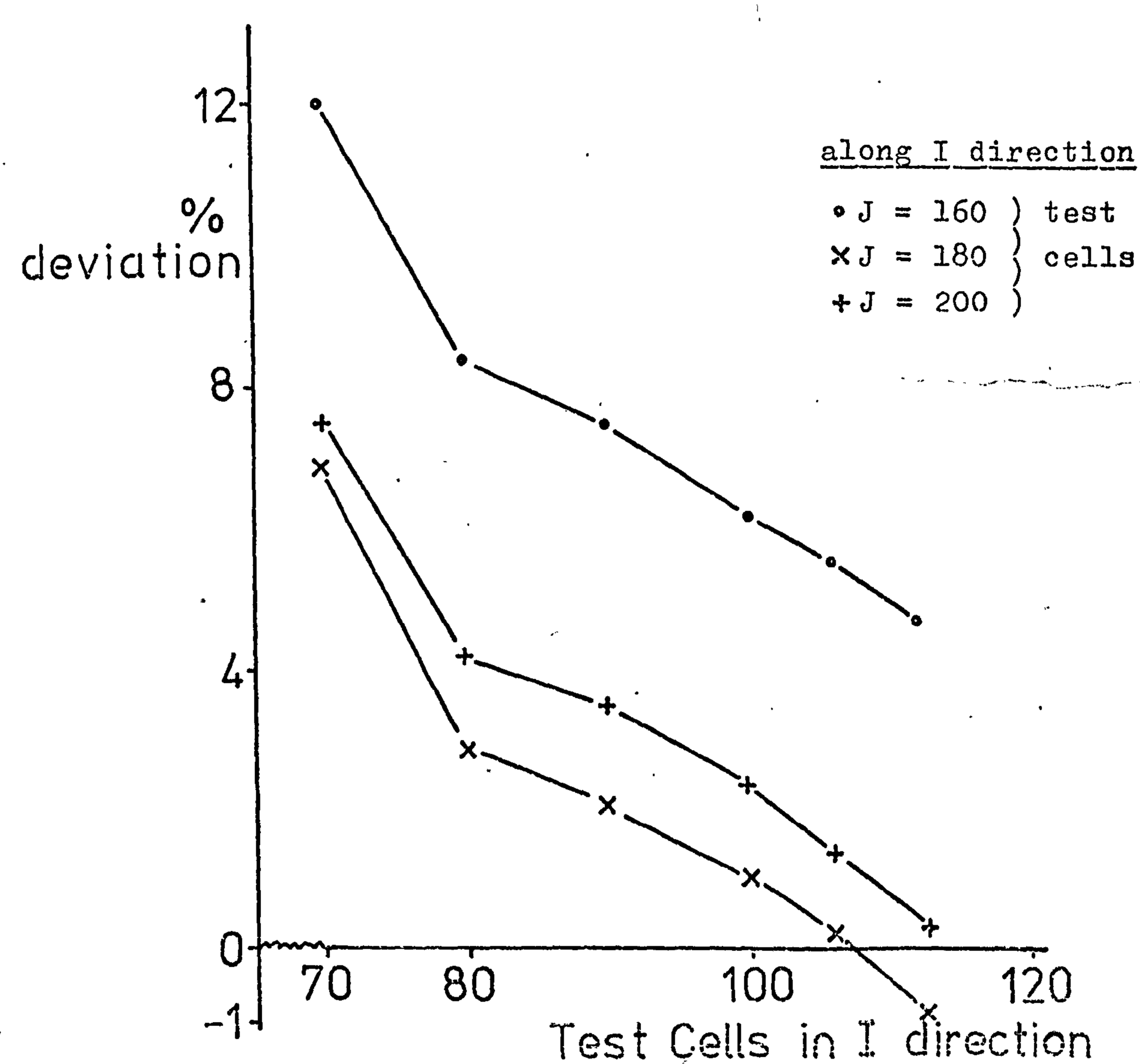

Figure 5.17 Percentage Deviations of Variances from

Table 5.4

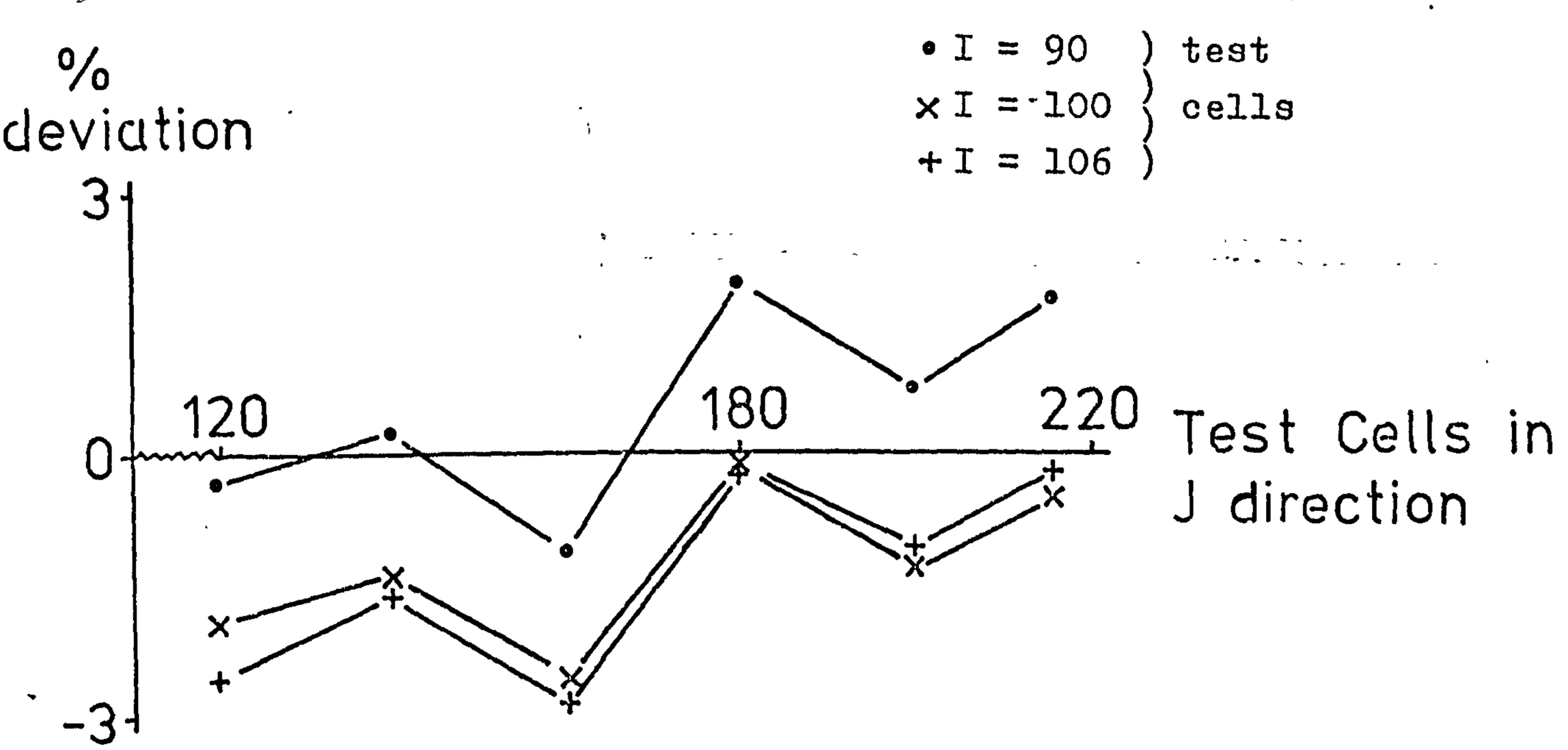

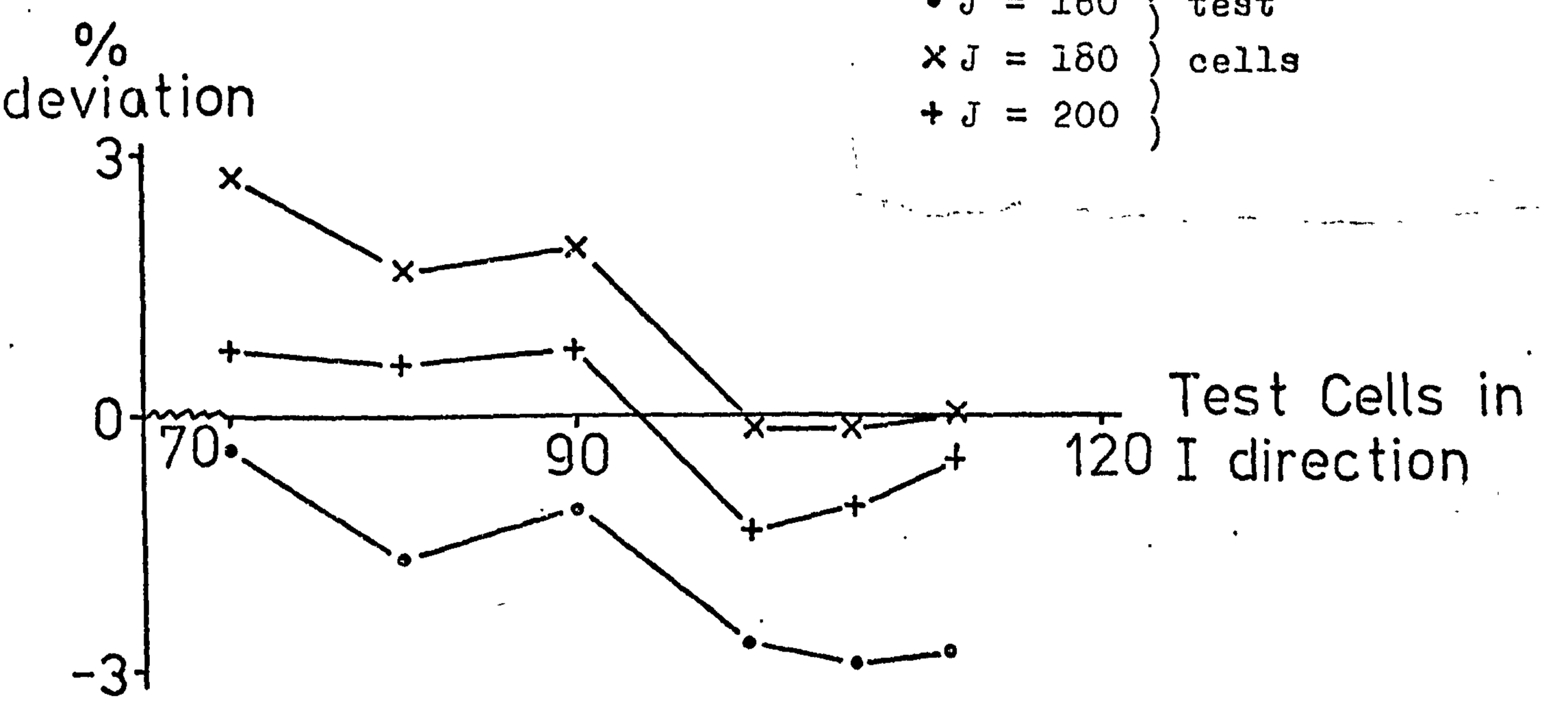

Figure 6.1 Four-Point Bend Test Arrangement

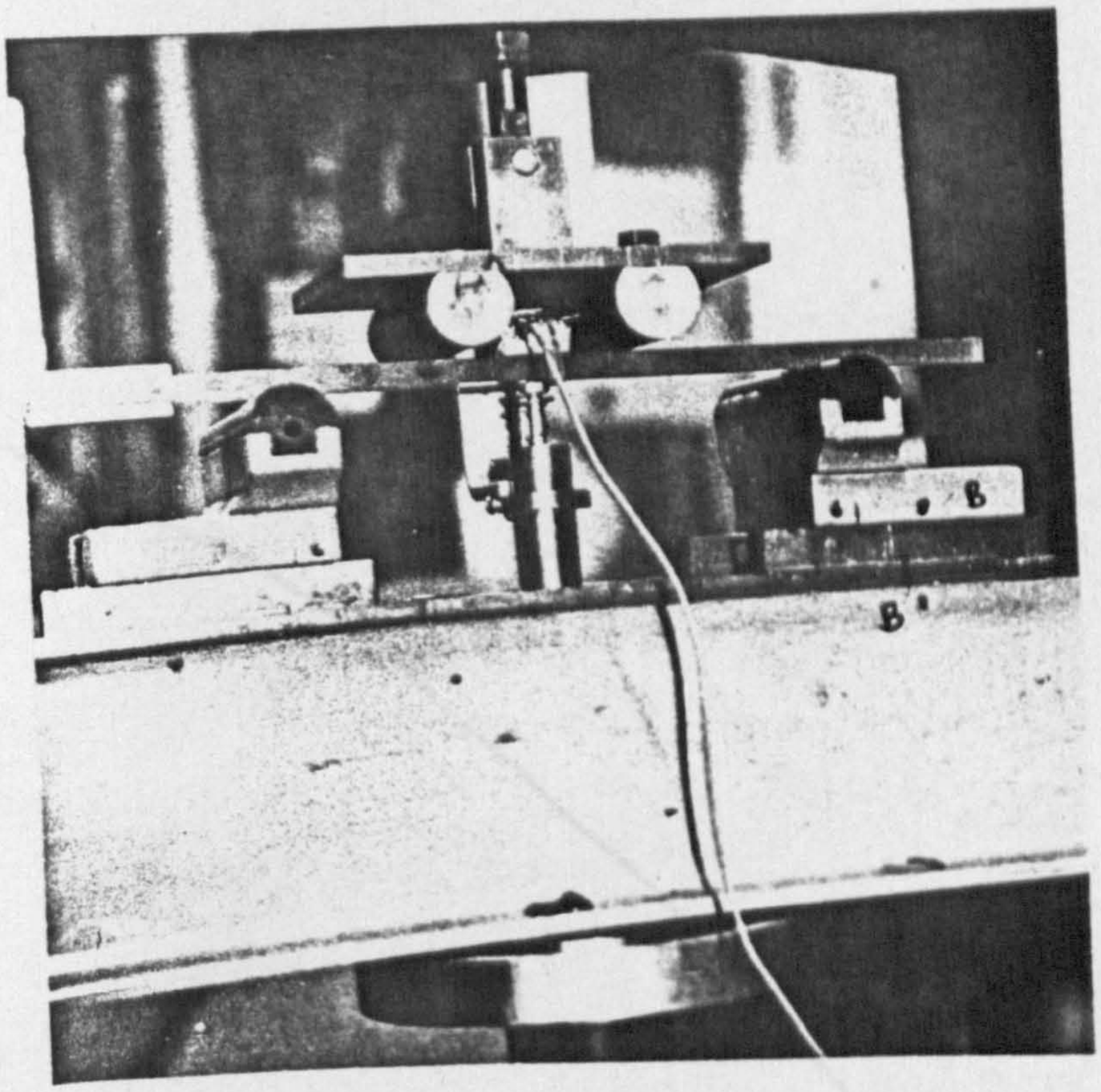

Figure 6.2 Four-Point Bend Test of Resin

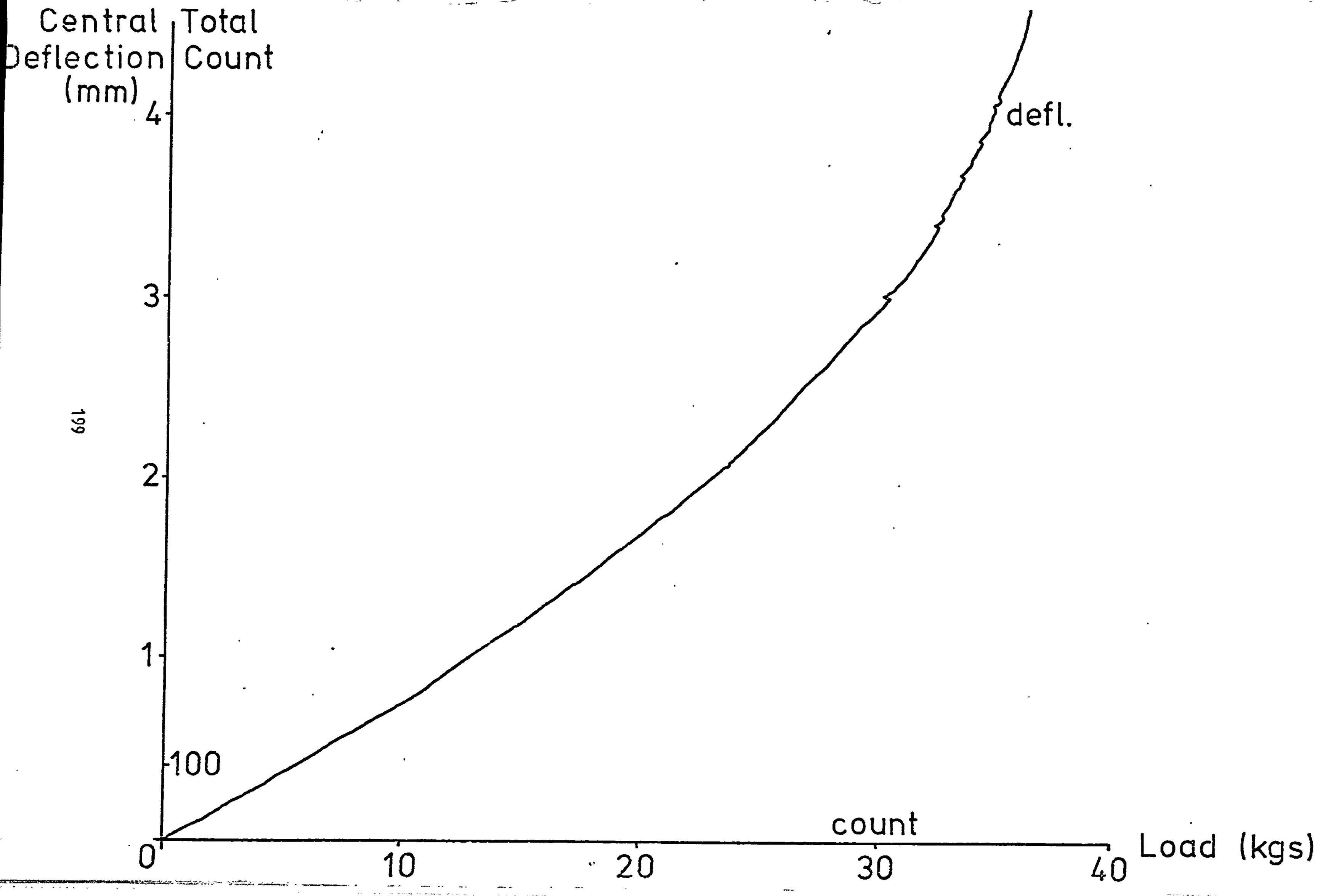

Figure 6.3 Load to Failure of a 0^{o} Beam

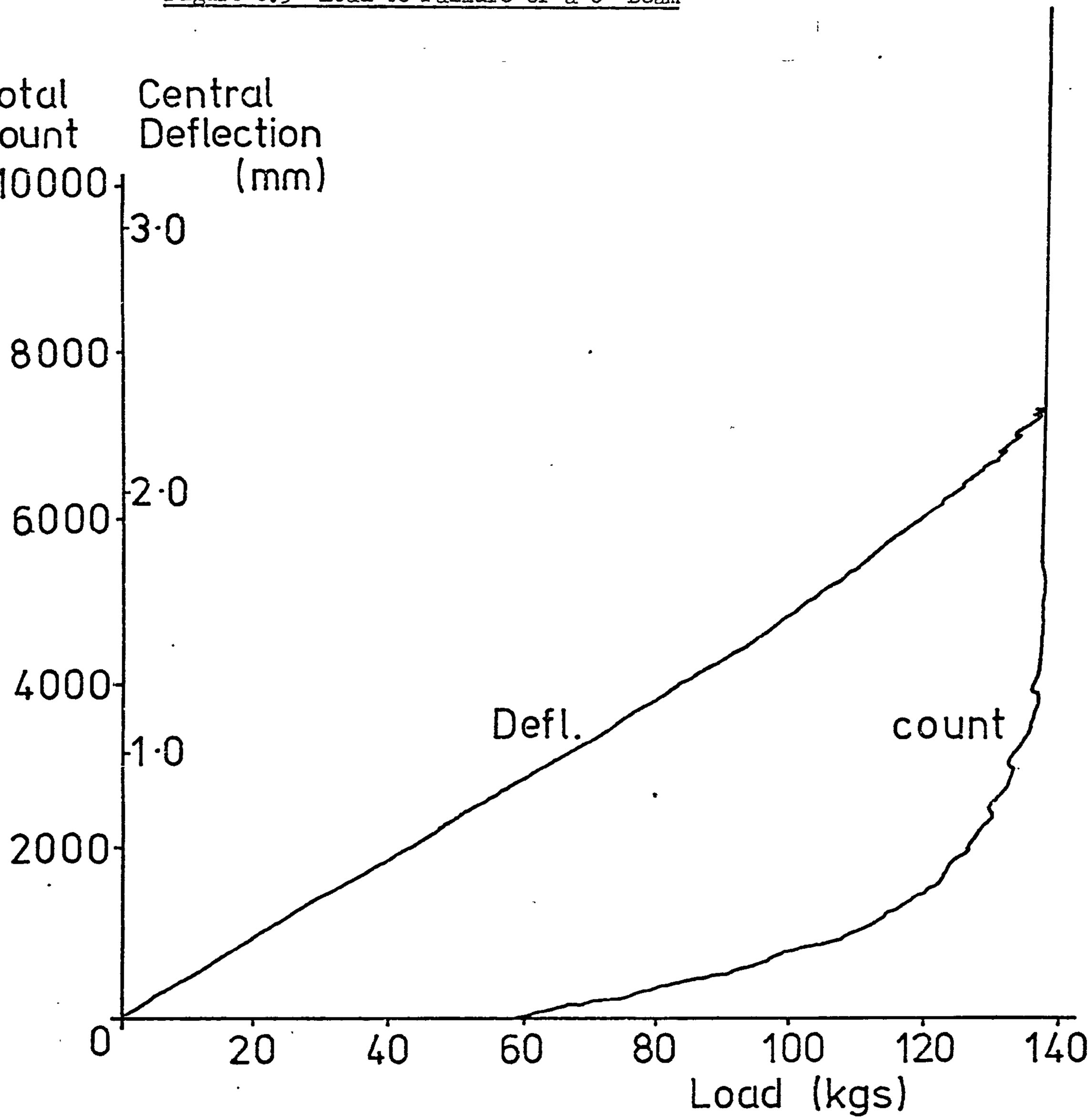

Figure 6.4 Repeated Tests on a 0° Beam; few counts in test 1

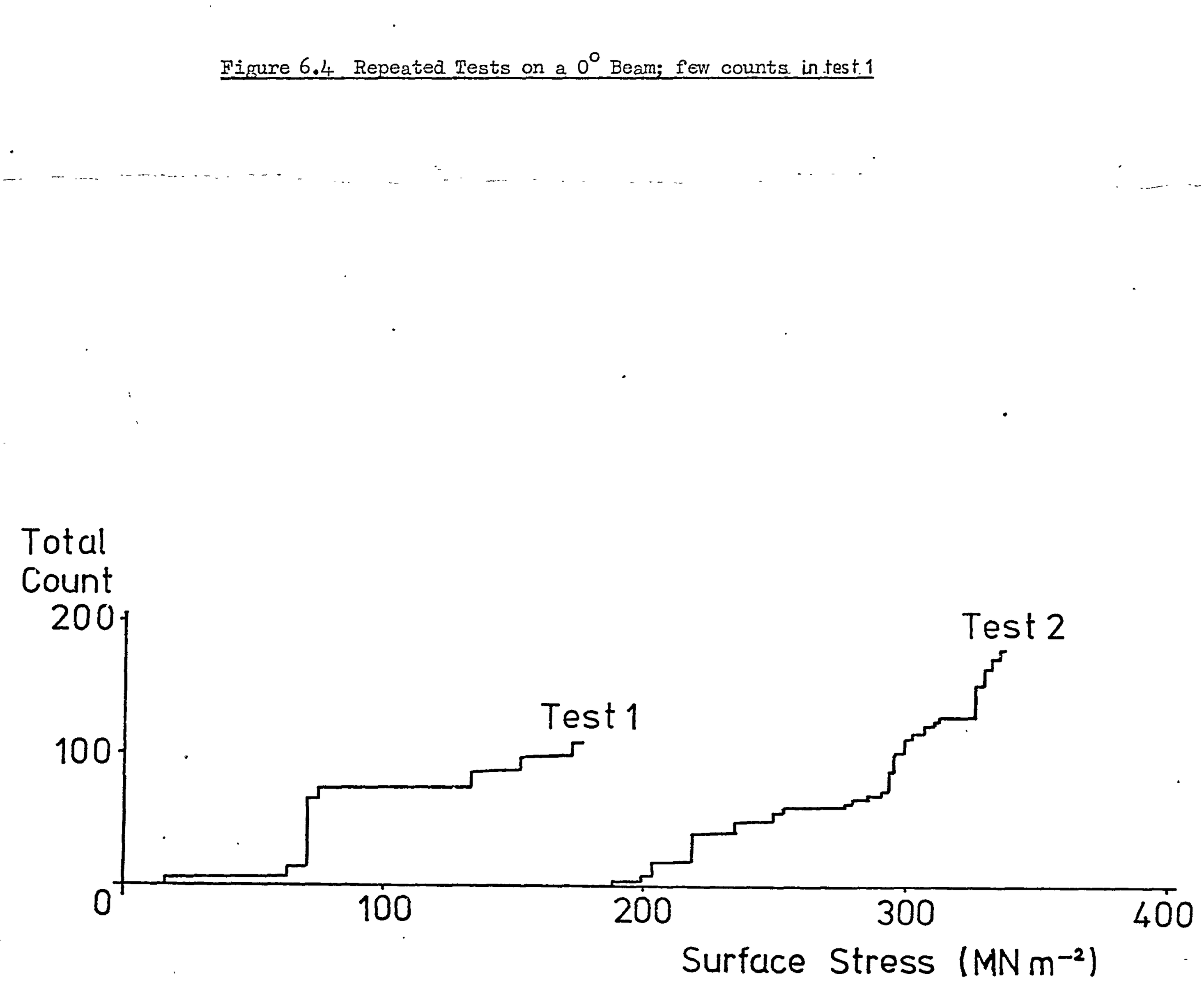

Figure 6.5 Repeated Tests on a 0° Beam; more counts in test 1.

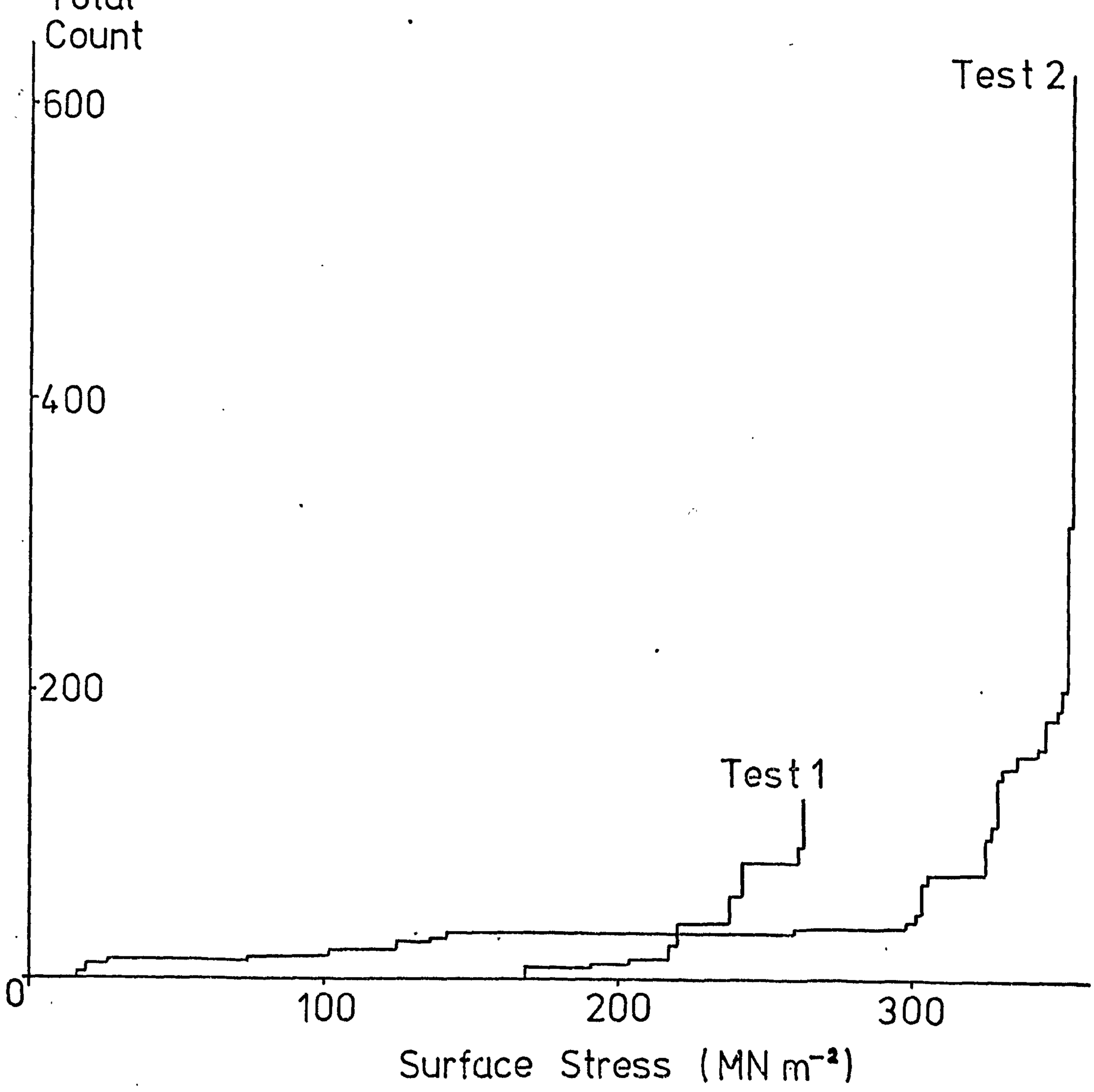

Figure 6.6 Results of Figure 6.5 with Total Count plotted Logarithmically

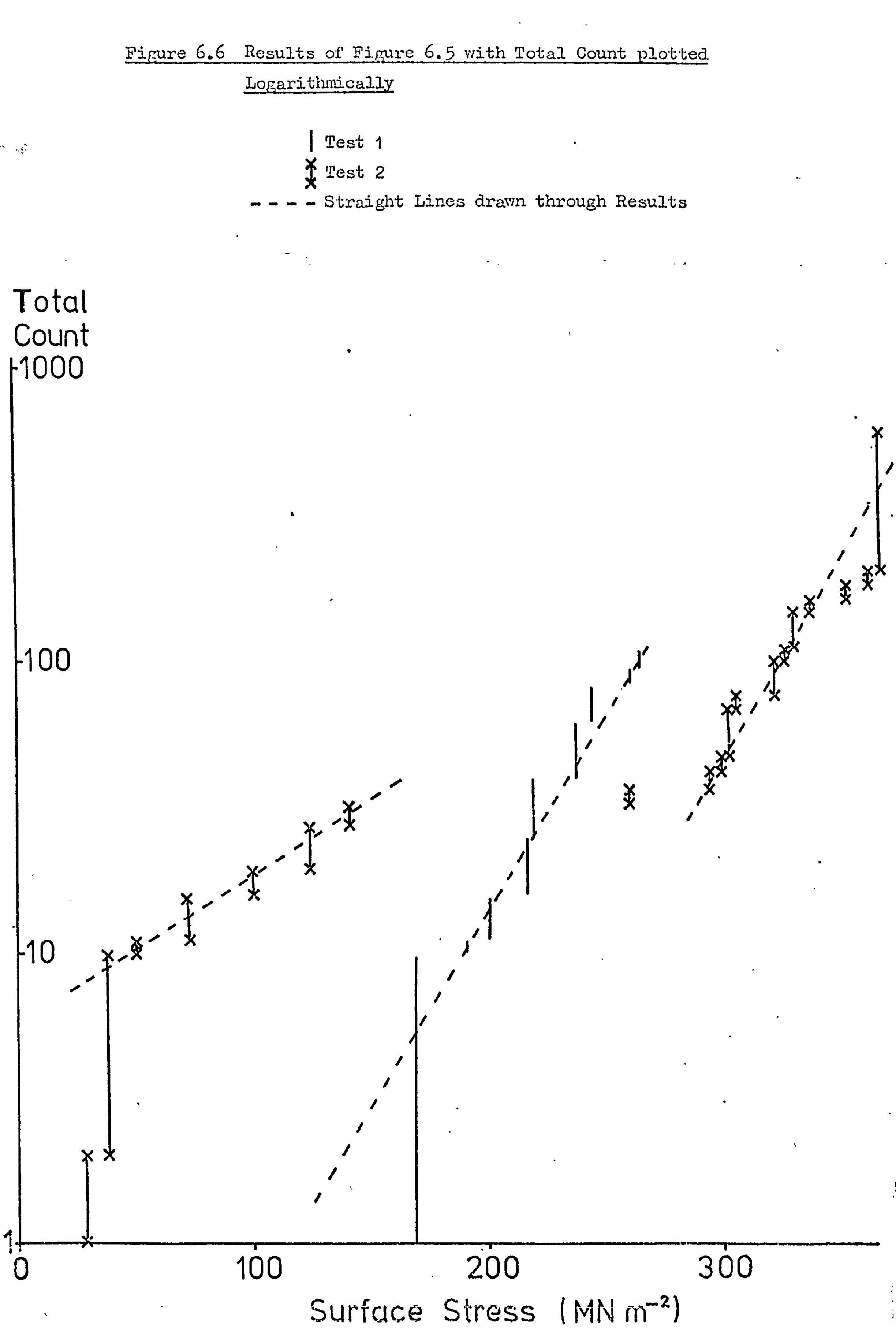

Figure 6.7 Load to Failure of a 90° Beam

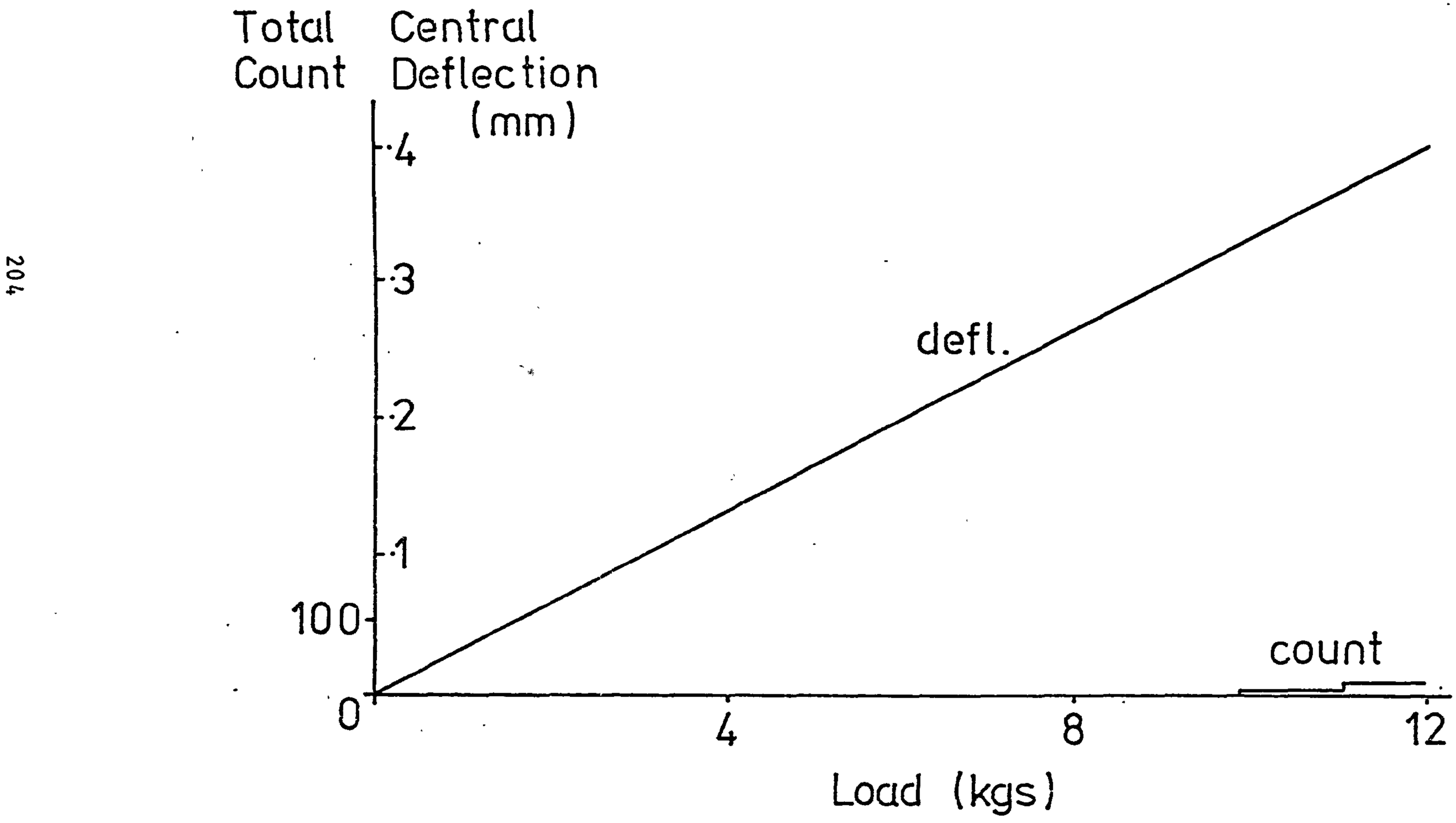

Figure 6.8 Re-loading of a Previously Failed 90° Beam

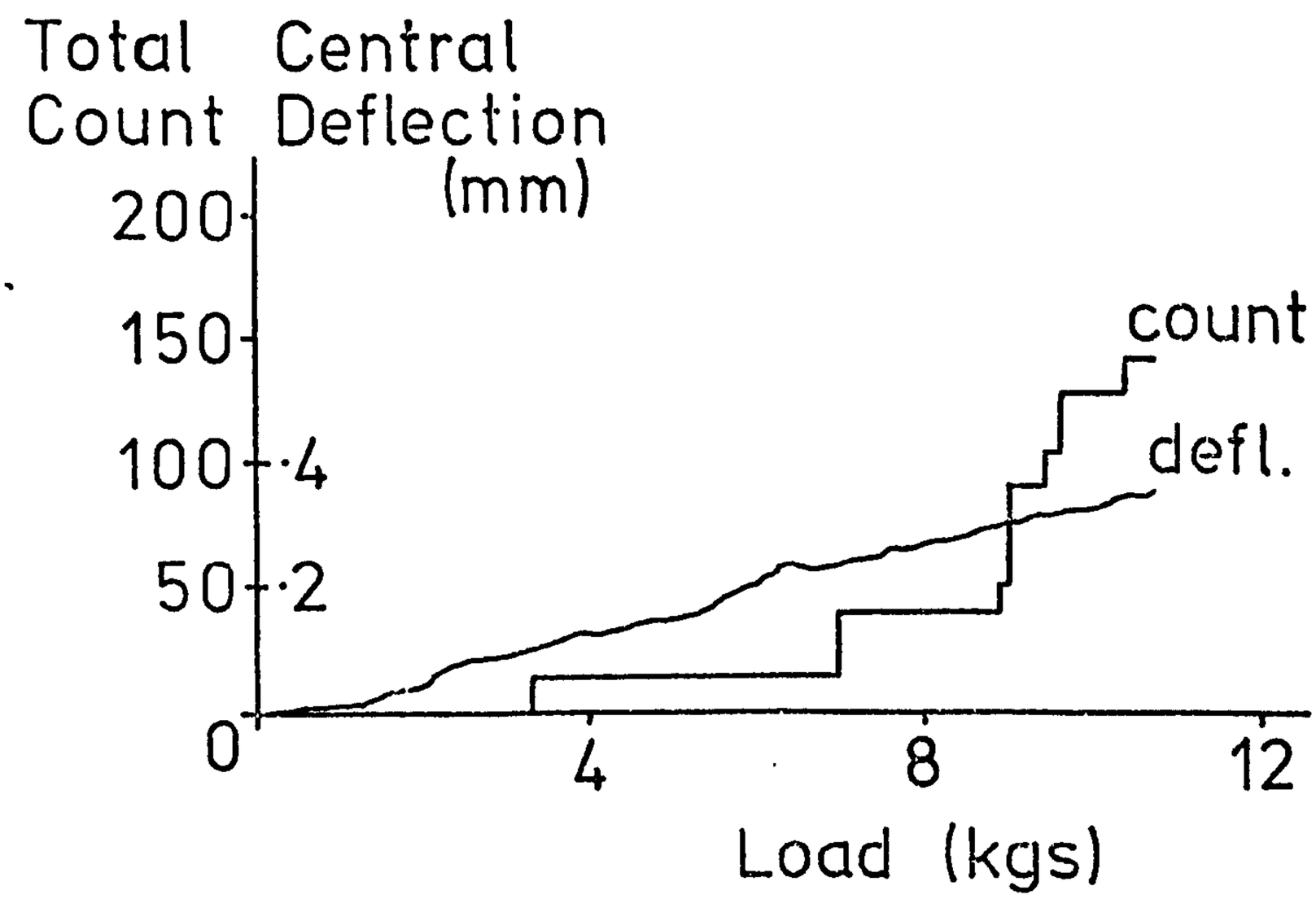

Figure 6.9 Crack Initiation in a 0° Beam

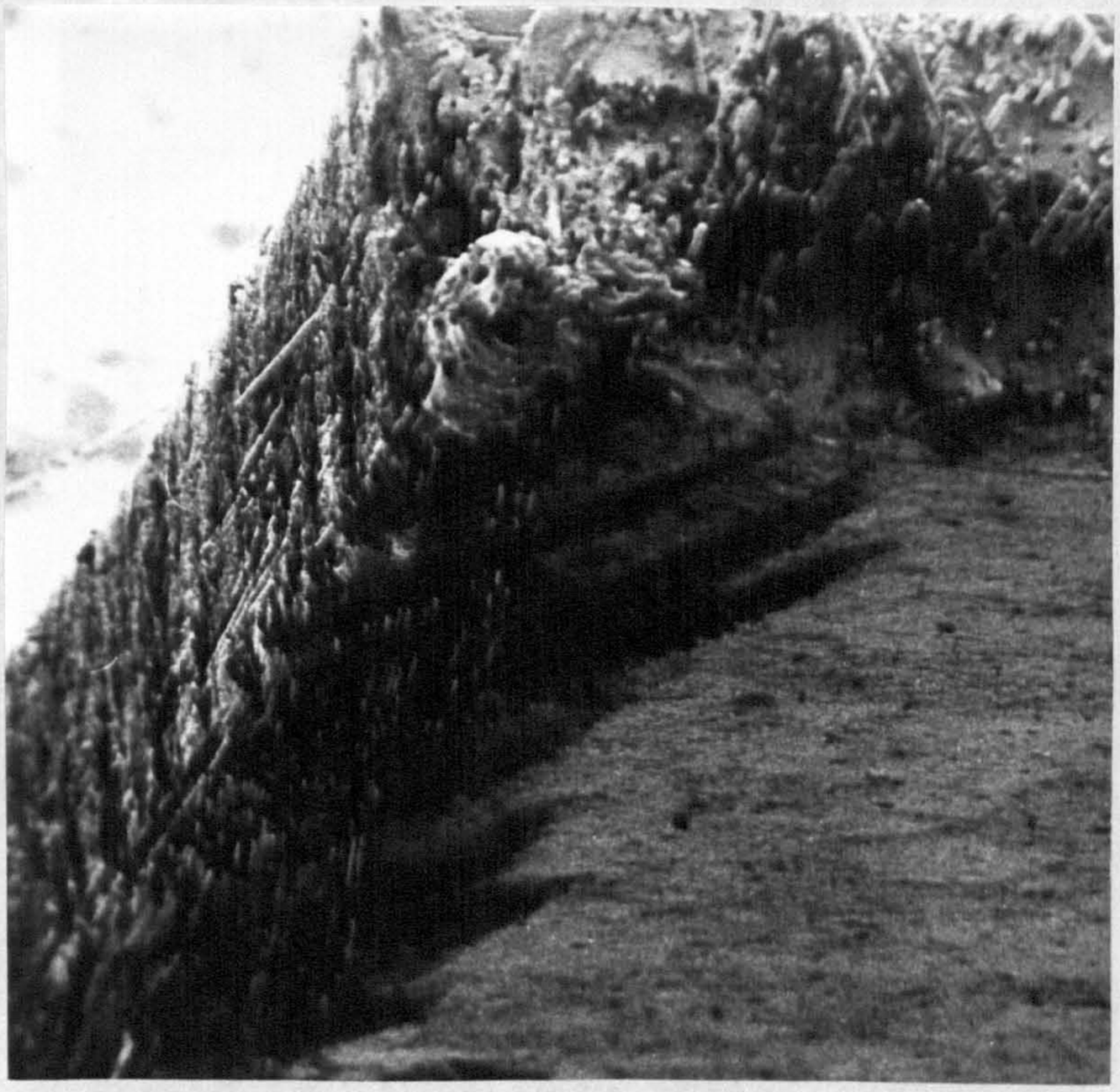

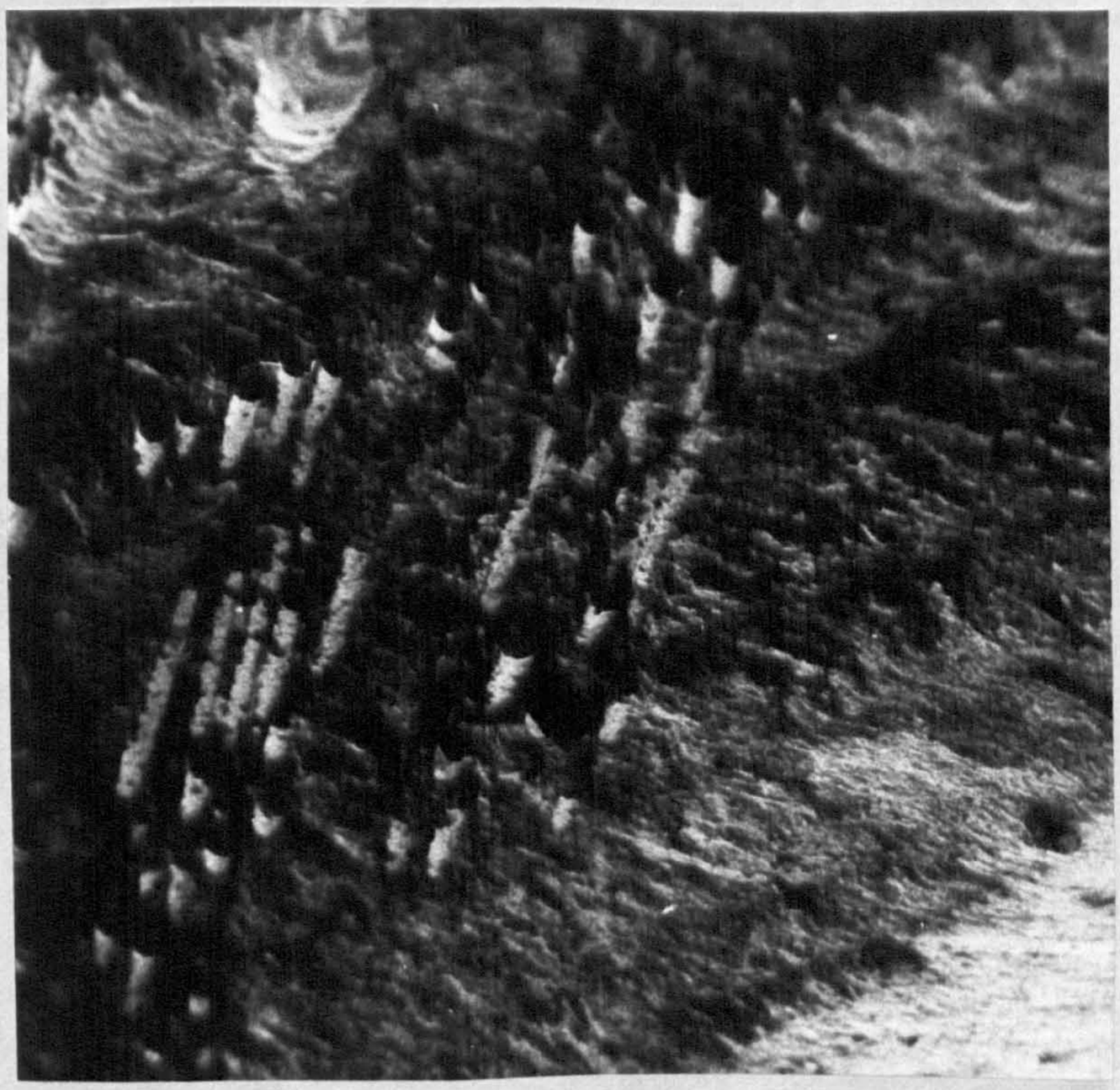

Figure 6.10 Fracture Surface of a 0° Beam

Figure 6.11 Step in Fracture Surface of a 0° Beam

Figure 6.12 'River Lines' in Resin Fracture Surface of a 0° Beam

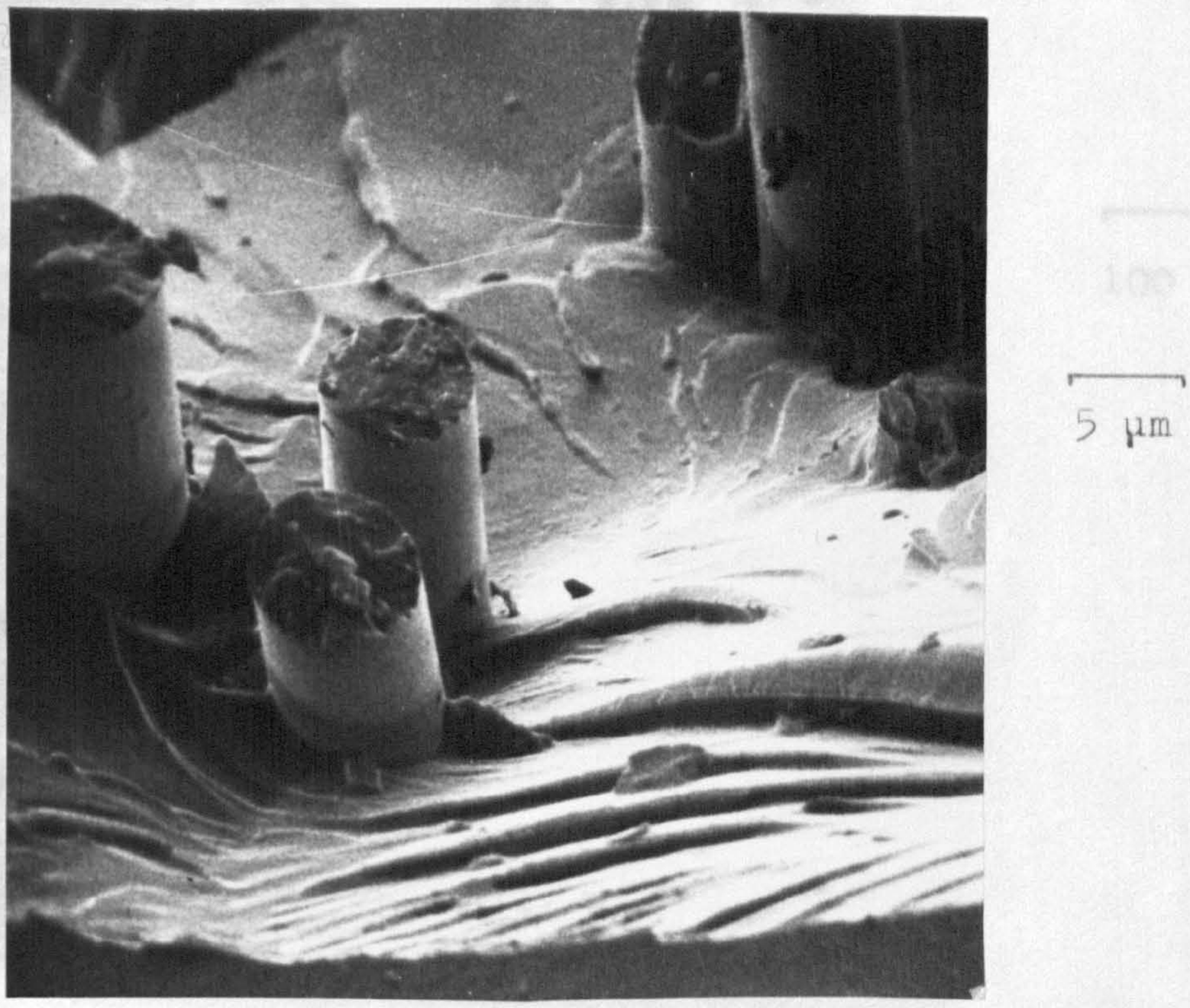

Figure 6.13 Fibre Fracture Surface

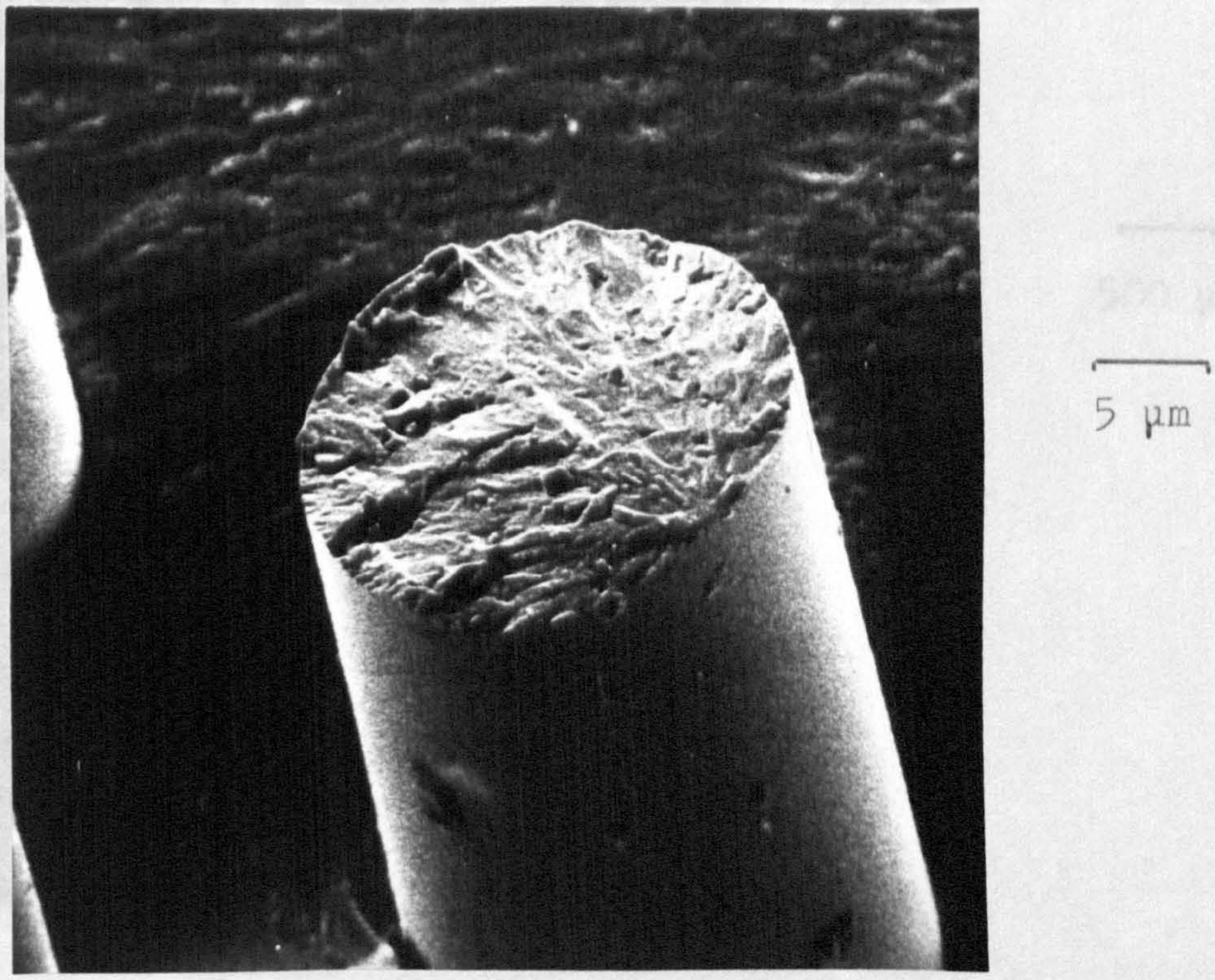

Figure 6.14 Debonding Plane of a 0° Beam

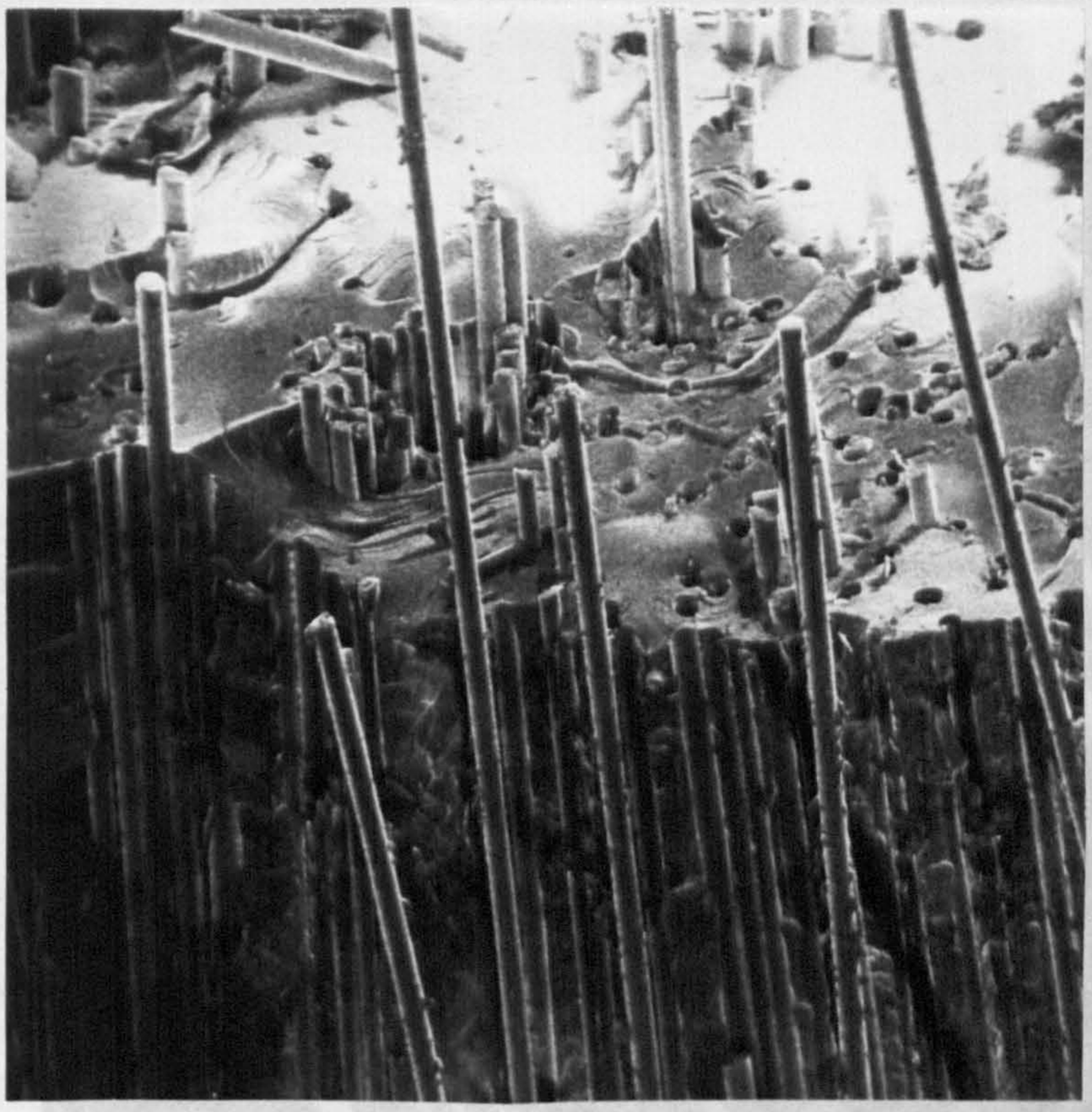

100 μm

Figure 6.15 Fracture Surface of a 90° Beam

500 μm

Figure 6.16 Fracture Surfaces of 90° Beams; higher magnifications

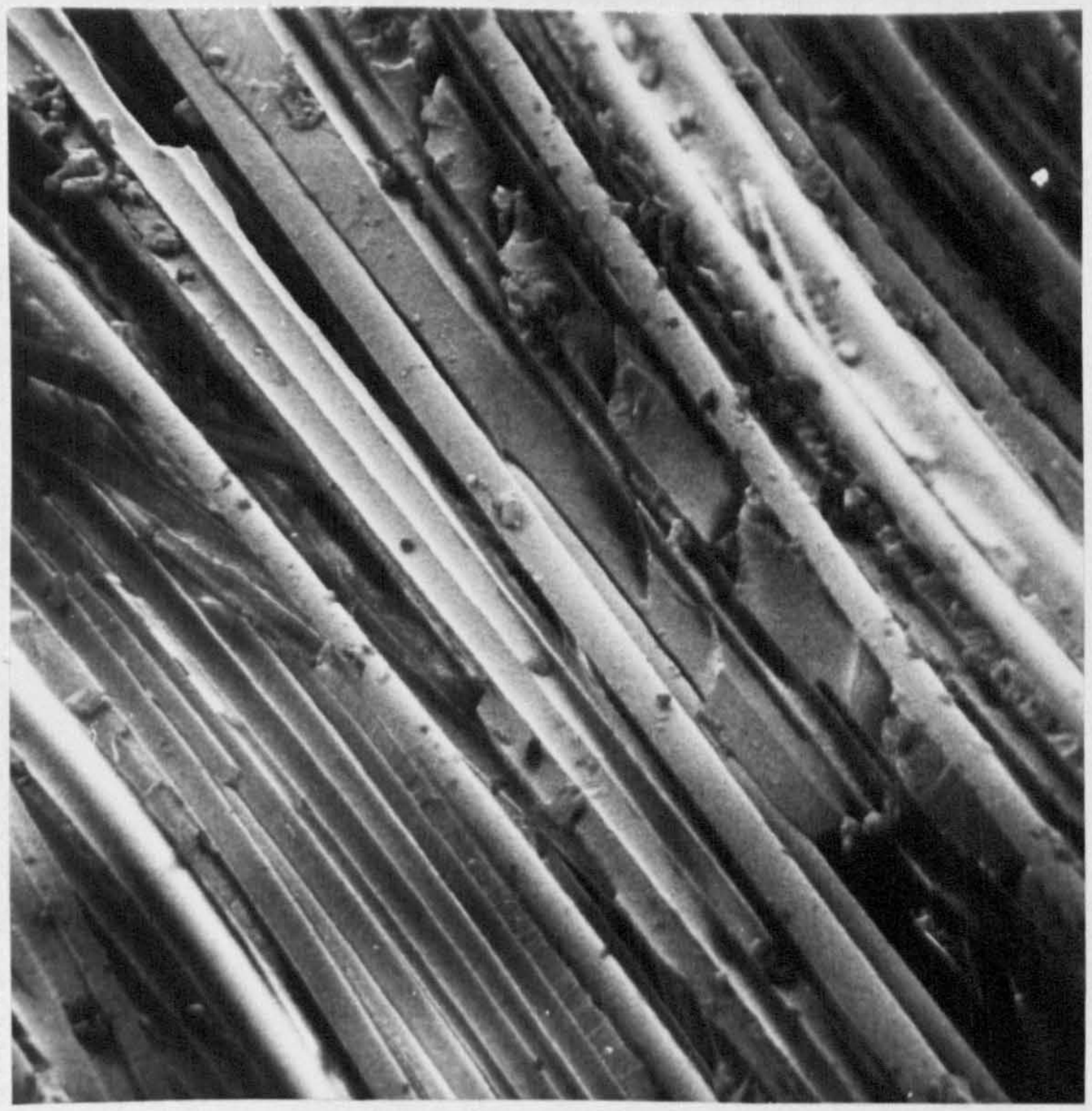

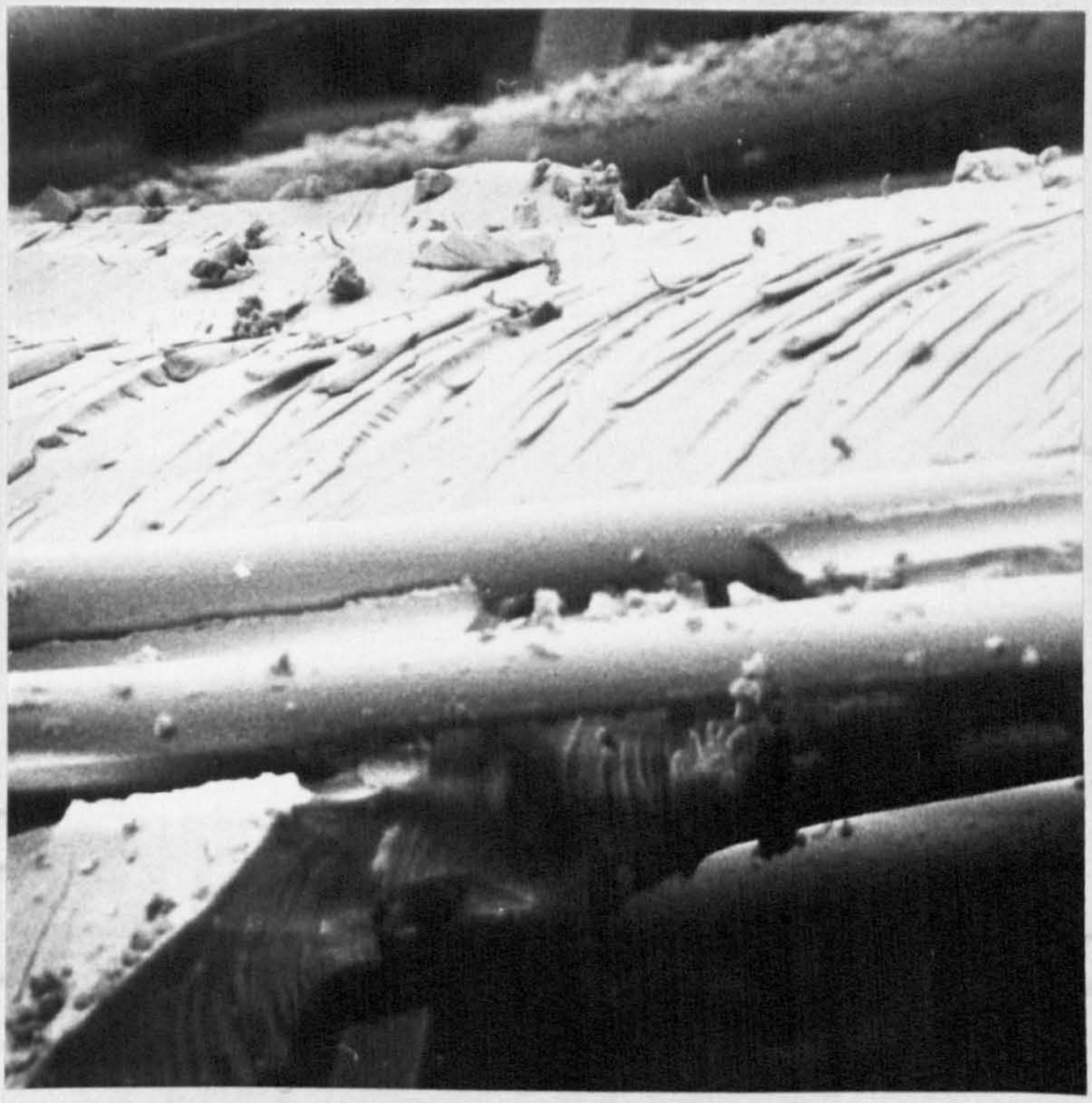

Figure 6.17 Histogram of Fibre Pull-Out Lengths

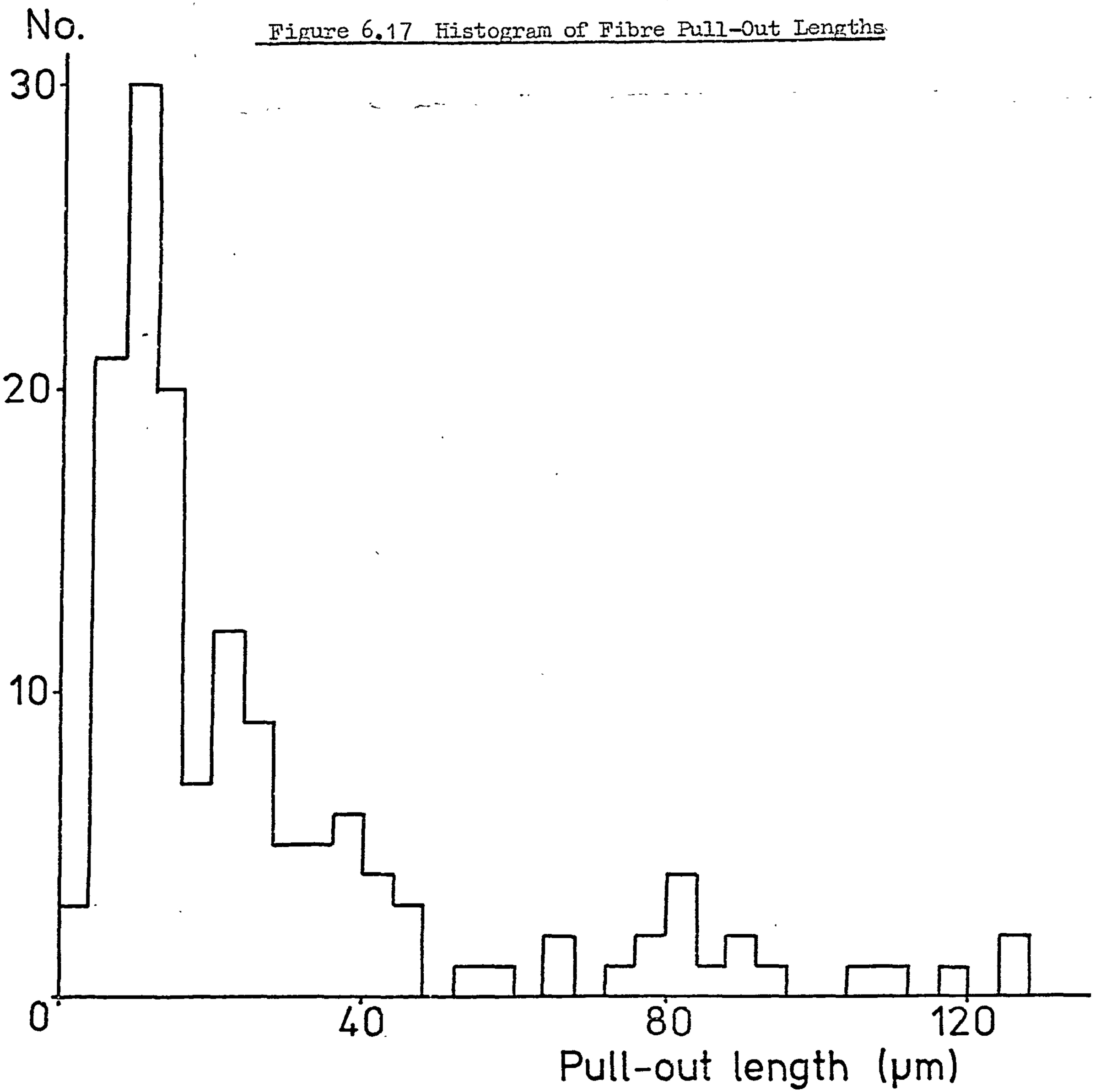

Figure 6.18 Crack Profile

Magnification x520

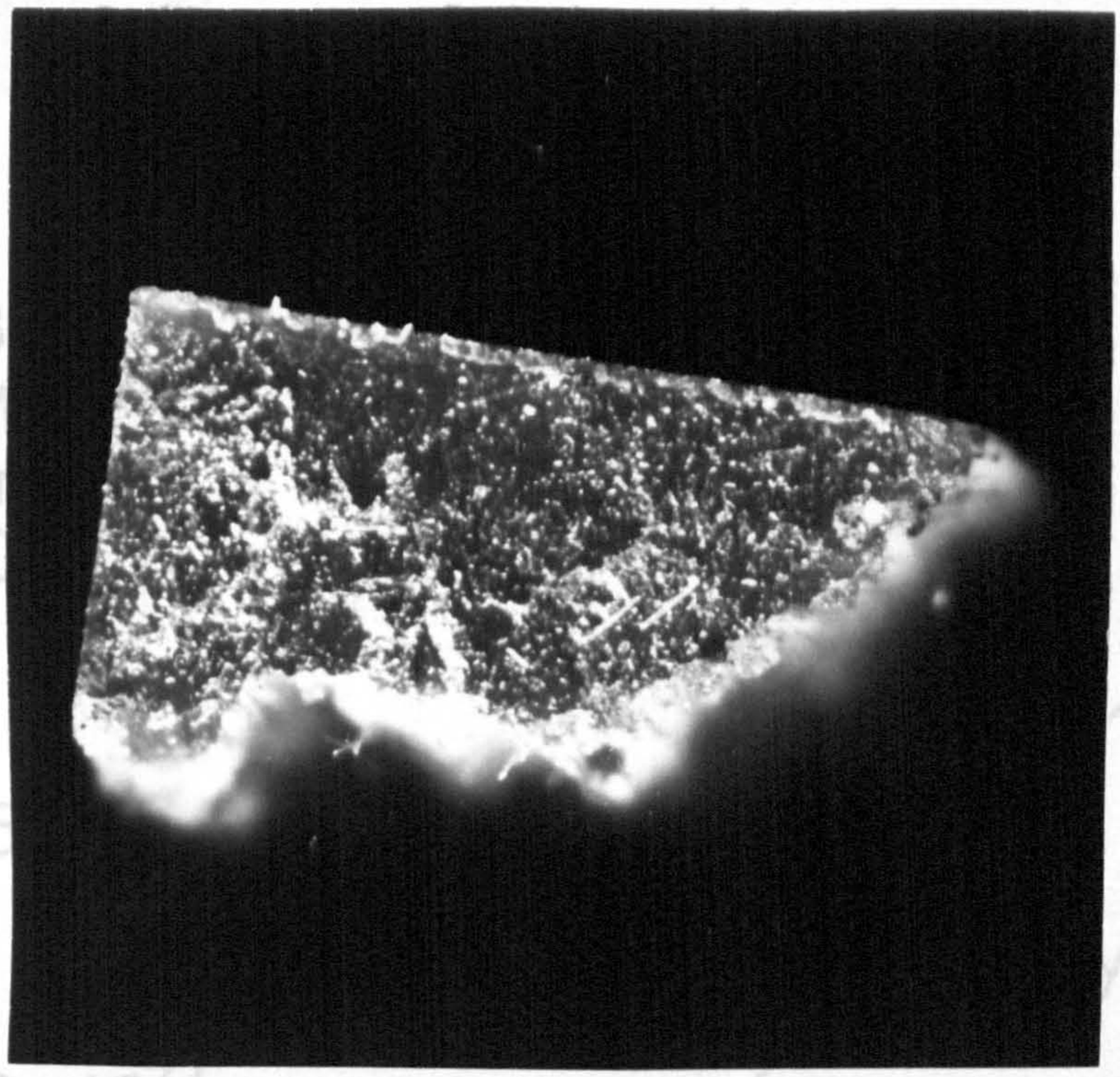

Figure 7.1 Comparison of Static and Dynamic Bending Moments in the Free-Free Rig

— 0° Beam

---90° Beam

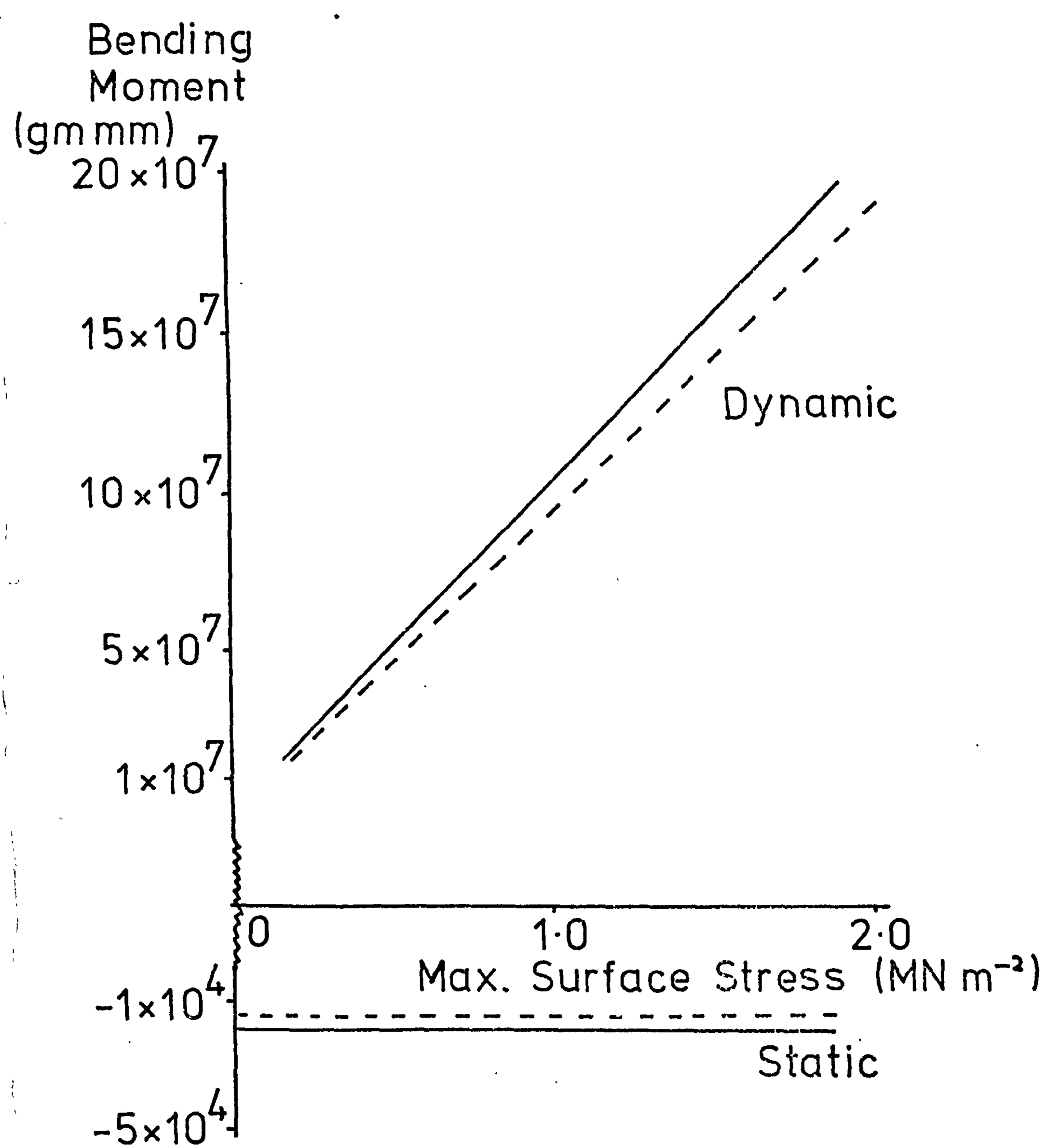

Figure 7.2 Comparison of Static and Dynamic Bending Moments in the Cantilever Rig

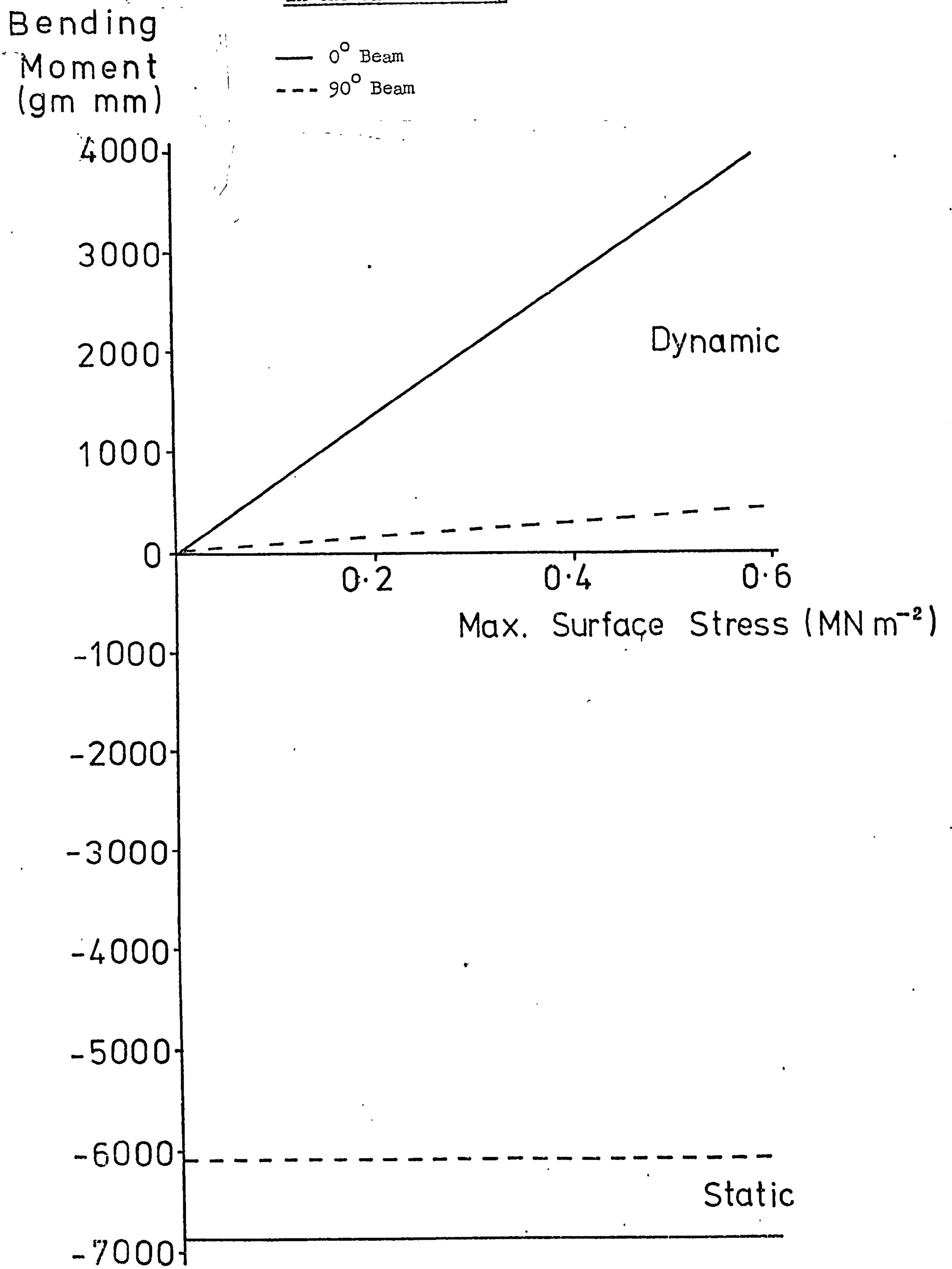

Figure 7.3 Specific Damping Capacity of Undamaged Beams, measured in the Free-Free Rig

× 0° Beam

• 90° Beam

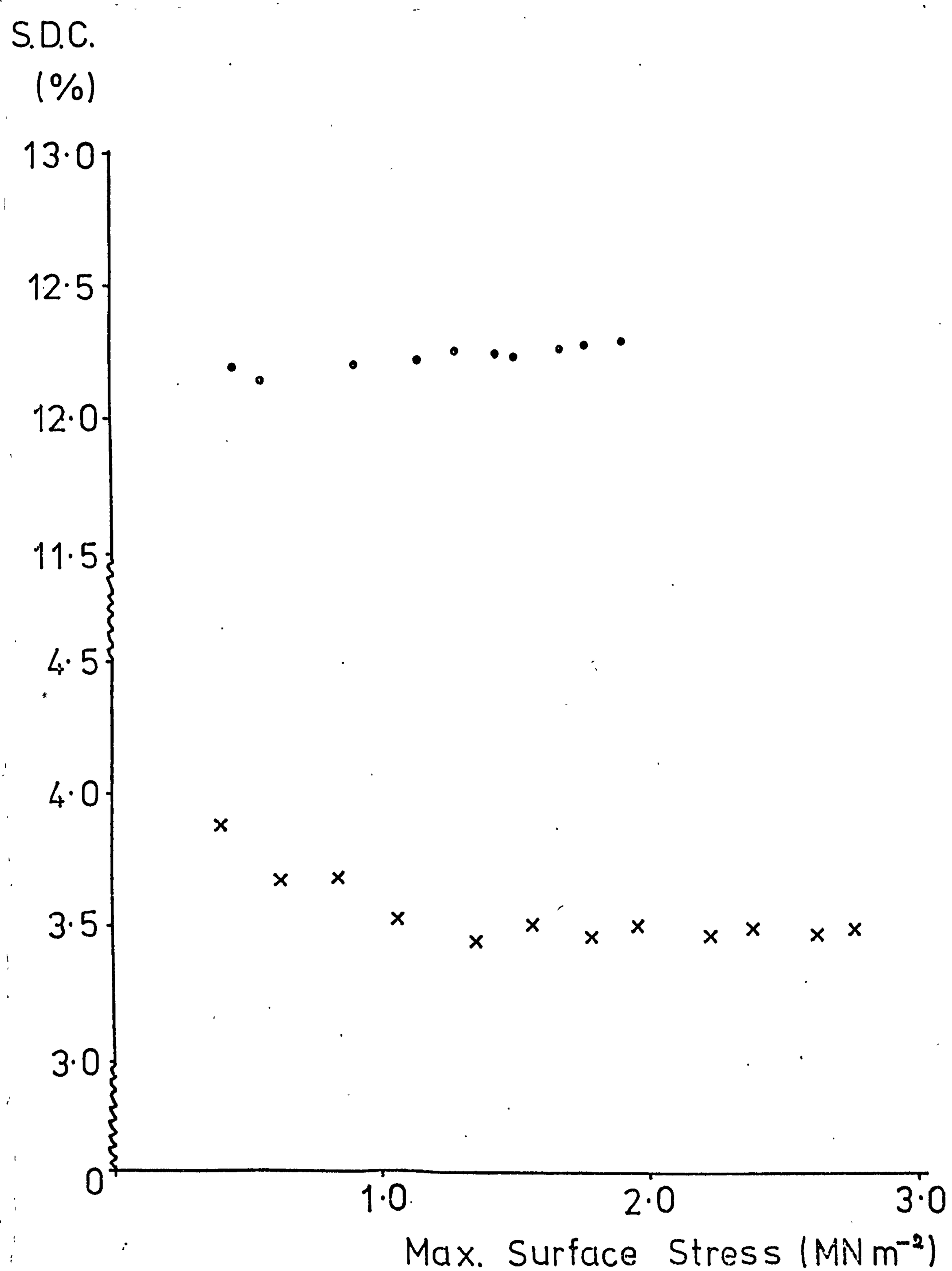

Figure 7.4 Specific Damping Capacity of Undamaged Beams, measured in the Cantilever Rig

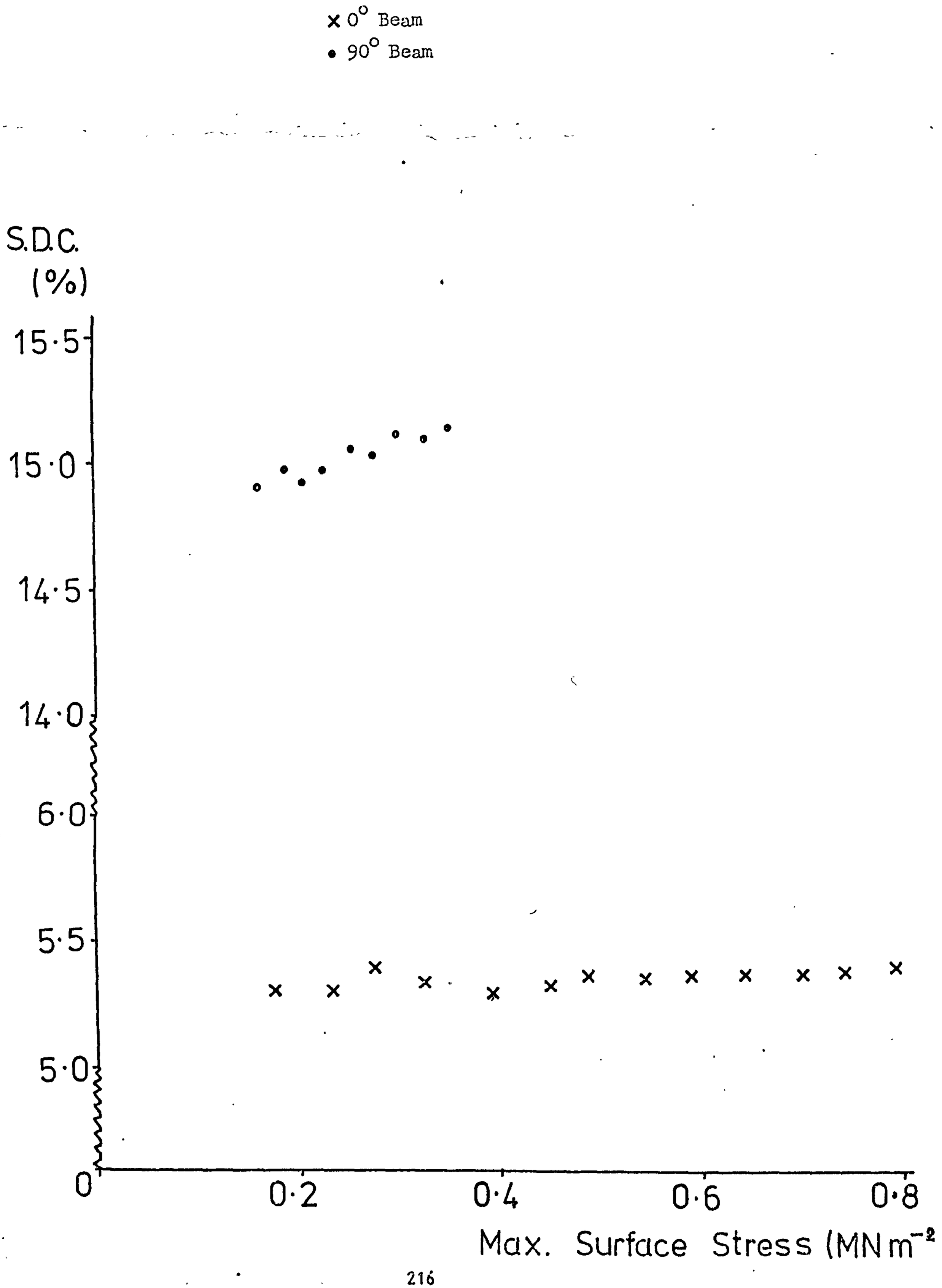

Figure 7.5 Effect of Temperature on the Specific Damping Capacity of a 90° Beam, measured in the Cantilever Rig

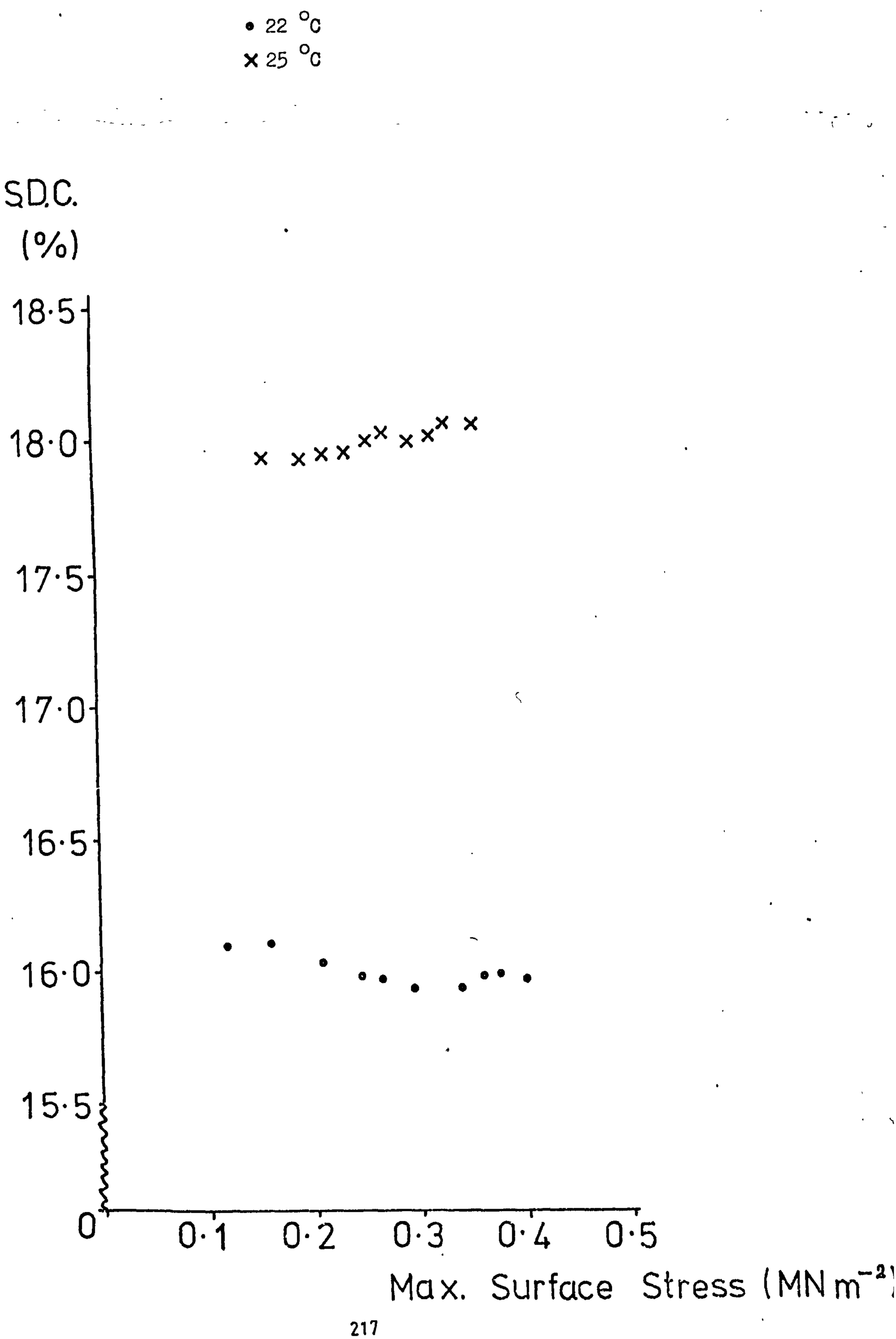

Figure 7.6 Specific Damping Capacity of a 0° Beam, stressed to the onset of acoustic emission, measured in the Free-Free Rig

× Tensile up

• Tensile down

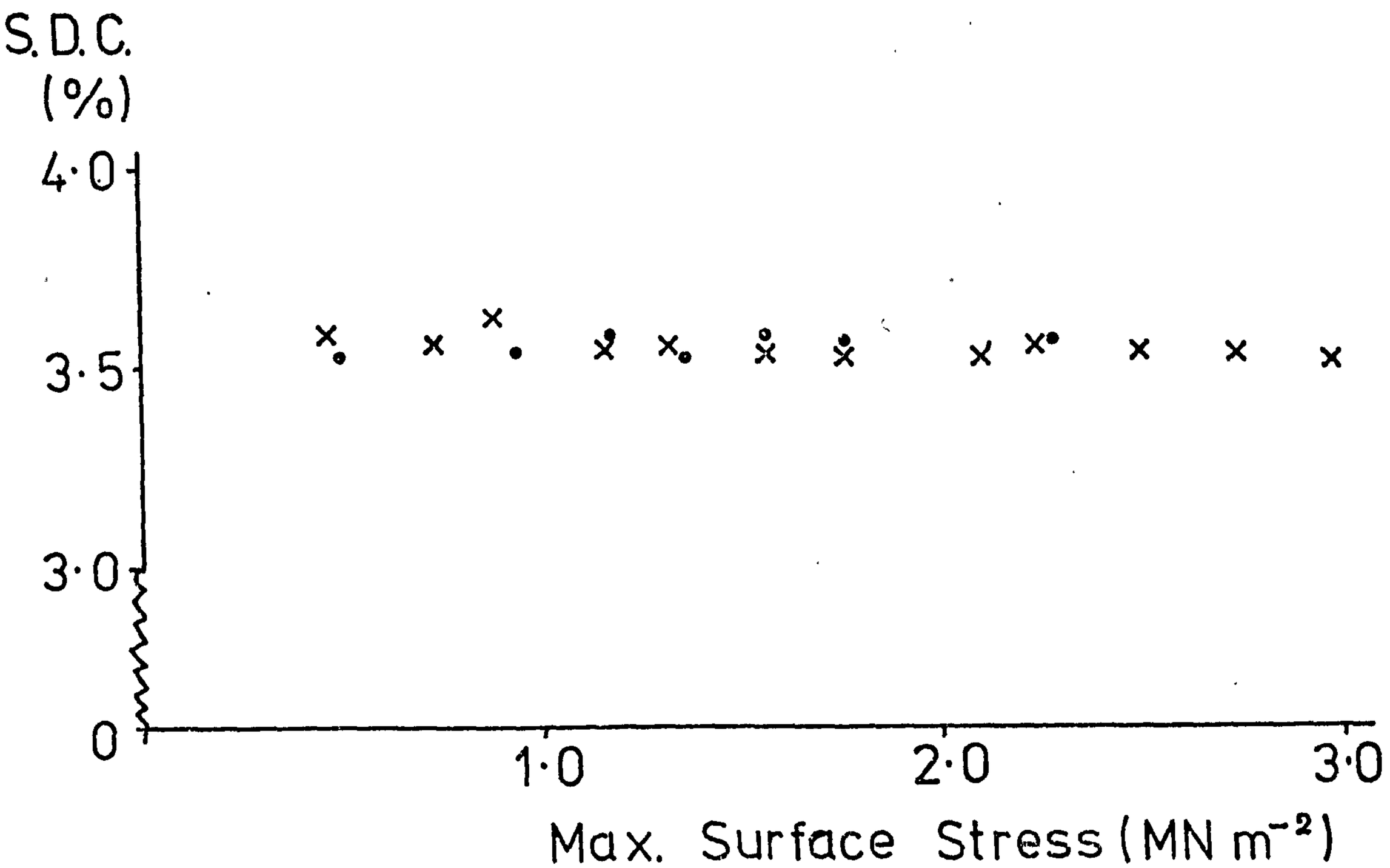

Figure 7.7 Specific Damping Capacity of a 0° Beam, measured after acoustic emission had been recorded, measured in the Free-Free Rig

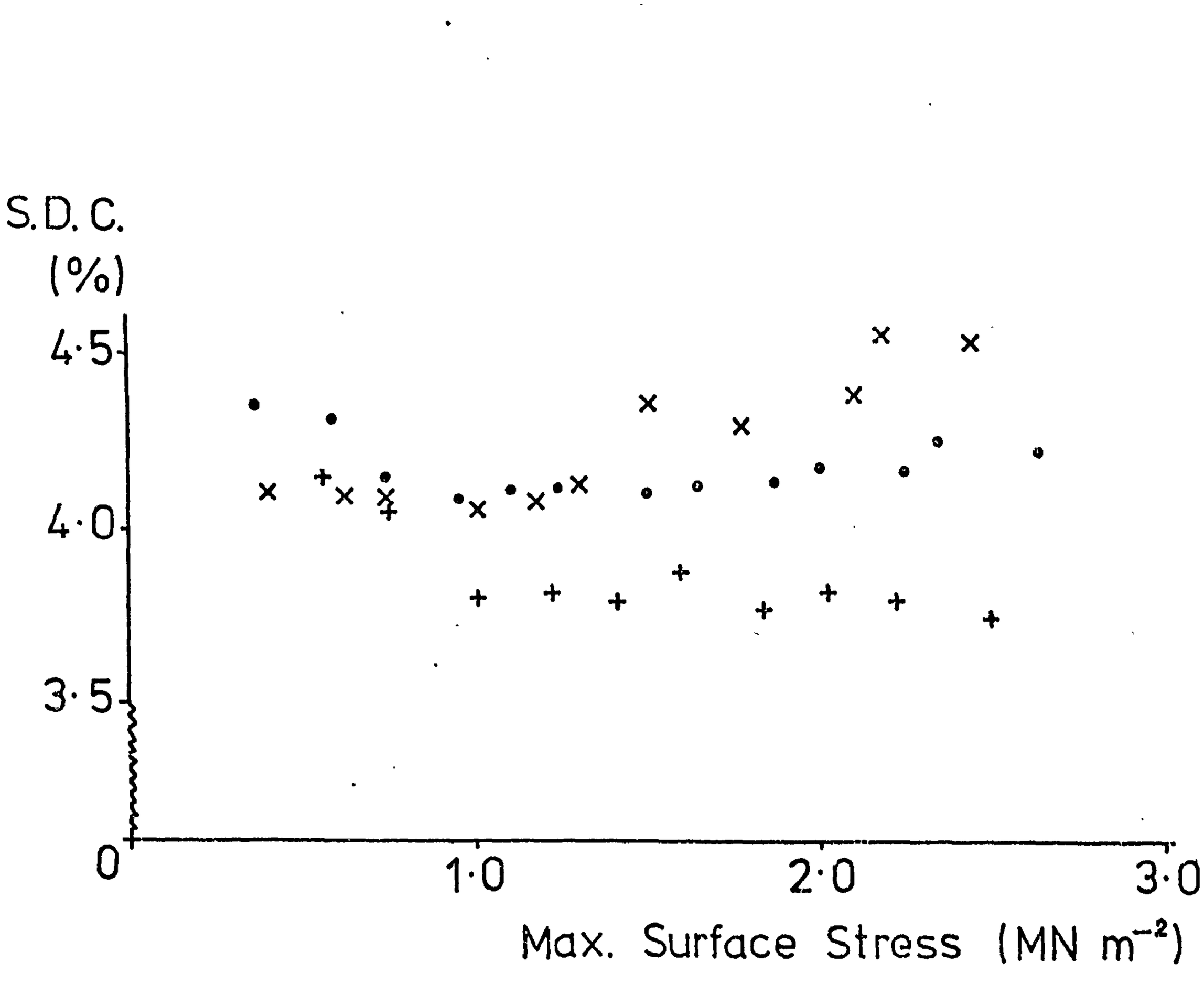

Figure 7.8 Specific Damping Capacity of a 0° Beam, containing a visible crack, measured in the Free-Free Rig

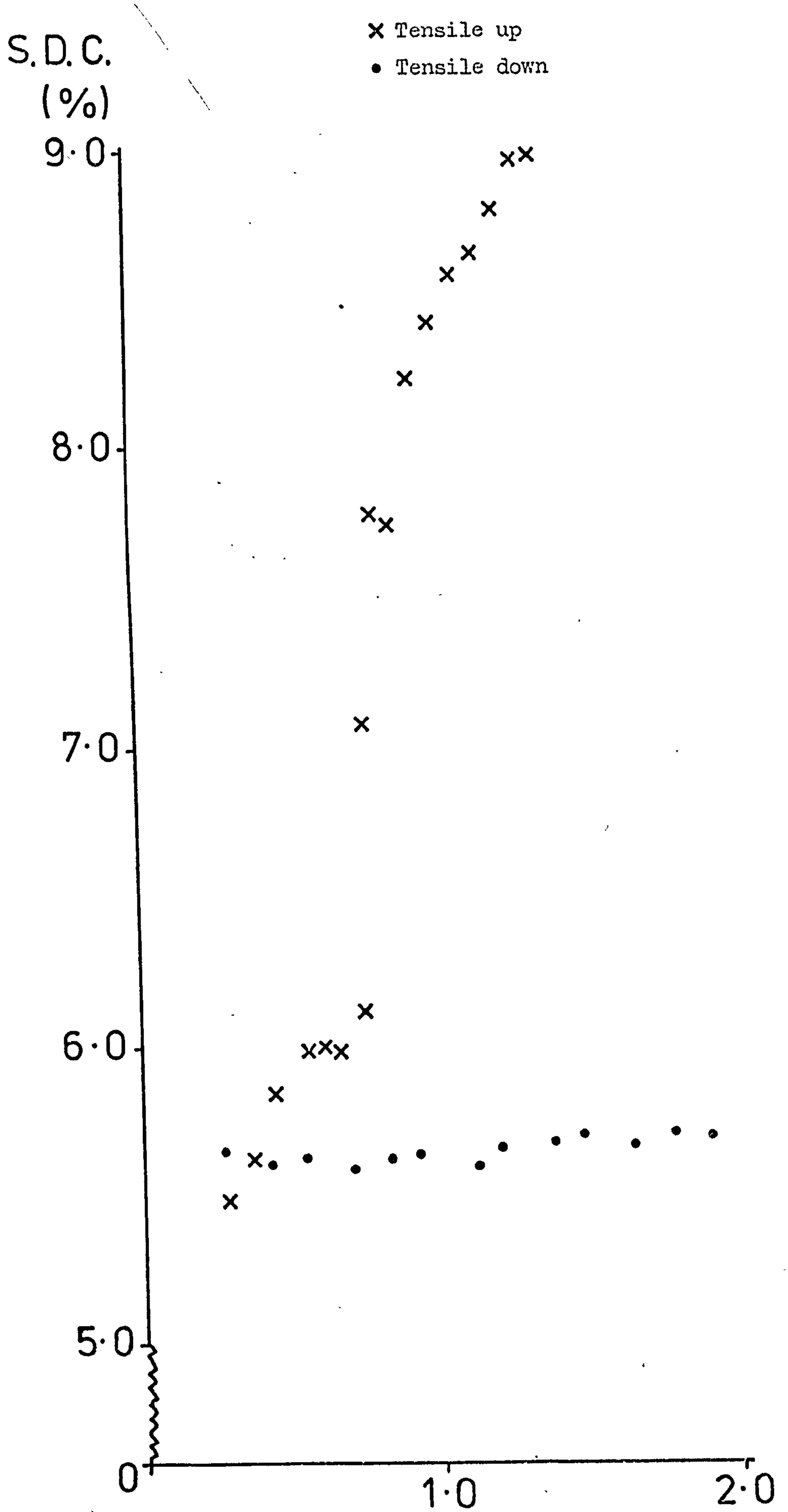

Figure 7.9 Apparent Energy Absorbed by the Crack from the Results in Figure 7.8

× Tensile up

• Tensile down

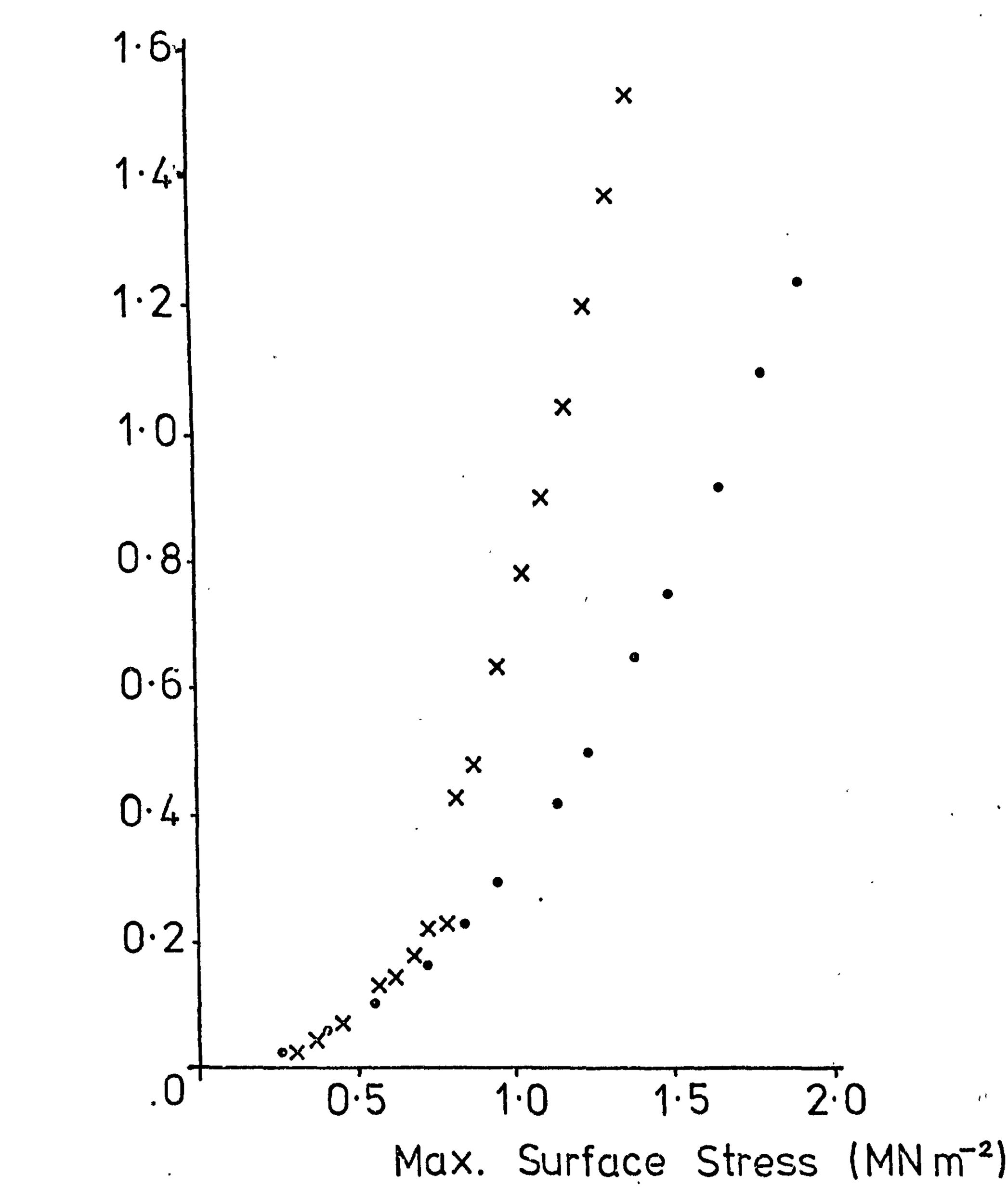

Figure 7.10 Specific Damping Capacity of a 0° Beam measured after Repeated Flexural Tests

• 1st measurement

+ 2nd measurement

× 3rd measurement

(Tensile face up in all measurements)

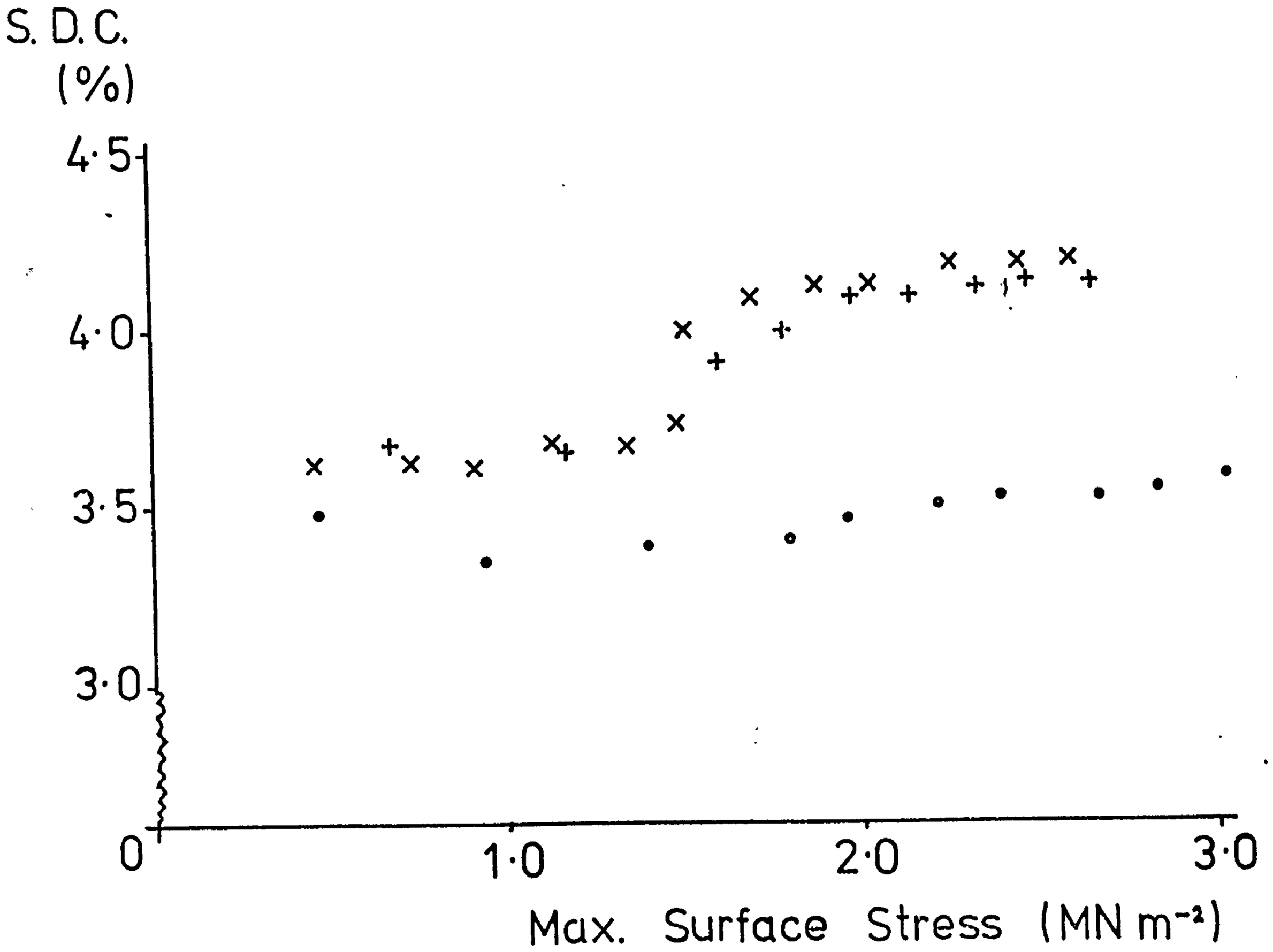

Figure 7.11 Comparison of Values of Specific Damping Capacity of a cracked 0° beam, calculated using the two analyses, measured in the Free-Free Rig

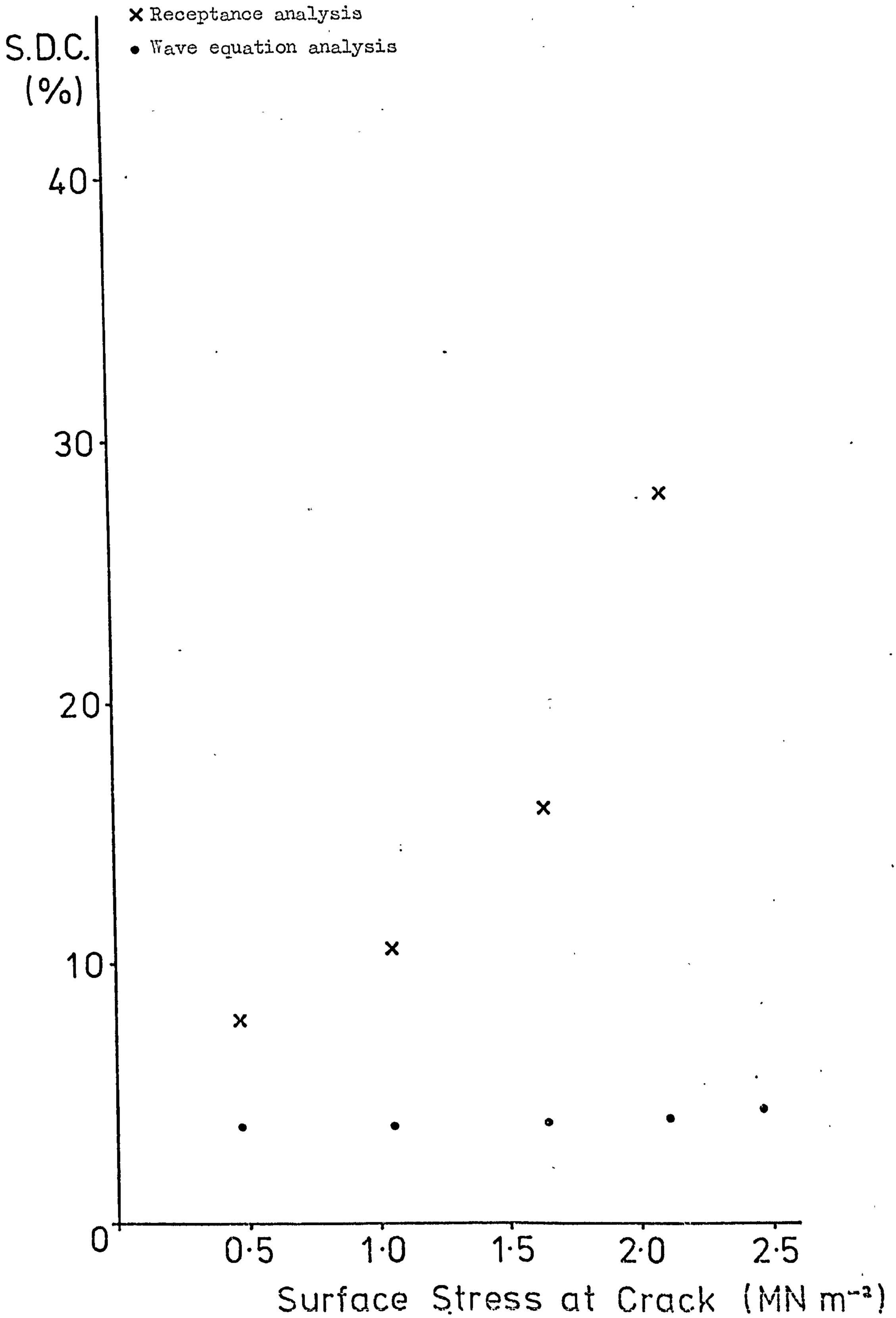

Figure 7.12 Specific Damping Capacity of a 90° Beam, stressed to just prior to anticipated failure, measured in the Free-Free Rig

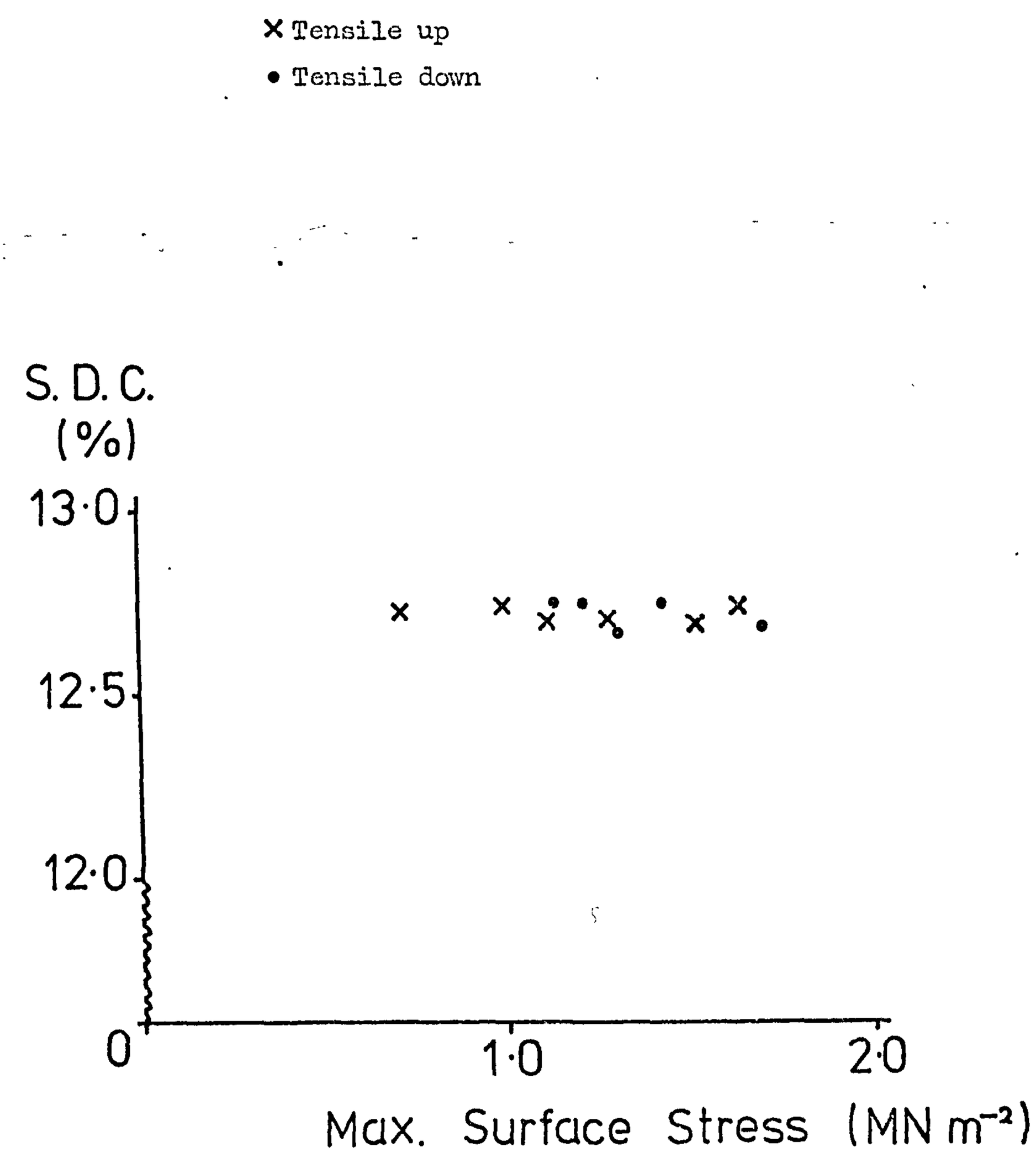

Figure 7.13 Modulus of a Cracked 90° Beam, calculated using the wave equation analysis, measured in the Free-Free Rig

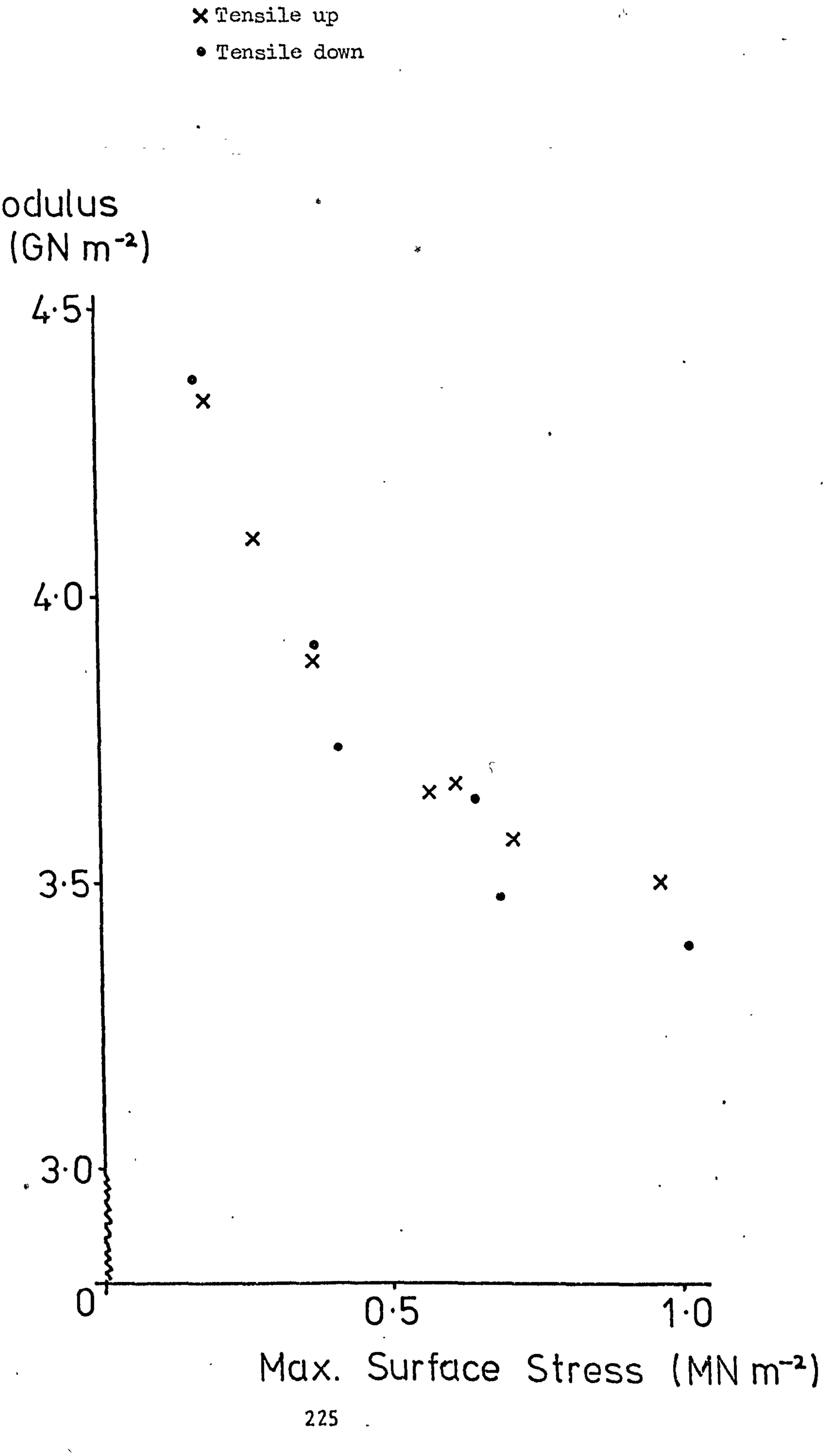

Figure 7.14 Specific Damping Capacity of a Cracked 90° Beam, calculated using the wave equation analysis, measured in the Free-Free Rig

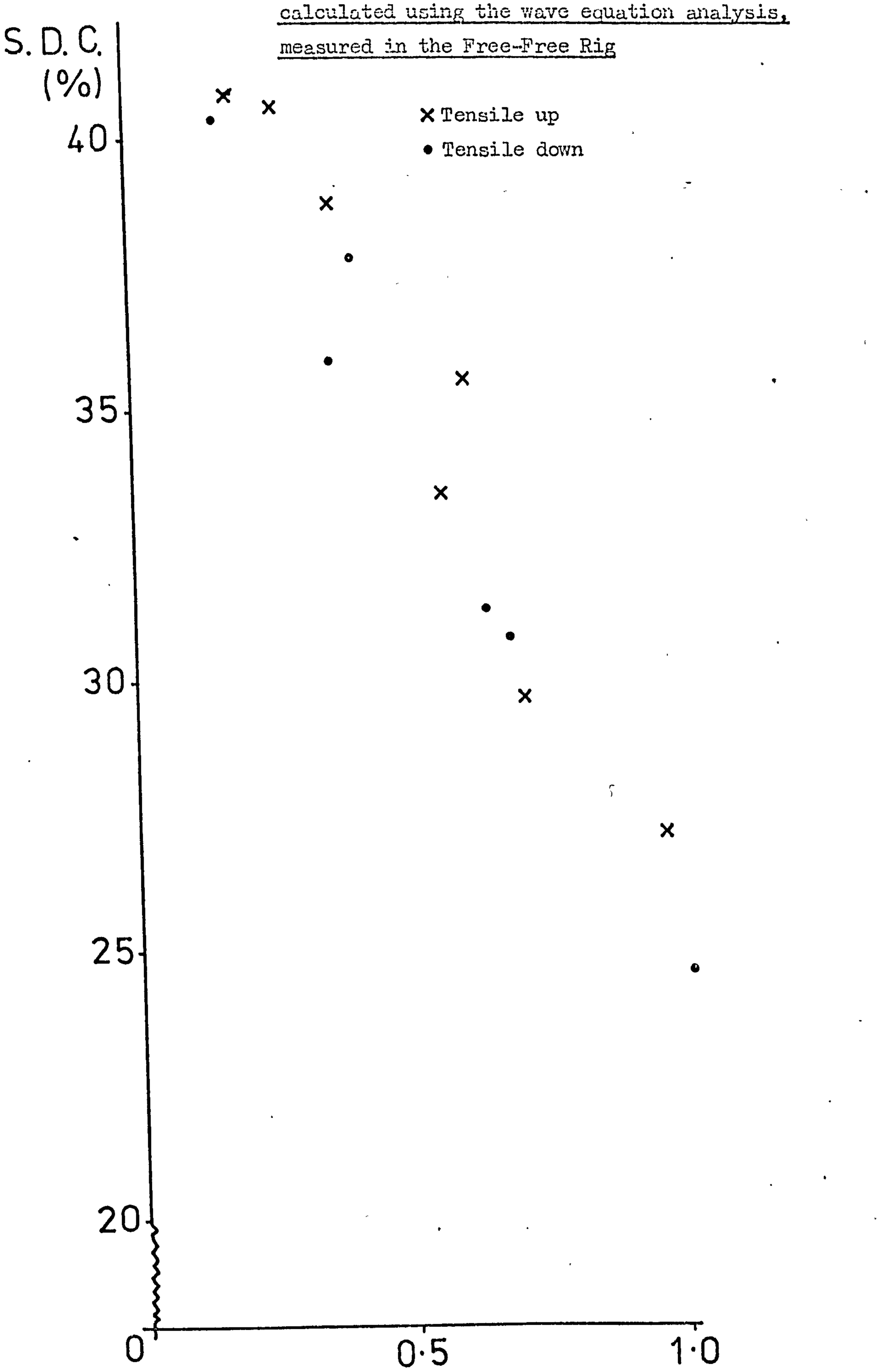

Figure 7.15 Apparent Energy Absorbed by the Crack from the Results in Figure 7.14

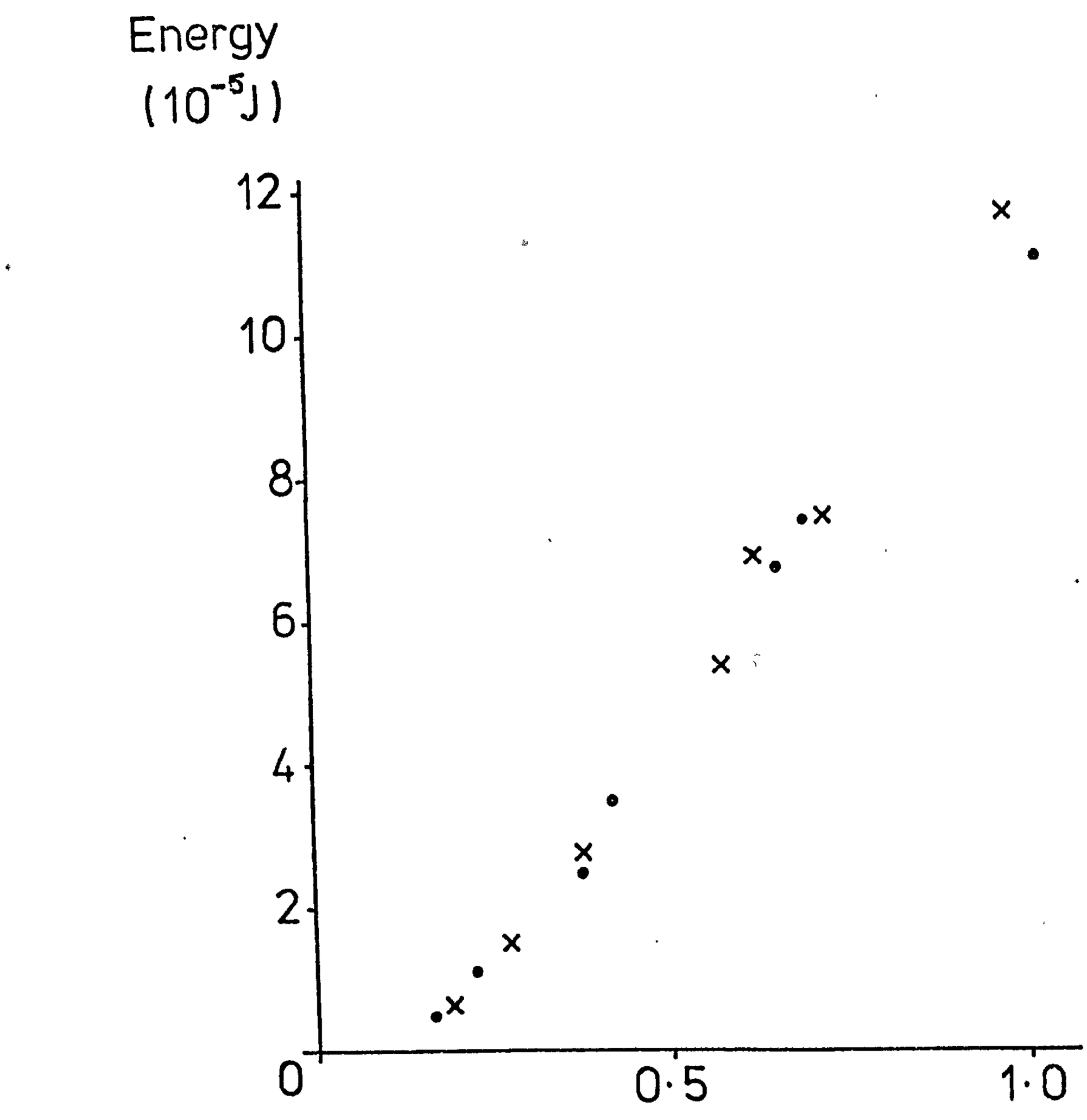

Figure 7.16 Specific Damping Capacity of a 0° Beam, stressed to the onset of acoustic emission, measured in the Cantilever Rig

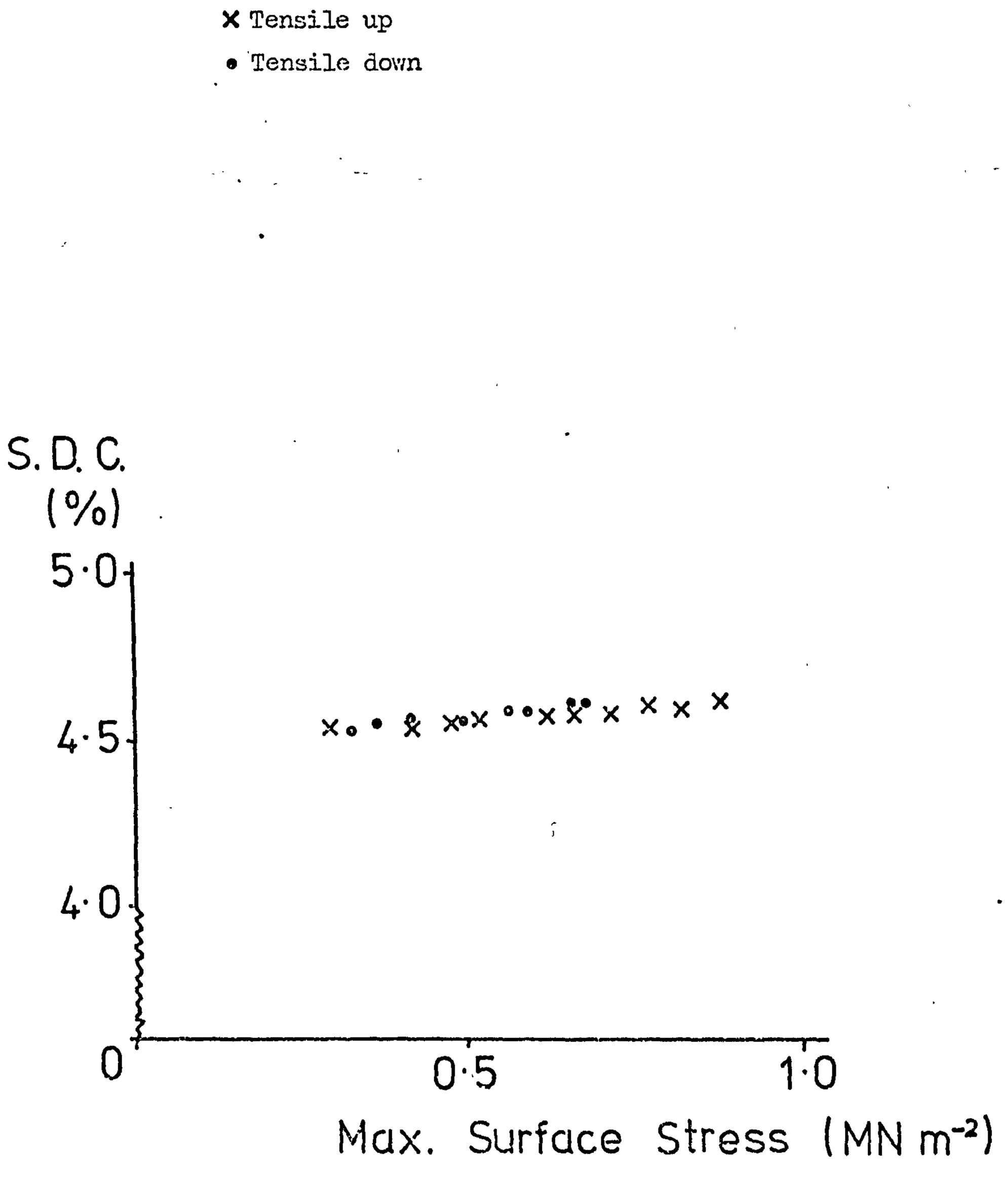

Figure 7.17 Specific Damping Capacity of a 0^{o} Beam, measured after acoustic emission had been recorded, measured in the Cantilever Rig

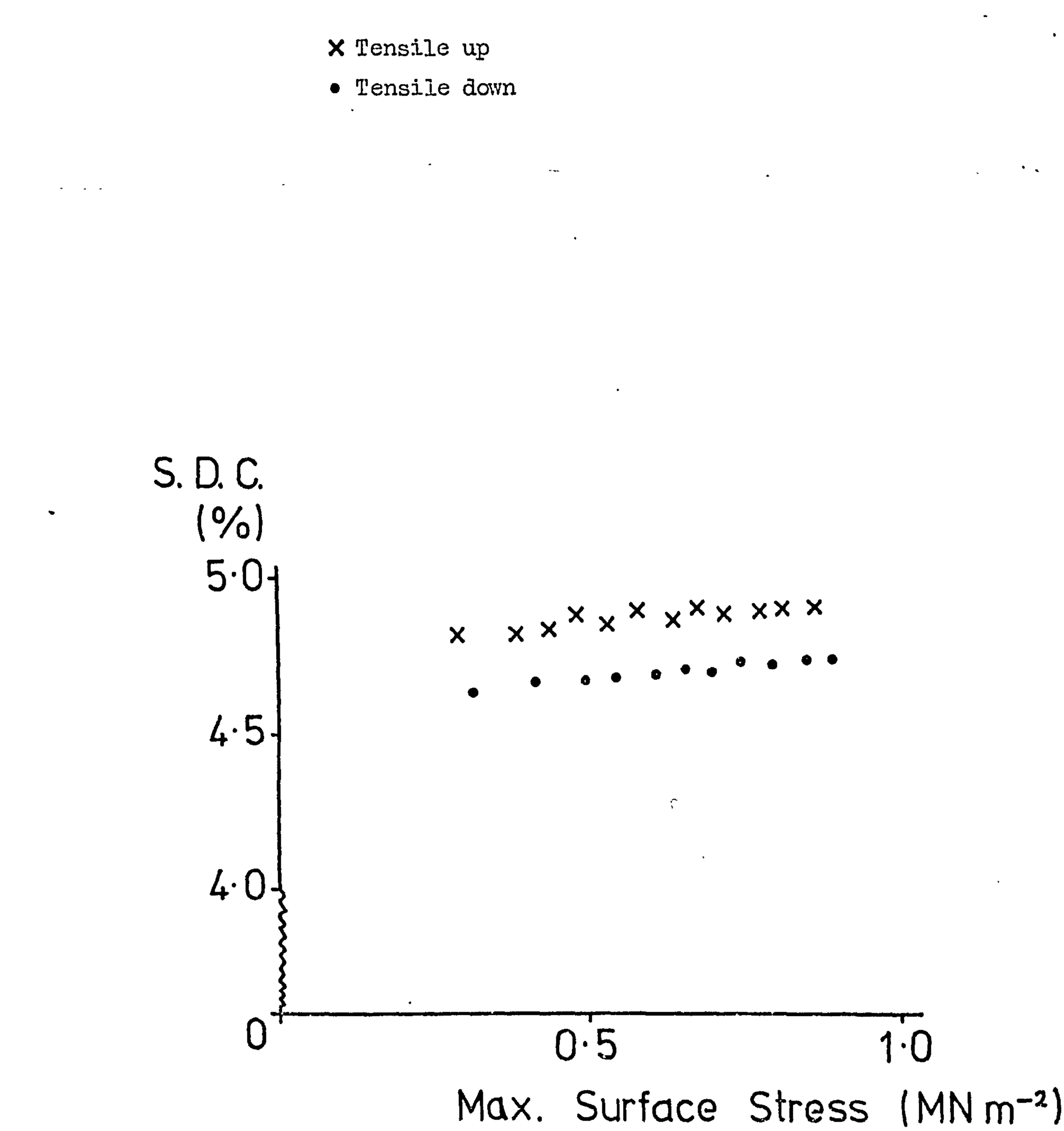

Figure 7.18 Specific Damping Capacity of a 0° Beam containing a visible crack, measured in the Cantilever Rig

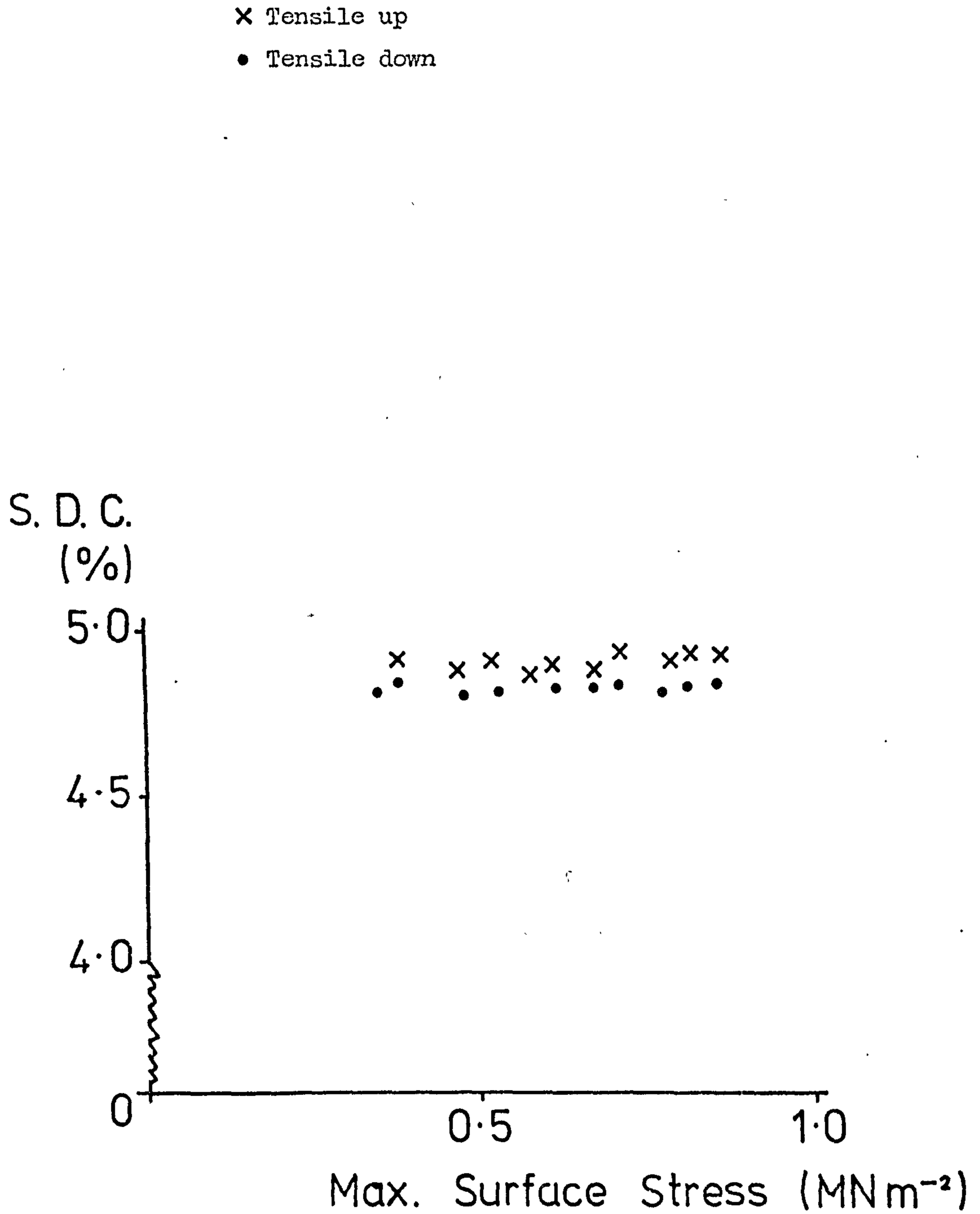

Figure 7.19 Comparison of Values of Specific Damping Capacity of a Cracked 0° Beam, calculated using the two analyses, measured in the Cantilever Rig

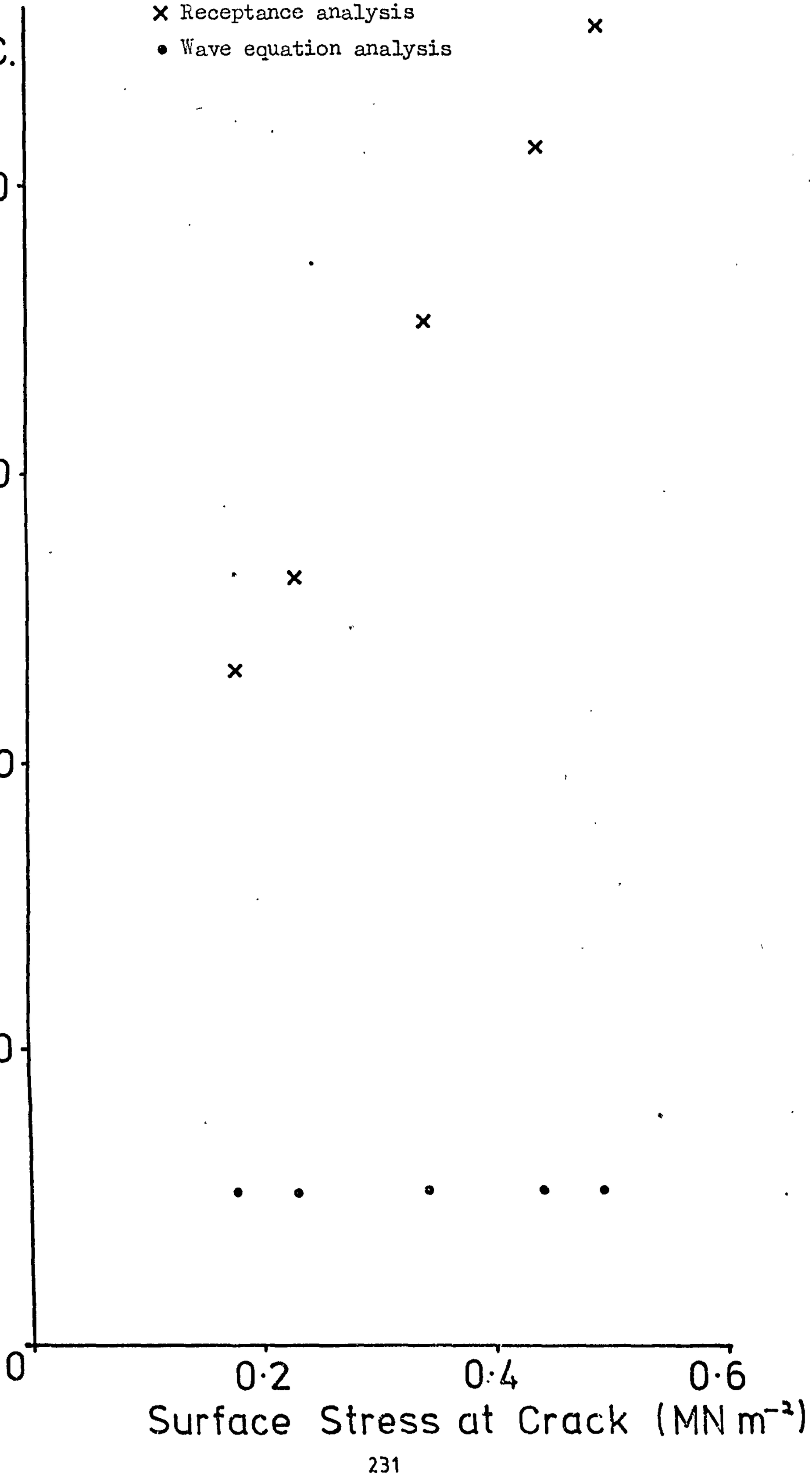

Figure 7.20 Specific Damping Capacity of a 90^0 Beam, stressed to just prior to anticipated failure, measured in the Cantilever Rig

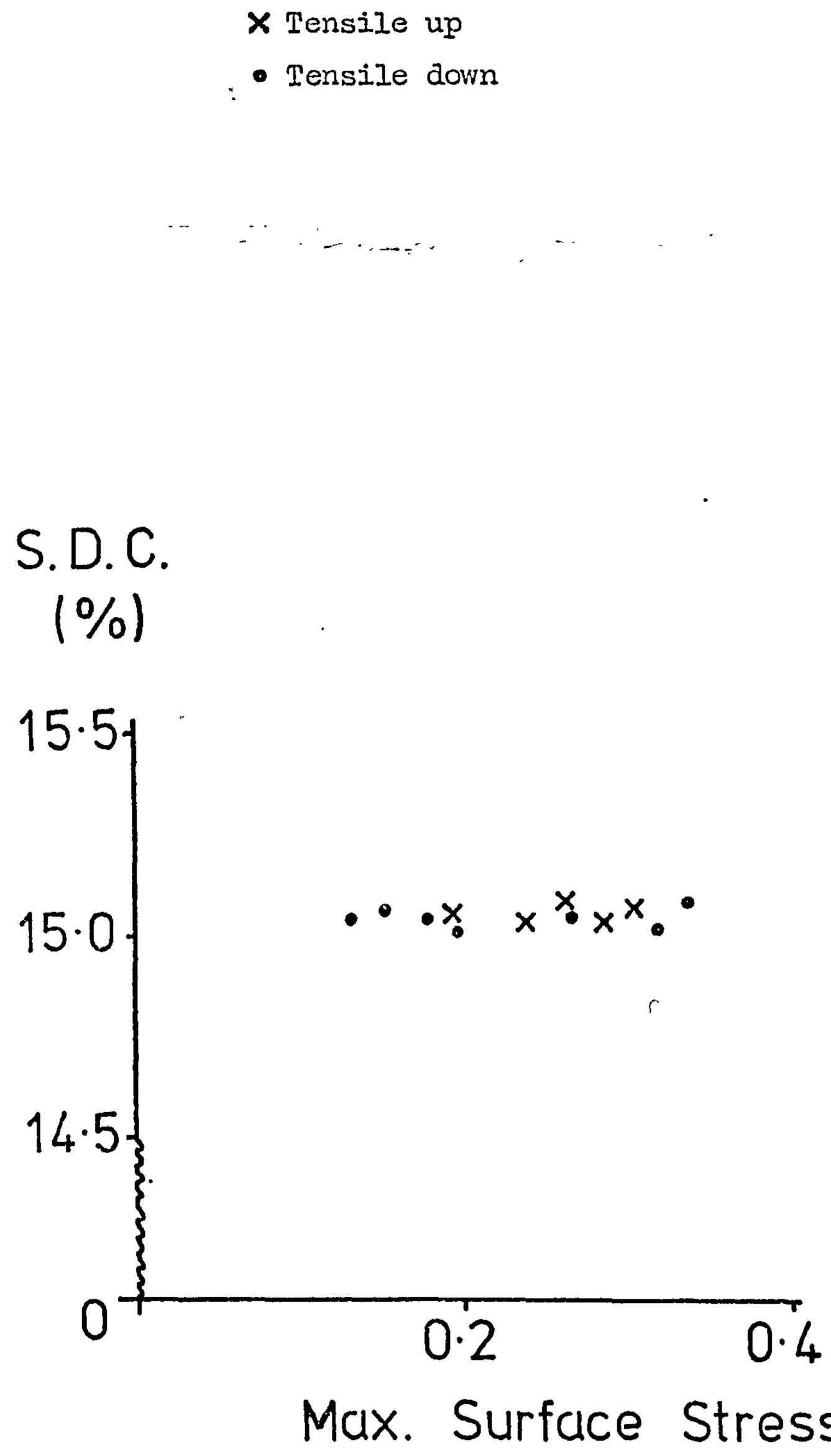

Figure 7.21 Modulus of a Cracked 90° Beam, calculated using the wave equation analysis, measured in the Cantilever Rig

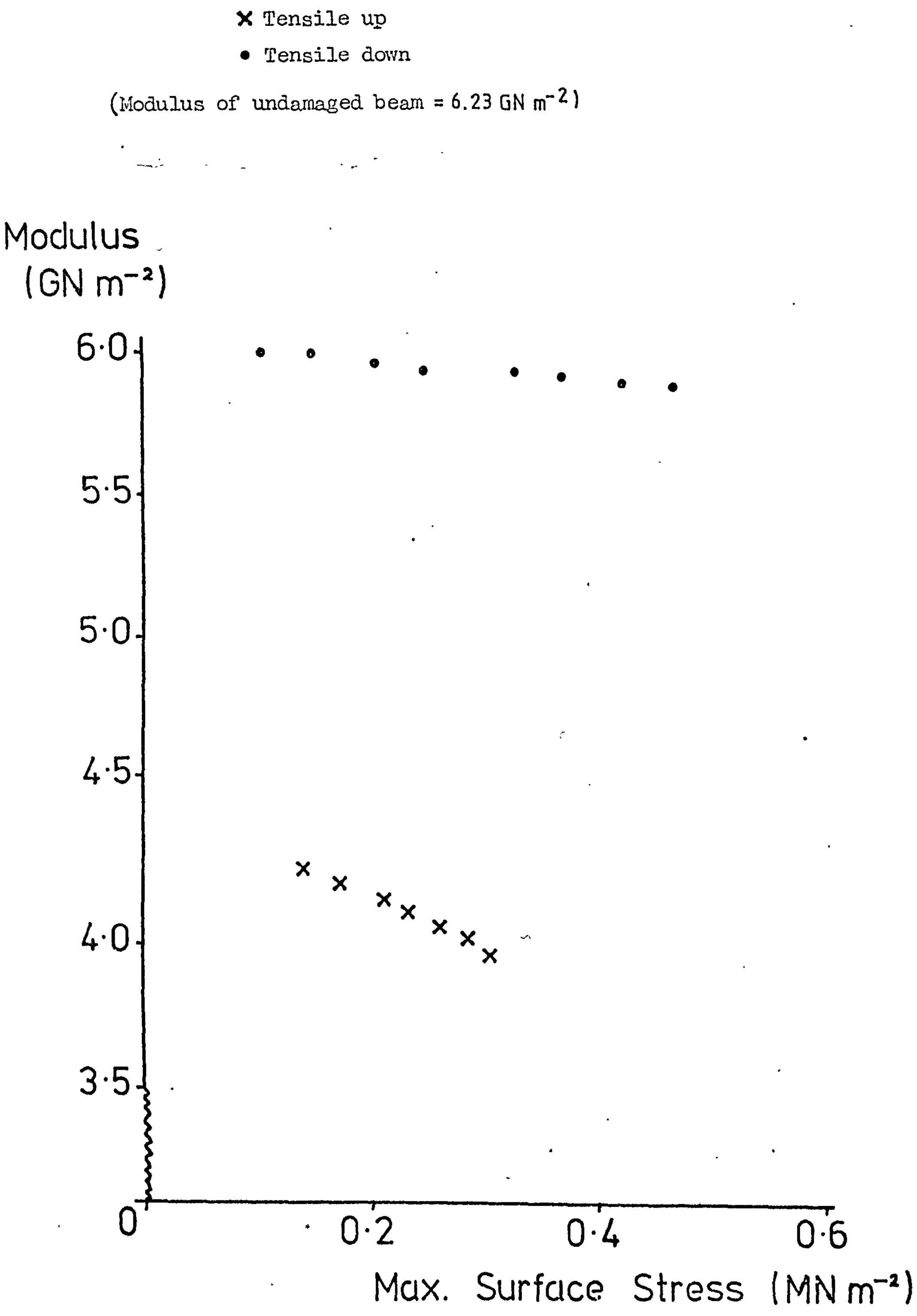

Figure 7.22 Specific Damping Capacity of a Cracked 90° Beam, calculated using the wave equation analysis, measured in the Cantilever Rig

× Tensile up

• Tensile down

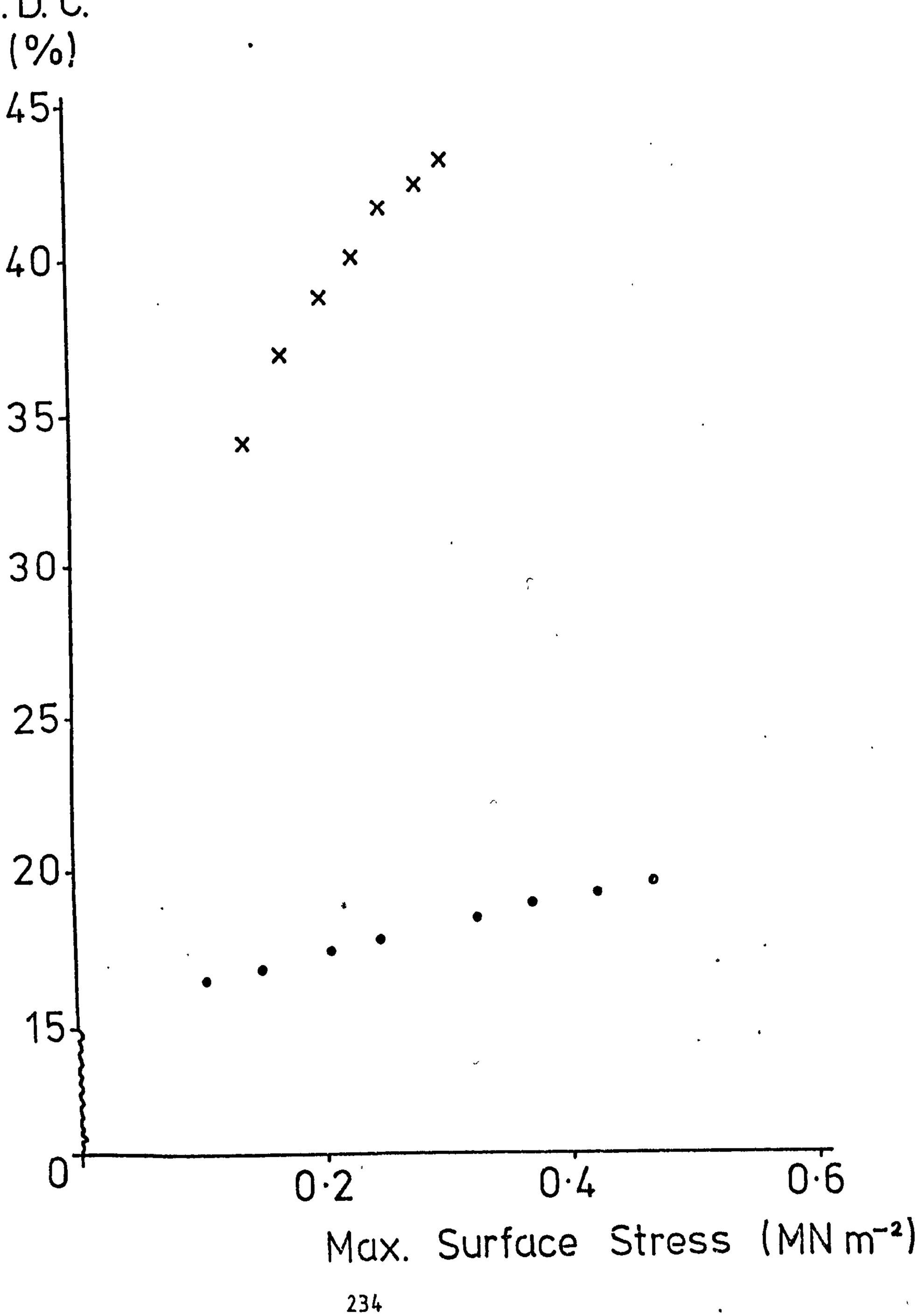

Figure 8.1 Experimental Values of Variance for Transects in J direction

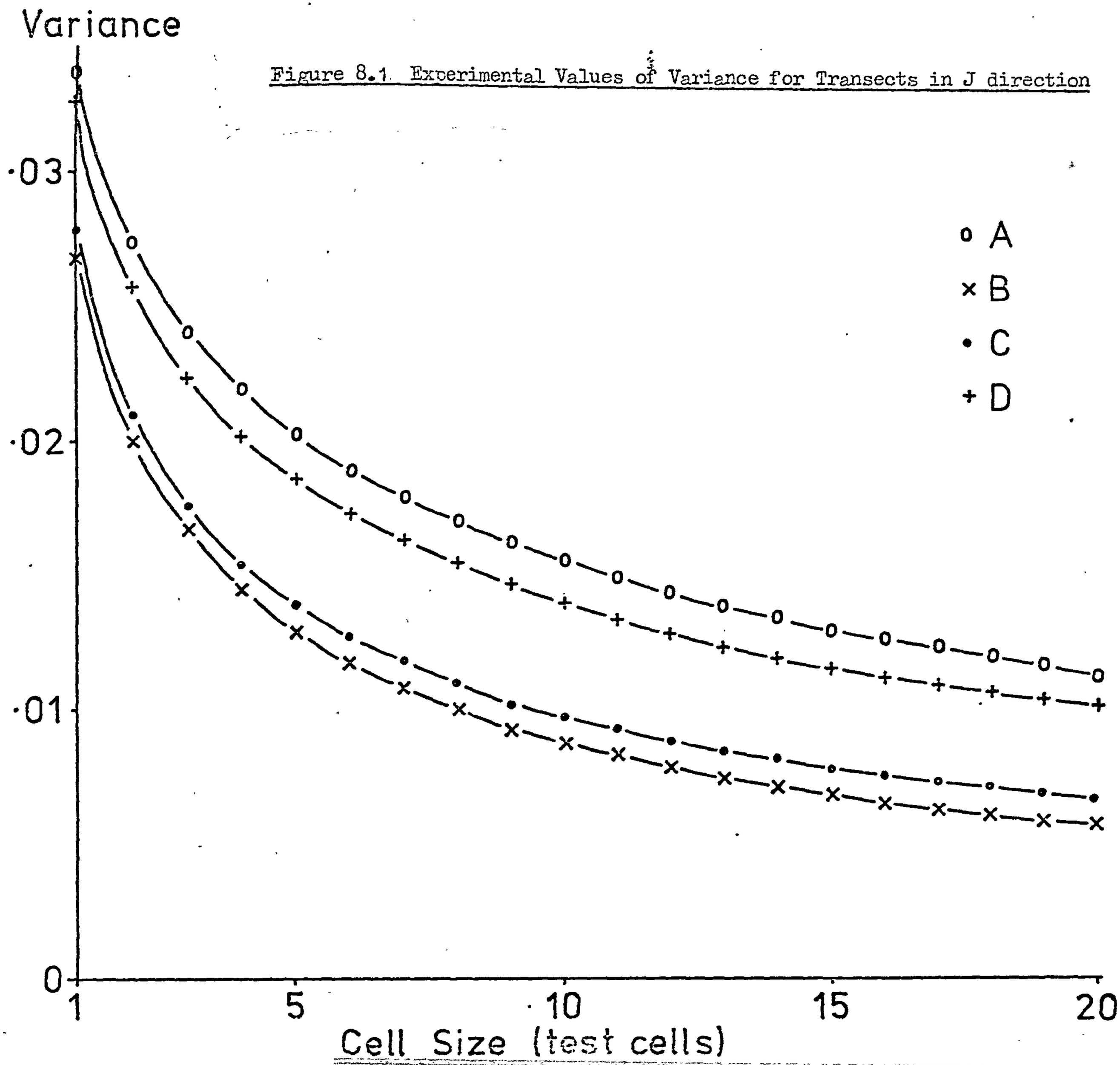

Figure 8.2 Values of Experimental/Theoretical Variance for Transects in J direction

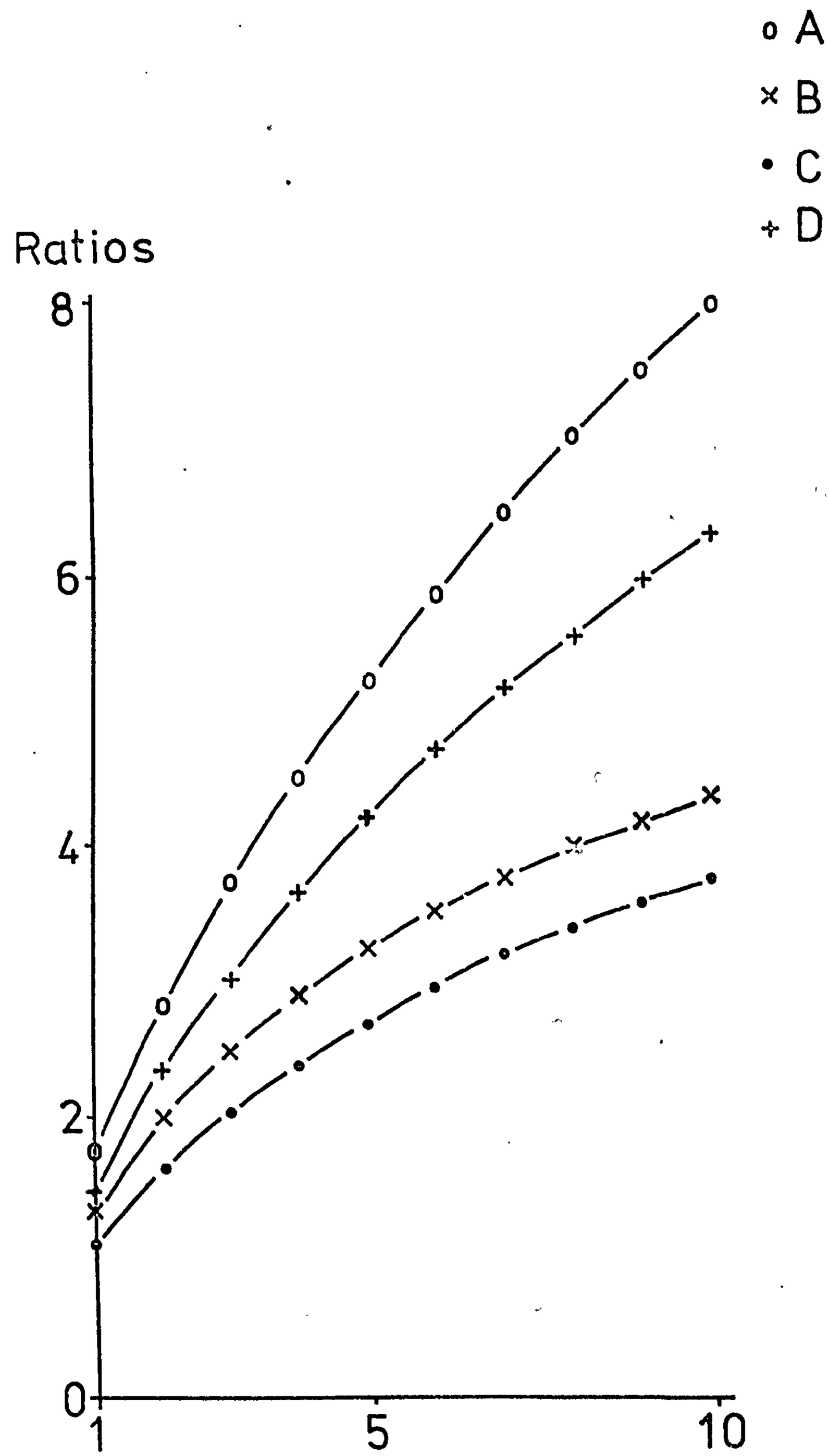

Figure 8.3 Experimental Values of Probability (cell is empty) for Transects in J direction

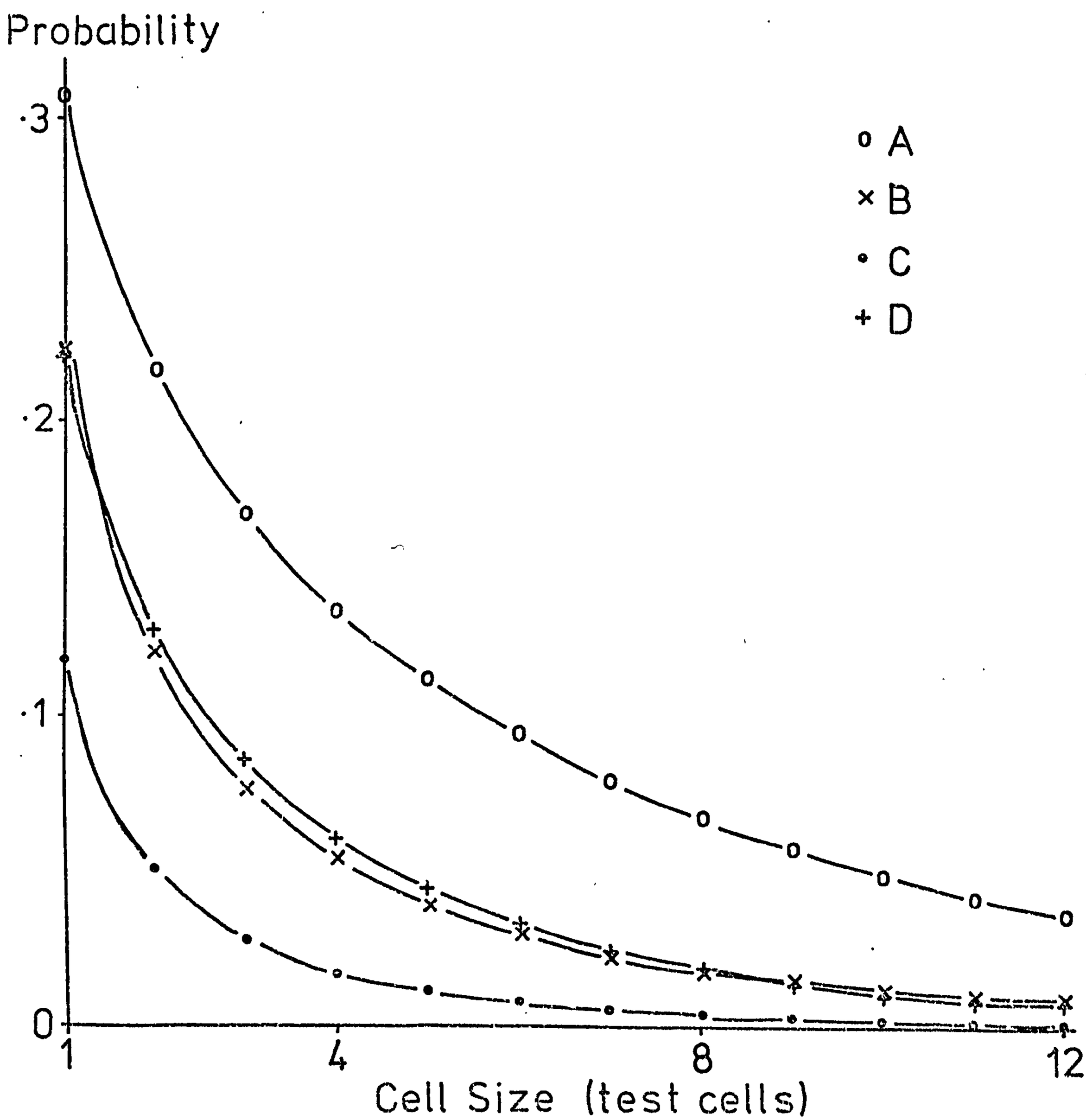

Figure 8.4 Values of Experimental/Theoretical Probability (cell is empty) for Transects in J direction

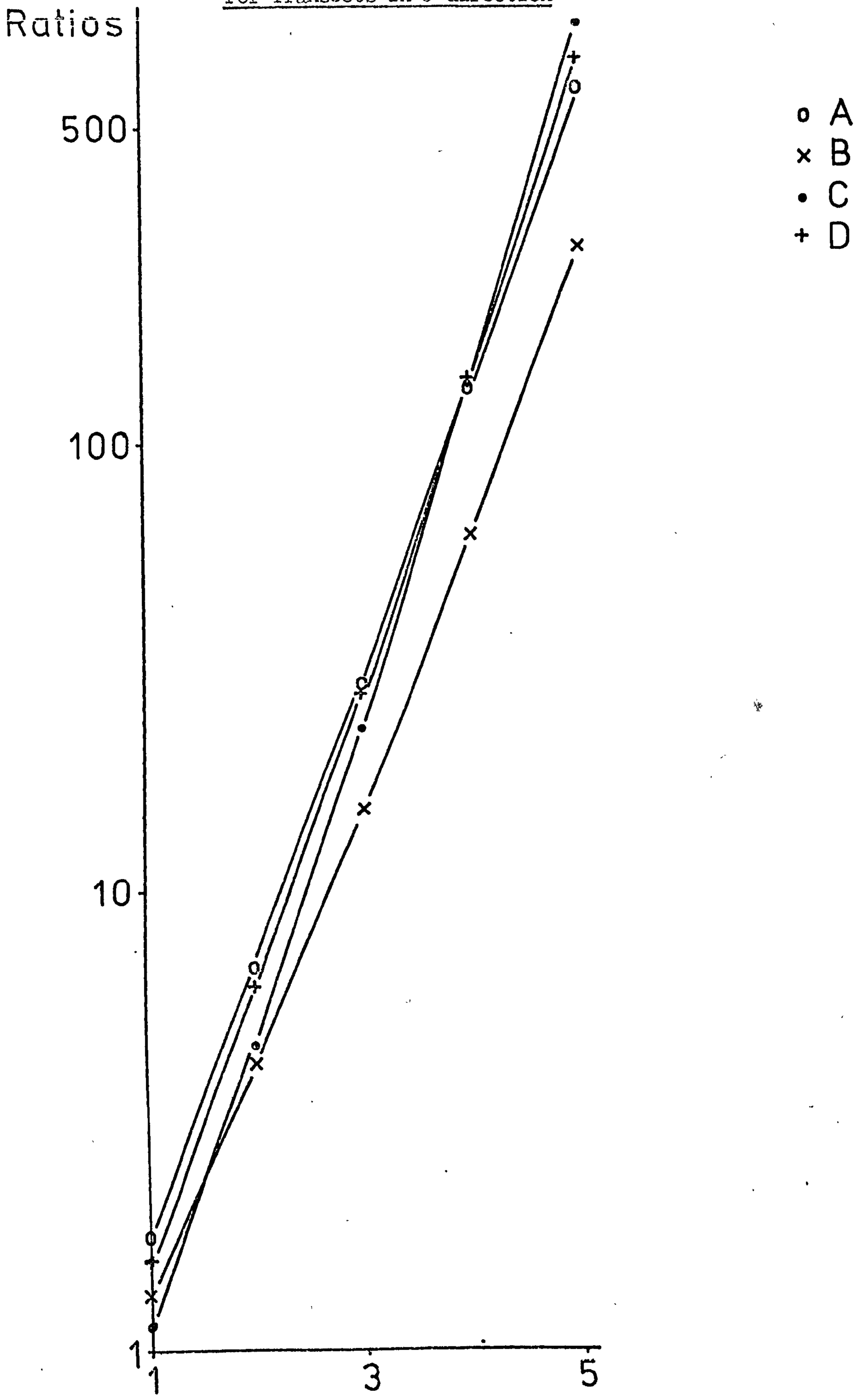

Appendix 2 Acoustic Emission Circuit

A.2.1 Mechanical Loading

An Instron screw driven universal testing machine was available. Such a machine is most suitable for acoustic emission testing as described in chapter 2. The mechanical loading system used was four-point bend. The system is described in chapter 6. The tensile crack initiates on the tensile outer face between the central rollers. The use of bending eliminates noise problems for specimen gripping. The acoustic emission transducer could be placed close to the source of emissions between the central rollers, resting horizontally on the specimen, thus eliminating noise problems from the transducer/specimen interface.

A.2.2 Transducer and Amplifier

The amplifier available was a Vibro-Meter Charge Amplifier type TA 3/C. As described in chapter 2, such amplifiers are suitable for piezoelectric transducers operating in the resonant mode.

The piezoelectric material is a disc of lead zirconate titanate PZT-5H, the most mechanically sensitive material available. The dimensions of the disc were as large as possible such that the completed transducer could easily fit between the central rollers. The disc was mounted to form the transducer after consultation with Plessey Ltd., who recommended that for maximum sensitivity at resonance the piezoelectric disc should be as unrestrained as possible. Polyether foam was therefore used to mount the transducer inside a small aluminium box. Electrostatic shielding was completed by wrapping the box in aluminium foil. Acoustic contact between the piezoelectric

disc and the specimen was ensured by using silicone grease on either side of the foil. The transducer was held in place on the beam by an elastic band. A cross section of the transducer attached to a beam is shown in figure A.2.1.

Events were observed and recorded using a storage oscilloscope. It was found that the frequency of the resonance inside an envelope representing a single event is approximately 130kHz. Thus the minimum time between events to allow their separate discrimination, one quarter of the period, is about 2 μsec It is believed that this frequency corresponds to a coupled thickness/diameter resonance of the disc (Dunegan and Harris 1969). The charge amplifier time constant was therefore set at 10 μsec, and its low pass filter on the highest setting, 300kHz. The variable voltage output of the charge amplifier was used at its maximum amplification, corresponding to a charge of 10 pC being converted to a voltage of 10 V.

A.2.3 Elimination of Background Noise

Several authors have found that a 30 kHz high pass filter was satisfactory for the elimination of background noise when a screw driven loading machine was used. The background noise in the present case consists mostly of audible laboratory noise and Instron noise, and a 30kHz high pass filter was found to be effective. The filter used is a Barr and Stroud Active Filter Module type EF22, wired for Butterworth response. The filter characteristic is shown in Figure A.2.2.

A.2.4 Signal Processing

It is intended that a single event should be recorded as a single count. The conversion of a resonance envelope to a

single pulse may be achieved by using a diode pump and a differentiating circuit*.

A.2.4.1 Diode Pump

A.2.4.1.1. Diode Pump response to a Ring-down Envelope

The object of the diode pump is to 'envelope' the oscillating signal as illustrated by the dotted line:

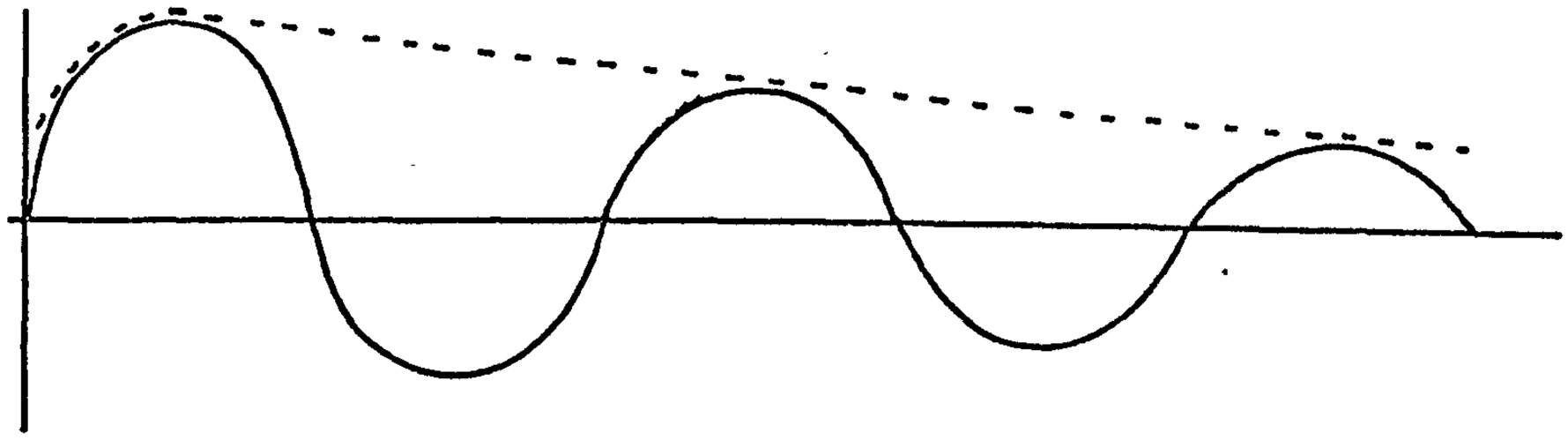

The enveloped signal is characterised by the time constant of the positive rise, T_p, which is the same as the rise time of the oscillating signal, and the time constant of the negative fall, T_N, which is sufficiently long to enclose the oscillating signal.

The general circuit of a diode pump is:

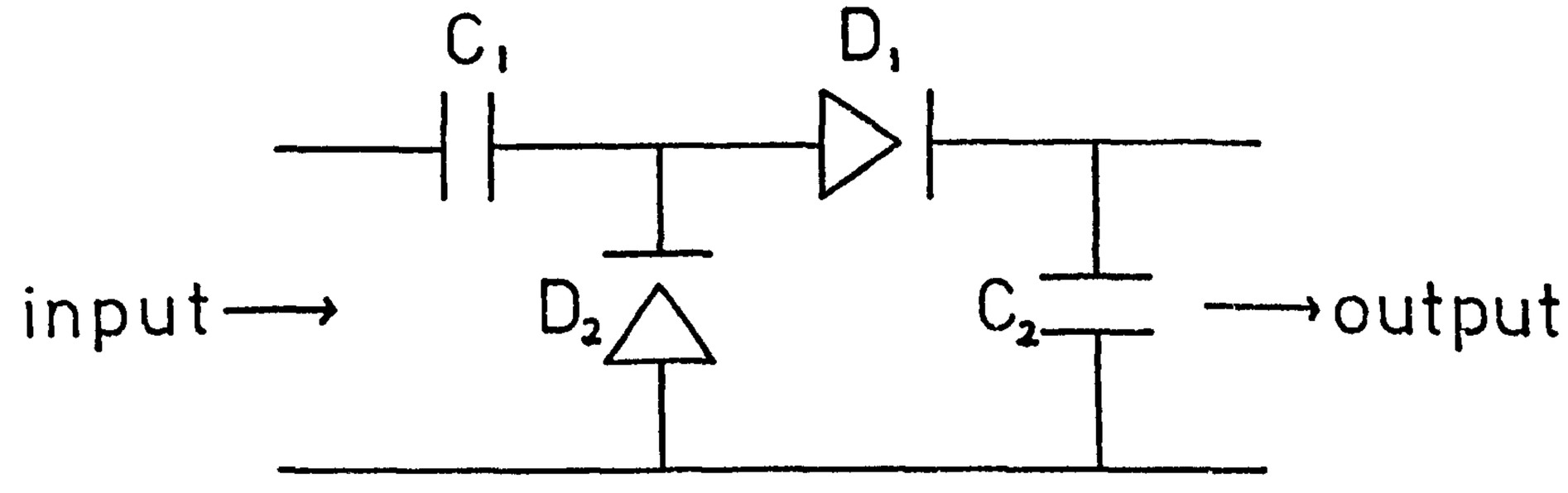

C_1 and C_2 are capacitances: $C_1 \gg C_2$

The diodes D_1, D_2 have forward resistance R_f.

---

* The author would like to thank Mr. R.W. Gerry, of the School of Electrical Engineering, Plymouth Polytechnic, for useful discussions regarding the use of these circuits.

The circuit open for the positive rise is:

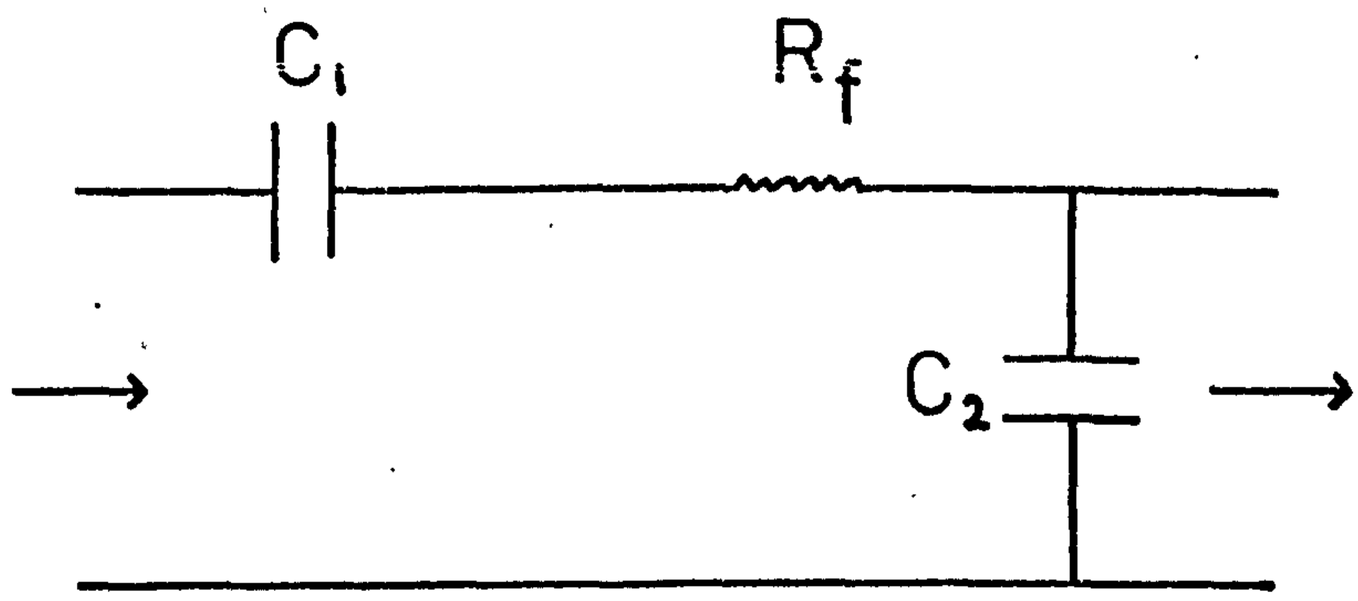

Time Constant, T_p, $= \frac{R_f C_1 C_2}{C_1 - C_2}$

But: $C_1 \gg C_2$

Therefore: $T_p \approx R_f C_2$

$$\text{Gain} = \frac{\text{Output Impedance}}{\text{Input Impedance}}$$

But: impedance arising from $R_f \ll$ impedance arising from C_1
$\ll$ impedance arising from C_2

Therefore: $$\text{Gain} = \frac{\text{Input Capacitance}}{\text{Output Capacitance}}$$

$$= \frac{C_1}{C_1 + C_2}$$

But: $C_1 \gg C_2$

Therefore: Gain ≈ 1

The circuit open for the negative fall is:

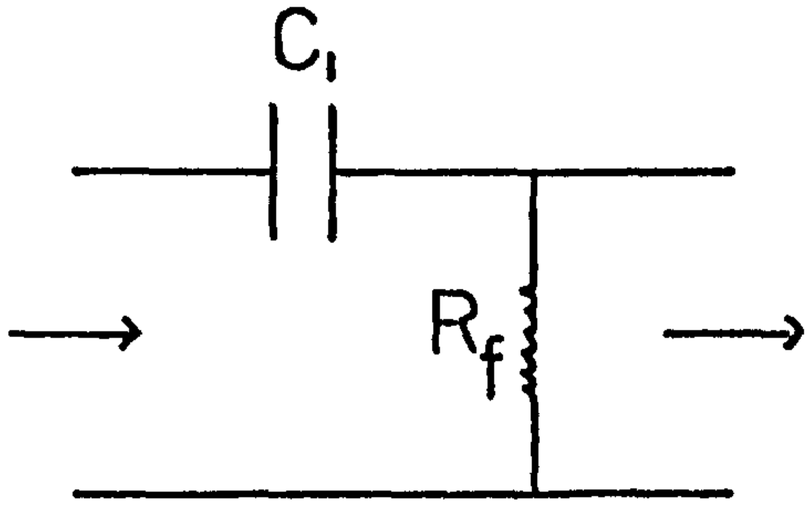

Time Constant, T_N, $= R_f C_1$

Thus by suitable choice of capacitance values, the circuit

be chosen to envelope the signal with negligible attenuation.

The components of the diode pump were selected by first choosing a suitable diode. The time constant of the negative fall is controlled by the forward resistance of the diode and the capacitance value C_1 only, so the capacitance value C_1 was then determined. Finally the capacitance value C_2 was chosen to give a suitable value of the time constant of the positive rise, which is controlled by the forward resistance of the diode and both capacitance values.

A.2.4.1.2 Choice of Diode

Suitable diodes must be chosen such that small signals are not lost and such that large signals do not cause failure of the diodes. Thus the specifications required are:

1. Low threshold current
2. Low forward resistance
3. High overload current

Such properties are shown by germanium point contact diodes. Two suitable diodes are OA 90 and OA 91. OA 90 has lower threshold current and initial resistance than OA 91, and was initially used. However the overload current of this diode is 200 mA, and high signals caused circuit failure from the diode burning out. OA 91 diodes, with overload current of 500 mA, were therefore used. It is noted that the threshold of the diode may act as an unwanted gate and prevent the detection of small signals. This possibility was checked as described in A.2.6; at the maximum amplification of the completed circuit, background noise exceeds the diode threshold.

A.2.4.1.3 Determination of Capacitance Value C_1

The capacitance value C_1, with the forward resistance of the diode, controls the time constant of the negative fall. The time constant should be sufficiently large to envelope the resonance, but should be as short as possible to allow detection of subsequent events. It was anticipated that a suitable time constant would be approximately twice the period of the resonance, about 15 μsec. Thus a suitable value of C_1 would be0.045 μF. The nearest preferred value, 0.047 μF, was therefore used. However it was observed experimentally that this value produced a time constant for the negative fall an order of magnitude greater than the predicted 15 μsec. Progressively smaller values for C_1 were therefore tried, and it was eventually found that a value of 270 pF produced the desired time constant; the time constant is as short as possible while enveloping the signal since the peaks of the oscillating signal may just be observed as discontinuities in the envelope. The theoretical time constant using this value is two orders of magnitude smaller than that observed. Thus further capacitance must be present in the circuit. It is postulated that such capacitance arises from the diode; switching capacitance may arise from the diode having significant switching time with respect to the rise time of the signal.

A.2.4.1.4 Determination of Capacitance Value C_2

The capacitance value C_2, with the capacitance value C_1 and the forward resistance of the diode, controls the time constant of the positive rise. This time constant should be smaller

than the rise time of the oscillating signal so that the charging of the diode pump follows the oscillating signal rise. It is shown in A.2.4.1.1 that the gain of a diode pump decreases with increasing value of C_2. Thus the value of C_2 must be as small as possible while allowing the diode pump charge to follow the oscillating signal rise. A value of 0.001 μF, corresponding to a theoretical time constant of 0.07 μsec, was found to be satisfactory.

A.2.4.1.5 Attenuation of Diode Pump

The capacitance values found to be required do not satisfy the normal condition for a diode pump, $C_1 \gg C_2$. Thus significant attenuation is introduced into the circuit; the theoretical gain of the diode pump is 0.21. This calculated value was confirmed to be approximately correct by experimental observation. It is noted that this attenuation value neglects the apparent diode capacitance encountered during the determination of the capacitance value C_1. This capacitance occurs during switching, thus it might arise when events occur during fall-off of a previous event. However no additional attenuation of such events was observed experimentally, and it is therefore assumed that the switching capacitance may be neglected in the attenuation calculation.

A.2.4.2 Differentiating Circuit

The object of the differentiating circuit is to convert the enveloped signal to a pulse as illustrated by the dotted line:

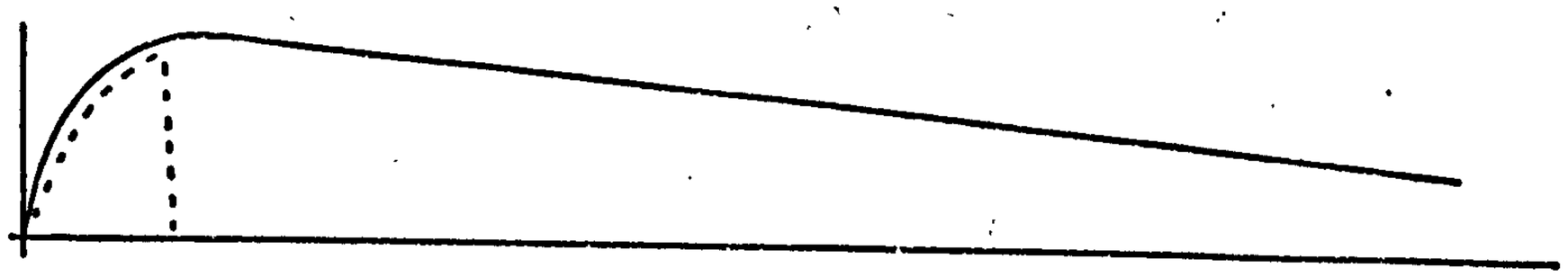

The pulse signal is characterised by its time constant.

The general circuit of a differentiating circuit is:

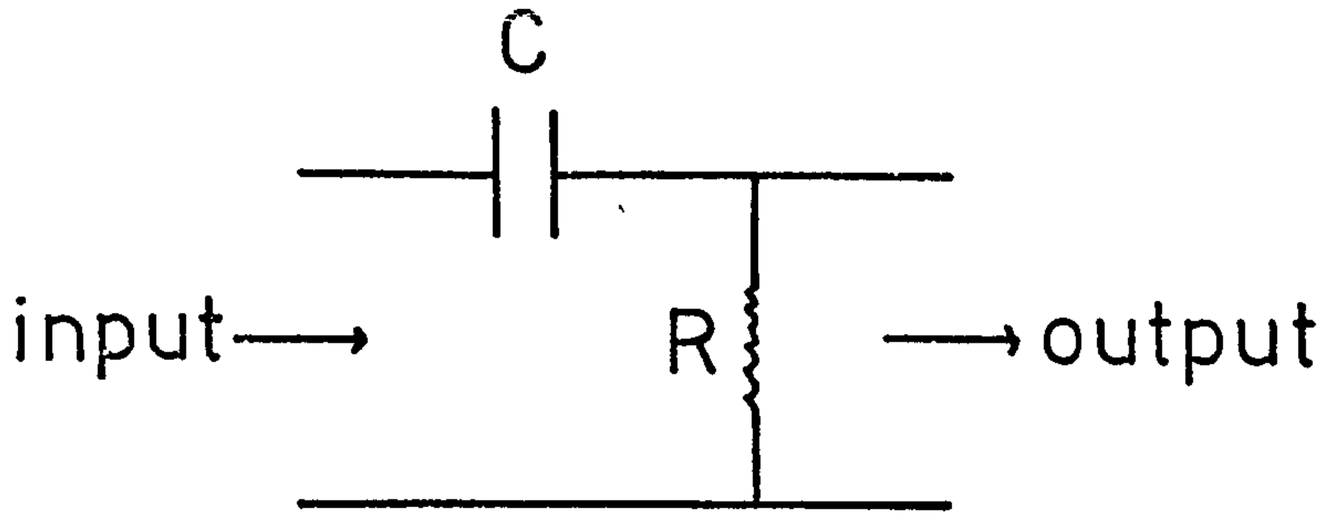

Time Constant = RC

$$\text{Gain} = \frac{\text{Output Impedance}}{\text{Input Impedance}}$$

$$= \frac{R}{(R^2 + 1/C^2)^{\frac{1}{2}}}$$

The conversion of the enveloped signal to a pulse ensures that consecutive signals have maximum opportunity of rising separately above the counter threshold and thus being recorded as separate events. The total pulse time should be smaller than the minimum time interval between consecutive events for their separate detection, 2 μsec.

It is shown above that the time constant of a differentiating circuit is controlled by the product of the resistance and capacitance values, but that the gain increases as the resistance value decreases. Thus a small value of resistance is required to minimise attenuation; however a small value of resistance would load the circuit and could cause change in circuit characteristics. Thus the resistance value was determined experimentally: it was found that 470 Ohms was the smallest value that did not appear to change the signal. The capacitance value was determined experimentally using an oscillator generating a step function. The behaviour of the

circuit recorded by a storage oscilloscope with a capacitance value 220 pF is shown in figure A.2.3; with this value the pulse has completely died down after 2 μsec.

The theoretical time constant and attenuation of this differentiating circuit may be calculated as shown above. The theoretical gain, 0.075, agrees well with that observed experimentally. However the theoretical time constant, 0.093 μsec, is an order of magnitude smaller than that observed. It is postulated that this discrepancy may arise from loading of the circuit by the counter, which was always connected during deduction of the differentiating circuit components.

A.2.4.3 Completed Signal Processing Circuit

The circuit diagram of the completed signal processing circuit is shown in Figure A.2.4. The gain of the circuit, the product of the gains of the diode pump and differentiating circuit, is very low, 0.016.

A.2.5 Counter

The counter available was a Racal type 9835 with a variable trigger level and a BCD output. The number of triggers corresponding to a single recorded count is variable in powers of ten. It was found experimentally that the counter threshold for the pulses produced by the differentiating circuit is 15 mV. To assist the decision of where to set the gate, at maximum sensitivity the circuit should be capable of recording background noise. It was found that additional amplification would be required if the counter was to detect background noise. A variable gain amplifier could be used with the counter trigger level to set the gate.

A.2.6 Second Amplifier

The background noise level after the charge amplifier and high pass filter was observed to be approximately 50 mV. Amplification of approximately x19 is required if this noise level is to be detected by the counter, after the signal processing circuit.

An operational amplifier with a variable gain up to x20 was thus required. It was essential that the amplifier chosen should operate at the resonance frequency, 130 kHz, and should have a recovery time after overload of less than 2 μsec, the rise time of the oscillating signal, so that events are not lost. A Burr-Brown operational amplifier type 3505J was found to meet these specifications. The frequency response of the amplifier at the gain used during test is shown in figure A.2.5; it is seen that the amplifier performs satisfactorily at frequencies above 130 kHz. The amplifier was connected after the charge amplifier. It was confirmed that when the amplifier was set at high gain background noise could be detected by the counter. Thus the two conditions for such detection, that the noise exceeded the counter threshold and that the resulting pulses could be detected by the counter, were fulfilled.

A.2.7 Data Recording

A Bryans two pen recorder was available. Following the usual convention acoustic count is plotted against load. Thus load is plotted on the X-axis and displacement and acoustic count on the two Y-axes.

The digital signal from the counter is converted to an analogue

signal by a Guest 16 bit D/A converter type 328V-4-BCD. Thus four decades were available and a maximum count of 9999 could be recorded in a single sweep of the recorder.

A.2.8 Completed Acoustic Emission Circuit

A block diagram of the acoustic emission circuit is shown in figure A.2.6. Typical events recorded by a storage oscilloscope at various stages in the circuit are shown in figure A.2.7. It can be seen that the signal processing circuit successfully reduces a resonance envelope to a single pulse. This is confirmed by the observation that at intermediate gain of the second amplifier, with the counter set at a low trigger level, an event triggered by a mechanical tap is recorded by a single count. Use of full gain on the second amplifier with the counter at the lowest trigger level allows the counting of background noise. Minimum gain of the second amplifier with the counter at the highest trigger level prevents the detection of any event triggered by a mechanical tap. Thus a full range of the detection gate has been achieved.

A.2.9 Setting of the Gate

The nature of the circuit prevented any quantitative assessment of the gate setting, and thus the decision was largely intuitive. However care was taken to ensure that after the settings were determined they were accurately recorded and reproduced for all tests.

Several trials were made with various settings of the second amplifier gain and counter trigger level. Eventually settings were found such that no counts are recorded during failure of

90° beams, and the number of counts recorded during failure of 0° beams is of the correct order of magnitude for the number of fractured fibres. The gain of the second amplifier is around the middle of its range, and the counter trigger is near its lowest level. The settings were recorded using the circuit shown in figure A.2.8. The potentials at the two points indicated at which an 120 kHz signal from the oscillator was just not recorded were found. Thus these settings are easily reproducable and were used for all tests.

Figure A.2.1 Cross-Section of Acoustic Emission Transducer

(All dimensions in mm)

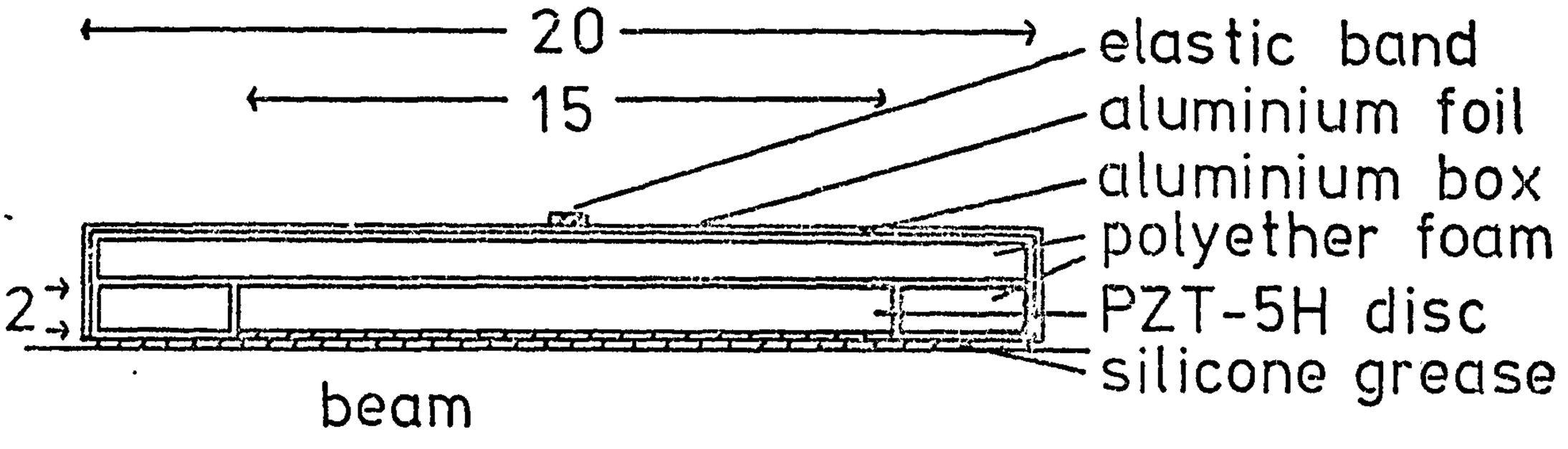

Figure A.2.2 High Pass Filter Characteristic

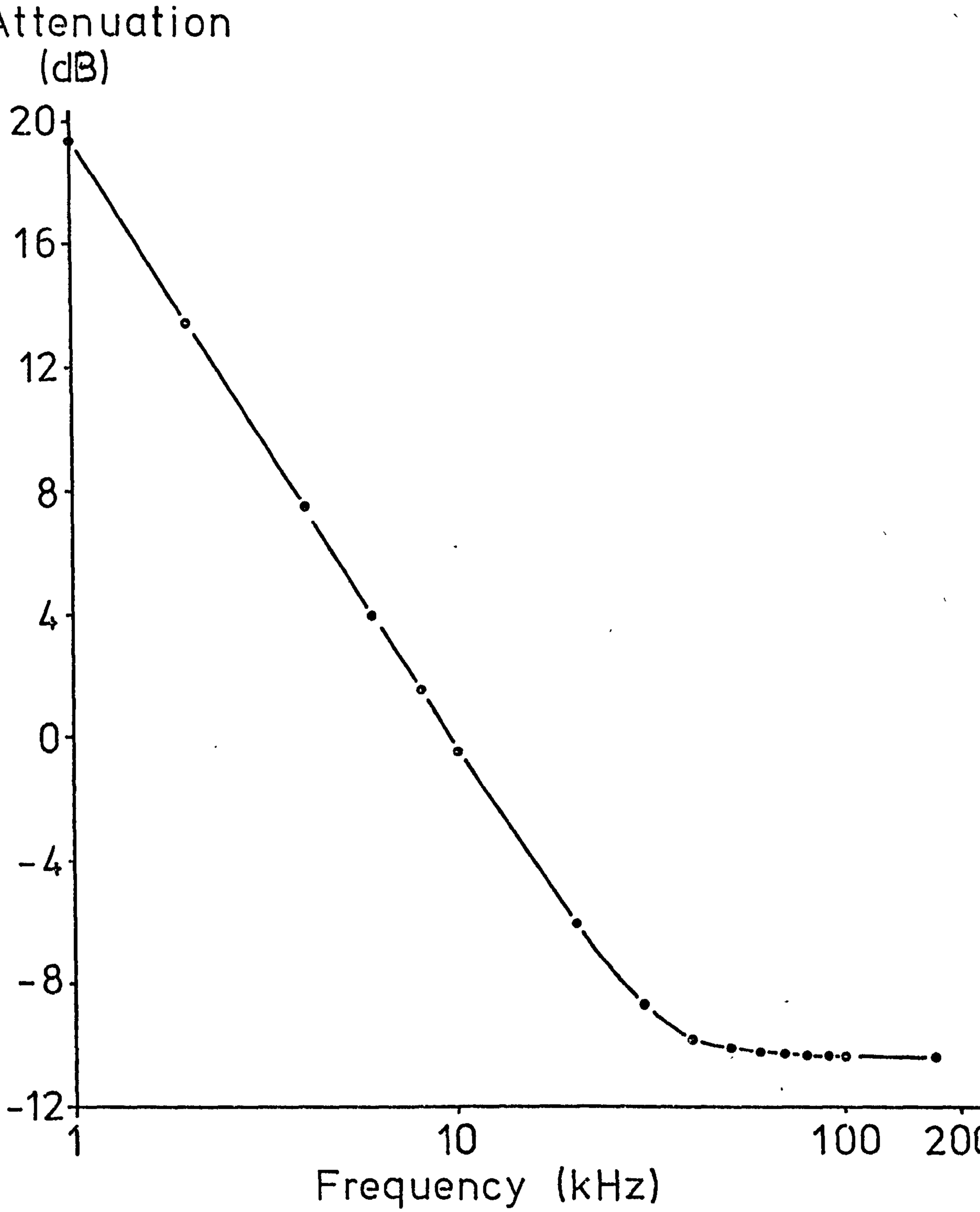

Figure A.2.3 Behaviour of Differentiating Circuit

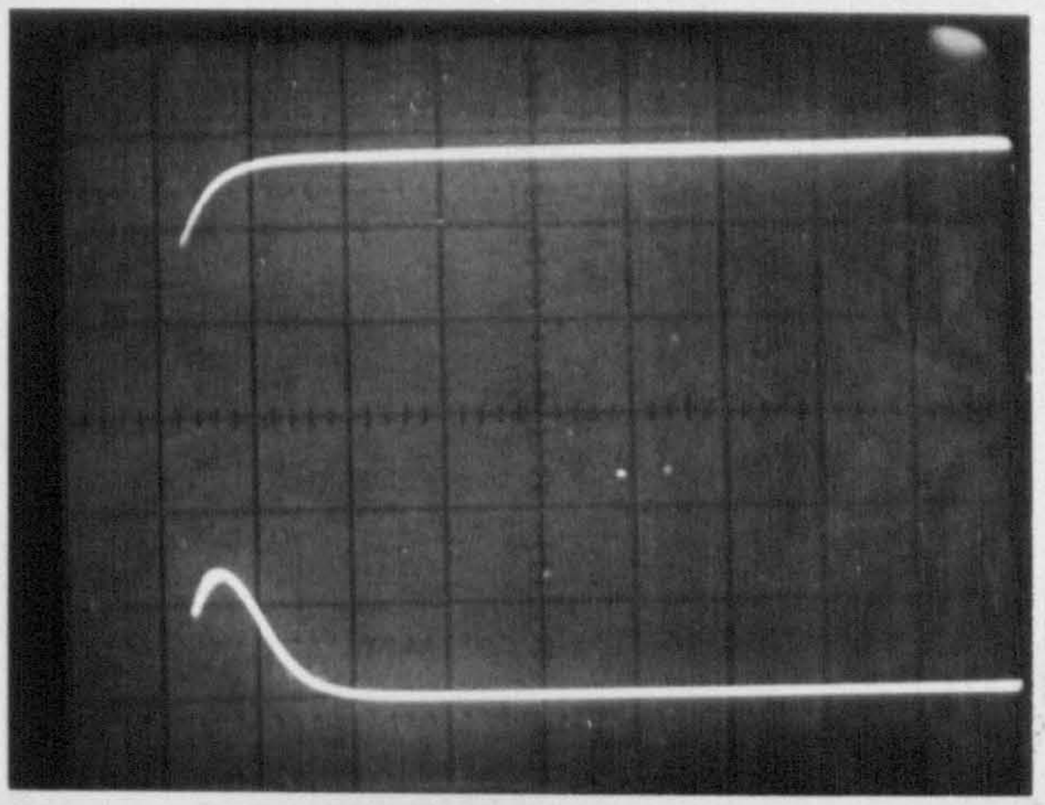

y-axis 1μsec/cm
x-axis Input Step Signal .5V/cm
Output Pulse 50 mV/cm

Figure A.2.4 Signal Processing Circuit

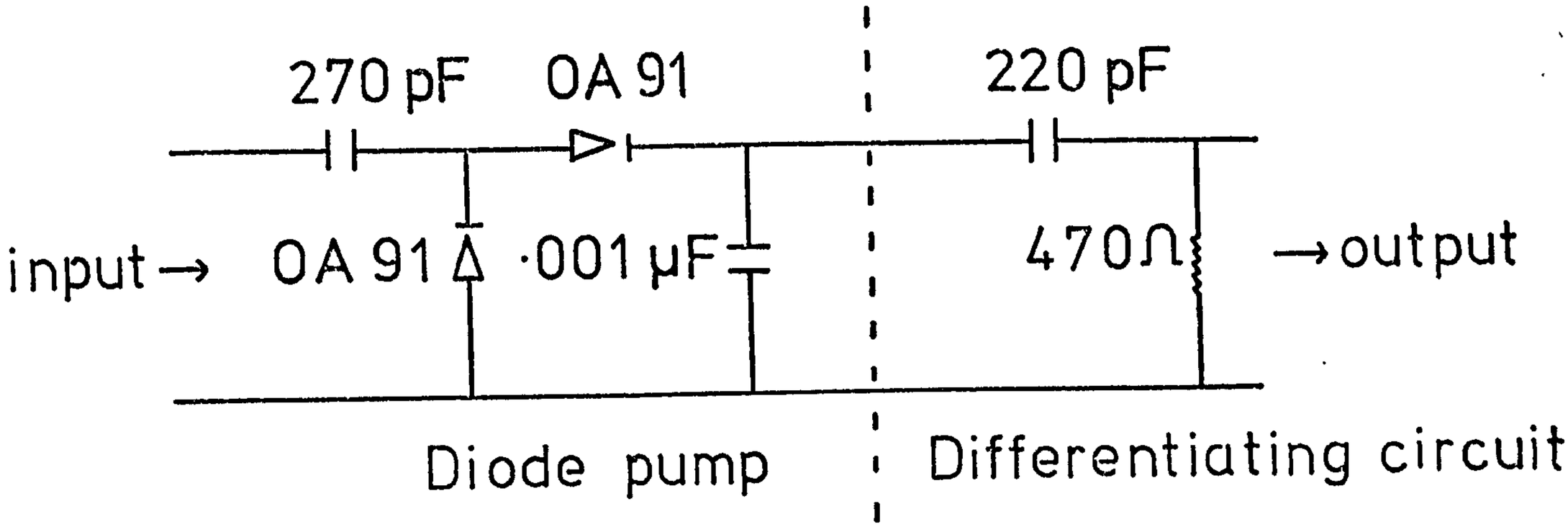

Figure A.2.5 Frequency Response of Second Amplifier at Gain used during Tests

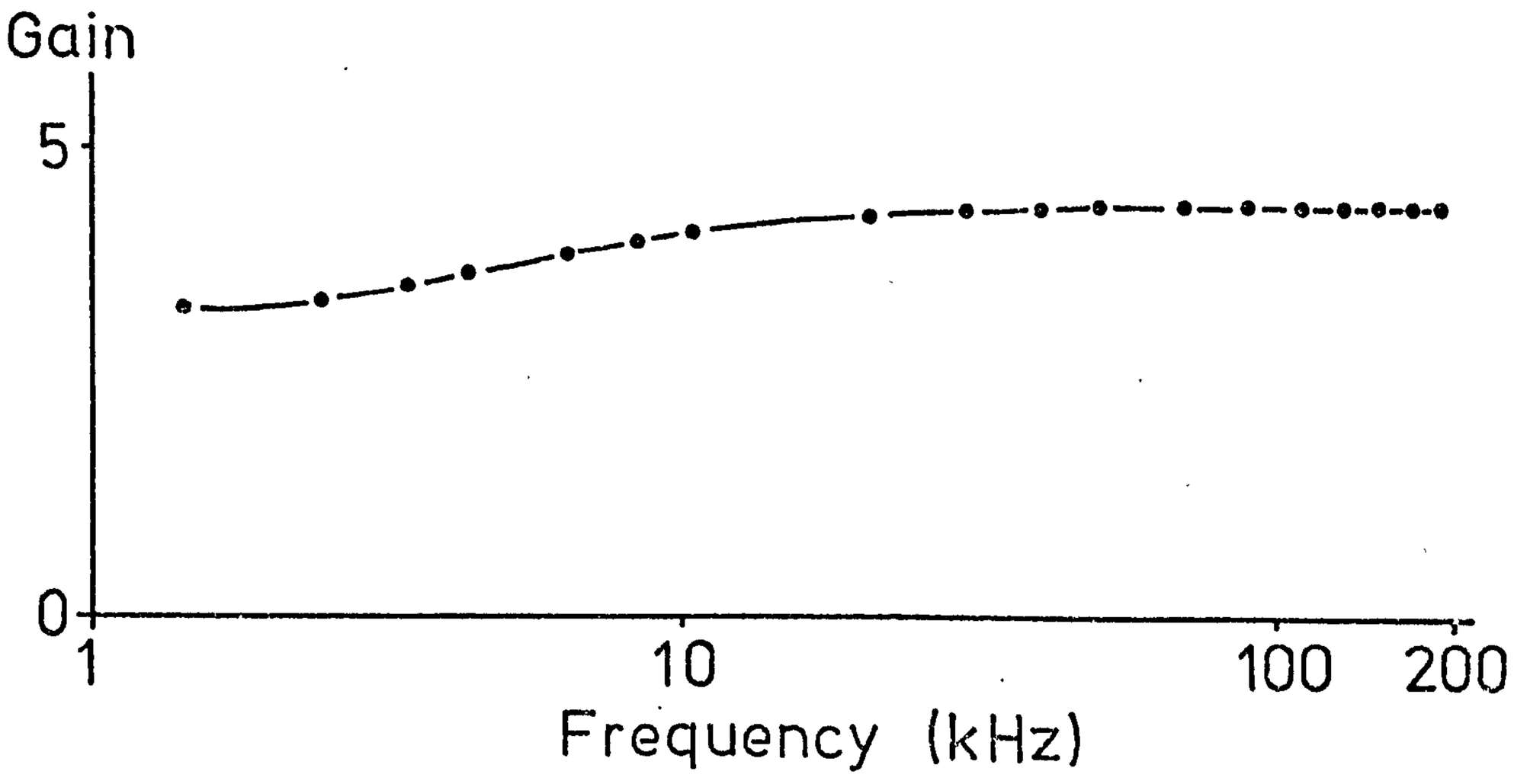

Figure A.2.6 Block Diagram of Acoustic Emission Circuit

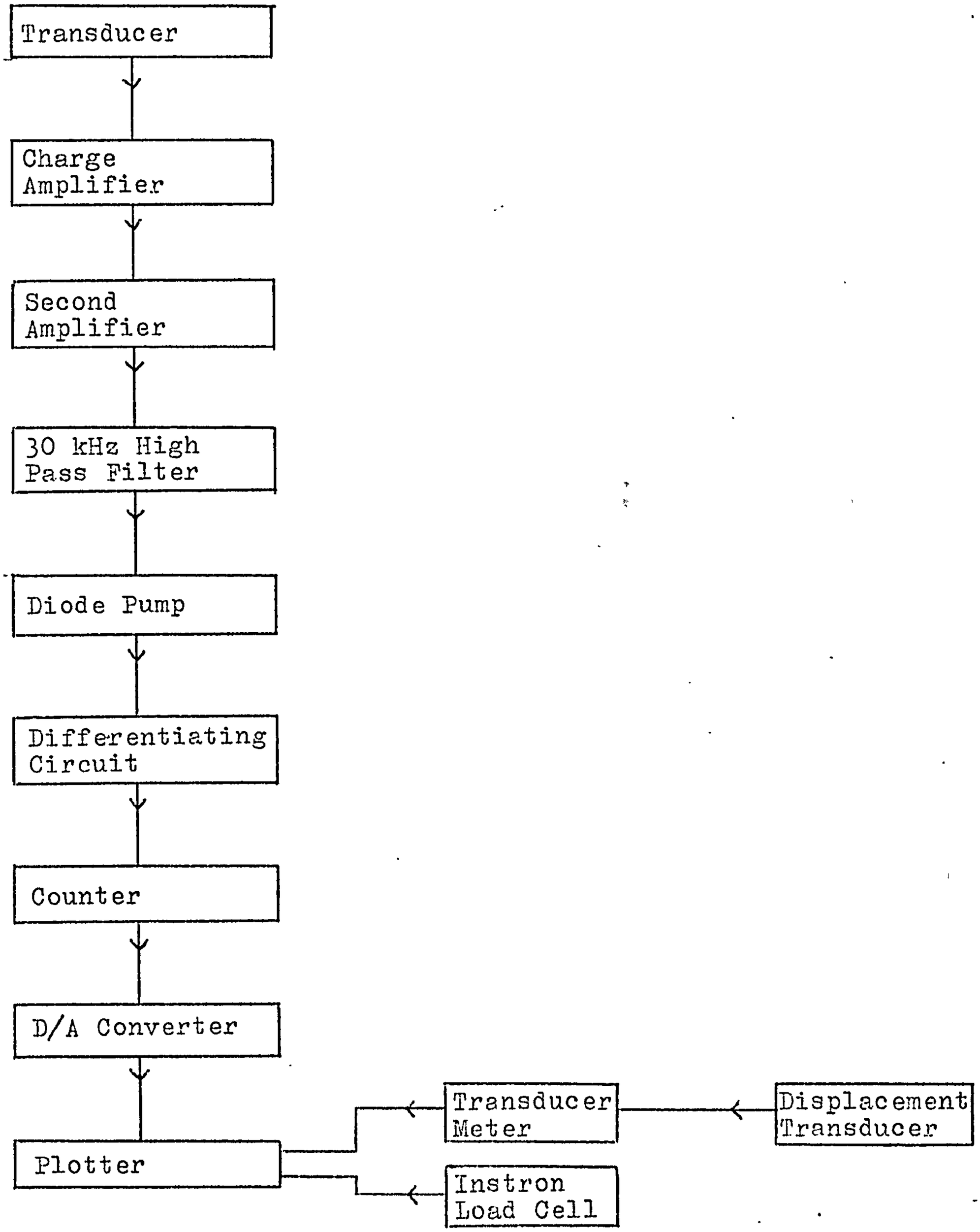

Figure A.2.7 Typical Events Recorded at Various Stages in the Acoustic Emission Circuit

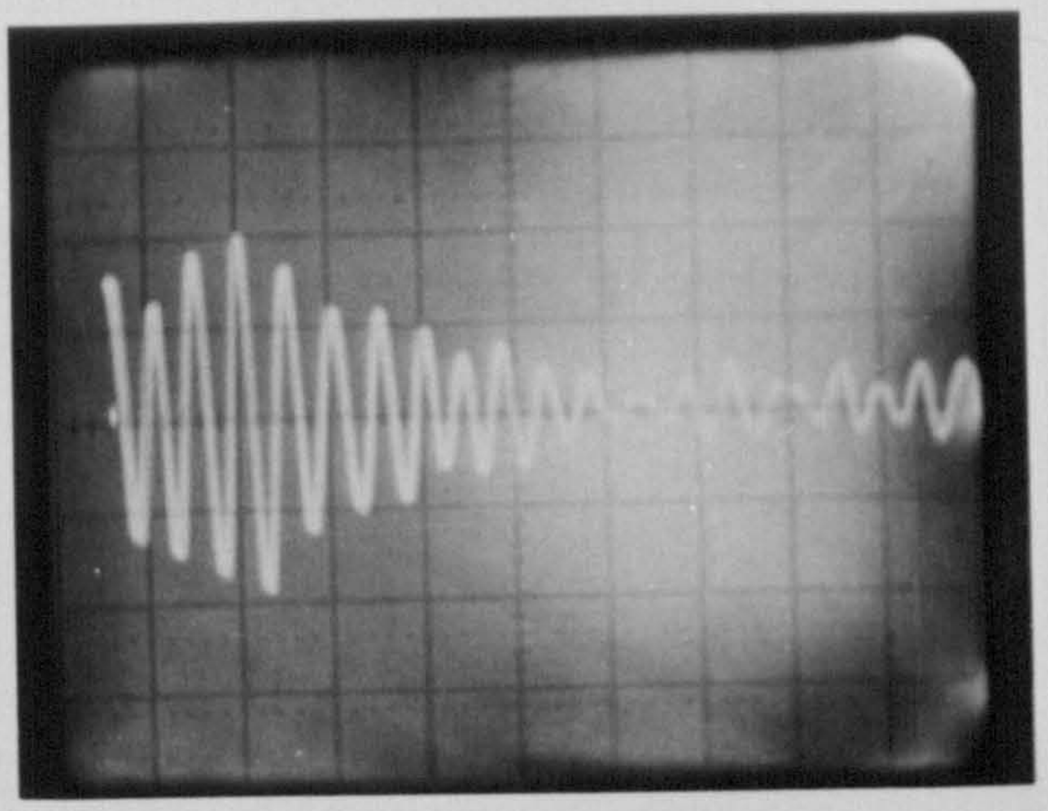

After High Pass Filter

y-axis 1V/cm
x-axis 20μsec/cm

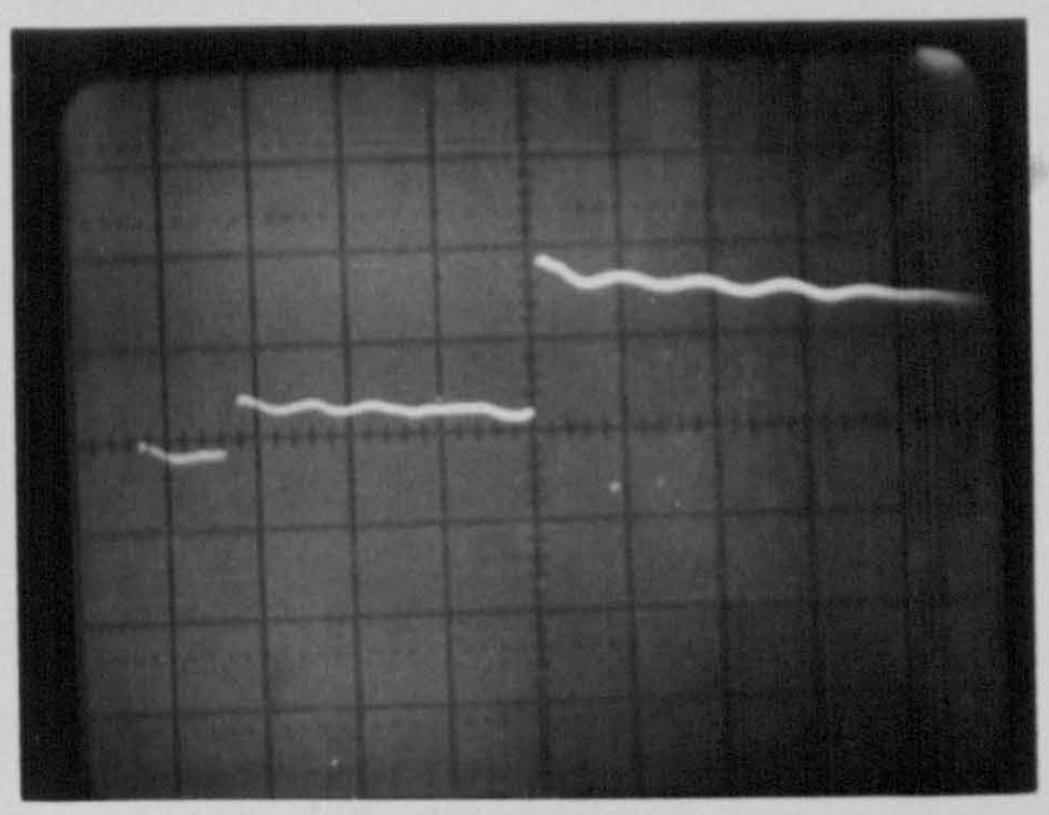

After Diode Pump

y-axis .5V/cm
x-axis 10μsec/cm

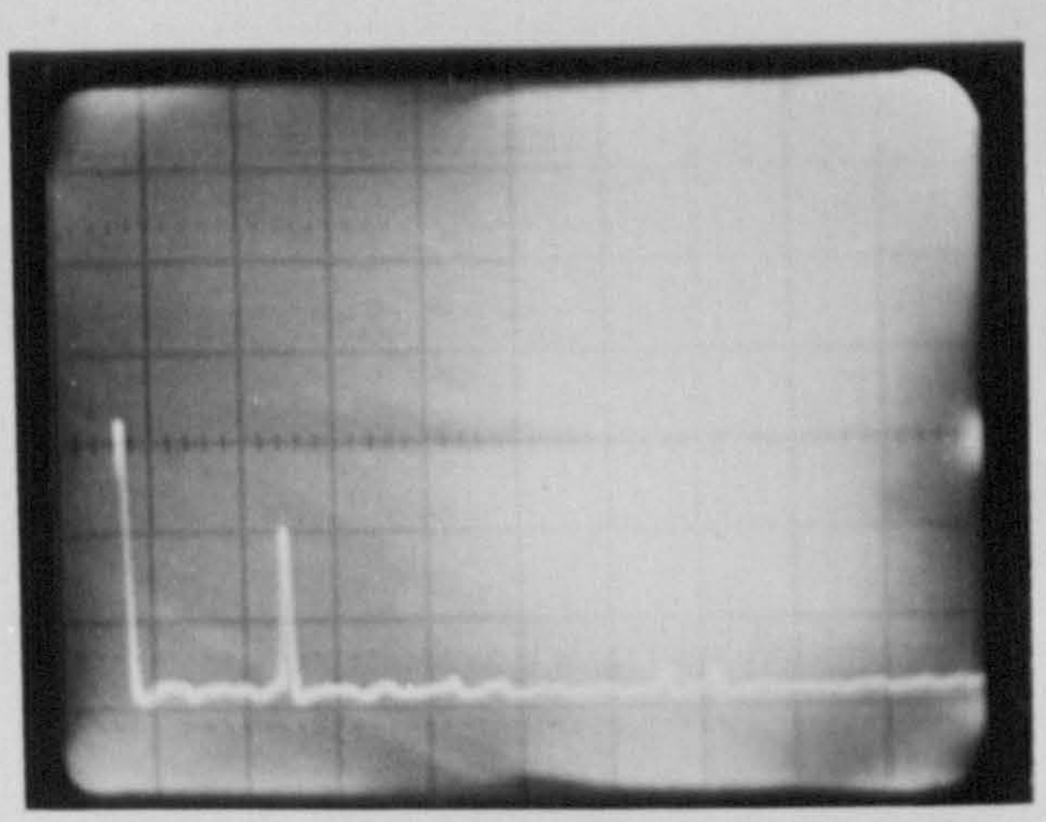

After Differentiating Circuit

y-axis 5 mV/cm
x-axis 20μsec/cm

Figure A.2.8 Circuit for Determination of Gate Settings

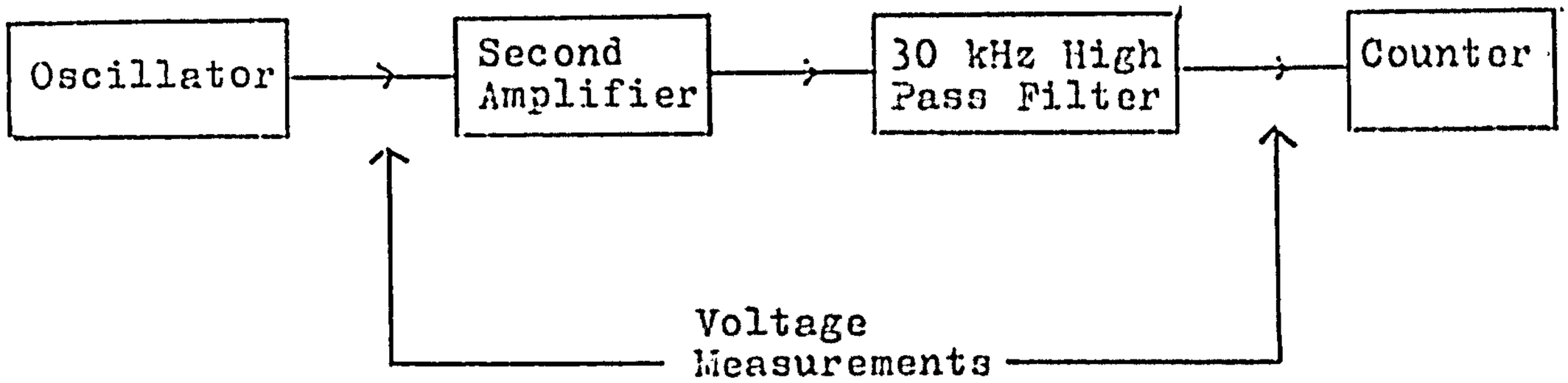

Appendix 3.1 Calculation of Energy Input per Cycle

A.3.1.1 Calculation of Force Exerted by a Moving Coil in terms of the Calibration Factor

During calibration, the coil is excited externally to move in the magnetic field. The voltage, V, induced in a conductor of length l, moving with velocity v, in a magnetic field of flux density B, is given by:

$$V = Blv$$

$$\text{Therefore: } \frac{V}{v} = Bl \qquad 1)$$

During tests, current is passed through the coil such that it moves in the magnetic field. The force, F, exerted on a conductor of length l, carrying a current i, in a magnetic field of flux density B, is given by:

$$F = Bli$$

$$\text{Therefore: } \frac{F}{i} = Bl \qquad 2)$$

Comparing equations 1) and 2); for the same conductor moving in the same magnetic field:

$$\left(\frac{F}{i}\right)_{test} = \left(\frac{V}{v}\right)_{calibration}$$

for an oscillating vibration, all values may be expressed as root mean square values:

$$\left(\frac{Frms}{irms}\right)_{test} = \left(\frac{Vrms}{vrms}\right)_{calibration} \qquad 3)$$

During calibration:

$$\frac{Vrms}{vrms} = Vrms \times \frac{T}{2\pi \times urms}$$

$$= Vrms \times \frac{T}{2\pi} \times \frac{\sqrt{2}}{umax}$$

But: $\frac{V_{rms} \times T}{u_{max}}$ = Calibration Factor, A 4)

Therefore: $\frac{V_{rms}}{v_{rms}} = \frac{A}{\sqrt{2}\pi}$ 5)

Using equation 5) in eq uation 3):

$$\left(\frac{F_{rms}}{i_{rms}}\right)_{test} = \frac{A}{\sqrt{2}\pi} \quad 6)$$

A.3.1.2 Calculation of Energy Input per Cycle in Terms of Force Exerted

At resonance, the displacement will lag the force in phase by 90^{o}, to a close approximation for low damping materials. Assuming motion is sinusoidal:

$$u = u_{max} \sin wt \quad 7)$$

$$F = F_{max} \sin (wt + \pi/2) = F_{max} \cos wt \quad 8)$$

$$\text{Energy Input per cycle} = \int_{t=o}^{T} F \, \delta u$$

Using 7) and 8) :

Energy Input per cycle $= \pi F_{max} u_{max}$ 9)

A.3.1.3 Calculation of Energy Input per Cycle in terms of the Calibration Factor

Equation 9);

Energy Input per cycle $= \pi F_{max} u_{max}$

$= \pi \sqrt{2} F_{rms} u_{max}$

Using equation 6)

Energy Input per cycle = A $i_{rms} u_{max}$.

Appendix 3.2 Vibration Analysis for the Free-Free Rig, neglecting the Rotary Inertia of the End Masses

A.3.2.1 Solution of the Classical Wave Equation

Making the usual assumptions for a Bernoulli-Euler beam, the equation of motion for free lateral vibration is:

$$EI\frac{d^4u}{dx^4} + \rho A\frac{d^2u}{dt^2} = 0$$

where: E = dynamic Youngs modulus

I = second moment of area

u = transverse displacement

x = distance along beam length

ρ = density of beam material

A = cross-sectional area of beam

t = time

The solution of the equation is of the form:

$$u_n(x) = A_n \sin k_n x + B_n \cos k_n x + C_n \sinh k_n x + D_n \cosh k_n x$$

where: k_n = wavelength number

$$k_n = \frac{\lambda_n}{l}$$

where: λ_n = frequency number

l = beam length

It is assumed that at least one of the constants A_n, B_n, C_n, D_n, is non-zero.

The boundary conditions for the free-free mode with equal masses M/2 at each end are given by:

at $x=0$ $\quad \frac{d^2u}{dx^2} = 0$ (zero bending moment) 1)

$$EI\frac{d^3u}{dx^3} + \frac{M}{2}\frac{d^2u}{dt^2} = 0$$ (zero net shear force) 2)

at $x=\frac{l}{2}$ $\quad \frac{du}{dx} = 0$ (zero gradient) 3)

$$\frac{d^3u}{dx^3} = 0$$ (zero shear force) 4)

Substituting the general solution into the boundary conditions 1) 3) and 4) yields the relationships between the constants:

$$B_n = D_n \qquad 5)$$

$$A_n = B_n \tan \frac{\lambda_n}{2} \qquad 6)$$

$$C_n = -B_n \tanh \frac{\lambda_n}{2} \qquad 7)$$

Substituting the general solution and 5) 6) and 7) into the boundary condition 2) yields the relationship between the frequency number and the mass ratio:

$$\sin \frac{\lambda_n}{2} \cosh \frac{\lambda_n}{2} + \cos \frac{\lambda_n}{2} \sinh \frac{\lambda_n}{2} + \frac{M}{m} \lambda_n \cos \frac{\lambda_n}{2} \cosh \frac{\lambda_n}{2} = 0$$

For the fundamental mode:

$$\sin \frac{\lambda}{2} \cosh \frac{\lambda}{2} + \cos \frac{\lambda}{2} \sinh \frac{\lambda}{2} + \frac{M}{m} \lambda \cos \frac{\lambda}{2} \cosh \frac{\lambda}{2} = 0 \qquad 8)$$

It is noted that for zero mass ratio, the equation reduces to that for symmetric free-free vibrations.

Using the relationship between the constants, 5), 6), and 7) and the condition that:

$$\text{at } x = l/2,\ u(x) = u_{max}$$

the mode shape for the fundamental mode is given by:

$$u(x) = \frac{u_{max}}{\cos\lambda/2 + \cosh\lambda/2} (\sin \lambda/2 \cosh \lambda/2 \sin \lambda x/l +$$
$$\cos\lambda/2 \cosh\lambda/2 \cos\lambda x/l - \cos \lambda/2 \sinh\lambda/2 \sinh\lambda x/l +$$
$$\cos\lambda/2 \cosh\lambda/2 \cosh \lambda x/l) \qquad 9)$$

A.3.2.2 Calculation of Bending Strain Energy Stored

The bending strain energy stored, U_B, is given by:

$$U_B = \frac{EI}{2} \int_0^l \left(\frac{d^2u}{dx^2} \right)^2 dx$$

From equation 9), using integration by parts:

$$U_B = \frac{EI}{4} u^2_{max} \left(\frac{\lambda}{l} \right)^3 \frac{1}{(\cos \lambda/2 + \cosh \lambda/2)}$$

$$[\cosh^2 \lambda/2 (\lambda - 2 \sin \lambda/2 \cos \lambda/2) + \cos^2 \lambda/2 (\lambda - 2 \sinh \lambda/2 \cosh /2)] \quad 10)$$

A.3.2.3 Calculation of Maximum Surface Stress

For a beam in pure bending:

$$\frac{\sigma}{z} = \frac{\text{Bending Moment}}{I}$$

where: σ = longitudinal stress

z = distance from neutral axis

But: Bending Moment = $EI \frac{d^2u}{dx^2}$

Therefore: $\sigma = zE \frac{d^2u}{dx^2}$

The maximum surface stress occurs at the mid-point of the beam on the beam outer surface.

Therefore: $\sigma_{max} = \frac{h}{2} E \left(\frac{d^2u}{dx^2} \right)_{x = l/2}$

Using equation 9)

$$\sigma_{max} = \frac{h}{2} E \left(\frac{\lambda}{l} \right)^2 u_{max} \frac{\cos \lambda/2 - \cosh \lambda/2}{\cos \lambda/2 + \cosh \lambda/2} \quad 11)$$

Appendix 3.3 Vibration Analysis for the Free-free Rig, including the Rotary Inertia of the End Masses

A.3.3.1 Solution of the Classical Wave Equation

Making the usual assumptions for a Bernoulli-Euler beam, the equation of motion for free lateral vibration is:

$$EI\frac{\partial^4 u}{\partial x^4} + \rho A\frac{\partial^2 u}{\partial t^2} = 0$$

where the notation is that defined in Appendix 3.2

The solution of the equation is of the form:

$$u_n(x) = A_n \sin k_n x + B_n \cos k_n x + C_n \sinh k_n x + D_n \cosh k_n x$$

where: k_n = wavelength number

$$k_n = \frac{\lambda_n}{l}$$

where: λ_n = frequency number

l = beam length

It is assumed that at least one of the constants A_n, B_n, C_n, D_n, is non-zero.

The boundary conditions for the free-free mode with equal masses M/2 with rotary inertia I_c at each end are given by:

at $x = 0$ $\quad EI\frac{\partial^2 u}{\partial x^2} - I_c\ddot{\theta} = 0$ (zero net bending moment) 1)

$$EI\frac{\partial^3 u}{\partial x^3} + \frac{M}{2}\frac{\partial^2 u}{\partial t^2} = 0 \quad \text{(zero net shear force)} \quad 2)$$

at $x = \frac{l}{2}$ $\quad \frac{\partial u}{\partial x} = 0$ (zero gradient) 3)

$$\frac{\partial^3 u}{\partial x^3} = 0 \quad \text{(zero shear force)} \quad 4)$$

where: θ = angular displacement at end.

$$\ddot{\theta} = \frac{\partial}{\partial x}\left(\frac{\partial^2 u}{\partial t^2}\right)$$

Substituting the general solution into the boundary conditions 3) and 4) yields the relationships between the constants:

$$C_n = -D_n \tanh \frac{\lambda_n}{2} \qquad 5)$$

$$A_n = B_n \tan \frac{\lambda_n}{2} \qquad 6)$$

Substituting the general solution and 5) and 6) into the boundary condition 1) yields the relationship:

$$D_n = B_n\left(\frac{ml^2 - I_c\lambda_n^3 \tan\lambda n/2}{ml^2 - I_c\lambda_n^3 \tanh\lambda_n/2}\right) \qquad 7)$$

Substituting the general solution and 5) and 6) into the boundary condition 2) yields the relationship:

$$D_n = -B_n\left(\frac{2\ m\ \tan\lambda_n/2 + \lambda_n M}{2\ m\ \tanh\lambda_n/2 + \lambda_n M}\right)$$

Comparing equations 7) and 8) yields the relationship between the frequency number and the beam and end mass parameters:

$$\frac{ml^2 - I_c\lambda_n^3 \tan\lambda_n/2}{ml^2 - I_c\lambda_n^3 \tanh\lambda_n/2} + \frac{2\ m \tan\lambda_n/2 + \lambda_n M}{2\ m \tanh\lambda_n/2 + \lambda_n M} = 0$$

For the fundamental mode:

$$\frac{ml^2 - I_c\lambda^3 \tan\lambda/2}{ml^2 - I_c\lambda^3 \tanh\ \lambda/2} + \frac{2\ m\ \tan\ \lambda/2 + \lambda M}{2\ m\ \tanh\lambda/2 + \lambda M} = 0 \qquad 9)$$

It is noted that for zero coil inertia, the equation reduces to equation 8) of appendix 3.2, when this inertia was ignored.

Using the relationships between the constants 5) and 6), and 7) or 8), and the condition that:

$$\text{at } x = l/2,\ u(x) = u_{max}$$

the mode shape for the fundamental mode is given by:

$$u(x) = \frac{u_{max}}{X\cos\lambda/2 + \cosh\lambda/2}\,(\sin\lambda/2\cosh\lambda/2\ \sin\lambda x/l$$

$$+\cos\lambda/2\cosh\lambda/2\cos\lambda x/l. - X\cos\lambda/2$$

$$\sinh\lambda/2\sinh\lambda x/l + X\cos\lambda/2\cosh\lambda/2\cosh\lambda x/l) \quad 10$$

where: $$X = \frac{ml^2 - I_c\lambda^3\tan\lambda/2}{ml^2 - I_c\lambda^3\tanh\lambda/2}$$

$$= -\frac{2\ m\ \tan\lambda/2 + \lambda M}{2\ m\ \tanh\lambda/2 + \lambda M}$$

It is noted that for zero coil inertia, that is X = 1, equation 10) reduces to equation 9) of Appendix 3.2, when this inertia was ignored.

A.3.3.2 Calculation of Bending Strain Energy Stored

The bending strain energy stored, U_B, is given by:

$$U_B = \frac{EI}{2}\int_0^l \left(\frac{d^2u}{dx^2}\right)^2 dx$$

From equation 10), using integration by parts:

$$U_B = \frac{EI}{4}\,u^2_{max}\left(\frac{\lambda}{l}\right)^3 \frac{l}{(X\cos\lambda/2 + \cosh\lambda/2)}$$

$$[\cosh^2\lambda/2(\lambda + 2\sin\lambda/2\cos\lambda/2(1-2X)) \quad 11)$$

$$+ X\cos^2\lambda/2(X\lambda + 2\sinh\lambda/2\cosh\lambda/2(X-2))]$$

It is noted that for zero coil inertia, that is X = 1, the equation reduces to equation 10) of Appendix 3.2, when this inertia was ignored.

A.3.3.3. Calculation of Maximum Surface Stress

For a beam in pure bending:

$$\frac{\sigma}{z} = \frac{\text{Bending Moment}}{I}$$

where: σ = longitudinal stress

z = distance from neutral axis

But: Bending Moment = $E\ I\ \frac{d^2u}{dx^2}$

Therefore: $\sigma = z\ E\ \frac{d^2u}{dx^2}$

The maximum surface stress occurs at the mid-point of the beam on the beam outer surface.

$$\text{Therefore: } \sigma_{max} = \frac{h}{2}\ E\ \left(\frac{d^2u}{dx^2}\right)_{x\ =\ l./2}$$

Using equation 10)

$$\sigma_{max} = \frac{h}{2}\ E\ \left(\frac{\lambda}{l}\right)^2\ u_{max}\ \frac{X\ \cos\lambda/2\ -\ \cosh\lambda/2}{X\ \cos\lambda/2\ +\ \cosh\lambda/2} \qquad 12)$$

It is noted that for zero coil inertia, that is X = 1, the equation reduces to equation 11) of appendix 3.2, when this inertia was ignored.

Appendix 3.4 Relationship between True and Measured Specific Damping

Capacity assuming Energy loss

$$\text{Specific Damping Capacity, } \Psi = \frac{\text{Energy absorbed during cycle, } \Delta U}{\text{Total Strain Energy stored during that cycle, } U}$$

Consider measured values:

$$\Psi_m = \Delta \frac{U}{U}_m$$

But: $\Delta U_m = \Delta U + Z$

where: ΔU = Energy absorbed by beam

Z = Energy Loss

Therefore: $\Psi_m = \frac{\Delta U + Z}{U}$

$$= \Psi_T + \frac{Z}{U}$$

Where: Ψ_T = true specific damping capacity of beam

Appendix 3.5 Vibration Analysis for the Cantilever Rig, including the Rotary Inertia of the End Mass

A.3.5.1 Solution of the Classical Wave Equation

Making the usual assumptions for a Bernoulli-Euler beam, the equation of motion for free lateral vibration is:

$$EI\frac{d^4u}{dx^4} + \rho A\frac{d^2u}{dt^2} = 0$$

where the notation is that defined in Appendix 3.2

The solution of the equation is of the form:

$$u_n(x) = A_n \sin k_n x + B_n \cos k_n x + C_n \sinh k_n x + D_n \cosh k_n x$$

where: k_n = wavelength number

$$k_n = \frac{\lambda n}{l}$$

where: λ_n = frequency number

l = beam length

It is assumed that at least one of the constants A_n, B_n, C_n, D_n, is non-zero.

The boundary conditions for the cantilever mode, encastré at x = 0, with mass M with rotary inertia I_c at the free end are given by:

at $x = 0$ $u = 0$ (zero deflection) 1)

$$\frac{du}{dx} = 0$$ (zero gradient) 2)

at $x = l$ $EI\frac{d^2u}{dx^2} + I_c\ddot{\theta} = 0$ (zero not bending moment) 3)

$$EI\frac{d^3u}{dx^3} - M\frac{d^2u}{dt^2} = 0$$ (zero net shear force) 4)

where: θ = angular displacement at end

$$\theta = \frac{d}{dx}\left(\frac{d^2u}{dt^2}\right)$$

Substituting the general solution into the boundary conditions 1) and 2) yields the relationships between the constants:

$$B_n = -D_n \qquad 5)$$

$$A_n = -C_n \qquad 6)$$

Substituting the general solution and 5) and 6) into the boundary condition 3) yields the relationship:

$$C_n = D_n \frac{I_c\lambda^3{}_n(\sin\lambda_n + \sinh\lambda_n) - ml^2(\cos\lambda_n + \cosh\lambda_n)}{I_c\lambda^3{}_n(\cos\lambda_n - \cosh\lambda_n) + ml^2(\sin\lambda_n + \sinh\lambda_n)} \qquad 7)$$

Substituting the general solution and 5) and 6) into the boundary condition 4) yields the relationship:

$$C_n = D_n \frac{m(\sin\lambda_n - \sin\lambda_n) + \lambda_n M(\cos\lambda_n - \cos\lambda_n)}{m(\cos\lambda_n + \cosh\lambda_n) - \lambda_n M(\sin\lambda_n - \sinh\lambda_n)} \qquad 8)$$

Comparing equations 7) and 8) yields the relationship between the frequency number and the beam and end mass parameters:

$$\frac{I_c\lambda^3{}_n(\sin\lambda_n + \sinh\lambda_n) - ml^2(\cos\lambda_n + \cosh\lambda_n)}{I_c\lambda^3{}_n(\cos\lambda_n - \cosh\lambda_n) + ml^2(\sin\lambda_n + \sinh\lambda_n)} -$$

$$\frac{m(\sin\lambda_n - \sinh\lambda_n) + \lambda_n M(\cos\lambda_n - \cosh\lambda_n)}{m(\cos\lambda_n + \cosh\lambda_n) + \lambda_n M(\sin\lambda_n - \sinh\lambda_n)} = 0$$

For the fundamental mode:

$$\frac{I_c\lambda^3(\sin\lambda + \sinh\lambda) - ml^2(\cos\lambda + \cosh\lambda)}{I_c\lambda^3(\cos\lambda - \cosh\lambda) + ml^2(\sin\lambda + \sinh\lambda)} -$$

$$\frac{m(\sin\lambda - \sinh\lambda) + \lambda M(\cos\lambda - \cosh\lambda)}{m(\cos\lambda + \cosh\lambda) + \lambda M(\sin\lambda - \sinh\lambda)} = 0 \qquad 9)$$

It is noted that for zero end mass and inertia, the equation reduces to that for a simple cantilever beam:

Using the relationships between the constants 5) and 6), and 7) or 8), and the condition that:

at $x = l$, $u(x) = u_{max}$

the mode shape for the fundamental mode is given by:

$$u(x) = \frac{u_{max}}{Y(\sinh\lambda - \sin\lambda) + (\cosh\lambda - \cos\lambda)} \left[Y(\sinh\lambda\, x/l - \sin\lambda\, x/l) + (\cosh\lambda\, x/l - \cos\lambda\, x/l) \right] \quad 10)$$

where: $$Y = \frac{I_c\lambda^3(\sin\lambda + \sinh\lambda) - ml^2(\cos\lambda + \cosh\lambda)}{I_c\lambda^3(\cos\lambda - \cosh\lambda) + ml^2(\sin\lambda + \sinh\lambda)}$$

$$= \frac{m(\sin\lambda - \sinh\lambda) + \lambda M(\cos\lambda - \cosh\lambda)}{m(\cos\lambda + \cosh\lambda) + \lambda M(\sin\lambda - \sinh\lambda)}$$

A.3.5.2 Calculation of Bending Strain Energy Stored

The bending strain energy stored, U_B is given by:

$$U_B = \frac{EI}{2} \int_0^L \left(\frac{d^2u}{dx^2} \right)^2 dx$$

From equation 10), using integration by parts:

$$U_B = \frac{EI}{4} \; u^2_{max} \left(\frac{\lambda}{l}\right)^2 \frac{1}{\left[Y(\sinh\lambda - \sin\lambda) + (\cosh\lambda - \cos\lambda)\right]}$$

$$\left[Y^2(-\sin\lambda\cos\lambda + 2\sin\lambda\cosh\lambda - 2\cos\lambda\sinh\lambda + \sinh\lambda\cosh\lambda) + Y(\sin^2\lambda + 4\sin\lambda\sinh\lambda - \cos^2\lambda + \sinh^2\lambda + \cosh^2\lambda) + (\sin\lambda\cos\lambda + 2\cos\lambda\sinh\lambda + 2\sin\lambda\cosh\lambda + \sinh\lambda\cosh\lambda + 2) \right] \quad 11)$$

A.3.5.3 Calculation of Maximum Surface Stress

For a beam in pure bending:

$$\frac{\sigma}{z} = \frac{\text{Bending Moment}}{I}$$

where: σ = longitudinal stress

z = distance from neutral axis

But: Bending Moment = $E\, I \frac{d^2u}{dx^2}$

Therefore: $\sigma = z\, E \frac{d^2u}{dx^2}$

The maximum surface stress occurs at the encastré end on the beam outer surface.

Therefore: $\sigma_{max} = \frac{h}{2} \quad E \quad \left(\frac{d^2u}{dx^2}\right)_{x=0}$

Using equation 10)

$$\sigma_{max} = h\ E \left(\frac{\lambda}{l}\right)^2 \frac{u_{max}}{Y(\sinh\lambda - \sin\lambda) + (\cosh\lambda - \cos\lambda)}$$

Appendix 3.6 Receptance Analysis of Flexural Damping Results

A.3.6.1 Introduction

A receptance is defined as the relationship between a harmonic force and a deflection:

Receptance = Deflection / Force

Receptances are functions of frequency since amplitude for a given force varies with the frequency of application of that force.

Receptances may be direct or cross. A direct receptance applies to the measurement of deflection at the same point as the implication of the force. A cross receptance applies to the measurement of deflection at a different point from the implication of the force.

Receptance analysis of beams in flexure is achieved by considering receptances on two axes: one axis represents deflection, the other slope. The net slope is the sum of two component slopes:

Net slope = Slope resulting from bending + slope resulting from shear

The receptances on the axis representing the slope used in the present analysis are those representing the slope from bending only. This is the distinction between the receptances used here and those presented by Bishop and Johnson (1960).

The analysis is used to determine specific damping capacity. However the effect is not included in the analysis of the vibration. This may be justified by the low values of specific damping capacity of all the materials tested.

A.3.6.1.1 The System Analysed

The system to be analysed consists of five parts:

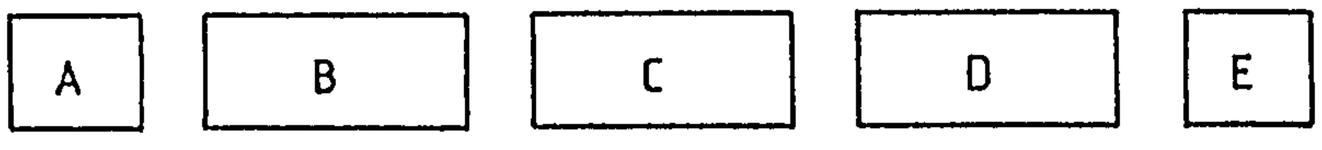

B,C,D represent the beam under test. If the beam is damaged part C will represent the damaged area and will thus have different stiffness parameters to parts B and D. For the free-free rig, parts A and E represent the exciting coils. For the cantilever rig, part A represents the abutement and part E the exciting coil.

A.3.6.1.2 Notation

The receptances of A are written as α, those of B as β, etc. The axis referring to deflection or applied shear force is P, that referring to slope or applied couple is Q. The use of a prime refers to axis Q.

Each part is designated O at its left hand edge, L at its right hand edge, and x at a distance x from its origin O. Thus $\beta_{Lo'}$ refers to the deflection of B at its right hand edge resulting from unit applied couple at its left hand edge. Forces F have a similar notation. Thus F_{BL} refers to the force acting on the P axis at the right hand side of B.

A.3.6.2 Analysis of Undamaged Beams

A.3.6.2.1 Calculation of Dynamic Modulus

The relationship between a receptance of the whole system and frequency is shown in Figure A.3.6.1. The relationship is the same for any receptance of the whole system. The value of the receptance rises to infinity at the natural frequencies of the system; the value of w at which the receptance reaches infinity varies with the dynamic Youngs modulus, E, of the beam under test.

The value of w at the first natural frequency is known. The receptance of the whole system must thus be calculated in terms of angular frequency and dynamic modulus, and an iterative procedure used to find the implied E value.

A.3.6.2.1.1 Calculation of Receptance of the whole system

The receptance of the exciting coil, are given by (Stone, 1975)

$$\varepsilon_{oo} = \varepsilon_{LL} = -\left(\frac{1}{Pw^2} + \frac{l_c^2}{4I_c w^2}\right)$$

$$\varepsilon_{Lo} = \varepsilon_{oL} = -\left(\frac{1}{Pw^2} - \frac{l_c^2}{4I_c w^2}\right)$$

$$\varepsilon_{o'o'} = \varepsilon_{L'L'} = -\varepsilon_{o'L'} = -\varepsilon_{L'o'} = -\frac{1}{I_c w^2}$$

$$\varepsilon_{oo'} = \varepsilon_{o'o} = \varepsilon_{L'o} = \varepsilon_{oL'} = -\varepsilon_{Lo'} = -\varepsilon_{o'L} = -\varepsilon_{L'L} =$$

$$-\varepsilon_{LL'} = -\frac{l_c}{2I_c w^2}$$

In the analysis of the free-free rig:

$$\alpha = \varepsilon$$

In the analysis of the cantilever rig:

$$\alpha = 0$$

The receptance of a part of the beam, B, are given by (Stone, 1975):

$$\beta_{oo} = \beta_{ll} = -\left[F_5\left(\frac{r a^2}{s b^2} - a\right) - F_4\left(\frac{s b^2}{r a} - b\right)\right] / \Delta$$

$$\beta_{o'o} = \beta_{oo'} = -\beta_{l'l} = -\beta_{ll'}$$

$$= -\left[F_1\left(\frac{s b^2}{a} - \frac{r a^2}{b}\right) + F_3(sb + ra)\right] / \Delta$$

$$\beta_{lo} = \beta_{ol} = -\left[\sinh al\left(\frac{r a^2}{s b} - a\right) - \sin bl\left(\frac{s b^2}{r a} - b\right)\right] / \Delta$$

$$\beta_{l'o} = \beta_{ol'} = -\beta_{o'l} = -\beta_{lo'} = -F_6(ra - sb) / \Delta$$

$$\beta_{o'o'} = \beta_{l'l'} = -\left[F_4 ra\left(\frac{ra}{b} - s\right) + F_5 sb\left(\frac{sb}{a} - r\right)\right] / \Delta$$

$$\beta_{l'o'} = \beta_{o'l'} = -\left(\sinh al\ \frac{sb}{a} - \sin bl\ \frac{ra}{b}\right)(sb - ra) / \Delta$$

where :

$$a = \left[\frac{-\rho I \omega^2\left(1 + \frac{E}{\lambda_s G}\right) + \sqrt{\rho I \omega^2\left[\rho I \omega^2\left(1 - \frac{E}{\lambda_s G}\right)^2 + 4EA\right]}}{2EI}\right]^{1/2}$$

$$b = \left[\frac{\rho I \omega^2\left(1 + \frac{E}{\lambda_s G}\right) + \sqrt{\rho I \omega^2\left[\rho I \omega^2\left(1 - \frac{E}{\lambda_s G}\right)^2 + 4EA\right]}}{2EI}\right]^{1/2}$$

$$s = \frac{\rho \omega^2}{\lambda_s G b} - b$$

$$r = \frac{\rho \omega^2}{\lambda_s G a} - a$$

$$F_1 = \sin bL \sinh aL$$

$$F_2 = \cos bL \cosh aL$$

$$F_3 = \cos bL \cosh aL - 1$$

$$F_4 = \sin bL \cosh aL$$

$$F_5 = \cos bL \sinh aL$$

$$F_6 = \cos bL - \cosh aL$$

$$\Delta = \rho \omega^2 A\left[2 - 2F_2 + \left(\frac{ra^2}{sb^2} - \frac{sb^2}{ra^2}\right)F_1\right]$$

The receptances of the whole system are calculated by adding one part at a time, working from left to right, to the receptances of the system up to that point. Thus the receptance of A and B are first added, and to that sum the receptances of C are added, etc. The final calculation for the receptances of the whole system is the addition of the receptances of E to the receptances of the system A+B+C+D.

The receptance ($\alpha+\beta$) of the system A+B are given by

(Stone, 1975)

$$(\alpha+\beta)_{LL'} = (\alpha+\beta)_{L'L} = -(\alpha+\beta)_{OO'} = -(\alpha+\beta)_{O'O}$$
$$= \beta_{LL'} + [(\beta_{L'O}\beta_{LO'} + \beta_{L'O'}\beta_{LO})(\beta_{OO'} + \alpha_{LL'}) - \beta_{L'O}\beta_{LO}(\beta_{O'O'} + \alpha_{L'L'})$$
$$- \beta_{L'O'}\beta_{LO'}(\beta_{OO} + \alpha_{LL})] / [(\beta_{OO} + \alpha_{LL})(\beta_{O'O'} + \alpha_{L'L'}) - (\beta_{OO'} + \alpha_{LL'})^2]$$

$$(\alpha+\beta)_{LL} = (\alpha+\beta)_{OO}$$
$$= \beta_{LL} + [(2\beta_{LO}\beta_{LO'}(\beta_{OO'} + \alpha_{LL'}) - \beta_{LO}^2(\beta_{O'O'} + \alpha_{L'L'}) - \beta_{LO'}^2(\beta_{OO} + \alpha_{LL})] /$$
$$[(\beta_{OO} + \alpha_{LL})(\beta_{O'O'} + \alpha_{L'L'}) - (\beta_{OO'} + \alpha_{LL'})^2]$$

$$(\alpha+\beta)_{L'L'} = (\alpha+\beta)_{O'O'}$$
$$= \beta_{L'L'} + [2\beta_{L'O}\beta_{L'O'}(\beta_{OO'} + \alpha_{LL'}) - \beta_{L'O}^2(\beta_{O'O'} + \alpha_{L'L'}) - \beta_{L'O'}^2(\beta_{OO} + \alpha_{LL})] /$$
$$[(\beta_{OO} + \alpha_{LL})(\beta_{O'O'} + \alpha_{L'L'}) - (\beta_{OO'} + \alpha_{LL'})^2]$$

Thus the receptances of the whole system may be calculated in terms of angular frequency and the dynamic modulus of the beam under test.

A.3.6.2.1.2 Iteration to find Dynamic Youngs Modulus

It may be seen from Figure A.3.6.1 that the range of w in which lies the natural frequency may be detected by the change in sign of the receptance. Receptance values $(\alpha+\beta+\gamma+\delta+\varepsilon)_{OO}$ are thus calculated for a given E for 10 successive values of w, separated by δw, the initial value w_1 being lower than the true value w_T. If a change of sign from positive to negative is detected, the value of w prior to that change of sign is compared with w_T. If the two

values are within 0.05% the value of E is considered correct. The flow chart for the iteration programme is shown in Figure A.3.6.2.

This calculated value of E and the angular frequency is substituted into all the receptance values described above.

A.3.6.2.2 Calculation of the Mode Shape

The net deflection of, for example part B of the beam, at a point x, is given by:

$$u_x = \beta_{xo} F_{BO} + \beta_{xo'} F_{BO'} + \beta_{xL} F_{BL} + \beta_{xL'} F_{BL'}$$

Thus the mode shape of the three parts of the beam may be calculated from the values of the receptances at x, and the values of the forces at the junctions. The deflections of the end masses are ignored and not calculated for their length is small compared with that of the beam.

A.3.6.2.2.1 Receptance Values along the beam

The receptances at a distance x along the length of, for example part B, are given by (Stone, 1975):

$$\beta_{xo} = -\left[b\left(\frac{ra^2}{sb^2} F_5 + F_4\right)\cos bx + b\left(\frac{ra^2}{sb^2} F_1 - F_3\right)\sin bx - a\left(\frac{sb^2}{ra^2} F_4 + F_5\right)\cosh ax + a\left(\frac{sb^2}{ra^2} F_1 + F_3\right)\sinh ax \right] / \Delta$$

$$\beta_{xo'} = -\left[b\left(\frac{ra}{b} F_3 + \frac{sb}{a} F_1\right)\cos bx - b\left(\frac{sb}{a} F_5 - \frac{ra}{b} F_4\right)\sin bx - a\left(\frac{ra}{b} F_1 - \frac{sb}{a} F_3\right)\cosh ax + a\left(\frac{sb}{a} F_5 - \frac{ra}{b} F_4\right)\sinh ax \right] / \Delta$$

$$\beta_{xL} = -\left[b\left(\frac{ra^2}{sb^2}\sinh aL + \sin bL\right)\cos bx - bF_6 \sin bx - a\left(\sinh aL + \frac{sb^2}{ra^2}\sin bL\right)\cosh ax - aF_6 \sinh ax \right] / \Delta$$

$$\beta_{xL'} = -\left[raF_6 \cos bx - \left(\frac{sb^2}{a}\sinh aL - ra\sin bL\right)\sin bx - sbF_6 \cosh ax - \left(sb\sinh aL - \frac{ra^2}{b}\sin bL\right)\sinh ax \right] / \Delta$$

where the substitution constants are identical to those in A.3.6.2.1.1.

A.3.6.2.2.2. Calculation of the Forces at the Junctions

Since the system is vibrating at resonance, and the effect of damping is ignored in this analysis, no net force is applied to the system. Forces will however exist at all junctions between parts of the beam and the end masses; for compatibility the net force at a junction on a given axis must be zero.

Forces are calculated working from right to left, discarding one part of the system at a time, and are calculated in terms of the receptances of the part being discarded, and those of the whole system remaining. Thus, for example, the forces F_{DO} and $F_{DO'}$ may be calculated from the receptance $(\alpha+\beta+\gamma)$ and δ, and the forces F_{Dl} and $F_{Dl'}$. The relationships are given by (Stone 1975):

$$F_{DO} = F_{Dl}\left[\frac{\delta_{lO'}(\delta_{OO'}+(\alpha+\beta+\gamma)_{ll'})-\delta_{lO}(\delta_{O'O'}-(\alpha+\beta+\gamma)_{l'l'})}{(\delta_{OO}+(\alpha+\beta+\gamma)_{ll})(\delta_{O'O'}+(\alpha+\beta+\gamma)_{l'l'})-(\delta_{OO'}+(\alpha+\beta+\gamma)_{ll'})^2}\right]$$
$$+F_{Dl'}\left[\frac{\delta_{l'O'}(\delta_{OO'}+(\alpha+\beta+\gamma)_{ll'})-\delta_{l'O}(\delta_{O'O'}-(\alpha+\beta+\gamma)_{l'l'})}{(\delta_{OO}+(\alpha+\beta+\gamma)_{ll})(\delta_{O'O'}+(\alpha+\beta+\gamma)_{l'l'}-(\delta_{OO'}+(\alpha+\beta+\gamma)_{ll'})^2}\right]$$

$$F_{DO'} = F_{Dl}\left[\frac{\delta_{lO}(\delta_{OO'}+(\alpha+\beta+\gamma)_{ll'})-\delta_{lO'}(\delta_{OO}+(\alpha+\beta+\gamma)_{ll})}{(\delta_{OO}+(\alpha+\beta+\gamma)_{ll})(\delta_{O'O'}+(\alpha+\beta+\gamma)_{l'l'})-(\delta_{OO'}+(\alpha+\beta+\gamma)_{ll'})^2}\right]$$
$$+F_{Dl'}\left[\frac{\delta_{l'O}(\delta_{OO'}+(\alpha+\beta+\gamma)_{ll'})-\delta_{l'O'}(\delta_{OO}+(\alpha+\beta+\gamma)_{ll})}{(\delta_{OO}+(\alpha+\beta+\gamma)_{ll})(\delta_{O'O'}+(\alpha+\beta+\gamma)_{l'l'})-(\delta_{OO'}+(\alpha+\beta+\gamma)_{ll'})^2}\right]$$

As described above, for compatibility:

$$F_{Cl} = -F_{DO}$$

$$F_{Cl'} = -F_{DO'}$$

Thus the next calculation is that of the forces F_{CO} and $F_{CO'}$ using the relationships stated above, replacing the forces F_{Dl} and $F_{Dl'}$, by F_{Cl} and $F_{Cl'}$, and replacing the receptances $(\alpha+\beta+\gamma)$ and δ, by $(\alpha+\beta)$ and γ. In this way the forces at

all junctions may be calculated in terms of F_{Dl} and $F_{Dl'}$.

In order to complete the calculation of all the forces, a relationship between F_{Dl} and $F_{Dl'}$ must be found. As described above, for compatibility:

$$F_{EO} = -F_{Dl}$$

$$F_{EO'} = -F_{D.l'}$$

F_{EO} and $F_{EO'}$ are related to the receptance ε and $(\alpha+\beta+\gamma+\delta)$ and the forces F_{El} and $F_{El'}$ by the relationships above, substituting ε and $(\alpha+\beta+\gamma+\delta)$ for δ and $(\alpha+\beta+\gamma)$ and F_{El} and $F_{El'}$ for F_{Dl} and $F_{Dl'}$. However since the system is vibrating at resonance no external force is applied, and thus F_{El} and $F_{El'}$ must be zero. It is observed however that the denominator of both equations above are identical. Thus a relationship between F_{EO} and $F_{EO'}$ may be obtained, assuming F_{El} has been excited.

if: $F_{EO} = 1$

$$F_{EO'} = \frac{\varepsilon_{lO}(\varepsilon_{OO'} + (\alpha+\beta+\gamma+\delta)_{LL'} - \varepsilon_{lO'}(\varepsilon_{OO'} + (\alpha+\beta+\gamma+\delta)_{ll})}{\varepsilon_{lO'}(\varepsilon_{OO'} + (\alpha+\beta+\gamma+\delta)_{LL'}) - \varepsilon_{lO}(\varepsilon_{O'O'} + (\alpha+\beta+\gamma+\delta)_{L'L'})}$$

if: $F_{El} = 0$

The relationship between F_{EO} and $F_{EO'}$ still stands. Thus the forces at the junctions may be calculated, and a mode shape obtained on an arbitrary scale with $F_{EO} = 1$. The mode shape is scaled to the experimental mode shape by comparing the predicted maximum deflection with that observed.

A.3.6.2.3 Calculation of Specific Damping Capacity assuming Stress Independence.

The specific damping capacity is defined by:

$$\psi = \frac{\Delta U}{U}$$

Δ U is calculated from the current input to the exciting coils. The total strain energy stored is the sum of two components:

$$U = U_B + U_S$$

Both the bending and shear strain energies stored may be calculated. The separation of the two component energies is possible since the receptances $\beta_{x'}$ represent the slope resulting from the bending only; the receptances β_x represent both the bending and shear deflections.

A.3.6.2.3.1 Calculation of Bending Strain Energy Stored

The bending strain energy stored in a beam is given by:

$$U_B = \frac{1}{2}EI\int_0^l \left(\frac{d^2 u_B}{dx^2}\right)^2 dx$$

Considering for example part B; The rate of change of slope arising from bending is given by:

$$\frac{d^2 u_B}{dx^2} = \frac{d}{dx}\left(\beta_{x'o}F_{Bo} + \beta_{x'o'}F_{Bo'} + \beta_{x'l}F_{Bl} + \beta_{x'l'}F_{Bl'}\right)$$

The equations for the receptance along the beam length are given by (Stone, 1975):

$$\beta_{x'o} = -\left[-sb\left(\frac{ra^2}{sb^2}F_1 - F_3\right)\cos bx + sb\left(\frac{ra^2}{sb^2}F_2 + F_4\right)\sin bx + ra\left(\frac{sb^2}{ra^2}F_1 + F_3\right)\cosh ax - ra\left(F_5 + \frac{sb^2}{ra^2}F_4\right)\sinh ax\right] / \Delta$$

$$\beta_{x'o'} = -\left[sb\left(\frac{F_4}{sb^2} - \frac{F_5}{ra^2}\right)\cos bx + sb\left(-\frac{F_3}{sb^2} - \frac{F_1}{ra^2}\right)\sin bx - ra\left(\frac{F_4}{sb^2} - \frac{F_5}{ra^2}\right)\cosh ax + ra\left(-\frac{F_3}{ra^2} + \frac{F_1}{sb^2}\right)\sinh ax\right]\left[\frac{\rho\omega^2 A}{EI\Delta}\right]$$

$$\beta_{x'l} = -\left[sb\,F_6\cos bx + sb\left(\frac{ra^2}{sb^2}\sinh al + \sin bl\right)\sin bx - ra\,F_6\cosh ax - ra\left(\sinh al + \frac{sb^2}{ra^2}\sin bl\right)\sinh ax\right] / \Delta$$

$$\beta_{x'l'} = -\left[\left(\frac{sb}{ra^2}\sinh al - \frac{\sin bl}{b}\right)\cos bx - \frac{F_6}{b}\sin bx + \left(\frac{\sinh al}{a} - \frac{ra}{sb^2}\sin bl\right)\cosh ax + \frac{F_6}{a}\sinh ax\right]\left[\frac{\rho\omega^2 A}{EI\Delta}\right]$$

where the substitution constants are identical to those in A.3.6.2.1.1.

The integration may be carried out on a computer using Simpson's rule, and all the forces have been calculated. Thus the bending strain energy stored in the beam may be calculated.

A.3.6.2.3.2 Calculation of Shear Strain Energy Stored

The shear strain energy stored in a beam is given by:

$$U_s = \frac{1}{2}\lambda_s G A \int_0^l \left(\frac{d u_s}{d x}\right)^2 dx$$

Considering for example part B; the slope arising from shear is given by:

$$\frac{\partial w_s}{\partial x} = \left(\frac{\partial}{\partial x}(\beta_{xo}) - \beta_{x'o}\right) F_{Bo} + \left(\frac{\partial}{\partial x}(\beta_{xo'}) - \beta_{x'o'}\right) F_{Bo'}$$
$$+ \left(\frac{\partial}{\partial x}(\beta_{xl}) - \beta_{x'l}\right) F_{Bl} + \left(\frac{\partial}{\partial x}(\beta_{xl'}) - \beta_{x'l'}\right) F_{Bl'}$$

The integration may becarried out on a computer using Simpson's rule, and all the forces have been calculated. Thus the shear strain energy stored in the beam may be calculated.

A.3.6.2.4 Calculation of Stress Dependent Specific Damping Capacity

The method used to analyse the stress dependence of specific damping capacity is identical to that in previous work (Bacon 1973). The specific damping capacity is assumed to be a fourth order polnomial in stress, and five simultaneous equations are set up which are solved for the coefficients.

The separation of bending and shear deflections allows consideration of both bending and shear stress dependence. However the assumption has to be made that all energy absorption takes place from either bending or shear, when bending stress dependence and shear stress dependence are considered respectively. Although this assumption cannot be justified, it is postulated that results may at least be qualitatively relevant as as indication of the extent of dependence of specific damping capacity on either bending or shear stress.

A.3.6.2.4.1 Calculation of Bending Stress Dependence Coefficients

Consider a bending stress σ_x, acting on an element length dx, width b, height dz, at a distance z from the neutral axis;

$$dU_B = \frac{\sigma_x^2}{2E} \; b \; dx \; dz$$

The specific damping capacity of this element, assuming energy absorption arises from bending only is:

$$\psi(\sigma_x) = \frac{d(\Delta U_B)}{d U_B}$$

$$\text{therefore: } d(\Delta U_B) = \frac{\sigma_x^2}{2E} \; b \; dx dz \; \psi(\sigma_x)$$

Thus the energy dissipated in the whole beam is:

$$\Delta U_B = \int_{z=0}^{\frac{h}{2}} \int_{x=0}^{L} \frac{b}{E} \sigma_x^2 \; \psi(\sigma_x) \; \partial x \; \partial z$$

It is assumed that $\psi(\sigma_x)$ is a fourth order polnomial with respect to σ_x:

$$\psi(\sigma_x) = a_0 + a_1\sigma_x + a_2\sigma_x^2 + a_3\sigma_x^3 + a_4\sigma_x^4$$

$$\text{therefore: } \Delta U_B = \int_{z=0}^{\frac{h}{2}} \int_{x=0}^{L} \frac{b}{E} \left(a_0\sigma_x^2 + a_1\sigma_x^3 + a_2\sigma_x^4 + a_3\sigma_x^5 + a_4\sigma_x^6 \right) dx \, dz$$

$$\text{but: } \sigma_x = zE\frac{\partial^2 u_B}{\partial x^2}$$

$$\text{therefore: } \Delta U_B = \frac{a_0 b}{24} E h^3 \int_0^L \left(\frac{\partial^2 u_B}{\partial x^2} \right)^2 dx + \frac{a_1 b}{64} E^2 h^4 \int_0^L \left(\frac{\partial^2 u_B}{\partial x^2} \right)^3 dx$$

$$+ \frac{a_2 b}{160} E^3 h^5 \int_0^L \left(\frac{\partial^2 u_B}{\partial x^2} \right)^4 dx + \frac{a_3 b}{384} E^4 h^6 \int_0^L \left(\frac{\partial^2 u_B}{\partial x^2} \right)^5 dx + \frac{a_4 b}{896} E^5 h^7 \int_0^L \left(\frac{\partial^2 u_B}{\partial x^2} \right)^6 dx$$

The values of $\left(\frac{\partial^2 u_B}{\partial x^2} \right)$ may be calculated as described in A.3.6.2.3.1 and the integration may be carried out on a computer using Simpson's rule. Thus the equation is reduced to:

$$\Delta U_B = a_0 R_0 + a_1 R_1 + a_2 R_2 + a_3 R_3 + a_4 R_4$$

where R_0, R_1 etc. are calculable for a given deflection. Thus

five simultaneous equations may be set up with values of ΔU_B, which is assumed equivalent to the measured ΔU, corresponding to different deflections, and the appropriate values of R_o, R_1 etc. These equations may be solved for the bending stress dependence coefficients a_o, a_1 etc.

A.3.6.2.4.2 Calculation of Shear Stress Dependence Coefficients

Consider a shear stress, τ_x, acting on an element length dx, width b, height dz, at a distance z from the neutral axis;

$$\delta U_s = \frac{\tau_x^2}{2G} b \, \delta x \, \delta z$$

The specific damping capacity of this element, assuming energy absorption arises from shear only is:

$$\psi(\tau_x) = \frac{\delta(\Delta U_s)}{\delta U_s}$$

therefore: $\delta(\Delta U_s) = \frac{\tau_x^2}{2G} b \, \delta x \, \delta z \, \psi(\tau_x)$

Thus the energy dissipated in the whole beam is:

$$\Delta U_s = \int_{z=0}^{\frac{h}{2}} \int_{x=0}^{l} \frac{\tau_x^2}{G} b \, \psi(\tau_x) \, \partial x \, \partial z$$

It is assumed that $\psi(\tau_x)$ is a fourth polynomial with respect to τ_x:

$$\psi(\tau_x) = a_0 + a_1 \tau_x + a_2 \tau_x^2 + a_3 \tau_x^3 + a_4 \tau_x^4$$

therefore: $$\Delta U_s = \int_{z=0}^{\frac{h}{2}} \int_{x=0}^{l} \frac{b}{G} (a_0 \tau_x^2 + a_1 \tau_x^3 + a_2 \tau_x^4 + a_3 \tau_x^5 + a_4 \tau_x^6) dx dz$$

but: $$\tau_x = \frac{3}{2}\left(1 - \frac{4z^2}{h^2}\right) G \frac{\partial u_s}{\partial x}$$

therefore: $$\Delta U_s = a_0 bh \frac{3G}{5} \int_0^l \left(\frac{\partial u_s}{\partial x}\right)^2 dx + a_1 bh \frac{27G^2}{35} \int_0^l \left(\frac{\partial u_s}{\partial x}\right)^3 dx$$
$$+ a_2 bh \frac{36G^3}{35} \int_0^l \left(\frac{\partial u_s}{\partial x}\right)^4 dx + a_3 bh \frac{108}{77} G^4 \int_0^l \left(\frac{\partial u_s}{\partial x}\right)^5 dx + a_4 bh \frac{1944}{1001} G^5 \int_0^l \left(\frac{\partial u_s}{\partial x}\right)^6$$

The values of $\frac{du_s}{dx}$ may be calculated as described in A.3.6.2.3.2 and the integration may be carried out on a

computer using Simpson's rule. Thus the equation is reduced to:

$$\Delta U_s = a_o R_o + a_1 R_1 + a_2 R_2 + a_3 R_3 + a_4 R_4$$

where R_o, R_1 etc are calculable for a given deflection. Thus five simultaneous equations may be set up with values of ΔU_s, which is assumed equivalent to the measured ΔU, corresponding to different deflections, and the appropriate values of R_o, R_1 etc. .These equations may be solved for the shear stress dependence coefficients a_o, a_1 etc.

A.3.6.3 Analysis of damaged beams

All beams are tested in the undamaged condition. Thus in the analysis of damaged beams the values of E and ψ are known for the undamaged parts, parts B and D. The object is to calculate modulus and damping values for the damaged part, part C.

A.3.6.3.1 Calculation of Dynamic Modulus

The analysis is carried out by the method described in A.3.6.2.1. The known value of E for parts B and D is used in the equations, and the receptance of the whole system is calculated in terms of angular frequency, and the dynamic Youngs Modulus of part C. Iteration is carried out, as described above, to find the modulus of part C. This calculated value of E and the angular frequency is substituted into the receptance equations.

A.3.6.3.2 Calculation of Mode Shape

The mode shape is calculated as described in A,3.6.2.2, using the previously known dynamic modulus value for

parts B and D, and the value found from the iteration procedure for part C.

A.3.6.3.3 Calculation of Specific Damping Capacity Assuming Stress Independence.

The bending and shear strain energies stored for the three parts of the beam are calculated as described in A.3.6.2.3. Since the damping capacity of parts B and D is known, the energy absorbed by these parts may be calculated. This energy absorbed by parts B and D may be subtracted from the experimental total energy absorbed to obtain the energy absorbed by part C. Thus the specific damping capacity of part C may be calculated.

A.3.6.3.4 Calculation of Stress Dependent Specific Damping Capacity

It is assumed that the specific damping capacity of parts B and D is stress independent, and thus the energy absorbed by part C may be calculated as described above. This energy is then used in simultaneous equations, as described in A.3.6.2.4, to find both the bending and shear stress dependence coefficients.

Figure A.3.6.1 Variation of Receptance $(\alpha + \beta + \gamma + \delta + \varepsilon)_{oo}$ of Cantilever with Angular Frequency

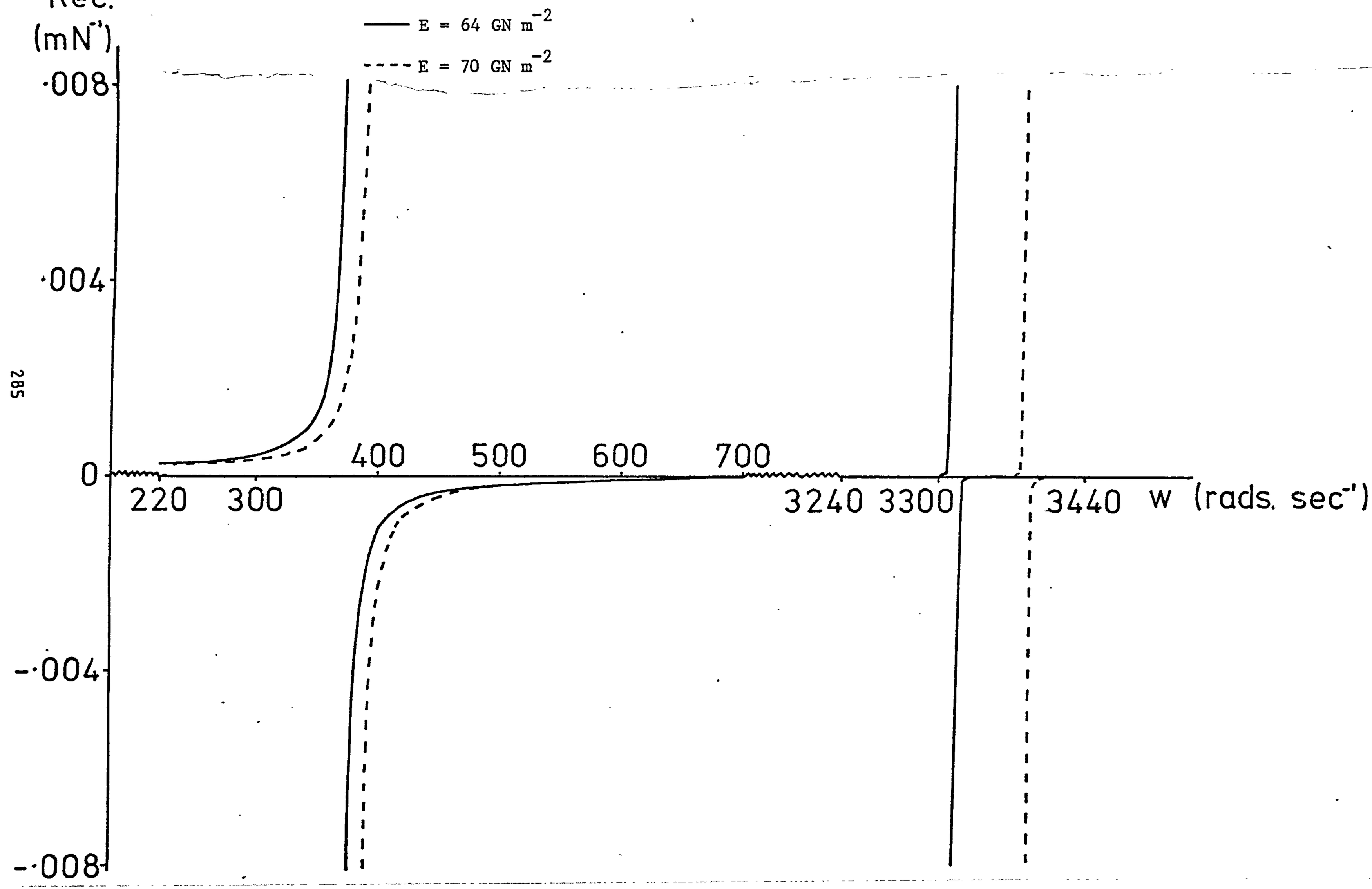

Figure A.3.6.2 Flowchart for Iteration Programme